Ga(^+) focused Ion beam irradiated Ni(_81)Fe(_19) thin films and Planar nanostructures investigated by the Magneto-Optical Kerr Effect

Faulkner, Colm Charles

Ga^+ Focused Ion Beam Irradiated $Ni_{81}Fe_{19}$ Thin Films and Planar Nanostructures Investigated by the Magneto-Optical Kerr Effect

by

Colm Charles Faulkner

A thesis submitted in partial fulfilment of the requirements for the degree of Doctor of Philosophy

Ustinov College
University of Durham

2004

Abstract

Patterned magnetic films are of interest for storing and sensing information, and possible logic applications, and find commercial applications in consumer goods such as personal computers. This thesis addresses the fast magnetic patterning of capped ultrathin $Ni_{81}Fe_{19}$ films in Chapter 5, and the patterning and controlled magnetic switching of planar nanowires in Chapter 4. Controlled domain wall switching of complex wire geometries with corner structures, artificial trapping sites, 3-terminal junctions and more complex wire circuits is described in Chapters 6-7.

The magnetic switching of planar $Ni_{81}Fe_{19}$ nanowires fabricated by 30 keV, focused ion beam Ga^+ ions was investigated, in the width range 60-500 nm. Experimentally measured wire easy axis coercivity is inversely proportional to width, similar to Stoner-Wohlfarth switching behaviour. Angular switching data for wires is presented. Significantly, wire coercivity and anisotropy field are shown to be strongly dependent on the ion beam raster direction during wire fabrication.

The controlled propagation of head-to-head domain walls in a 27 Hz anti-clockwise rotating magnetic field, through smoothly rounded corners is experimentally demonstrated. Domain wall propagation fields, 7 ± 3 Oe, just above the intrinsic domain wall coercivity were found. Using an L-shaped rounded corner geometry, the magnetic fields at which domain walls are introduced into wires and the domain wall propagation field were separated. Reproducible pinning and depinning of single domain walls on artificial domain wall traps with depths from 35-125 nm is demonstrated.

3-Terminal continuous $Ni_{81}Fe_{19}$ wire junctions, suitable for AND/OR domain wall logic operations are described, in which the magnetic switching field of the device output is strongly dependent on the number of domain walls (0, 1, or 2), at the junction. An operating field phase diagram is presented in the context of junction integration with existing domain wall logic elements.

Capped $Ni_{81}Fe_{19}$ films were ferromagnetically quenched by radiation induced transport of bilayer interfacial atoms. For $Si/Ni_{81}Fe_{19}/Al$ or $Si/Ni_{81}Fe_{19}/Au$ bilayers, the critical Ga^+ ion dose to quench ferromagnetic ordering (Φ), measured by the magneto-optical Kerr (MOKE) effect, is demonstrated to be linearly proportional to the square of $Ni_{81}Fe_{19}$ thickness, $(t_{NiFe})^2$. Therefore ultrathin-capped $Ni_{81}Fe_{19}$ films can be magnetically quenched at ion doses ~ an order of magnitude lower then $Ni_{81}Fe_{19}/Si$ samples, which are typically patterned by radiation sputtering from the vacuum-surface interface. Bilayer coercivity, uniaxial anisotropy field, remanent magnetization, and saturation magnetization as measured by MOKE, were tailored by controlled localized ion doses. Ga^+ ion doses as low as 8×10^{13} ions.cm^{-2} reproducibly quenched measured room temperature ferromagnetism in 2 nm thick buried $Ni_{81}Fe_{19}$ films. Patterning of 200 nm wide in-plane magnetized wires embedded between a non magnetic cap and substrate is demonstrated.

Declaration

I hereby declare that the work contained in this thesis is my own and has not been partially or fully previously submitted for any other degree. Use of previously published articles and reference materials is referenced in the text as appropriate.

The work of colleagues or collaborators is acknowledged where relevant. The author performed sample growth, patterning, and characterization for all results set forth here. Grazing Incidence X-Ray measurements [Chapter.2], were performed with generous help from J. D. R. Buchannan, who was solely responsible for fitting of X-Ray data.

This thesis has not been submitted in partial or full fulfilment of another degree or professional qualification.

Colm Charles Faulkner
Durham, 2004

Acknowledgements

I thank R.P. Cowburn.

I pay tribute to D. Atkinson, who was generous with time, suggestions, encouragement and enthusiasm. He is a good teacher. I acknowledge D. Allwood for always being helpful.

Gang Xiong was a pleasure to work with and M. Cooke showed me how to get my hands dirty.

J'ai appris beaucoup en partagant le bureau avec D. Petit et C. Thirion.

Matt, Paul, and Vanessa. They taught me a lot. I hope I taught them a little.

Kevin, our technician who never kept me waiting.

J. Ferré who took me into his lab in France for 4 months, and J. P. Jamet who made me feel welcome. A. Thiaville for introducing me to the world of imaging Kerr microscopy.

H. Bernas was very generous with time and suggestions in discussing ion patterning of in-plane magnetized magnetic films.

Aurelie Gentils for time consuming TEM work.

S.Giblin (SQUID), J. Buchannan (GIXR), T. Hase (GIXR), B. Tanner.

Lydia Heck for computer support.

I thank Eastgate Investments Ltd. for financial support.

Most of all I thank my parents who worked hard to give me opportunities they did not have.

List of Publications

Artificial Domain Wall Nano-Traps in $Ni_{81}Fe_{19}$ Wires
C.C. Faulkner, M.D. Cooke, D.A. Allwood, D. Petit, D. Atkinson, R.P. Cowburn
Journal of Applied Physics, **95**, 6717 (2004)*

Controlled Switching of Ferromagnetic Wire Junctions by Domain Wall Injection
C.C. Faulkner, D.A. Allwood, M.D. Cooke, Gang Xiong, D. Atkinson, R.P.Cowburn
IEEE Transactions on Magnetics, **39**, 2860 (2003)

Nanometer scale patterning using focused ion beam milling
D. Petit, C. C. Faulkner, S. Johnstone, D. Wood, R. P. Cowburn
Review of Scientific Instruments, **76**, 26105 (2005) *

Characterisation of submicrometer ferromagnetic NOT gates
D.A.Allwood, Gang Xiong, M.D.Cooke, C.C.Faulkner, D.Atkinson, R.P.Cowburn
Journal of Applied Physics, **95**, 8264 (2004)*

Magnetic domain wall dynamics in a Permalloy nanowire
D. Atkinson, D.A. Allwood, C.C. Faulkner, Gang Xiong, M.D. Cooke, R.P. Cowburn
IEEE Transactions on Magnetics, **39**, 2663 (2003)

Magnetic domain wall dynamics in a sub-micrometre ferromagnetic structure
D. Atkinson, D.A. Allwood, Gang Xiong, M.D. Cooke, C.C. Faulkner, R.P. Cowburn
Nature Materials **2**, 85 (2003)

Thin single layer materials for device applications
M.D. Cooke, D.A. Allwood, D. Atkinson, G. Xiong, C.C. Faulkner, R.P. Cowburn
Journal of Magnetism and Magnetic Materials, **257**, 387 (2003)

Shifted hysteresis loops from magnetic nanowires
D.A. Allwood, N. Vernier, G. Xiong, M.D. Cooke, D. Atkinson, C.C. Faulkner, R.P. Cowburn
Applied Physics Letters, **81**, 4005 (2002)*

Submicrometer ferromagnetic NOT gate and shift register
D.A. Allwood, Gang Xiong, M.D. Cooke, C.C. Faulkner, D. Atkinson, N. Vernier, R..P. Cowburn
Science, **296**, 2003 (2002)

* Also published electronically as a selected highlight: Virtual Journal of Nanoscale Science & Technology, www.vjnano.org/nano

Contents

"...that now is magnetism.
Back of everything magnetism.
Earth for instance pulling this and being pulled.
That causes movement."

Ulysses, James Joyce

Chapter 1. Aspects of Ferromagnetism

1.1 Introduction

In magnetism, reducing dimensions of bulk systems, to continuous thin-films and layered media, to sub-micron structures and 1-d particles has led to a wealth of new discoveries and observations of new and interesting physical phenomena. Magnetic applications, from field sensors, to bi-polar memory storage bits are increasingly guided by a deeper understanding of underlying physical processes. The study of magnets of reduced dimensions can lead to new discoveries, enhanced understanding of existing physical phenomena, and the prospect of potentially useful applications and technologies.

This chapter aims to give a summary of some of the phenomena relevant to ferromagnetism in systems with reduced dimensions. Section 1.2 briefly gives a treatment of key developments in ferromagnetism in the last 100 years. These ideas are developed in greater theoretical detail in Section 1.3, where the physics of domains, domain boundaries, dynamics, and switching mechanisms are treated. In Section 1.4, the idea of reducing the dimensions of a ferromagnetic system, and some of the characteristic length-scales are addressed. New phenomena can result with reduction of length scales. Several cases are treated to underline to the reader the variety of exciting effects that become evident on these lengthscales.

1.2 Historical Perspective

Ferromagnetic materials possess a spontaneous magnetization – small volumes possess a magnetic moment per unit volume. Weiss in 1907 proposed the existence of an internal "molecular" field in ferromagnets to explain magnetic hysteresis, and the fact that all ferromagnets become paramagnetic above a finite temperature, the Curie

temperature. He proposed there was a certain ordering field in ferromagnets to align the magnetic dipoles of atoms in preferred directions, opposing thermal fluctuations. The fact that hysteresis curves can have many different shapes was explained by the division of finite volumes of a ferromagnet into areas of aligned magnetization, called domains. Each domain could be magnetized to saturation for a given temperature below the Curie point, M_s(T), where M_s is saturation magnetization and T is temperature, but could have different directional orientations [Aharoni 2000].

The domain theory of Weiss was expanded via the wall concept of Landau and Lifshitz in 1935, and had gained experimental validation through the experimental switching studies in iron whiskers performed by Sixtus and Tonks [Sixtus/Tonks 1931]. Thus the study of magnetic domains, their configuration, domain boundaries and their interaction with an externally applied field became a research field in it's own right.

Bitter patterning facilitated the microscopic study of domain wall motion in thin film samples, from the 1940's [Williams 1949], and this experimental method was soon complimented by other optical techniques such as the Kerr effect [Williams 1951], which eventually permitted the completion of many important dynamic studies [Konishi 1971] in thin films such as NiFe. Other magnetometry methods include ferromagnetic resonance and torque magnetometry.

One trend in magnetism in the 20th century is the fabrication, measurement and investigation, of magnetic systems with lower critical dimensions, quicker switching times, and increasing geometrical complexity. These developments have in part been facilitated by improving fabrication and microscopy techniques. Researchers can now avail of topographical and magnetic microscopy at atomic resolution, due to the development of the scanning probe microscope, for example [Pratzer 2001], with the

associated magnetic (MFM) and atomic force microscopies (AFM). Lorentz microscopy [Kirk 1999], and transmission electron TEM), use the electron to probe magnetic and structural properties of samples. DC microscopy (micro-SQUID devices are now capable of probing states of single nanomagnets, and of operating above the critical superconducting temperature [Thirion 2002]. Many reviews and texts treat modern magnetic microscopy techniques, including detail of dynamic and optical techniques [Hubert 1998][Freeman 2001].

1.3 Micromagnetics

1.3.1 Domain Theory

Lifshitz in 1935 proposed that magnetic domains originate from the minimization of the magnetostatic energy stemming from the magnetic dipolar interaction. Domain configurations are contingent on which of four principal energy terms are dominant – exchange, anisotropy, Zeeman, and demagnetizing. The domain configuration is determined by a competition between sample geometry, material constants, and what the magnetic history is. Domain structure originates in the possibility of lowering the energy of a system [Kittel 1949].

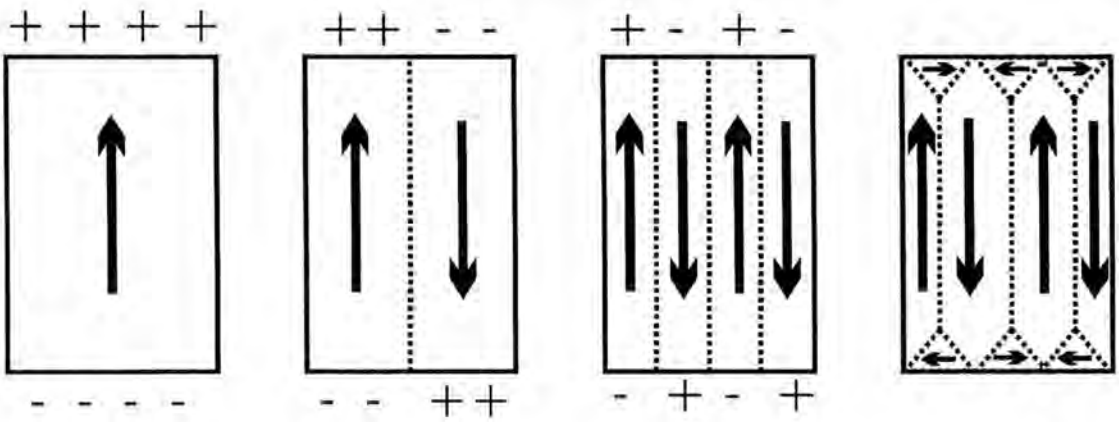

Figure 1.1: Domain configurations in a rectangular element. + and – represent surface free charges. Domains are formed to reduce these free charges.

Exchange Energy

Assume magnetization to be a continuous vector field $M(\mathrm{r})$ with r the position vector. Thus we can write:

$$M(\mathrm{r}) = M_s \mathrm{m}(\mathrm{r});\ \mathrm{m} \bullet \mathrm{m} = 1 \qquad [1.1]$$

M_s is the spontaneous magnetization. A fundamental ferromagnet property is a preference for a given magnetization orientation, deviations from this direction cost an energy penalty which may be described by a "stiffness." This is the exchange energy, proportional to the cosine of the angle between two spins and first proposed by Vleck. Exchange energy favours uniform magnetization without regard for direction – it tries to align spins in a ferromagnet. It is a short-range effect, decaying rapidly with distance. This force, an electrostatic effect between two interacting spins, S_i and S_j can be written as a Hamiltonian:

$$E_{Exchange} = -\sum_{ij} J_{ij} S_i \bullet S_j \qquad [1.2]$$

The coefficients J_{ij} are referred to as the exchange integrals (positive for ferromagnetic ordering), and spins are assumed not to interact with themselves. However, consider a lattice of a large number of interacting spins. A "*molecular field approximation*" or "*mean field approximation*" must be used to solve the system due to the large number of elements present in this real system – a quantum mechanical solution is too detailed or intricate to perform on many body systems.

One spin may be tagged and investigated in detail, while a mean value (the quantum-mechanical expectation value) is ascribed to others. Therefore, discrete exchange may be represented as:

$$-\sum_{ij} J_{ij} S_i \bullet S_j \rightarrow -JS^2 \sum_{neighbours} \cos\varphi_{ij} \qquad [1.3]$$

where φ_{ij} is defined as the angle between adjacent spins i and j. If φ_{ij} is assumed to be sufficiently small, then it may be rewritten as $\cos\varphi = 1 - 1/2\varphi^2$, and

$$\varphi_{ij}^2 \cong \left| \vec{m}_i - \vec{m}_j \right|^2 \cong \left| \vec{r}_{ij} \bullet \vec{\nabla} m \right|^2 \Rightarrow [\nabla m_x^2 + \nabla m_y^2 + \nabla m_z^2] \qquad [1.4]$$

Here $\vec{r}$ is a position vector joining the lattice points i and j. Therefore the exchange energy density is expressed as:

$$W_{Exchange} = (JS^2)/a\, k_{neighbour} [\nabla m_x^2 + \nabla m_y^2 + \nabla m_z^2] \qquad [1.5]$$

Where $k_{neighbour}$ is the number of nearest neighbours, i.e. for simple cubic, bcc, and fcc crystals, 1, 2, and 4 respectively, and "a" is the length of the edge of the unit cell. It is convenient to define an exchange constant or stiffness constant, A:

$$A = (JS^2)/a\, k_{neighbour} \qquad [1.6]$$

$W_{Exchange}$ may be expressed as an integral over an entire body, so that for cubic crystals:

$$E_{Exchange} = \int_V W_{Exchange}\, dV \qquad [1.7]$$

Anisotropy Energy

Anisotropy energy is dependent on the orientation of the magnetization relative to the structural or crystalline axes, and originates locally on the atomic level. The magnetization of a sample depends on the direction in which it is measured. We can also differentiate between crystal and induced anisotropies; the bulk anisotropy is developed along the crystallographic main axes of the crystal.

The energy density for a cubic symmetry is typically represented as:

$$W_{Anisotropy} = K(\alpha_x\alpha_y + \alpha_y\alpha_z + \alpha_z\alpha_x) \qquad [1.8]$$

Here α represents the x, y, and z direction cosines relative to the crystalline axis, and K is the anisotropy constant. The following forms may be employed in the uniaxial case:

$$W_{Anisotropy} = K \sin^2\theta \qquad [1.9]$$

$$W_{Anisotropy} = + K_1\cos^2\theta + K_2\cos^4\theta + \ldots \qquad [1.10]$$

Here θ is the angle between the easy direction and the sample magnetization. Higher order terms in K are generally only significant at low temperatures. Thus to a good approximation, one "easy-axis" exists, with 2 energy minima, leading to hysteresis effects. It is convenient to express anisotropy in terms of an effective field, H_k:

$$H_k = 2K/\mu_0 M_s \qquad [1.11]$$

The permeability of free space, $\mu_0 = 4\pi \times 10^{-7}$ H/m. Anisotropy can originate in crystal symmetry, shape, stress, or directed atomic pair ordering. The crystal or magnetocrystalline anisotropy is the only anisotropy component intrinsic to a material. For example surface anisotropy terms can exist due to non-symmetrical atomic environments, and thus different spin-orbit coupling. Alternately interfacial anisotropies may be due to large growth induced strains. Anisotropy may be induced, for example by applying mechanical stress [Sixtus/Tonks 1931], or by thin film growth in a magnetic or even electric field, or with the sample oriented at an angle to the growth direction [Aharoni 2000].

Zeeman Energy

Magnetic field can be resolved into an external field and internal field. Zeeman energy (E_{Zeeman}) is the magnetic potential energy due to an externally applied field, H_{ext}, i.e. spins couple to the externally applied field. :

$$E_{Zeeman} = -\mu_0 \int H_{ext} \bullet M \, dV \qquad [1.12]$$

For a sufficiently high applied field, H_{ext}, the magnetization of a particle or an assemblage or particles is generally aligned with the field.

Demagnetizing Field Energy

The demagnetizing field energy, E_{Demag}, results from interaction between spins and the field from all other spins. It tries to avoid uncompensated spins at a sample surface (pole avoidance principle) and is largely concerned with sample boundaries. Each single domain produces free surface magnetic poles (North and South), which give rise to stray fields, and therefore magnetostatic energy. It is this dipole-dipole force that is responsible for the formation of domains. The dipole-dipole force is also dependent on sample shape (the actual domain configuration is also partially determined by the total anisotropy energy). The cost of forming a domain wall is offset by the reduction in the demagnetisation energy. We may write:

$$E_{Demag} = (\mu_0/2)N_D M^2 \qquad [1.13]$$

In this instance, N_D is a demagnetizing factor depending on the shape of the sample. The contribution of the "internal field" per volume is much lower than that of the Weiss field, explaining why large samples can become demagnetized, while smaller samples in general favour a single domain state.

To obtain the stray field energy, it is convenient to start from Maxwell's equations:

$$\mathrm{div}B = \mathrm{div}(\mu_0 H + J) = 0 \qquad [1.14]$$

The magnetic polarization, $J = \mu_0 M$. We define as the stray field H_d the field generated by the divergence of the magnetization J:

$$\mathrm{div}H_d = -\mathrm{div}(J/\mu_0) \qquad [1.15]$$

The energy connected to the stray field is:

$$E_d = \frac{1}{2}\mu_0 \int_{allspace} H_d^2 dV = -\frac{1}{2}\int_{sample} H_d \bullet J dV \qquad [1.16]$$

The first integral extends over all space; it shows that the stray field energy is always positive, and is only zero if the stray field itself is zero everywhere. The second integral is mathematically equivalent for a finite sample. Using potential theory, the reduced volume charge density λ_v and the surface charge density σ_s are defined in terms of the reduced magnetization, eqn. 1.1, $m(r) = J(r)/J_s$.

$$\lambda_v = -\text{div } m \qquad [1.17]$$

$$\sigma_s = m \bullet n \qquad [1.18]$$

where n is the outward directed surface normal. With these quantities the potential of the stray field at potition r is given by the integral over r′:

$$\Phi_d(r) = \frac{J_s}{4\pi\mu_0}\left[\int \frac{\lambda_v(r')}{|r-r'|}dV' + \int \frac{\sigma_s(r')}{|r-r'|}dS'\right] \qquad [1.19]$$

From this expression the stray field can be derived by:

$$H_d(r) = -\text{grad}\,\Phi_d(r) \qquad [1.20]$$

Another integration yields the stray field energy:

$$E_d = J_s\left[\int \lambda_v(r)\Phi_d(r)dV + \int \sigma_s(r)\Phi_d(r)dS\right] \qquad [1.21]$$

Therefore both volume and surface integrals are involved, and the stray field energy calculation amounts to a six-fold integration if volume charges λ_v are present.

The above two equations represent closed form solutions for the potential and demagnetizing fields. The total energy of the system involves an integral over the volume as follows:

$$E_d = \frac{1}{2}\mu_0 \int_{allspace} H_d^2 dV \qquad [1.22]$$

Calculations concerning this energy term rapidly become quite complex, because it is a long-range energy term, defined by a six-fold integral in three dimensions. This contrasts with the exchange term, which decays on an exponential length scale and is strongest interacting with nearest neighbours, or next nearest neighbours.

Total Energy

Thus the total free energy of a typical ferromagnetic system, $\sum E$, is expressed as:

$$\sum E = E_{Exchange} + E_{Anisotropy} + E_{Zeeman} + E_{Demag} \qquad [1.23]$$

Strictly speaking, a fluctuating thermal energy term should be considered, which may be included in micromagnetics calculations, in the form of a field randomly fluctuating over time. In addition, other energy terms such as the magnetoelastic energy can to be considered. Magnetoelastic energy is that part of the energy of a crystal which arises from the interaction between the magnetization and the mechanical strain of a system, and is defined to be zero in an unstrained lattice, and in general is small with respect to the other energy terms.

1.3.2 LLG Dynamics

Dynamic effects are of vital importance in the study of small magnetic particles. Magnetic switching events can now be measured on timescales of the order of picoseconds, yet the data recording industry requires magnetic bits to be thermally stable for at least 10 years, and magnetic processes in rocks can take place over millions of years.

Consider a magnetic vector, M, whose response we want to study over time in the presence of an externally applied H field. Dynamically, the angular momentum

connected with magnetic moment will lead to a gyrotropic reaction if a torque (M × H) is applied:

$$dM/dt = \gamma M \times H \qquad [1.24]$$

Here γ is the gyromagnetic ratio, $\gamma = \mu_o ge/2m_e$. The value of the spectroscopic splitting factor, g, can be taken as 2, for a typical 3d ferromagnetic material, such as Permalloy, giving $\gamma = 1.76 \times 10^7$ $Oe^{-1}s^{-1}$. The mass of the electron is m_e, "e" the charge of an electron, and μ_o is the permeability in a vacuum. This equation describes the precession of the magnetization vector about a magnetic field, over time t.

Using this equation, the angle between magnetization and field remains invarient, because no losses have been considered, so the length of the vector M never changes. From experiment, magnetization is known to decay over time. Losses can arise from eddy currents, diffusion, spin scattering, and sample imperfections. Even idealised samples, have an intrinsic loss, represented in the Landau-Gilbert-Gilbert, also known as the LLG equation. In this equation, a dimensionless empirical damping factor is introduced, α, to describe local dissipative phenomena, like the relaxation of magnetic imputities, or scattering of spin waves on lattice defects.

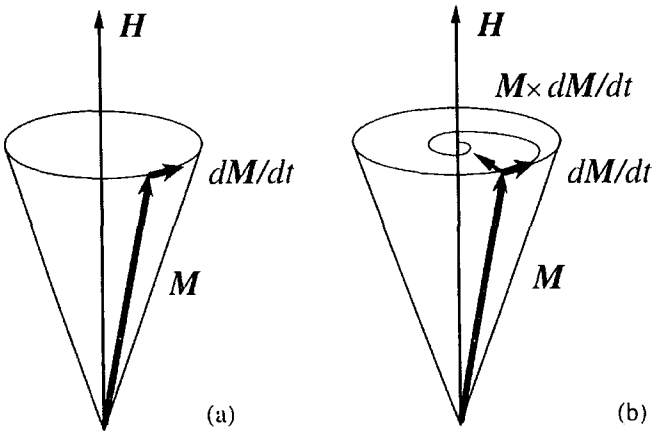

Figure 1.2: Precessional motion of the magnetization vector M, over time t, in the presence of an applied field. The case without damping present is shown in (a), and with damping present (b). After [Miltat 2002].

The original Landau-Lifshitz equation of motion is expressed as:

$$\dot{M} = -\gamma_{LL} M \times H_{eff} + \alpha_{LL} M \times (M \times H_{eff}) \qquad [1.25]$$

$\dot{M}$ describes the evolution of system magnetization over time in the presence of an effective field, H_{eff}. The effective field acting on a spin,

$$H_{eff} = -\frac{1}{\mu_0} \frac{\partial E}{\partial M} \qquad [1.26]$$

Thus the damping term allows the magnetization to align itself with the effective field. The Gilbert expression [Gilbert 1955] is a variant of the original Landau-Lifshitz expression, and is written as:

$$\dot{M} = -\gamma_G M \times H_{eff} - \alpha_G M \times \dot{M} \qquad [1.27]$$

The two forms can be shown to be equivalent for low damping systems, with the Gilbert equation often being preferred for higher damped systems. For a detailed discussion of these equations see for example [Baryakhtar 1997]. Neither Gilbert or Landau-Lifshitz equations account for temperature effects.

1.3.3 The Single Domain Particle

Single Domain

In bulk ferromagnets it is energetically favourable to form domains to reduce the magnetostatic energy. If a magnetic particle has sufficiently reduced dimensions, it is not energetically favourable to support domain boundaries. Brown's fundamental theorem notes that the state of lowest free energy of a ferromagnetic particle is one of uniform magnetization if the particle is sufficiently small [Brown 1968], thus it may be dubbed "single domain."

In the ground state the magnetization should be nearly spatially invariant across the whole particle, and magnetization reversal generally takes place by rotation

in unison - the entire magnet behaves as a giant dipole. For single particle behaviour to be supported particle shape and size are important, as are material constants.

The exchange energy tends to dominate in small particle sizes, helping to align spins tightly parallel to each other. Typically these particles are small (dimensions ~order of magnitude) relative to the magnetostatic exchange length, $\delta = (A/\mu_0 M_s^2)^{1/2}$ of the parent material, and they tend to have higher switching fields than thin films for example. The exchange length is the length below which atomic exchange interactions dominate magnetostatic fields. Using parameters appropriate for $Ni_{81}Fe_{19}$, $A = 1.3 \times 10^{-11}$ J/m and $M_s = 8.0 \times 10^5$ A/m, gives a value of $\delta \sim 4.0$ nm. Structures of this type can be extremely sensitive to geometrical modification - small variations in critical dimensions can have a profound impact on the ground state spin configuration, anisotropy field, and switching field [Cowburn 1999][Cowburn 2000].

Stoner-Wohlfarth

The Stoner-Wohlfarth (S-W) model allows calculation of the hysteresis of small, thermally stable magnetic particles [Stoner/Wohlfarth 1948]. In this model, the exchange energy of the system under consideration is deemed to be constant - spins remain collinear. Only the anisotropy energy of the particle, and an interaction with the applied field need to be considered. The S-W theory assumes that a material is made up of small particles, which are sufficiently separated from each other so that they can be treated as non-interacting.

Consider a particle with uniaxial anisotropy, and an easy axis at some angle ψ to the applied H field. The magnetization of the particle has an angle θ to the easy axis, and $(\theta - \psi)$ to the applied field. The magnetic moment of the particle is $M_s V$, where V is the particle volume. Assuming that the atomic magnetic moments always

remain parallel [coherent rotation, Section 1.3.5], the energy of the particle is simply the sum of the anisotropy and field energies.

$$E = KV\sin^2\theta - M_sVH\cos(\theta - \psi) \qquad [1.28]$$

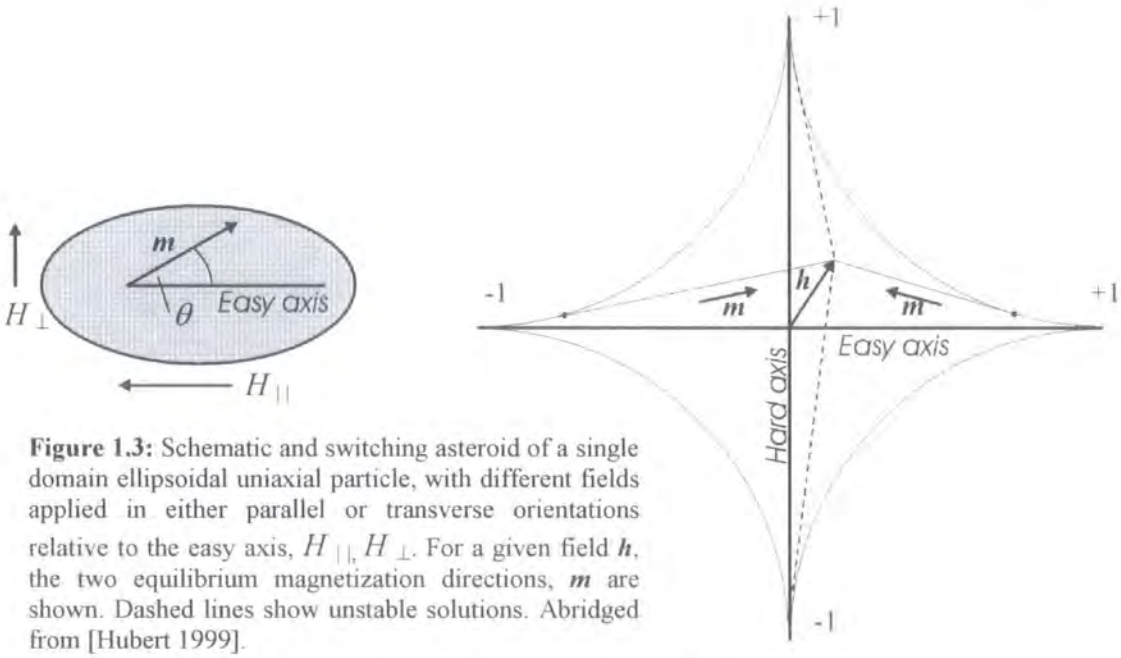

Figure 1.3: Schematic and switching asteroid of a single domain ellipsoidal uniaxial particle, with different fields applied in either parallel or transverse orientations relative to the easy axis, $H_{||}$, $H_{\perp}$. For a given field $\boldsymbol{h}$, the two equilibrium magnetization directions, $\boldsymbol{m}$ are shown. Dashed lines show unstable solutions. Abridged from [Hubert 1999].

The orientation of the magnetic moment is determined by minimizing E, therefore setting $dE/d\theta = 0$.

$$\frac{dE}{d\theta} = 2KV\sin\theta\cos\theta + M_sVH\sin(\theta - \psi) = 0 \qquad [1.29]$$

In general there are 4 solutions to this equation, two minima, separated by two maxima. Considering the case where $\psi = 0$, when the easy axis becomes aligned with the field. The expression reduces to:

$$2KV\sin\theta\cos\theta + M_sVH\sin(\theta) = 0 \qquad [1.30]$$

This equation has solutions at $\sin\theta = 0$, *i.e.* $\theta = 0$ or π. For magnetization to alternate between these two energetically preferred configurations it must pass over the energy barrier posed by the hard axis.

The maximum coercive force of a particle, H_c, can thus be expressed as $2K/M_s$, and it is noted that the coercive force decreases at some angle ψ. S-W theory is extensively used - as it is quite a simple formalism it can be extended. It is however, challenging to quantitively match experimental data exactly to this theory – in addition to thermal effects, a quantitive understanding of many other factors such as impurities, lattice imperfections, internal strains, roughness, and thickness inhomogeneity is needed.

1.3.4 Domain Boundaries

Sixtus and Tonks attributed the idea of a boundary between areas of opposing magnetization, which undergoes displacement in an applied H field, to Langmuir. A domain wall is the transition region which separates adjacent domains magnetized in different directions. In general the domain wall width will be determined by energy minimization considerations.

In the past domain walls had often been quite difficult to isolate and study experimentally at meaningful resolution. Micromagnetics calculations were recently carried out on the configuration of head-to-head domain walls at NIST [McMichael 1997]. It is a subject well suited to micromagnetic modelling due to the lower computational overhead required to study domain wall structure as opposed to more spatially extended geometries. Computationally a high mesh density can be employed, while still keeping the number of cells employed in the calculation to a manageable, but meaningful number.

The change of spin direction in the transition region does not tend to take place over a single atomic layer – rather a less abrupt change occurs, in order to reduce the exchange energy. See Figure 1.4.

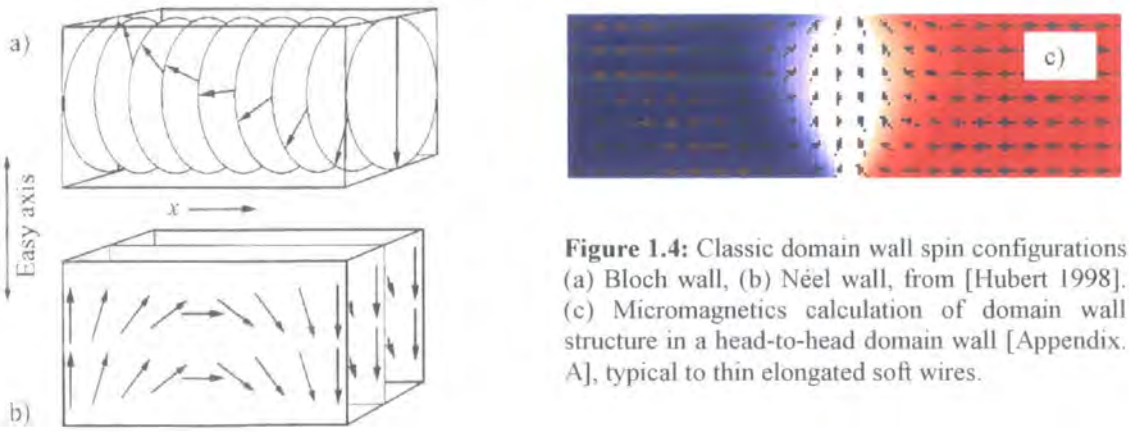

Figure 1.4: Classic domain wall spin configurations (a) Bloch wall, (b) Néel wall, from [Hubert 1998]. (c) Micromagnetics calculation of domain wall structure in a head-to-head domain wall [Appendix. A], typical to thin elongated soft wires.

Areas of uniform magnetization tend to grow by the displacement of these domain walls. Magnetic domain wall configurations are contingent on the magnetic material properties in question, and geometrical considerations, and are vulnerable to influence from stray fields and other walls.

Permalloy polycrystalline films have low intrinsic anisotropy and generally support either Bloch, cross-tie, or Néel walls as a function of decreasing thickness. Symmetric Néel walls are observed in NiFe films of thickness under 30 nm as demagnetizing fields force magnetization in-plane.

Due to the effects of spatial confinement, for the wire widths, w, and thicknesses, t, considered here [typically w = 55-600 nm, t = 5 nm] the domain wall type is known to be a head-to-head domain wall. (The length of wires is very large with respect to other dimensions and so does not influence domain boundary configuration). Vortex and multiple vortex-type configurations may be energetically favoured in thicker wires. The domain wall width, W_{dw} from a one-dimensional model may be expressed as follows:

$$W_{dw} = \pi(A/K)^{1/2} \qquad [1.31]$$

For many of the patterned wire systems considered in this work, the micromagnetic structure of the domain wall may be quite highly influenced by wire geometry (for example as it propagates through corners, and interacts with trapping sites and other domain walls). Additionally one notes that a propagating wall will not have the same structure as a stationary wall for two reasons – one is the effect of the applied field and the other is the gyromagnetic effect.

1.3.5 Magnetization Reversal Modes

Much of the initial analytic work on magnetization reversal modes was performed on two model systems – an infinite cylinder and a sphere [Frei 1957]. An infinite cylinder with no imperfections, has a magnetostatic energy of zero, because there are no free poles.

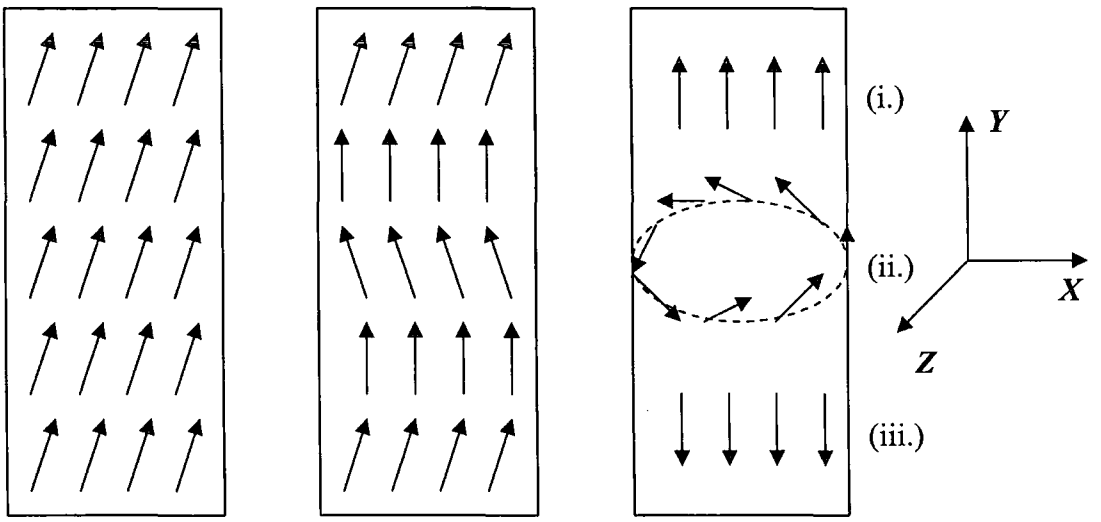

Figure 1.5: Magnetization reversal modes for an ideal infinite cylinder. (a) represents spins rotating in unison, (b) magnetization buckling, and (c) the reversal steps (i)-(iii) involved in magnetization curling.

Considering an infinite cylinder and the sphere nucleation fields, H_n, (the field at which spins of a previously saturated ferromagnetic particle cease to be aligned)

were calculated analytically assuming three mechanisms of magnetization reversal; spin rotation in unison, magnetization curling, and magnetization buckling.

Spin rotation in unison occurs in small particles, where all spins are coupled, and was already extensively treated in the work of Stoner and Wohlfarth. In the case of magnetization curling, magnetization changes occur by spin rotation from the z-axis to a plane perpendicular to the radius. This is demonstrated schematically in steps (i)-(iii) of Fig. 1.5 which shows two ground state opposing magnetization orientations and an intermediate spin configuration. Magnetization buckling describes spin reversal confined to the x plane alone, by a type of rippling with a given wavelength. Which magnetization reversal mechanism dominates was demonstrated to be a function of sample geometry (i.e. radius) and the strength of the exchange interaction. Consider an elongated wire platelet with magnetization constrained to lie parallel to the long axis, in this case the y-axis. Consider a system with $t < w << l$, representing thickness, width and length respectively. Such a system has free poles, and a demagnetizing energy. The magnetic ground state is the single domain state - magnetization is constrained to lie in-plane.

Reversal in these types of system is by an incoherent reversal process – for low l/w (aspect ratio), this reversal has mode has been classified as a special type of buckling [Yuan 1992]. This reversal mode means magnetic moment is not oriented in the z-direction during reversal (being too energetically costly).

Wernsdorfer demonstrated that in thermally activated studies of high aspect ratio elongated Ni electrodeposited wires of widths from 40-100 nm magnetization reversal was initiated at a volume 200 times smaller than the volumes of the wires [Wernsdorfer 1996]. Elongated wires with free poles are reversed by a nucleation-propagation process, not treated in the Frei model. Wernsdorfer showed the number of

sites for nucleation increased as a function of wire radius. Above an activation threshold or field energy, localised reversal events occur either at wire ends (where all spins may not be full aligned with the sample easy axis and thus "see" more of the applied field), or in the presence of a defect or contaminant causing a local softening of the magnetic environment. When the external field is applied parallel to the magnetization of one domain, the spins inside both domains experience no torque resulting from the field, simply because their directions are either parallel or antiparallel to the field. Since the spins inside the domain walls do make some angle with the field, under torque, they start to rotate towards the field direction. Resulting from rotation of the spins inside the wall, the centre of walls becomes displaced, resulting in an increase in the volume of the domain with spins aligned parallel to the applied field, at the expense of spins magnetized in the opposing orientation. The process is known as domain wall displacement, and over time the entire wire becomes reversed in this manner.

1.4 Mesomagnetism

1.4.1 Critical Length Scales

As one reduces the dimensions of magnetic systems from bulk crystals, to 2-D thin films, to isolated particles, new phenomena may be observed as system dimensions are of the order of several characteristic length scales. The length scales addressed in this thesis are from approximately 10 inter atomic distances to a few tens of microns. The exchange length, domain wall width, and domain size are some fundamental length scales in mesoscopic Permalloy systems, and are driven by energy minimization considerations.

Another important characteristic length scale is the spin diffusion length – this is the average distance that a spin can travel before it flips, driven by diffusion

considerations. This length is a direct result of diffusion processes for momentum and magnetization and can be understood in terms of a random walk model. However transport is not directly addressed in this thesis.

If one of the dimensions of a bulk magnet is reduced to nanoscale dimensions, a thin film is created. Now energy terms may be considered in terms of energy per unit volume, or energy per unit surface. In general a reduction in the system thickness will result in an increased importance of the system surface boundaries. As one or more dimensions of a system are reduced, it is also interesting to either fabricate layered or patterned structures of increasing complexity.

Fabrication of layered media can result in phenomena such as shifted or "displaced" hysteresis loops relative to zero field, in exchange coupled, or 'exchange-biased' systems of ferromagnetic and anti-ferromagnetic materials [Meiklejohn 1956]. Bean and Meiklejohn first observed this effect in Co particles encased in a CoO oxide layer.

By reducing film lateral dimensions, it is possible to pattern thin films - structures commonly studied include wires, dots, nanojunctions, and wire circuits. It is interesting to study the magnetic and transport properties of such systems, and the reduced dimensionality makes it possible to engineer spin orientation and hence switching mechanisms and switching field to a high level of precision.

However in such systems, defects, grain boundaries, surface and interface roughness may all have pronounced effects. For some recent review articles of magnetic systems of reduced dimensions, refer to for example; [Bobo 2004][Grünberg 2001][Skomski 2003]. The rest of this section details some phenomena that become apparent in magnetic systems of reduced dimensions, which can either lead to new applications – giant magnetoresistance (GMR), perpendicular

magnetic anisotropy (PMA), or pose fundamental limits on existing or future technologies – current induced switching (CIS), and superparamagnetism.

1.4.2 Giant Magnetoresistance

Magnetoresistance is a transport property defined as the change of the resistance of a given material under an applied magnetic field, and is of critical importance for modern device applications. The critical length scale is the spin diffusion length, l_{sd}. Giant magnetoresistance (GMR) arises as a result of spin dependent transport within a layered or granular system or wires. Spins can be scattered differently depending on the relative orientations of magnetic layers, leading to different resistivities for different magnetic configurations [Baibich 1988]. For the normal effect the resistivity is highest when adjacent layers are anti-aligned. Layers with aligned magnetic moments have less scattering at the interfaces, longer mean free paths and lower resistance. The effect is more pronounced if the layers are thinner than the spin diffusion length, which becomes the defining length scale of these systems. For GMR studies, differing geometries exist, such as CIP (current in plane), and CPP (current perpendicular to plane). CPP systems have been shown to have a more pronounced GMR effect, however the CIP geometry may facilitate easier fabrication and straightforward voltage measurements. In magnetoresistive multilayers, you get increasing MR with decreasing temperature, decreasing film thickness, and an increased number of layers. If one layer is made magnetically harder by exchange pinning it to an antiferromagnet, or by varying layer thickness, then it is known as a spin valve.

IBM introduced GMR read-write heads into hard disks in 1997. GMR sensors are also available commercially in a number of field and motion sensors. Some other forms of magnetoresistance are worth mentioning:

Anisotropic magnetoresistance (AMR) measures the change in resistance when the current flows parallel to the magnetization and when it flows perpendicular. AMR in a NiFe system may only be about 1 %, but the resistance measurements can be made with an accuracy of about one part in 10^5. AMR reflects the distortion of electron clouds due to spin orbit coupling. Tunnelling magnetoresistance (TMR) combines quantum tunnelling with magnetoresistance, and values of over 80 % have been obtained at room temperature. The defining length scale is the tunnel barrier. Colossal magnetoresistance (CMR) is a specialised form of magnetoresistance pertaining mostly to a group of mixed valence manganites with a perovskite structure. The topics of domain wall magnetoresistance and point contact magnetoresistance, in spatially confined or constricted geometries have exploded in recent years. Spatial confinement reduces wall critical dimensions, leading to increased MR effects through the wall. The domain wall effectively replaces the non-magnetic interface in a layered GMR structure. For a summary of some of the major experimental results see for example, [Xu 2004].

1.4.3 Perpendicular Magnetic Anisotropy

This is an effect where the direction of the magnetization vector over an entire thin film or nanostructure may be turned from in-plane, to out of plane, purely by the addition of an upper interface. Surface or interface anisotropy was seen experimentally for the first time in 1968. The presence of interfaces is seen to change the spin orientation from in-plane to out of plane alignment – surface energies per unit

volume have an increased influence over volume charges per unit volume. Strong perpendicular anisotropy was reported in Co/Pd multilayers in 1985 [Carcia 1985]. Much work has been done to fine tune materials with a strong effect [Grünberg 2001], and calculate the spin anisotropy in films of reduced coordination [Gay 1986]. Structures patterned in these high anisotropy films afford the possibility of enhanced thermal stability of binary data recording bits. Many systems exhibiting out of plane magnetization in this manner have high magneto-optical signals, which is also attractive for the data recording industry. These systems are returned to, in the context of ion irradiation studies, in Chapter 5.

1.4.4 Current Induced Switching

The effect of current on magnetization in systems of reduced dimensions yields many interesting effects. Characteristic length scales can be the spin tunnelling length across an interface in spin tunnelling experiments, or the reduced domain wall width in experiments treating ballistic electron passage across domain walls in magnetoresistance experiments. Recently Slonczewski treated the excitation of the magnetic state of ferromagnets via "spin transfer" in magnetic multi-layers [Slonczewski 1996]. He considered thin ferromagnetic layers sandwiched between paramagnetic spacers, in CPP geometries, and predicted effects such as precession and switching due to current flow through layered systems [Buhrman 1999]. Other interesting effects are current induced domain wall motion, current triggered wire switching, and current induced spin waves. For an overview of this research area, see the references in, for example, [Ansermet 2004].

1.4.5 Superparamagnetism

New effects need to be considered upon considering variables such as particle size and temperature, which are not directly addressed in the energy equations described in Section 1.3.1, for example superparamagnetism. Superparamagnetism involves thermally exciting a particle's magnetization state over an energy barrier, even in the absence of field.

As the lateral dimensions of a single domain particle are reduced, there is an increased likelihood that random thermal effects will impart enough energy to the system to trigger switching [Bean 1955]. Thus at elevated temperatures an assemblage of monodomain ferromagnetic particles can act as a classical paramagnet.

Superparamagnetism is a thermal effect defined over a given lifetime, and may be described in an Arrhenius-Néel type equation:

$$\frac{dp}{dt} = \frac{1}{\tau_0} \exp\left(\frac{-\Delta UV}{k_B T}\right) \qquad [1.32]$$

which describes a probability per unit time, dp/dt, of a given single domain particle of volume V switching from one magnetic orientation to another other over a separating energy barrier of magnitude ΔU. τ_0 is a semi-phenomenological constant related to the gyromagnetic precession period of the magnetic system and is usually given a value of around 10^{-10} s. T is the temperature of the system and the Boltzmann constant k_B = 1.38×10^{-23} J/deg. Analysis of this equation shows that $\Delta UV \geq 50\ k_B T$ is the stability criterion for an acceptably long data lifetime, taken nominally as 10 years.

For example, consider a monodomain particle, with the simplest form of uniaxial anisotropy. It may be written:

$$E_{Anisotropy} = K_u V \sin^2\theta \qquad [1.33]$$

where θ is the angle between the magnetic moment and the particle symmetry axis, V is the particle volume, and K_u is the uniaxial anisotropy energy density. Applying a

field component oriented parallel to the to the symmetry axis, then the energy becomes:

$$E = K_u V \sin^2\theta - \mu H \cos\theta \qquad [1.34]$$

where μ is the particle magnetic moment, $M_s V$. In the simplest configuration the magnetic moment is quantised either parallel or anti-parallel to the applied field, H.

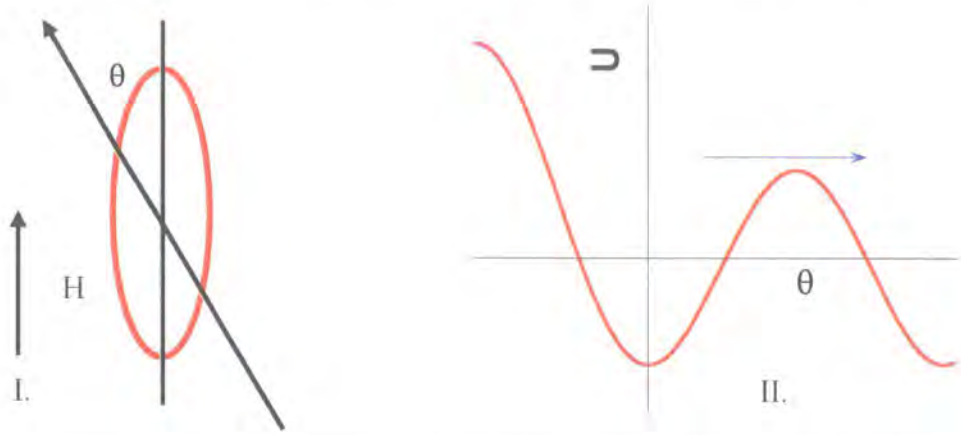

FIG 1.6: (I.) Represents a monodomain particle with a uniaxial anisotropy, and (II.) shows the energy barrier posed by the particle anisotropy, in the case of superparamagnetism. The blue arrow represents the particle magnetization reversing by thermal excitation over an energy barrier.

The energy barrier for magnetization reversal is simply given by $\Delta U = K_u V$ – this energy may be supplied to a system by thermal energy, Figure 1.6. Thus for a given random assembly of ferromagnetic single domain particles, the probability of a given percentage switching in unit time, dt, is related to size, shape and anisotropy field of particles.

1.5 Thesis Outline

This thesis has two principal themes. The first is the use of focused ion beam (FIB) 30 keV Ga^+ ions for the quenching of measured room temperature ferromagnetism in capped ultrathin $Ni_{81}Fe_{19}$ films. The second is the fabrication of complex planar wire geometries to enable precise control of magnetic switching mechanisms and switching field values.

Chapter 2 details the Kerr effects magnetometer used in the course of this study, and magnetic thin film sample preparation and properties are described in Chapter 3. Chapter 4 describes the fabrication of planar magnetic nanowires, and investigates wire magnetic switching field values. Chapter 5 investigates the fast quenching of measured ferromagnetism in $Ni_{81}Fe_{19}$ bilayers by radiation-induced transports of interfacial atoms. Chapter 6 describes the isolation of a single domain wall in a nanowire, and discusses the propagation of domain walls through smoothly rounded corner geometries, and artificial pinning sites, in an externally applied rotating magnetic field. Chapter 7 describes the switching of 3-terminal wire junctions, as a function of the number of domain walls at the junction, and suggests possible logic applications.

1.6 Summary

Some developments in ferromagnetism in the last 100 years have been treated. Concepts such as the single domain state, the nucleation/propagation model, domain walls, and dynamics were introduced, and will be further treated in this thesis. We have shown that studying systems of reduced dimensions results in new discoveries, many of which have important technological applications, such as GMR and PMA. Other phenomena such as superparamagnetism and CIS may be thought of as fundamental limits which define operating limits of existing and currently unimagined devices.

1.7 References

[Aharoni 2000] A. Aharoni, *"Introduction to the Theory of Ferromagnetism"*, Oxford University Press, New York, **109** (2000)

[Ansermet 2004] J. Ph. Ansermet, IEEE Trans. Magn. **40**, 358 (2004)

[Baibich 1988] M. N. Baibich, J. M. Broto, A. Fert, F. Nguyen Van Dau, F. Petroff, P. Eitenne, G. Creuzet, A. Friederich, J. Chazelas, Phys. Rev. Lett. **61,** 2472 (1988)

[Baryakhtar 1997] V. G. Baryakhtar, B. A. Ivanov, A. L. Sukstanskii, E. Yu. Melikhov, Phys. Rev. B, **56**, 619 (1997)

[Bean 1955] C. P. Bean, J. Appl. Phys. **26**, 1381 (1955)

[Bobo 2004] J. F. Bobo, L. Gabillet, M. Bibes, J. Phys. Condens. Matter **16**, 471 (2004)

[Brown 1968] W. F. Brown, J. Appl. Phys. **39**, 993 (1968)

[Brown 1963] W. F. Brown, *"Micromagnetics"*, Interscience Publishers, John Wiley & Sons, New York, **18** (1963)

[Buhrman 1999] E. B. Myers, D. C. Ralph, J. A. Katine, R. N. Louie, R. A. Buhrman, Science, **285**, 867 (1999)

[Carcia 1985] P. F. Carcia, A. D. Meinhaldt, A. Suna, Appl. Phys. Lett. **47**, 178 (1985)

[Cowburn 2000] R. P. Cowburn, J. Phys. D **33**, R1 (2000)

[Cowburn 1999] R. P. Cowburn, D. K. Koltsov, A. O. Adeyeye, M. E. Welland, D. M. Tricker, Phys. Rev. Lett. **83,** 1042 (1999)

[Frei 1957] E. H. Frei, S. Shtrikman, D. Treves, Phys. Rev. **106,** 446 (1957)

[Freeman 2001] M. R. Freeman, B. C. Choi, Science **294,** 1484 (2001)

[Gilbert 1955] T. L. Gilbert, Phys. Rev. **100,** 1243 (1955)

[Grünberg 2001] P. Grünberg, J. Magn. Magn. Mater. **226**, 1688 (2001)

[Miltat 2002] J. Miltat, *"Topics in Applied Physics 83, Spin dynamics in confined magnetic structures I,"* B. Hillebrands, K. Ounadjela (eds.), Springer-Verlag, Berlin Heidleberg (2002)

[Hubert 1998] A. Hubert, R. Schäfer, *"Magnetic Domains – The analysis of magnetic microstructures,"* Springer-Verlag, Berlin Heidleberg (1998)

[Kittel 1949] C. Kittel, Rev. Mod. Phys. **21**, 541 (1949)

[Kirk 1999] K. J. Kirk, J. N. Chapman, C. D. W. Wilkinson, J. Appl. Phys. **85**, 5237 (1999)

[Konishi 1971] S. Konishi, S Yamada, T Kusuda, IEEE Trans. Mag. **7**, 722 (1971)

[McMichael 1997] R. D. McMichael, M. J. Donahue, IEEE Trans. Mag. **33**, 4167 (1997)

[Meiklejohn 1956] W. H. Meiklejohn, C. P. Bean, Phys. Rev. **102,** 1413 (1956)

[Pratzer 2001] M. Pratzer, H. J. Elmers, M. Bode, O. Pietzsch, A. Kubetzka, R. Wiesendanger, Phys. Rev. Lett. **87,** 127201 (2001)

[Sixtus/Tonks 1931] K. J. Sixtus, L. Tonks, Phys. Rev. **37,** 930 (1931)

[Skomski 2003] J. Phys. Condens. Matter **15**, 841 (2003)

[Slonczewski 1996] J. Magn. Magn. Mater. **159**, L1 (1996)

[Ston./Wohlf. 1948] E. C. Stoner, E. P. Wohlfarth, Phil. Trans. Roy. Soc. A **240**, 599 (1948)

[Thirion 2002] C. Thirion, W. Wernsdorfer, M. Jamet, V. Dupuis, P. Mélinon, A. Pérez, D. Mailly, J. Magn. Magn. Mat. **242**, 993 (2002)

[Tusoda 2004] L. Tusoda, C. Stamm, A. B. Kashuba, F. King, H. C. Siegmann, J. Stöhr, G. Ju, B. Lu, D. Weller, Nature **428**, 831 (2004)

[Wernsdorfer 1996] W. Wernsdorfer, B. Doudin, D. Mailly, K. Hasselbach, A. Beniot, J. Meier, J. –Ph. Ansermet, B. Barbara, Phys. Rev. Lett. **77**, 1873 (1996)

[Williams 1949] H. J. Williams, R. M. Bozorth, W. Shockley, Phys. Rev. **75**, 155 (1949)

[Williams 1951] H. J. Williams, F. G. Foster, E. A. Wood, Phys. Rev. **82**, 119 (1951)

[Xu 2004] S. Lepadatu, Y. B. Xu, Phys. Rev. Lett. **92**, 127201 (2004)

[Yuan 1992] S. W. Yuan, H. N. Bertram, J. F. Smyth, S. Schultz, IEEE Trans. Mag. **28**, 3171 (1992)

Chapter 2. Spatially Resolved MOKE

2.1 Introduction

This thesis treats the magnetic characterisation of thin films and bilayers, patterned arrays, individual planar nanowires, and complex planar 2-d wire circuits measured by a spatially resolved magneto-optical Kerr effect (MOKE) magnetometer. The MOKE system is configured in the longitudinal orientation, to probe the component of magnetization lying in the optical plane of incidence and parallel to the sample surface. This chapter briefly treats some of the literature concerning Kerr effect microscopy in Section 2.2, with a more detailed description of the macroscopic and microscopic origins of the Kerr effect presented in Section 2.3. The details of the MOKE instrument and experimental set-up used here are put forward in section 2.4. High laser stability and differential detection contributes to excellent S/N, signal-to-noise ratio. This facilitates magnetic hysteresis measurements of single isolated nanostructures - this technique is described in Section 2.5. The technique of locally mapping and probing the magnetization state of samples to is also described. Single field sweep measurements of nanostructures are briefly described in Section 2.6, which allow stochastic processes to be studied. The chapter concludes with a short summary (Section 2.7).

2.2 Magneto-Optical Kerr Effect: Literature

The magneto-optical Kerr effect (MOKE), first reported by Kerr in 1877 [Kerr 1877], is based on the measurement of small rotations in the plane of polarization of light reflected from a magnetic surface. The Kerr effect has been experimentally demonstrated to be proportional to the net magnetization of the sample [Argyres 1955], thus it can be used as a non-invasive probe of the magnetization state of a

sample. The first observation of magnetic domains by this method was reported in cobalt [Williams 1951], with the effect soon documented in other materials, such as silicon iron [Fowler 1952]. More recently quantitative imaging techniques have been facilitated by image processing methods [Rave 1987], such as digital background subtraction, and signal averaging.

Along with an associated phenomenon, the Faraday effect, in which light is transmitted through a sample, MOKE has many applications in the characterization of magnetic systems of reduced dimensions, having a sensitivity to magnetic moment lower than $\mu = 6 \times 10^{-12}$ emu [Allwood 2003]. Due to the high sensitivity, samples as thin as one atomic layer may be investigated [Qiu 2000]. Traditionally MOKE has been used to measure the global properties of thin films, or more recently assemblies of dot and wire arrays, and structures of increasingly reduced dimensions. In particle arrays much important information of the magnetic response of structures to externally applied field is lost due to particle interaction, defects, and dispersion of particle magnetic responses. However the advent of more stable lasers, means this largely non-invasive characterization technique, is increasingly used for investigating single particle magnetically isolated nano-structures [Cowburn 1998], and for ground-breaking studies in magnetization reversal dynamics[1]. The far-field nature of many MOKE experimental set-ups makes the Kerr effect an excellent candidate for time resolved pump-probe studies. Time resolved MO kerr effect [TRMOKE] domain observation and imaging stroboscopic techniques are suitable for measurements down

[1] The interested reader is referred to the following papers [Choi 2001][Gerrits 2002/1][Gerrits 2002/2][van Kampen 2002], and references therein. Magnetization reversal modes and switching speeds of increasingly smaller particle sizes are being studied magneto-optically. Novel shapes and applied field profiles used to suppress ringing effects, and M_x, M_y, and M_z can be simultaneously investigated after sample excitation as a function of time.

to the picosecond limit - stroboscopic lasers with pulses as short as 70 fm being used [Koopmans 2000].

MOKE is versatile - longer experiments over hours of data acquisition can be performed, for example in the study of high anisotropy media and domain wall creep processes [Lemerle 1998]. Experiments can be performed *in situ*, during growth of monolayers, over a wide range of temperatures, and in vacuum [Xu 1998]. Therefore the Kerr effect can be used to magnetically investigate a thin film or layered sample as it is grown. In addition spatial probing of a sample is possible, and in many cases little or no additional sample preparation is needed. It is rapid, and largely non-invasive and non destructive. Finally wavelength discrimination techniques may be made for magnetic investigations of samples such as multilayers, for detailed investigation of interface effects – this is MOKE spectroscopy [Kim 1998].

Traditionally, the resolution was limited by optical diffraction effects to between 400 – 700 nm, and by the numerical aperture of the objective lens. This may be improved by the use of a solid immersion lens. A spatial resolution close to 0.1 μm was recently reported in thin NiFe samples [Argyle 2000]. Techniques such as scanning near-field optical microscopy (SNOM), using an optical fibre that has been tapered by a technique such as chemical etching also promises resolution of this order. Using a suitable combination of dielectric over-layers to enhance the MO signal from magnets of reduced dimensions is another promising avenue to enhanced S/N, and hence characterisation of smaller isolated structures. For recent developments in MOKE the reader is referred to the following works and references therein [Hubert 1998][Freeman 2001][Ferré 1999]. Interesting historical references on much of the original work performed by Faraday concerning the interaction between a light wave and a magnetic medium are contained in Qiu's review [Qiu 2000].

2.3 Magneto-Optical Kerr Effect

2.3.1 Geometry

MO measurements in reflection are traditionally performed utilizing one of three standard sample light-source configurations; the polar, transverse and longitudinal geometries respectively (Fig.2.1).

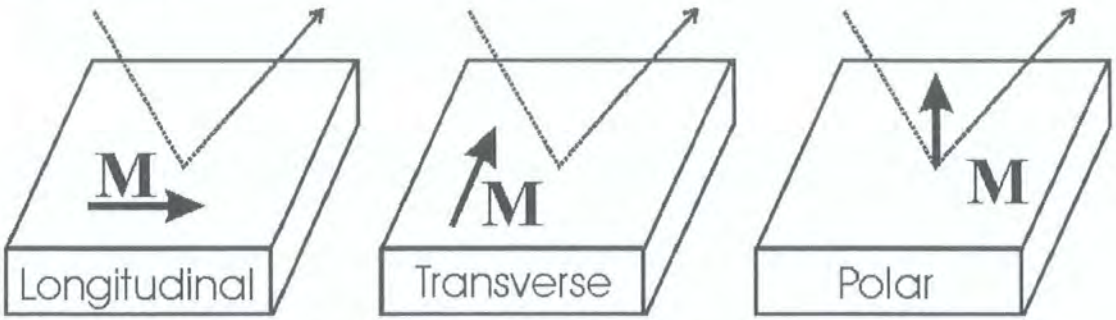

Figure 2.1: Magneto-optical effects as an incident light wave interacts with spontaneously magnetized semi-infinite thin slabs, with the sample magnetization, ***M***, varied with respect to a fixed incident beam.

Polar MOKE entails measurement of the magnetization vector component perpendicular to the sample surface and can be carried out at normal beam incidence. Transverse and longitudinal effects involve a polarized light beam incident at an oblique angle of incidence relative to a sample with in-plane magnetic ordering.

Longitudinal MOKE magnetometry measures the magnetization component parallel to the optical plane of incidence, while the transverse effect concerns the magnetization component perpendicular to this plane. This thesis treats field induced magnetization reversal in spontaneously magnetised NiFe systems. The sample magnetization is typically oriented in-plane.

2.3.2 Microscopic Treatment

Consider a linearly polarized light wave as the superposition of left hand, and right hand circularly polarized components. The electric field of a beam of light propagating in a medium excites the electrons in the medium. In the absence of a magnetic field, left hand circularly polarised light (LCP) drives electron motion in left

hand circular motion, and right hand circularly polarised light (RCP), drive electrons in right hand circular motion. The radius of electron motion in the excited sample is the same for LCP and RCP light. No Kerr rotation results.

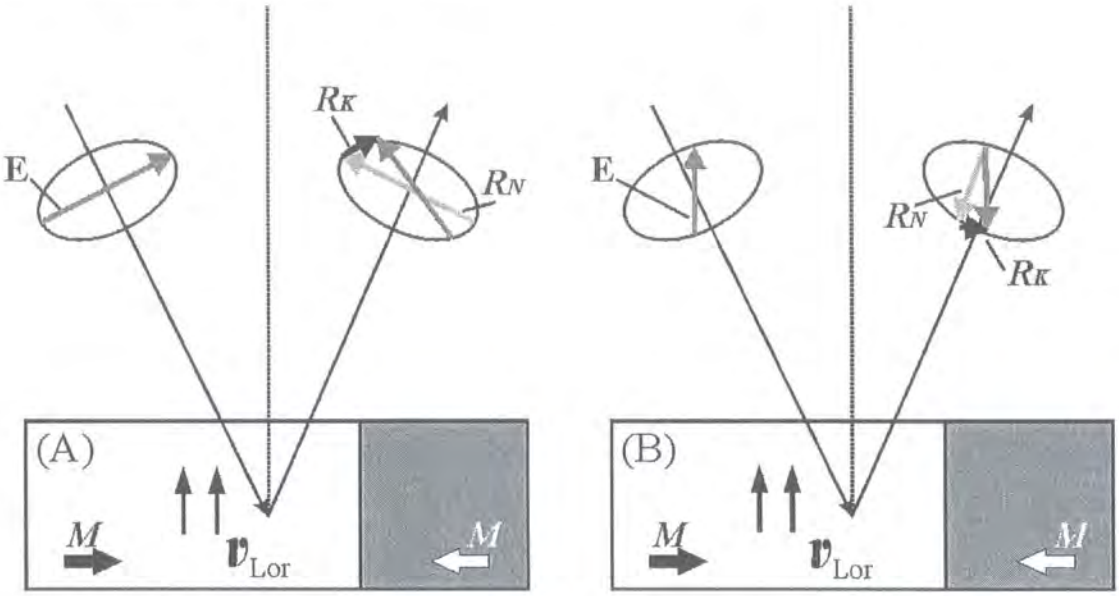

Figure 2.2: Longitudinal magneto-optical effects. $\mathbf{R_N}$ is the regularly reflected electric field amplitude. $\mathbf{R_K}$ is the magneto-optical kerr effect amplitude. (A) represents the case for p-polarized light, and (B) the case for s-polarized light.

Now consider the magnetic component of the same plane polarized light beam incident upon an in-plane magnetized magnetic infinite thin film. We consider the magnetization direction to be parallel to the incident light polarization. A proportion of light is reflected from the surface in the same plane as the incident light – this regular component of the reflected electric field we can call $\boldsymbol{R}_N$. It undergoes a phase shift of 180° for a non-absorbing medium.

A Lorentz force on oscillating electrons, due to the sample magnetization $\boldsymbol{J}$, (proportional to $v_{Lor} = \mathbf{m} \times \mathbf{E}$) induces a small secondary component to the reflected light, $\boldsymbol{R}_K$ – the Kerr component. The force felt by each electron, and the change in electron orbit is different for LCP and RCP light in an external field [Freiser 1968]. It is the combination of $\boldsymbol{R}_N$ and $\boldsymbol{R}_K$ that leads to Kerr rotation, which can be positive,

negative, or zero. The vector sum of the reflected light is therefore rotated in polarization direction due to orientation of the sample magnetization, relative to the incident light polarization. Note that 's' polarized light is perpendicular to the plane of incidence, and 'p' polarized light is parallel to the plane of incidence. In short magneto-optical effects arise from different responses of electrons in a medium to polarized electromagnetic waves, depending on the sample magnetization orientation.

2.3.3 Macroscopic Treatment

All magneto-optical effects can be explained in terms of a circular birefringence effect observed when a light wave propagates in a medium in the presence of a magnetic field. The left and right circularly polarized components of a linearly polarized electromagnetic wave have different indices of refraction relative to the medium, in which they are travelling.

Optical properties of a medium are determined by a dielectric tensor that is determined by the motion of electrons in the medium [Ferré 1984]. Consider an electromagnetic wave propagating from a non-magnetic to a magnetic medium. The dielectric constant, ε, describes the optical response of an isotropic material, or a non magnetic material of high symmetry (such as cubic). The constant ε is a single wavelength dependent parameter. The dielectric constant links the displacement $\vec{D}$ to the electric field, $\vec{E}$, by the relation $\vec{D} = \varepsilon \vec{E}$. If the system symmetry is lowered, then a more complex tensor formulation is required.

For a ferromagnet the system symmetry is broken due to the finite spontaneous magnetization of the sample, $\vec{M}$. In a cubic ferromagnetic material, a dielectric tensor $\overline{\overline{\varepsilon}}$ treating magneto-optical effects can be expressed as:

$$\overline{\overline{\varepsilon}} = \begin{bmatrix} \varepsilon_{xx} & \varepsilon_{xy} & \varepsilon_{xz} \\ -\varepsilon_{xy} & \varepsilon_{xx} & \varepsilon_{yz} \\ -\varepsilon_{xz} & -\varepsilon_{yz} & \varepsilon_{xx} \end{bmatrix} \qquad [2.1]$$

Additionally the Onsager relationship stipulates $\varepsilon_{nn}(\vec{M}) = \varepsilon_{nn}(-\vec{M})$ and $\varepsilon_{nm}(\vec{M}) = -\varepsilon_{nm}(-\vec{M})$, so diagonal components of the matrix are even- and off- diagonal components are odd in the magnetization. Considering effects only to the first order of M, the diagonal elements are independent of the magnetization. Considering the case where both the incident light and the magnetization are parallel to the z-axis, one can simplify the expression to:

$$\overline{\overline{\varepsilon}} = \begin{bmatrix} \varepsilon_{xx} & \varepsilon_{xy} & \\ -\varepsilon_{xy} & \varepsilon_{xx} & \\ & & \varepsilon_{xx} \end{bmatrix} \qquad [2.2]$$

Due to off-diagonal elements, ε_{xy}, an electric field along $\hat{x}$ will induce a finite polarization along the $\hat{y}$ direction. Now since ε_{xy} depends on M, this will cause a magnetization dependent polarization change. It is convenient to define a set of cylindrical co-ordinates such that:

$$\hat{e}_- = 1/\sqrt{2}(\hat{x} - i\hat{y}) \qquad \hat{e}_+ = 1/\sqrt{2}(\hat{x} + i\hat{y}) \qquad \hat{e}_z = \hat{e}_z \qquad [2.3]$$

Here we have a description of circularly polarized light of 2 opposing chiralities. $\hat{e}_-$ describes left-handedness and $\hat{e}_+$ right-handedness, similar to the microscopic description. Now transforming to cylindrical co-ordinates one finds:

$$\overline{\overline{\varepsilon'}} = \begin{bmatrix} \varepsilon_{xx} - i\varepsilon_{xy} & & \\ & \varepsilon_{xx} + i\varepsilon_{xy} & \\ & & \varepsilon_{xx} \end{bmatrix} \qquad [2.4]$$

In this new co-ordinate system the dielectric tensor is diagonalised. Different dielectric constants can be written for the two different polarization states:

$$\varepsilon_{\pm} = \varepsilon_{xx} \pm i\varepsilon_{xy} \qquad [2.5]$$

By recording the difference between transmission or reflection, (and also respective phases), of left and right-hand polarised light, the magnetization state of a sample can be probed by examining the magnetization dependence of ε_{xx}. By sweeping an externally applied field over time, and saturating a sample magnetically in the positive and negative orientations, a sample M-H loop can thus be obtained.

2.4 Experimental Apparatus

2.4.1 System Schematic

In Fig. 2.3 a schematic ray diagram of the optical paths and principal optical components of the magnetometer is shown.

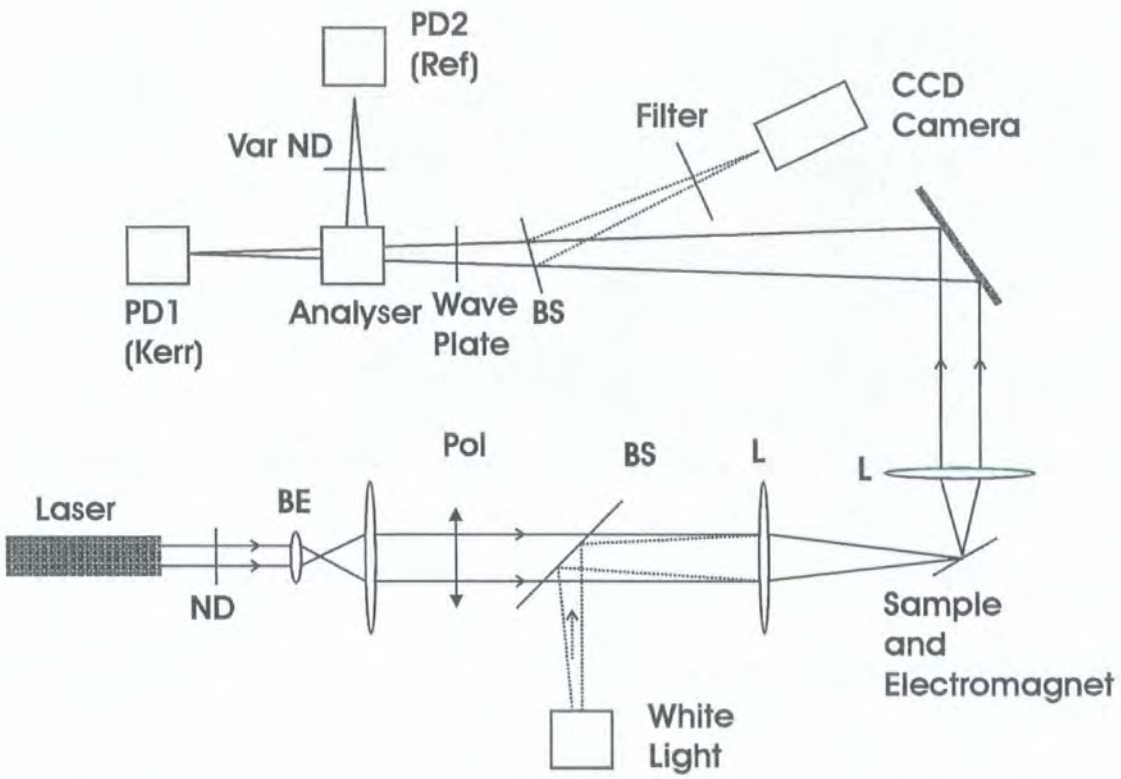

Figure 2.3: A schematic diagram of the principal components of the MOKE magnetometer experimental apparatus. The following abbreviations are employed; (1) ND – neutral density filters and half-wave plate/polarizer for laser beam attenuation; (2) BE – beam expander; (3) Pol – polarizer; (4) BS – beam splitter; (5) L – lens; (6) Wave Plate – this is a λ/4 plate; (7) Var ND – variable neutral density filter; (8) PD1 and PD2 – 2 separate photodiodes for Kerr effect and reference signals.

Two optical systems are merged in the experimental apparatus to allow optical and magnetic interrogation of the sample without the need for sample re-positioning. The CCD camera allows samples to be located relative to the path of the laser beam in real time. A marker system on each patterned sample was used to locate and differentiate small samples on the CCD monitor. In practise samples can be positioned to sub 10-μm accuracy employing this technique.

2.4.2 Experiment

We now describe the experimental apparatus in more detail, first treating the ray diagram from light source to detectors. The magnetometer employs a Nd:VO_3 laser at a constant wavelength of $\lambda = 532$ nm. The incident power of the laser was 20 mW. The power of the laser was chosen so as not to cause undesirable sample heating, but to maintain a high S/N [Allwood 2003/1]. Allwood measured a beam power of 70 mW, as the laser power at which sample magnetic properties become significantly affected by heating, leading to a heat induced reduction in coercivity. The light beam passes from the laser (Figure 2.3), through a beam expander and a Glan-Taylor polarizing prism to enhance the beam polarization ratio. The laser beam is then focused down to a spot diameter, ~5 μm on the sample surface. The small laser spot size permits local magnetic probing of continuous films and spatially resolved measurements of single structure magnetization states in an externally applied field. The laser spot profile is Gaussian in nature. Samples are oriented at 45° relative to the incident light beam, and this causes a further small distortion to the laser beam profile, resulting in a slightly elliptical spot size.

Light reflected 90° from the sample surface is channelled through identical achromat doublet lenses, through a quarter wave plate, and onto a Glan-Taylor

polarizing analyser. For light incident normal to the sample surface there is no MOKE effect observed (the cross product is zero), so light is incident on the sample surface at a 45° angle. Permalloy exhibits a low Kerr rotation ≅ 0.01°, meaning that nearly crossed polars are required, throwing away most of the laser light. Transmitted and reflected beams from the analyser are detected using Si photodiodes and constitute the Kerr signal and an additional reference signal.

Additionally, white light is introduced into the principal laser optical path prior to the sample, using a beam splitter between the polarizer and the sample surface, enabling a CCD to image the sample surface for location of samples. A dichroic mirror protects the CCD chip from the laser beam. With the current configuration direct sample optical imaging and Kerr effect characterisation are not possible simultaneously – the white light is turned off prior to magnetic measurements.

Magnetic fields applied in the plane of the sample are generated by iron-core and air spaced electromagnets, powered by Kepco power amplifiers (type BOP 20-5M). The magnetic field for measurement typically oscillated at a 27 Hz operating frequency. Fields could be applied in the x or y orientation relative to the easy axis of a fixed sample. By using a phase shift of ± 90° between the two electromagnets, a rotating field in the plane of the sample could be applied. Furthermore, by regulating the current applied to the x and y electromagnets an elliptical rotating field profile could be generated.

Samples were metallic, fabricated on Si substrates, with smooth optically reflective surfaces. Non-magnetic adjustable tufnel stubs held the sample in the magnetic field. Samples could be rotated 360° manually or on a rotation stage relative to the incident light beam. The sample orientation relative to incident light is accurate

to within ≈ 2° using the optical camera. In practice the sample could be rotated by ± 0.001°, using an XYθ stage sample controller. Samples as thin as 2.0 nm (of continuous magnetic film), or as narrow as 55 nm (patterned wire arrays), were found by positioning the structure of interest close to the laser spot, using the CCD, and a marker system as a guide.

The sample surface is first focused using the CCD camera monitor, and then the laser beam is centred on the sample surface and the spot profile adjusted. The polarisation optics are set up for measurements by first minimizing the Kerr signal with iterative adjustments to the wave-plate and the analyser, and then setting the analyser to an appropriate angle. Magnets were demagnetized prior to measurement. Data was taken as a function of externally applied magnetic field to generate magnetic hysteresis loops, by measuring the longitudinal Kerr signal as a function of magnetic field.

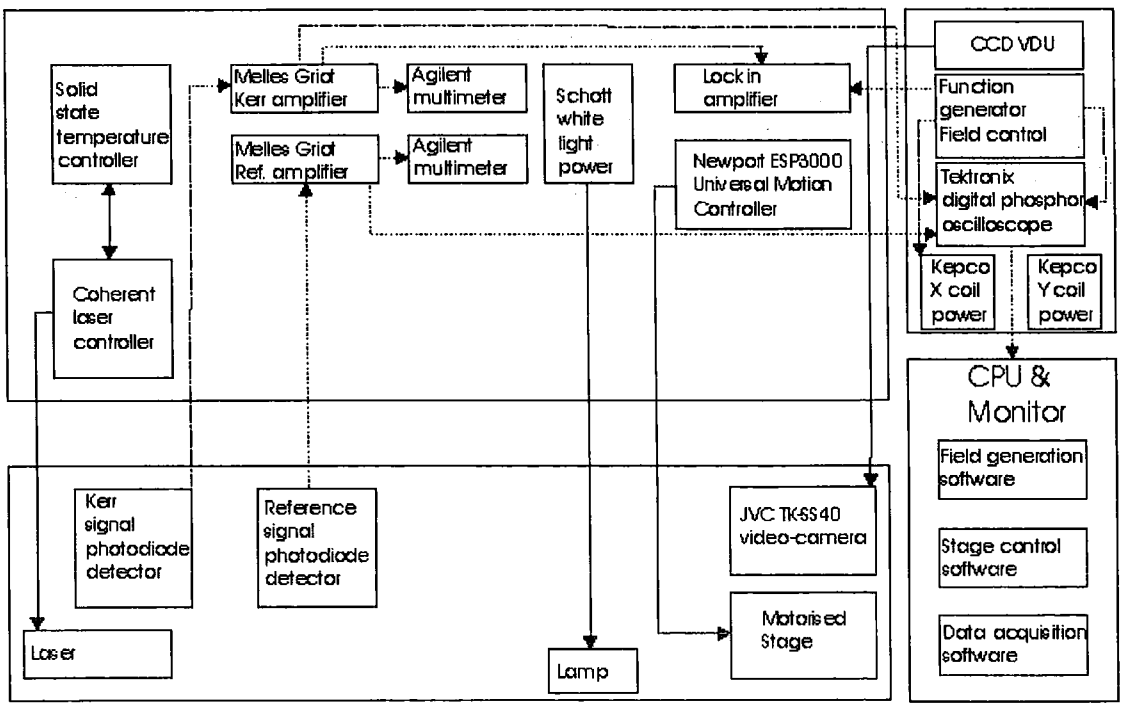

Figure 2.4: A schematic diagram of the MOKE system hardware and software.

The magnetic field amplitude and frequency can be controlled either from a commercial signal generator or from a digital-to-analog personal computer output. Voltage vs. time traces were relayed through a GPIB interface which connected X and Y coils and the power supplies. The M-H loop averaging process is performed on a Tektronix oscilloscope. Additionally the GPIB interface facilitated interfacing between hardware such as the multimeters, lock-in amplifier, oscilloscope, motion controller, and custom built software modules on the PC. Figure 2.4. shows a diagram of the data acquisition hardware and software. Signal from photodiode detectors is routed via amplifiers to the oscilloscope, and a custom-built data-recording program on a PC. Measurements were performed at room temperature.

2.4.3 Differential Detection

For many samples (such as $Ni_{81}Fe_{19}$) the magnetization dependent change in polarization of incident polarized light is small, so a sensitive detection technique is required. The information depth of light in NiFe films is approximately 20 nm, and above this sample thickness no additional signal results. Techniques exist to enhance measured signal, such as dielectric coatings, and the use of an Au coating of appropriate thickness [Qureshi 2004]. This might be a fruitful avenue for MO investigations of even smaller magnets of reduced dimensions in the future.

The Durham MOKE uses a "differential detection" technique whereby a second Si photodiode detector records laser beam intensity during signal averaging of each M-H loop. The Kerr signal can therefore be adjusted for laser instability, giving much improved S/N. The reference signal in the differential detection scheme is obtained after the laser beam is reflected from the sample surface, taking the rejected beam from the analyser. Prior to measurement the position of the reference detector is

adjusted to measure all of the reflected laser light, which is attenuated using a suitable neutral density filter to give a reference signal similar to the signal measured at the Kerr detector photodiode. In this manner instrument noise may be partially compensated for.

Furthermore, the Kerr and reference photo detectors are connected to amplifiers with a voltage adjustment of ± 2 V. When laser light is incident on the detectors, offsets are adjusted so that the net output signal of each amplifier is nearly zero. This step improves the effective dynamic range of the measurement, and offsets are recorded and integrated into the data acquisition process.

2.4.4 Signal Vs Noise

A Coherent Verdi V-5 diode pumped solid-state laser was used, being a more stable light source than, for example, Hg lamps or diode light sources. It is a ring cavity laser, intensity stabilised, to 0.02% from 10 Hz to 1 GHz. To take full advantage of this very high stability, the laser was typically operated in a high power mode relative to conventional MOKE systems, and the laser beam is then attenuated prior to interaction with the sample. Attenuation of the beam, for example by a neutral density filter, means typically 20 mW power was delivered at the sample. The magnetometer is housed in a subterranean lab, on an optical table with anti-vibration legs.

Data averaging is performed on a digital storage oscilloscope. Averaging each loop N times, in principle improves the signal to noise ratio (S/N) of measured hysteresis loops by a factor of $N^{1/2}$. The various sources of noise associated with the system are detector dark noise, thermal noise, shot noise and instrument noise and are

treated in detail by Allwood, [Allwood 2003/1], see also Hubert [Hubert 1998].

2.5 Sample Investigation

The magnetometer measures magnetization within the focused laser spot. Under a focused laser spot, single structures can yield a measurable Kerr signal, even if sample dimensions are below the incident laser wavelength. The signal amplitude, S_k, as compared to a virgin unpatterned film is approximated by:

$$S_k = A_{pattern}/A_{spot}$$

where $A_{pattern}$ is the pattern surface area, and A_{spot} is the focused spot size. An XYθ translation stage was used to control the position of the sample, in the Z-plane of optimum focus of the beam incident on the sample surface. The translation stage is specified to displacement steps with a lateral resolution of 55 nm. In practise the translation stage position can be controlled manually using a Newport Universal Motion Controller (model ESP300) or from an external PC, moving or scanning the sample surface in either the x or y direction relative to the fixed incident laser beam.

Then an alternating x-direction magnetic field of sufficient strength to magnetically saturate the sample at 270 Hz was applied to the sample, while rastering the sample in a 2-D grid. The field was generally applied to the long axis of samples. The sample magnetization vector generally follows the long axis of an elongated patterned sample at remanence, and by applying an alternating field a contrast map of the magnet relative to a non-magnetic or paramagnetic background is generated.

Using lock-in amplification of the signal, a sample susceptibility map [Allwood 2003/1] is generated (Fig. 2.5.a), which can be spatially probed in more detail by moving the sample relative to the laser spot.

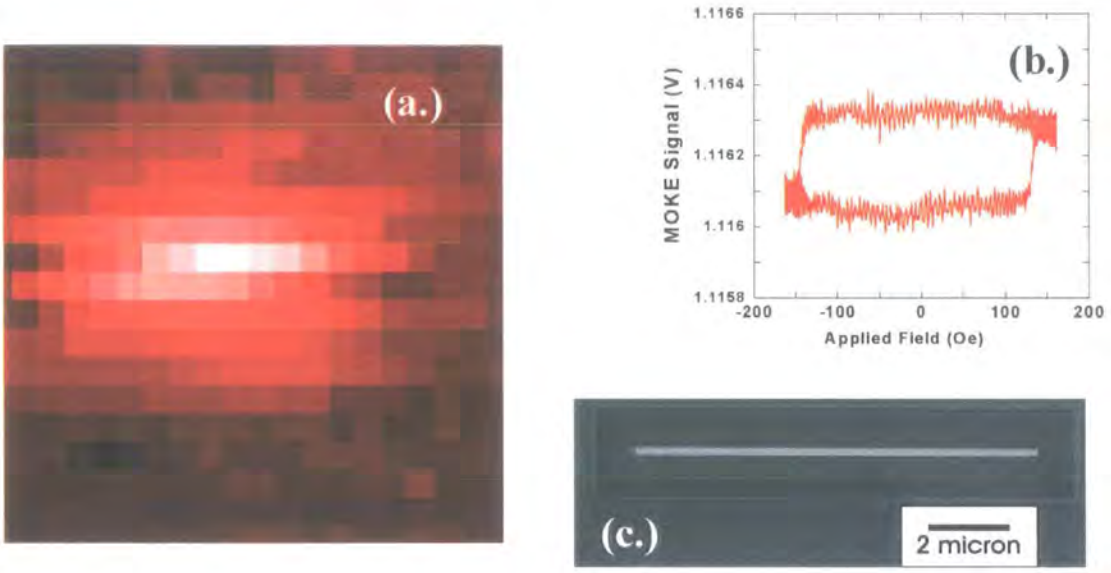

Figure 2.5: Magnetization map of a focused ion beam (FIB) milled 10 μm × 200 nm × 5 nm NiFe planar wire, fabricated on a Si substrate. (a.) represents a 20 × 20 μm map with 1 μm pixel resolution. The resultant M-H loop (b.), and a secondary electron image from and irradiated wire structure (c.) are also shown.

Lightest areas of the map denote regions of highest measured signal, which represents the magnetically active area. The MOKE laser spot was placed to take the time averaged M-H loop, in Fig. 2.5.b. Pinker areas represent lower measured MOKE signal, and dark red corresponds to non-ferromagnetic regions at room temperature. Each pixel in Fig. 2.5.a is 1 μm^2. By stepping the stage in smaller increments, over a longer mapping time, 500 nm^2 map pixelation is achievable. Measured MOKE signal levels are a convolution of focused laser beam profile and the sample geometry. In the secondary electron image from focused ion beam (FIB) irradiation, Fig.2.5.c, the wire is the white structure in the centre of the image, and other different contrast areas on the image correspond to non-magnetic areas of Si substrate irradiated at Ga^+ beam currents of either 100 pA or 20 nA.

In the case of thin or ultrathin patterned magnetic films and structures, the MOKE signal scales approximately linearly with the volume of magnetic material investigated. Some light may be scattered off sample edges. Therefore the MOKE

signal percentage for a given laser position on a sample, relative to a background or reference signal, can be an additional source of information. In order to demonstrate this, tapered magnetic wires were fabricated by FIB milling and characterised by the MOKE magnetometer. The geometry employed was a 20 μm long wire, patterned in a 5 nm thick NiFe film. The wire widened from 100 nm at the narrow end (position "A" in Fig. 2.6) to 1 μm at the wide end (position "B"). By scanning this structure parallel to the wire easy axis relative to a fixed laser spot, and locally measuring the percentage MOKE signal we can obtain a quantitative slice of a magnetic susceptibility map. This is particularly useful for geometrically complex samples, or samples with complicated magnetic reversal mechanisms, where different parts of a magnetically isolated continuous sample may switch at different applied fields.

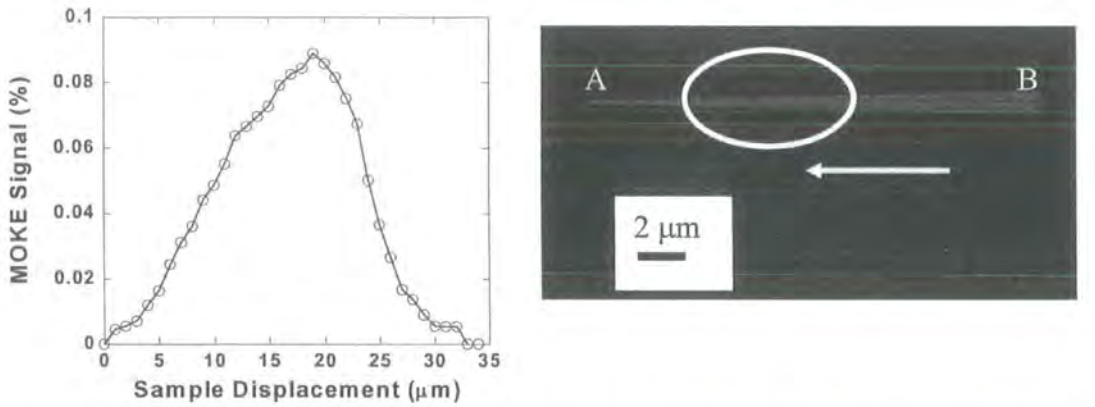

Figure 2.6: Measured percentage MO signal, obtained by moving an in-plane magnetized needle shaped wire, relative to the fixed laser probe. The arrow represents the direction of sample displacement relative to the fixed laser probe position.

The plot shown is consistent with the 20 μm long sample being scanned along the major axis, beneath an approximately 5-6 μm wide laser spot. We define a zero point on our graph, as the last sample position where no hysteresis is observed for the laser spot located to the left of position "A" on the needle. As the edge of the laser spot is moved close to point "A", a hysteresis loop with very low signal is measured. The rate of MOKE signal increase vs. displacement increases, when the laser spot is fully on the sample, and a greater surface area of magnetically active material is under

the spot. At a sample displacement between 20-25 μm from the zero point there is a sharp fall in MOKE signal as the laser beam scans over edge "B" of the sample. Both susceptibility maps and local measures of MOKE signal greatly enhance our ability to perform spatially resolved magnetometry measurements, in single structures with critical dimensions below the wavelength of a conventional optical microscope.

2.6 Single shot hysteresis measurements

Traditionally, functional magnetic nano-structures have been characterised magnetically in large arrays, to enhance S/N. Micro-SQUID (superconducting quantum interference device) offers the best S/N for single particle investigation, but is a time consuming low temperature technique, and magnetic force microscopy can be hindered by stray field from the probe tip interacting with the isolated sample. Investigating arrays has several disadvantages such as inter-particle magnetic interactions [Heyderman 2004], sample inhomogenities, or thickness variation across a sample. Statistical smearing of M-H loops averaged over an array can hinder a deeper insight into physical switching mechanisms.

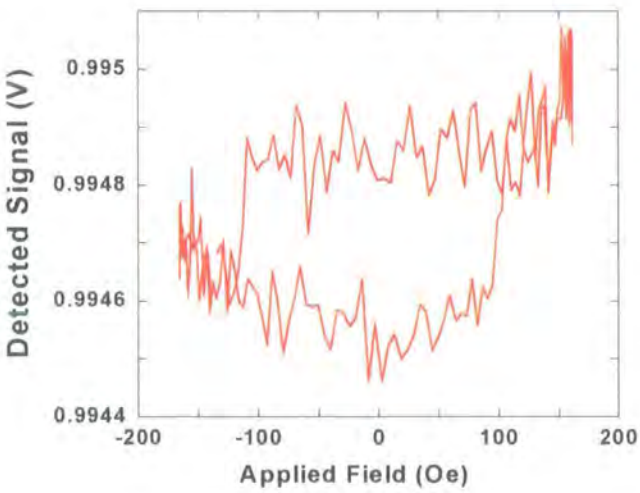

Figure 2.7: Single shot M-H loop of an individual planar nano-wire, taken at room temperature. The wire dimensions are width = 200 nm, thickness = 5 nm, length = 10 μm.

This experimental set-up permits magnetic interrogation of single magnetically isolated nano-structures. Furthermore single shot measurement of isolated nano-structures without the need for time averaging of switching data is also possible.

Shown is a single shot measured hysteresis loop for an individual NiFe wire of high aspect ratio, which is single domain at remanence – Fig 2.7. The measurement shown has a S/N ≈ 4, and two distinct switching transitions are clearly evident at ± 105 Oe, interpreted as a single domain where switching is between bistable single domain magnetization states of opposing polarities.

2.7 Summary

In this chapter some of the literature concerning MOKE has been surveyed, and the theory of the magneto-optical Kerr effect has been treated from a macroscopic and a microscopic viewpoint. The magnetometer used as the principal experimental apparatus in the course of this study has been described in detail. I have detailed some representative magnetization measurements, including the location of structures studied, and how structures are subsequently characterised magnetically.

2.8 References

[Allwood 2003/1] D. A. Allwood, Gang Xiong, M. D. Cooke, R. P. Cowburn, J. Phys. D. **36**, 2175 (2003)

[Argyle 2000] B. E. Argyle, J. G. McCord, J. Appl. Phys. **87**, 6487 (2000)

[Argyres 1955] P. N. Argyres, Phys. Rev. **97**, 334 (1955)

[Choi 2001] B. C. Choi, M. Belov, W. K. Hiebert, G. E. Ballentine, M. R. Freeman, Phys. Rev. **86**, 728 (2001)

[Cowburn 1998] R. P. Cowburn, D. K. Koltsov, A. O. Adeyeye, M. E. Welland, Appl. Phys. Lett. **73**, 3947 (1998)

[Ferré 1984] J. Ferré, G. A. Gehring, Rep. Prog. Phys. **47**, 513 (1984)

[Ferré 1999] J. Ferré, J. P. Jamet, P. Meyer, Phys. Stat. Sol. (a) **175** 213 (1999)

[Fowler 1952] C. A. Fowler, E. M. Fryer, Phys. Rev. **86**, 426 (1952)

[Freeman 2001] M. R. Freeman, B. C. Choi, Science **294**, 1484 (2001)

[Freiser 1968] M. J. Freiser, IEEE. Trans. Magn. **4**, 152 (1968)

[Gerrits 2002/1] Th. Gerrits, H. A. M. van der Berg, J. Hohlfeld, O. Gielkens, L. Bär, Th. Rasing, J. Magn. Magn. Mat. **240**, 283 (2002)

[Gerrits 2002/2] Th. Gerrits, H. A. M. van der Berg, J. Hohlfeld, L. Bär, Th. Rasing, Nature, **418**, 509 (2002)

[Heyderman 2004] L. J. Heyderman, H. H. Solak, C. David, D. Atkinson, R. P. Cowburn, F. Nolting, Appl. Phys. Lett. **85**, 4989 (2004)

[Hubert 1998] A. Hubert, R. Schäfer, *"Magnetic Domains – The Analysis of Magnetic Microstructures"*, Springer (1998)

[Hunt 1967] R.P. Hunt, J. Appl. Phys. **38**, 1652 (1967)

[Kerr 1877] J. Kerr, Philos. Mag. **3**, 321 (1877)

[Kim 1998] W. S. Kim, W. Kleemann, J. Tappert, W. Keune, J. Appl. Phys. **84**, 4384 (1998)

[Koopmans 2000] B. Koopmans, M. van Kampen, J. T. Kohlhepp, W. J. M. Jonge, Phys. Rev. Lett. **85**, 844 (2000)

[Langford 2002] R. M. Langford, G. Dale, P. J. Hopkins, P. J. S. Exen, A. K. Petford-Long, J. Micromech. Microeng. **12**, 111 (2002)

[Lemerle 1998] S. Lemerle, J. Ferré, C. Chappert, V. Mathet, T. Giamarchi, P. LeDoussal, Phys. Rev. Lett. **80**, 849 (1998)

[Qui 2000] Z. Q. Qui, Rev. Sci. Instrum. **71**, 1243 (2000)

[Qureshi 2004] N. Qureshi, H. Schmidt, A. R. Hawkins, Appl. Phys. Lett. **85**, 431 (2004)

[Rave 1987] W. Rave, R. Schäfer, A. Hubert, J. Magn. Magn. Mat. **65**, 7 (1987)

[van Kampen 2002] M. van Kampen, C. Jozsa, J. T. Kohlhepp, P. leClair, L. Lagae, W. T. M. de Jonge, B. Koopmans, Phys. Rev. Lett. **88**, 227201 (2002)

[Williams 1951] H. J. Williams, F. G. Foster, E. A. Wood, Phys. Rev. **82**, 119 (1951)

[Xu 1998] Y. B. Xu, E. T. M. Kernohan, D. J. Freeland, A. Ercole, M. Tselepi, J. A. C. Bland, Phys. Rev. B. **58**, 890 (1998)

Chapter 3. Thin film Growth & Properties

3.1 Introduction

A description of the growth and basic structural and magnetic properties of thin and ultra-thin polycrystalline single layer $Ni_{81}Fe_{19}$ films and bilayers is presented. Samples were subsequently patterned by focused ion beam (FIB) ion beam lithography, and studied magneto-optically (Chapters 4-7). Section 3.2 treats the substrate preparation and continuous film ($Ni_{81}Fe_{19}$) growth process by thermal evaporation. Section 3.3 details the basic magnetic and structural properties of resultant as-deposited thin films. The properties of layered samples such as $Si/Ni_{81}Fe_{19}/Al$ and $Si/Ni_{81}Fe_{19}/Au$ with a ferromagnetically active layer and a non-magnetic protective cap are set forth in Section 3.4, followed by a brief summary.

3.2 Evaporated film preparation

3.2.1 Substrate preparation

Single crystal commercially available Si <100> wafers were cleaved in a clean room environment using a diamond scribe. Source Si wafers were 625 ± 25 μm thick, with a resistivity of 8.5 – 11.5 Ωcm. Square chiplets with an edge length of 5 mm were used for thin film growth. Substrates were washed in an ultrasonic bath, used to dislodge impurities or dust particles from sample surfaces. Chip immersion was first in acetone, $(CH_3)_2CO$, for 60 seconds, followed by immersion in isopropanol $(CH_3)_2CHOH$ for 60 seconds. The cleaned silicon wafer chiplets were doused dry with a Ni gun. Substrates such as glass, and SiO_2 were also investigated. Si was a suitable substrate for samples subsequently patterned by focused ion beam Ga^+ irradiation. Glass and SiO_2 showed quite strong charging effects as Ga^+ ions interacted with the substrate. In future a buffer layer between NiFe film and insulating substrate may reduce charge artefacts during ion beam milling.

3.2.2 Source materials

$Ni_{81}Fe_{19}$ is the principal ferromagnetic species studied in this thesis, known for its weak magnetocrystalline anisotropy. In addition, it is known for a high anisotropic magnetoresistance, and low magnetostriction [Brückner 2001]. A powdered alloy was used as a source, with a maximum particle size of 45 microns. Non-magnetic overlayers were evaporated over NiFe films without breaking vacuum. For example Aluminium pellets, 6 mm^2, and typically 99.999% pure were used as a source for non-magnetic capping layers on some thin films. Gold was also used as a capping species, from Advent temper annealed wires of 99.99 % purity.

3.2.3 Evaporator Details

A custom built high vacuum thermal evaporator was used for the growth of parent single layer films and bilayer samples treated in this thesis – Fig. 3.1.

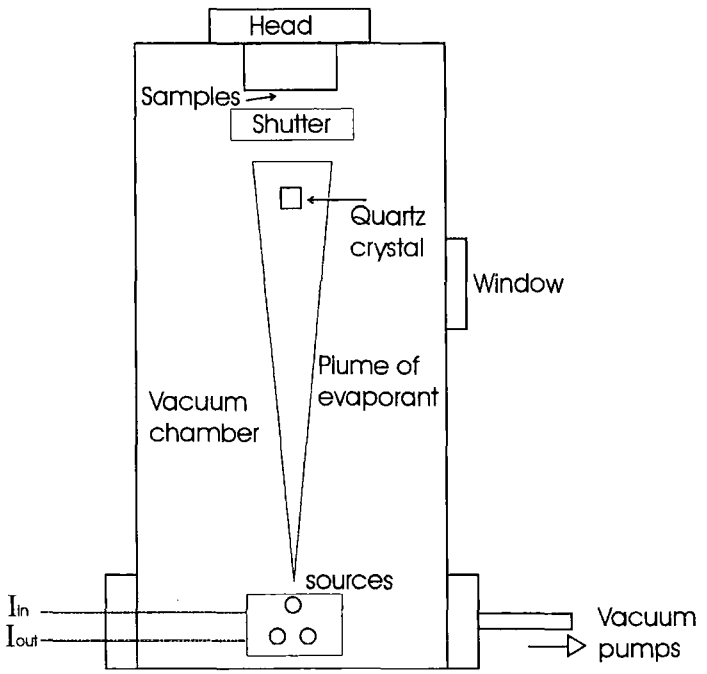

Fig 3.1: Schematic of high vacuum thermal evaporation system.

Up to four crucibles for sources materials were positioned in the base of the chamber. The crucibles were chosen according to the material to be evaporated. Tungsten crucibles coated with Alumina were used for NiFe. Wound tungsten wire crucibles were used to hold source Al pellets. The source materials were heated by passing a current through the crucibles. Current was controlled by a Wayne Kerr Electronics AP3080A power supply. This caused a plume of metal vapour to rise upwards in the chamber. Target chiplets were placed at a large distance from sources (~395 mm) to ensure minimum magnetic and structural inhomogeneity of resultant deposited samples. For the same reasons Si pre-cleaned substrates were placed in close proximity to each other in the chamber. There are four baskets for source materials in the lower part of the chamber so layered samples can be easily prepared.

A manually controlled mechanical shielding system was used to regulate substrate exposure time during film growth. At least six different sample thicknesses

could be grown in a single deposition. Therefore single thickness films of varied thickness and multi-layer samples could be grown under uniform conditions without breaking vacuum. An Edwards roughing pump was used to back a VAT turbo pump. Base pressures of the order of 10^{-8} mbar are attainable in the evaporator system. Deposition rate was recorded using a calibrated quartz crystal rate meter accurate to 0.1 Å/s, which was located close to target substrates, but in a position where it would not distort or block the rising plume of vaporised material. The quartz crystal in the chamber was connected to a Sigma Instruments SQM-160 monitor. The film growth rate was controlled by regulating the current passed through the crucibles on the external power supply, to an accuracy limited by the quartz crystal of 0.1 Å/s.

3.2.4 Deposition

A vacuum chamber bake out prior to each sample evaporation, using the crucible, helped to remove any residual water vapour and contaminents from source materials and the interior of the evaporator chamber. Better as-deposited film quality, and a controlled and steady deposition rate resulted. Better film quality resulted because:

- A lower base pressure is attained after pre-baking, lessening oxide formation during growth.
- The evaporator chamber is effectively cleaned, the interior being coated with a protective metal skin.
- The response of the metal source to different currents was established in the pre-bake stage. Therefore an appropriate current could be used to ensure a constant controlled rate of film growth.

After vacuum chamber pump down, the following procedure was followed:

1. Samples were shuttered for pre-baking. A low current (~20 A) was passed through the source material crucibles. The current was gradually increased to melt the source, and allow outgasing.
2. After pre-baking, the chamber was left pumping to re-attain a good base pressure (~10^{-7} mbar). The sources were re-ignited, with substrates shielded.
3. When the rate was stabilised, by tuning the current setting, substrates were exposed by opening the shutter, and thin films were deposited.

Substrates were not heated during film growth, and were secured to a mount attached to the vacuum chamber lid. PMMA (polymethylmetacrylate) was used as the substrate-mount adhesive. This minimizes stressing the sample substrate during film growth, and contamination by outgasing. Films could be grown between bar magnets to preferentially define hard and easy axis anisotropy directions if required. A Bayard-Alpart ionisation gauge tube monitors chamber pressure. The chamber was typically operated at a base pressure of 2-4 × 10^{-7} mbar rising to between 8 × 10^{-7} mbar and 3 × 10^{-6} mbar during film growth. Films were typically deposited at a constant rate of 1 Å/s to ensure low coercivity (1-3 Oe), low roughness (~ 3-5Å films) [Cooke 2003].

3.3 $Ni_{81}Fe_{19}$ Films

3.3.1 Structural properties

Polycrystalline single layer NiFe films from 3-25 nm thick were grown for subsequent patterning by focused ion beam (FIB) milling. The tooling factor of the ratemeter, and hence film thickness of evaporated films was calibrated and monitored using a dektak stylus profilometer – Fig 3.2. Masks were screwed over substrate surfaces to shield parts of a surface so profilometry measurements could be performed to verify or calibrate film thickness. Superconducting quantum interference device

(SQUID) magnetometer measurements were also performed to verify film thicknesses.

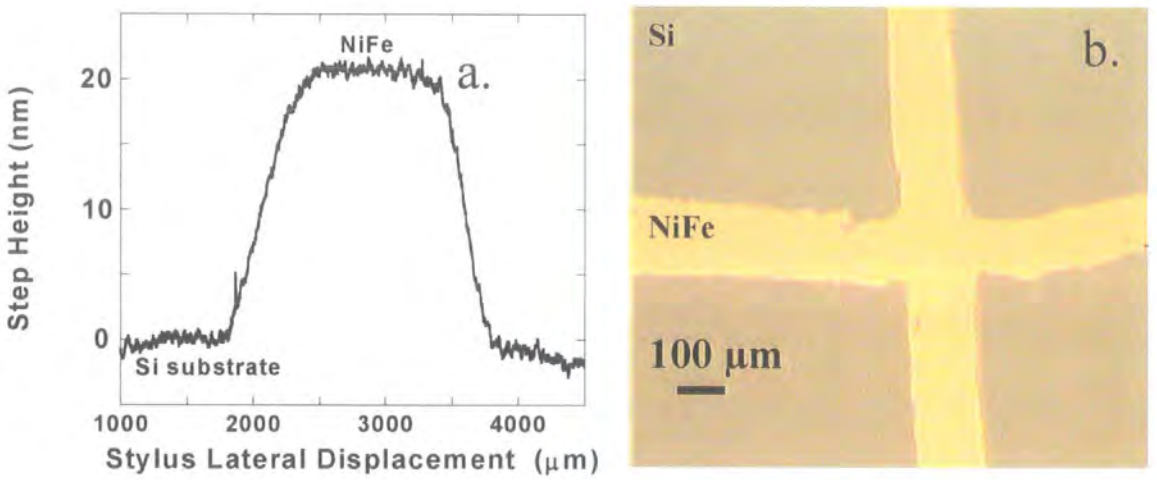

Fig 3.2: Typical Dektak profilometer cross sectional line-scan from a 20 ± 1 nm thick NiFe film, used for film thickness calibration measurements (a.). Step heights were defined using a cross shaped shadow mask, to partially expose substrates during thin film growth (b.).

Grazing incidence X-ray (GIXR) scattering experiments were performed on as-deposited samples to determine experimental parameters - roughness at the free surface or the NiFe/Si interface, and the NiFe structural thickness. GIXR measurements were made on a *Bede* GXR1 reflectometer [Buchanan 2002/1], using a monochromated Cu K_β source. The true specular profile provided averaged in-plane structural information as a function of depth.

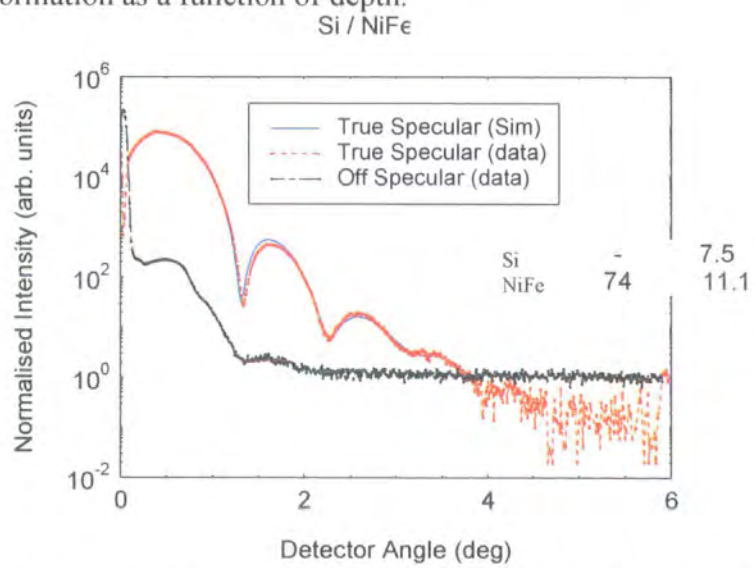

Fig 3.3: True specular and off-specular GIXR fringes from a Si/NiFe film.

The specular and off specular X-ray scattering data from a thermally evaporated NiFe film on Si are shown in Fig. 3.3. From a simulated fit to the true specular data, structural thickness was determined at 74 ± 5Å. The average interface width averaged across a whole 5 mm wide chip was determined at 7.5 ± 1 Å at the Si/NiFe boundary. Average interface width is a combination of surface and interface roughness. Surface roughness of the NiFe was determined to be 11.1 ± 1Å. Atomic force microscopy measurements performed locally on a different as deposited NiFe film found a lower r.m.s. surface roughness of 3 ± 1 Å. The chemical composition of thermally evaporated $Ni_{81}Fe_{19}$ films was verified to within 1% accuracy by energy dispersive X-ray spectroscopy measurements [Cooke 2003]. This composition was invarient across an entire surface.

3.3.2 Magnetic Properties

For a soft ferromagnetic material such as NiFe, from 2-25 nm thick, spontaneous magnetization is generally aligned in the film plane. When magnetic moments are directed along a certain crystallographic axis, determined by the symmetry of the crystal, system energy is minimized – this is the in-plane easy axis (Fig. 3.4).

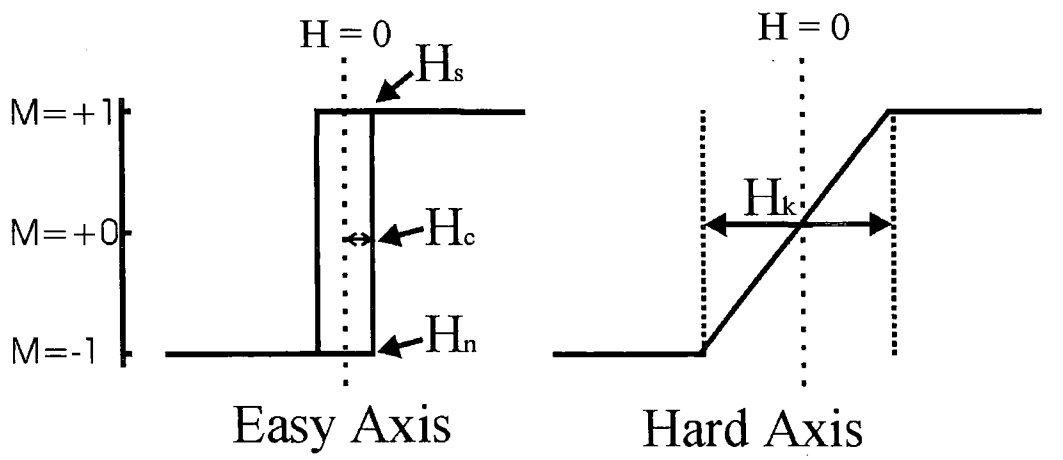

Fig 3.4: Easy and hard axis M-H loops with a definition of nucleation, coercive and saturation fields, H_n, H_c, and H_s respectively. H_k denotes the hard axis anisotropy field – the field at which a sample is magnetically saturated in the hard direction.

We define the nucleation field, H_n, as the applied field value at which spin deviation from the easy-axis saturated state is observed. The sample coercivity, H_c, is the field at which half of the sample magnetization has been reversed. The saturation field, H_s, is the field at which a sample becomes fully magnetized in the opposite direction.

All as-deposited samples studied exhibited square hysteresis loops when a magnetic field was applied parallel to the easy axis direction – Fig 3.5. The field-induced magnetization reversal process proceeds by easy domain wall motion. Square M-H loops indicate good film quality with a low distribution of intrinsic pinning sites.

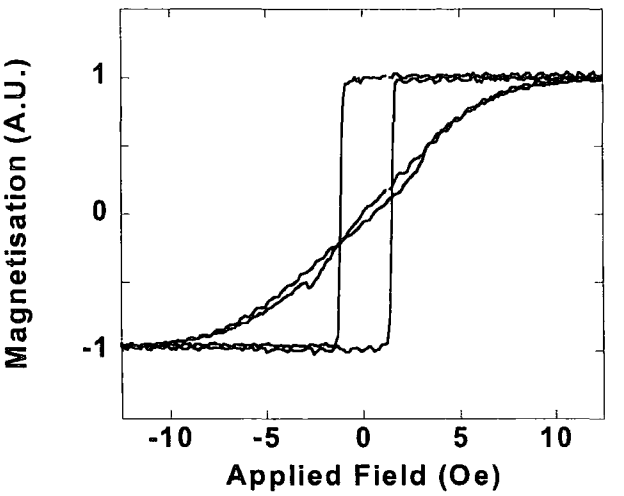

Fig 3.5: Hysteresis loops taken on the easy and hard axes of a 5 nm thick NiFe film.

The critical field for domain wall propagation is lower than the nucleation field. Along other directions, referred to as the hard axes, the energy is maximized. Relatively low hard axis anisotropy fields were measured, consistent with the fact that $Ni_{81}Fe_{19}$ alloy is virtually isotropic. The hard axis anisotropy field, H_k, tends to increase with film thickness, all other growth factors being equal. H_k ranged from 4 – 15 Oe for samples with thicknesses of 3 - 25 nm respectively. H_k was measured by measuring the intercept of linear fits between saturated and non-saturated parts of hard axis M-H loops [Cullity 1972]. H_c ranged from 1-3 Oe for single layer NiFe

films studied, and tends to increase as a function of film thickness, similar to results in NiFe reported by other workers [Akhter 1997]. The low H_c values are consistent with a small grain size. The magneto-optical Kerr effect (MOKE) system used here is a localized magnetometry technique, spatially probing magnetization reversal events only in the surface area covered by the laser spot [Chapter. 2]. Magnetic switching was therefore investigated at random locations on a film surface. H_c was found to vary by less than 10 % across an entire 5 × 5 mm^2 chiplet.

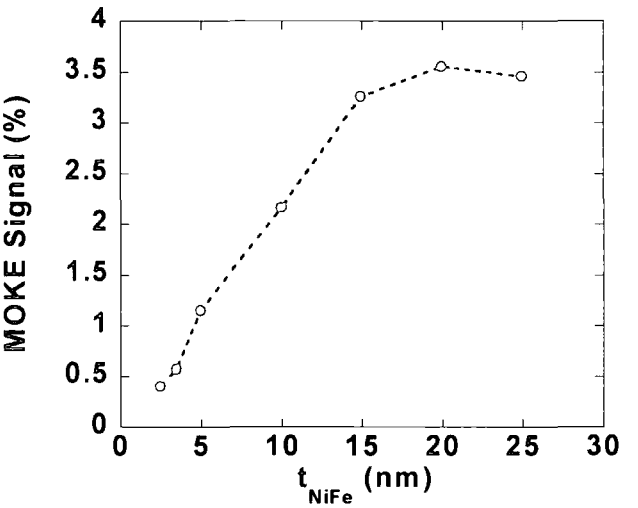

Figure 3.6: Measured MOKE signal for virgin NiFe films as a function of thickness.

Film thickness was further verified by MOKE signal measurements as a function of Nife thickness, t_{NiFe}, for as-grown thin films – Fig 3.6. In the thickness range t_{NiFe} = 2.5-15 nm the relationship between film thickness and MOKE signal is linear. In this thin film limit, all of the generated MOKE signal is generated in-phase. For t_{NiFe} = 20 nm the increase in signal with t_{NiFe} is not so pronounced, and for t_{NiFe} > 20 nm the MOKE signal becomes saturated. This skin depth value is similar to other reported values for the information depth of light in metals [Hubert 1998][Park 2002].

3.4 Bilayers

3.4.1 Structural Properties

Virgin NiFe films are vulnerable to surface oxidation, which can lead to a change of magnetic properties in a sample [Wernsdorfer 1997]. For example, a surface magnetic oxide layer can reduce the effective magnetic thickness of a sample. This is undesirable in the laboratory, and in the context of device development. Furthermore the study of layered films and hetrostructures has many interesting applications, for example [Wolf 2001]. Principal capping species chosen were Aluminium and Gold. A bright field transmission electron microscopy (TEM) image of a typical as deposited bilayer investigated is shown in Fig. 3.7

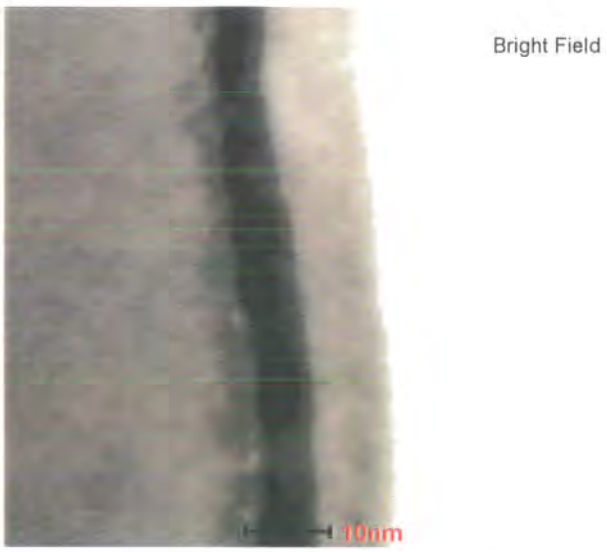

Figure 3.7: Cross-sectioned transmission electron image of a Si/$Ni_{81}Fe_{19}$(8nm)/Al(10nm) bilayer.

A bilayer was cross-sectioned by Ga^{+} ion beam milling, [Langford 2001], and analysed by workers at the University of Glasgow, providing direct confirmation of thickness measurements of magnetic and non-magnetic layers. TEM measurements verified reasonable quality of interfaces with no long range intermixing in bilayer samples, at either the upper Al/NiFe, or the lower NiFe/Si interfaces. Low Z-number contrast between Ni and Fe atoms may be responsible for some of the interfacial blurring apparent in Fig. 3.7.

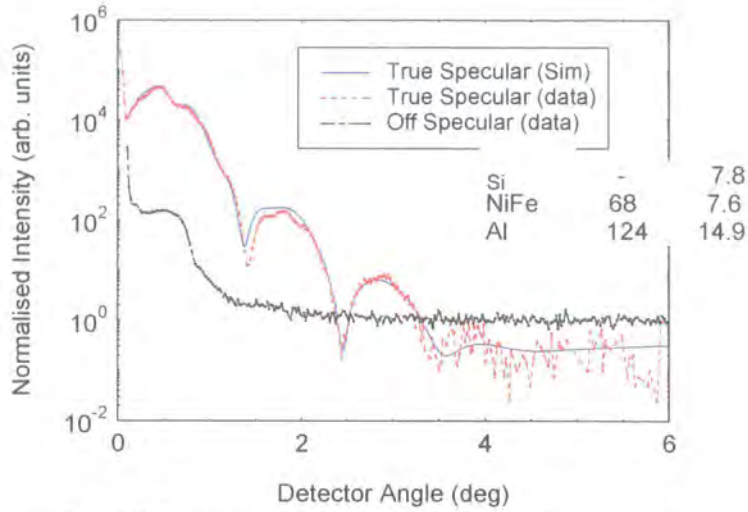

Figure 3.8: GIXR measurements of an Si/NiFe/Al bilayer sample.

Fig. 3.8 shows shallow angle x-ray intensity fringes measured from a Si/NiFe/Al bilayer, with a measured NiFe thickness of 68 Å, and Al thickness of 124 Å. GIXR measurements indicated some swelling of the Al thickness which is interpreted in terms of the formation of a surface oxide layer. The average interface width between NiFe and Al layers was measured at 7.5 ± 1 Å averaged across a 5 mm^2 surface. This experimentally determined interface width corresponds well with the interface width at $Al/Ni_{80}Fe_{20}$ samples evaluated by Egelhoff and co-workers - 6 Å, again by grazing incidence x-ray reflectometry, fitted by BEDE software [Egelhoff 2001].

3.4.2 Magnetic Properties

M-H loops of NiFe/Al films with varied capping layer thickness were investigated. The presence of a protective non-magnetic capping layer attenuates reflected Kerr signal from a ferromagnetic NiFe underlayer. Figure 3.9 shows the

quenching of measured Kerr effects signal from NiFe films as a function of Al thickness.

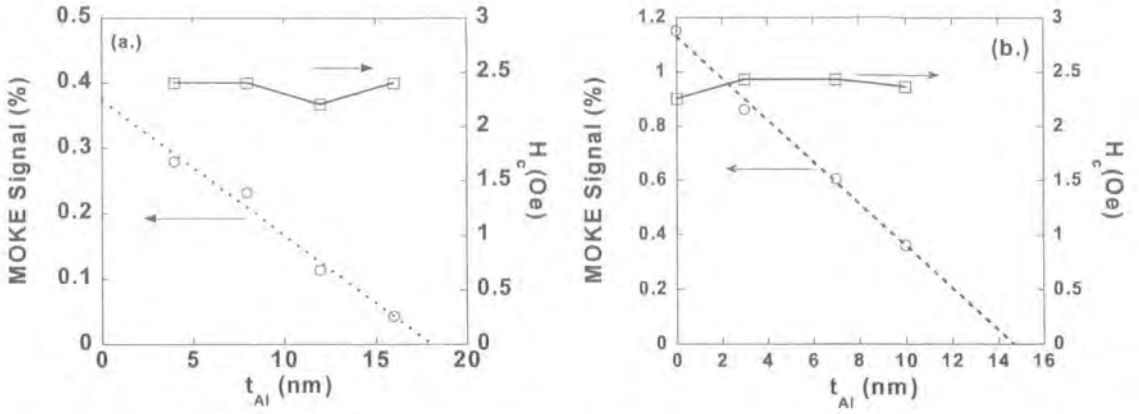

Figure 3.9: Measured MOKE signal (%) (--○--) and easy axis coercive field, H_c (—□—), as a function of Al capping layer thickness, t_{Al}. Graph (a.) corresponds to a 2nm thick NiFe layer and (b.) to a 5 nm thick NiFe layer.

The measured Kerr effect signal from buried NiFe layers shows a linear decrease with increasing Al thickness. From the straight-line fit intercept value of MOKE signal plotted against t_{Al}, we infer a skin depth of light in Al of ~ 20 nm, similar to Permalloy.

It is known that magnetic and structural properties of thin films are modified by the addition of a capping layer, due to effects such as in-plane strain [Vaz 2001], and interfacial intermixing [Buchanan 2002/2]. Some magnetic and structural modification of NiFe layers is inevitable with the addition of a non-magnetic upper interface to the Si/NiFe system, due to symmetry considerations, changes in electronic structure at interfaces, and morphological modification of the magnetic layer with the addition of an additional interface.

It is noted that the measured variance of switching fields between overcapped and uncapped control samples is less than 10 % - this represents good experimental agreement given that measurements were made on separate wafers. H_c is not affected

by increasing overlayer thickness. Additionally the linear fit to MOKE signal vs. t_{Al} suggests that the thickness of the active ferromagnetic NiFe layer is not compromised greatly by the addition of an overlayer. The presence of an uncapped control sample in the data of figure 3.9b adds increased weight to this assertion.

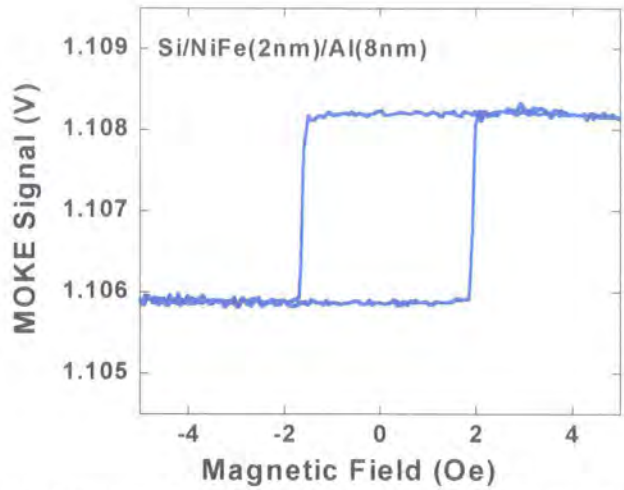

Figure 3.10: M-H loop for a 2 nm thick $Ni_{81}Fe_{19}$ film embedded between a non-magnetic Al cap and a Si substrate.

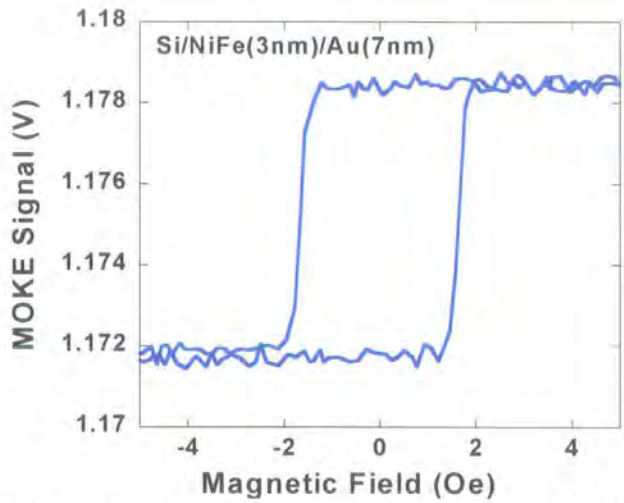

Figure 3.11: M-H loop for a 3 nm thick $Ni_{81}Fe_{19}$ film embedded between a non-magnetic Au cap and a Si substrate.

Fig. 3.10, and Fig 3.11 display M-H loops for as-deposited ultrathin NiFe films on Si with Al or Au protective overlayers. The magnetization reversal mechanism for overcapped NiFe films is presumed to be by easy domain wall motion.

High M-H loop squareness and sharp switching transitions suggest a low density of pinning sites - a domain wall can propagate freely once nucleated, reversing large parts of the sample.

3.5 Summary

Thermally evaporated Si/$Ni_{81}Fe_{19}$, and Si/$Ni_{81}Fe_{19}$/X samples were grown by thermal evaporation, for subsequent patterning by focused ion beam, where X = Al or Au. A summary of the principal samples grown and subsequently patterned for further investigations in Chapters 4-7 is presented in Table. 1.

Sample	t_{NiFe} *(nm)*	t_{Al} *(nm)*	t_{Au} *(nm)*
Si/NiFe	3-25	-	-
Si/NiFe/Al	2	4, 8, 12,16	-
Si/NiFe/Al	3, 5, 8, 12	10	-
Si/NiFe/Al	3.5	10	-
Si/NiFe/Al	5	3, 7, 10	-
Si/NiFe/Au	2,3,4,6	-	7

Table 1: Summary of samples investigated

3.6 References

[Akhter 1997] M. A. Akhter, D. J. Mapps, Y. Q. Ma Tan, A. Petford-Long, R. Doole, J. Appl. Phys. **81**, 4122 (1997)

[Brückner 2001] W. Brückner, S. Baunack, M. Hecker, J. Thomas, S. Groudeva-Zotova, C. M. Schneider, Mat. Sci. Eng. B, **86**, 272 (2001)

[Buchanan 2002/1] J. D. R. Buchanan, T. P. A. Hase, B. K. Tanner, N. D. Hughes, R. J. Hicken, Appl. Phys. Lett. **81**, 751 (2002)

[Buchanan 2002/2] J. D. R. Buchanan, T. P. A. Hase, B. K. Tanner, P. J. Chen, L. Gan, C. J. Powell, W. F. Egelhoff, Phys. Rev. B, **66,** 104427 (2002)

[Cooke 2003] M. D. Cooke, D. A. Allwood, D. Atkinson, X. Giong, C. C. Faulkner, J. Magn. Magn. Mat. **257**, 387 (2003)

[Cullity 1972] B. D. Cullity, "*Introduction to Magnetic Materials*," Addison-Wesley, Massachusetts (1986)

[Egelhoff 2001] W. F. Egelhoff, P. J. Chen, R. D. McMichael, C. J. Powell, R. D. Deslattes, F. G. Serpa, R. D. Gomez, J. Appl. Phys. **89**, 5209 (2001)

[Hollingworth 2003] M. P. Hollingworth, M. R. J. Gibbs, S. J. Murdoch, J. Appl. Phys. **94**, 7235 (2003)

[Hubert 1998] A. Hubert, R. Schäfer, "*Magnetic Domains – The analysis of magnetic microstructures*," Springer-Verlag, Berlin Heidleberg (1998)

[Langford 2001] R. M. Langford, A. K. Petford-Long, J. Vac. Sci. Technol. A. **19**, 982-985 (2001)

[Park 2002] C. M. Park, J. A. Bain, IEEE Trans. Magn. **38**, 2237 (2002)

[Wernsdorfer 1997] W. Wernsdorfer, K. Hasselbach, A. Benoit, B. Barbara, B. Doudin, J. Meier, J. –Ph. Ansermet, D. Mailly, Phys. Rev. B, **55**, 11552 (1997)

[Vaz 2001] C. A. F. Vaz, G. Lauhoff, J. A. C. Bland, B. D. Fulthorpe, T. P. A. Hase, B. K. Tanner, S. Langridge, J. Penfold, J. Magn. Magn. Mater. **226**, 1618 (2001)

[Wolf 2001] S. A. Wolf, D. D. Awschalom, R. A. Buhrman, J. M. Daughton, S. von Molnár, M. L. Roukes, A. Y. Chtchelkanova, D. M. Treger, Science **294**, 1488 (2001)

Chapter 4: Focused Ion Beam patterning of planar magnetic nanowires

4.1 Introduction

The use of a focused ion beam (FIB) of 30 keV Ga^+ ions for the topographic structuring of $Ni_{81}Fe_{19}$ films to fabricate functional planar magnetic nanowires is described. Energetic heavy ion bombardment is known to lead to the sputtering of surface atoms at a vacuum-target interface, with a resultant thinning of the surface as a function of radiation dose. By controlled radiation exposure of a target, the prospect of localised modification of the surface morphology exists, with a concomitant modification of magnetic properties.

Section 4.2 presents some of the applications of focused ion beam milling in condensed matter physics and the research community at large, and briefly lists some important work by other groups using FIB in the field of magnetism. The experimental apparatus is described in Section 4.3. A method of dose testing to determine the optimum fluence of ions to magnetically pattern a continuous film is described. Localized ion patterning of functional magnetic structures is treated in Section 4.4. The coercivity and switching field angular dependence of high aspect ratio wires, of width 60-500 nm is investigated in Section 4.5. The effect on magnetic properties of ion beam raster direction relative to the major axis of nanowires is addressed in Section 4.6. Ion beam raster direction is demonstrated to have a strong effect on nanowire coercivity and hard axis anisotropy field. A brief discussion and conclusion closes the chapter – Section 4.7.

4.2 Literature

Ion beam irradiation in general can be used in modify samples by thinning, polishing, depth sectioning, doping or milling [Reyntjens 2001]. Specifically, the FIB was initially used for fault control and defect analysis in microelectronics, and sample doping, but now finds applications as diverse as nano-pore preparation for DNA studies [Li 2001], rapid patterning of poly(methylmethacrylate) (PMMA) films for microfluidic and molecular gate applications [Cannon 2004], or even ordering assemblies of carbon nanotubes [Jung 2004].

Some advantages of the Ga^+ FIB tool over other fabrication technologies such as electron beam lithography or photo-lithography are:

- It is a dry, localized fabrication process, free from masks and resists, which can be costly, and add additional time consuming stages to the fabrication process.
- It can be used to subtractively mill and modify materials not easily patterned by other techniques.
- Direct deposition of metals [Langford 2002], or local property modification by intermixing [Gierak 2004] are possible.
- It is easily customised, curved substrates can be patterned, and angular cuts made, and it is well suited to 3-D uses such as Josephson junctions [Bell 2003].
- In the development environment it can be used for rapid prototyping of structures. Reasonably high patterning speeds are attainable, with beam dwell times down to 100 ns/point – in principle device throughput can be enhanced with multi-beam systems.

In the magnetism community, Ga^+ ion beam irradiation has applications as diverse as magneto-electronics logic device fabrication [Johnson 2000], and transmission electron microscope cross-section preparation [Langford 2001], in which samples are cut and thinned by FIB, making them electron transparent. Magnetic FIB patterning of Co structures as thin as 2 atomic layers, with 100 nm lateral resolution was reported as early as 1998 [Stamm 1998]. It has been used in the ongoing development of increased density data recording media [Lohau 2001]. For example nanometer scale patterns in a $Co_{70}Cr_{18}Pt_{12}$ film were fabricated to act as servo patterns for recording head positioning [Albrecht 2002]. In addition FIB has been used in magnetic force microscope (MFM) tip modification [Folks 2000], to lessen stray field from the probe. Recent reviews of ion beam erosion of surfaces [Carter 2001], and of FIB applications [Matsui 1996] are useful references.

4.3 Dose Test: Critical ion fluence

4.3.1 Focused Ion Beam

The experimental apparatus employed was a commercial FEI 200 xP FIB workstation. By applying a voltage to a liquid metal ion source, a stream of Ga^+ ions can be drawn from a point-like tip, and focused onto a sample located on a 5-axis moveable stage. A tungsten needle-like tip is coated by a gallium liquid metal coating. A potential energy, typically 10-50 kilo-volts, is applied to the needle relative to the tip, extracting a stream of positive metallic ions from the apex of the tip. Electrostatic lenses and deflectors are used for focusing the heavy gallium ions. The liquid metal ion source in this study was operated at an accelerating voltage of 30 keV. Upon application of this voltage to the gallium source, an emission current is drawn, and a

pencil of ions is focused before interaction with the target. The emission current was maintained at 2.2 μA.

The stage can be both rotated and tilted relative to the ion beam, and was maintained perpendicular to the beam for results described herein. The stage was at eucentric focus at a working distance of 1.7 cm from the ion gun. The eucentric focus is where the beam focus and the stage tilt axis intersect in 3-d space. Using an iterative process of focusing on smaller surface features, while tilting the stage, the optimum eucentric focal position can be quickly found to within ± 3 μm. By focusing the ion spot of the sample surface in the plane of eucentric focus, no matter how the stage is rotated or tilted the sample is still in focus at this position. The chamber was typically operated at 5×10^{-7} mbar, and the beam column at 8×10^{-8} mbar. Due to the low base pressure, the collisional free path of sputtered target atoms is high. This reduces redeposition of sputtered atoms on the target surface. To a good approximation mono-energetic, mono-directional ions are incident on the surface.

We note that the heavy mass of Ga^+ incident ions in FIB as compared to light electrons in conventional electron lithography can be an advantage – allowing sputtering and mixing effects at the target surface. Ga^+ ions are much less likely to be deflected by stray magnetic field emanating from the patterned material than electrons. Furthermore, secondary electron emission takes place with the excitation of metal surface electrons during FIB irradiations, facilitating imaging during the fabrication process. This makes FIB a particularly versatile laboratory tool.

4.3.2 Surface Sputtering

Figure 4.1 shows a schematic of the geometry treated in this chapter, and a schematic of the surface sputtering process. When an energetic ion impacts on a surface, if the energy is great enough to overcome the repulsive energy barrier posed

by the surface atoms, the incident ion penetrates the target, and sputtering at the surface can result. Neutral atoms, ions, and electrons are sputtered at the vacuum-target interface.

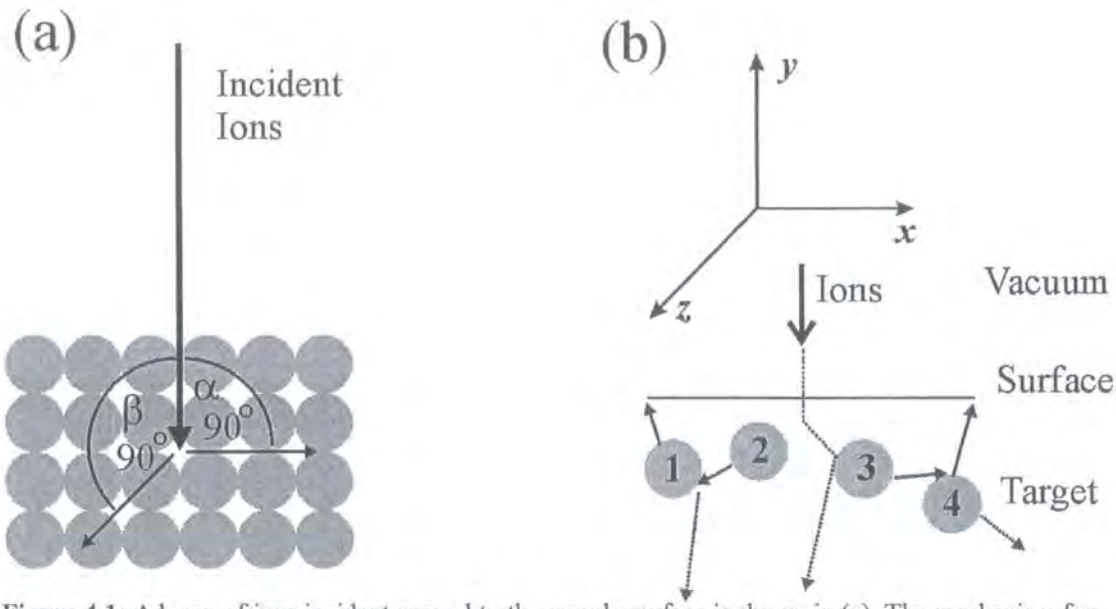

Figure 4.1: A beam of ions incident normal to the sample surface is shown in (a). The mechanism for surface sputtering of target atoms by incident ions is outlined in (b), where atoms "1" and "3" escape from the vicinity of the target surface into the vacuum.

On considering the interaction of ions with a target, in a phenomenon such as surface sputtering, the following variables should be considered; ion mass, species, energy, azimuthal and polar angles with respect to the surface normal and a specified crystallographic direction, flux density and fluence and substrate mass, species, crystallographic orientation and temperature [Carter 2001].

An energetic ion deposits a proportion of its energy spatially on a target surface; the spatio-temporal evolution of the target under irradiation is also a function of local properties of the target surface such as existing surface features and steps, surface roughness and curvature. Surface sputtering is in general confined to the first few atomic layers of a target material (approximately 0.5nm), and can occur as a result of the first ion-surface collision, or recoils from the initial impact – Figure 4.1.

The sputtering yield is highly dependent on the beam angle relative to the sample surface. An ion incident perpendicular to a target atom in a head-on-collision will in general transfer a velocity component to the target atom, driving the target atom into the sample bulk. Thus no sputtering results directly from the first collision, but possibly from secondary collisions if the ion energy is high enough. For an inclined sample surface relative to the ion beam, a larger sputter yield may therefore result (velocity transfer is more likely to occur in directions not parallel to the y-axis). If the incident angle between ion and target is near grazing, the ion is reflected from the sample surface, without penetrating the target bulk. The sputtered atom energy, direction, and the sputtered atom yield per incident ion all reflect the statistical nature of the irradiation process.

By controlling the exposure time of a sample to incident radiation, the sample surface may be thinned, or sectioned. Section 4.3.3 describes dose testing, which is equivalent to performing a depth sectioning across a sample surface for many different controlled doses, and was described recently by Gang Xiong [Xiong 2001].

4.3.3 Dose Test

The effect of homogeneous Ga^+ irradiation on a polycrystalline 10 nm thick continuous film of NiFe on a Si substrate is investigated, and interpreted mainly in terms of surface sputtering by energetic ion irradiation. By exposing defined areas of a ferromagnetic thin film to controlled radiation doses, and then probing the evolution of the sample magnetization as a function of incident ion fluence, the Ga^+ dose required to remove room-temperature ferromagnetic ordering is determined. We call this the critical ion fluence, Φ.

Minimizing exposure of the thin film to energetic Ga^+ ions reduces damage to the surface, reduces sidewall damage of patterned nanostructures, and lessens

fabrication time, increasing device throughput. Furthermore, using a high ion dose can make samples more vulnerable to stage drift [Petit 2004] and associated feature broadening. Therefore an ion dose just in excess of Φ was typically used for patterning magnetic nanostructures.

The areal dose, D, defined as the total number of ions incident on a surface per unit area is defined as:

$$D = \frac{I \times t}{eA} \qquad [4.1]$$

Here I represents the ion current, t is the exposure time in seconds, $e = 1.602 \times 10^{-19}$ C, and A is the irradiated area in cm^2. Similar to other workers, we use a unit of ion/cm^2 to describe the areal dose.

Uniformly exposed FIB irradiated samples were prepared for magneto-optical characterisation in the following manner. A 3 nA beam of Ga^+ ions was scanned normal to the sample surface, with an X and Y beam overlap of 50 %. Large 100 μm^2 "windows" of a 10 nm thick NiFe film were irradiated for exposure times, from 0-84 seconds (Fig. 4.2). The exposure time was a multiple of the time taken for a 3 nA beam to raster once over a window, at a beam dwell time per pixel of 1 μs – in this case 0.686 s. 100 μm^2 'windows' dimensions facilitated easy sample location and localized characterization by MOKE. The results described here are for a 10 nm thick $Ni_{81}Fe_{19}$ film, but the technique was applied across many samples.

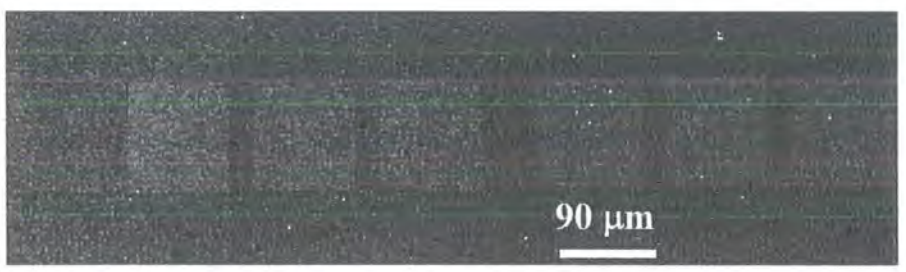

Figure 4.2: Scanning electron micrograph of 100 × 100 μm^2 Ga^+ irradiated windows, suitable for localised MOKE investigation, in a continuous 10nm $Ni_{81}Fe_{19}$ film on Si.

Typically a 20 μm distance was used between irradiated windows. Unirradiated reference areas of each tested films were also probed magnetically, as a reference. By positioning the laser spot in the middle of each irradiated window, the local change in magnetic properties as a function of D was investigated. All irradiations were performed at room temperature.

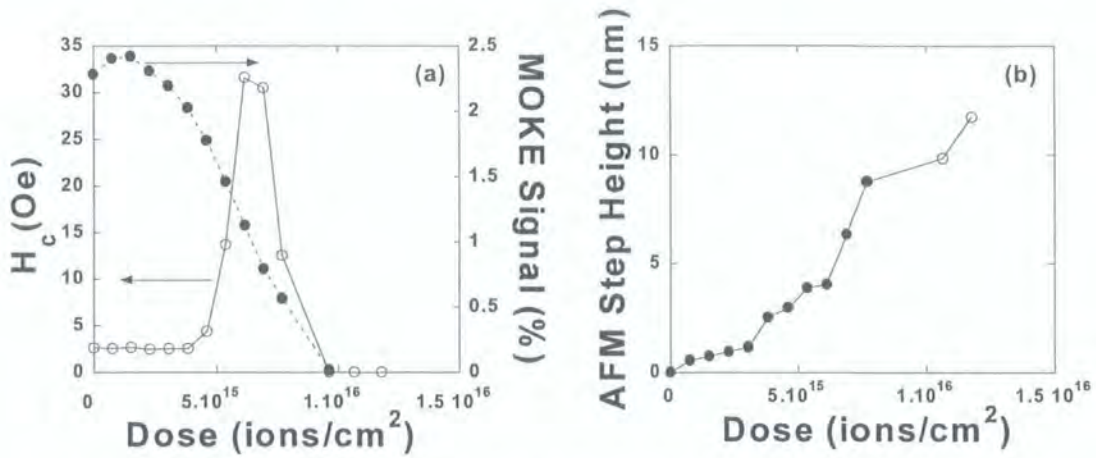

Fig 4.3: Dose test results for 100 μm^2 irradiated areas on a 10 nm continuous NiFe film. (a) displays the change of magnetic properties as a function of fluence, where H_c (—o—) is the measured easy axis coercivity, and the MOKE signal (---•---) gives an estimation of sample spontaneous magnetization.
(b) shows the measured step height between irradiated and unirradiated areas of film as a function of dose. (•) represents the step heights at which magneto-optical measurements indicate room temperature magnetic ordering is still present, (o) indicates the measurement heights at which no magnetic hysteresis is observed. All lines are a guide for the eye.

Representative dose test results for a 10 nm thick NiFe film on Si are shown in Figure 4.3. Results may be summarised as follows.

The magneto-optical Kerr effect (MOKE) signal [Chapter 2] changes for lowest applied ion doses. MOKE signal shows an anomalous peak at Ga^+ ion fluences, $D \leq 2.3 \times 10^{15}$ ions/cm^2, where the measured MOKE signal is greater than for an as- deposited film. [The physical origin of this peak is not thought to be an increase in sample spontaneous magnetization and is treated in Chapter 5, Section.5.3.1.]. For $D \geq 3.1 \times 10^{15}$ ions/cm^2 there is a monotonic decrease in MOKE signal as a function of Ga^+ radiation, concomitant with a loss of spontaneous

magnetization within the sample. At a critical dose, $\Phi = 9.6 \times 10^{15}$ ions/cm^2, no room temperature ferromagnetic ordering is measured by the magnetometer on the irradiated area. H_c, decreases slowly as a function of dose from $0 < D \leq 3.85 \times 10^{15}$ ions/cm^2 due to radiation thinning of the sample [See Section 5.3.2 for more detail]. For $D > 3.85 \times 10^{15}$ ions/cm^2 slightly more rounded hysteresis loops with a higher H_c are measured, prior to extinction of room temperature hysteresis – Figure 4.4. In addition we note that a higher saturation field, H_s, is measured with increasing Ga^+ fluence. For doses close to the critical ion dose, M-H loops are significantly rounded, and have an s-shaped form. Magnetisation reversal is then no longer characterised by easy domain wall motion, in which the domain wall propagation field is lower than the domain wall nucleation field.

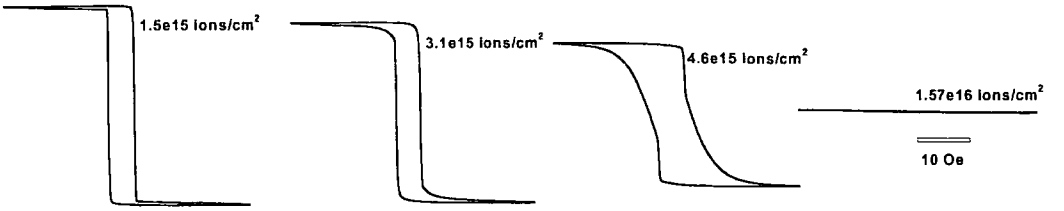

Fig 4.4: Kerr effect loops from a 10 nm thick film uniformly irradiated with increasing fluences of Ga^+ ions. All loops were taken in uniform field conditions at a field sweep rate of 54 Oe/s. Signal levels are normalised to an un-irradiated reference sample.

Heavy Ga^+ ions are known to cause damage [Ozkaya 2002] and amorphization to the crystal lattice. The M-H loops in Figure 4.4, and the radiation induced increase in H_c are interpreted in terms of pinned domain wall motion through a disordered medium, with a higher frequency of pinning sites, than a virgin film. There may be a higher concentration of domain wall nucleation centres, due to irradiation-induced damage in the film.

Domain walls in thin films are very sensitive to the top and bottom surfaces of a thin film. In a more disordered medium, field induced domain wall motion is

frustrated by a higher frequency of domain wall pinning sites, meaning a higher applied field needs to be applied for domain walls to be depinned, and for the film to become magnetically saturated.

The atomic force microscopy step-height measurements[1] indicate a thinning of the irradiated area as a function of ion dose, due to the sputtered removal of target atoms, from the surface-vacuum interface. This sputtering is by momentum transfer [Tseng 2004]. A sputter rate of ~ 8 Ni or Fe atoms/ion is estimated. Roughness measurements of irradiated areas as a function of D, (shown in Figure 4.5.A), add weight to the assertion that material is sputtered from the sample surface, and indicate with increasing flux, roughness increases considerably, making multiple domain wall pinning sites probable in any 100 × 100 μm^2 Ga^+ exposure window at higher radiation doses.

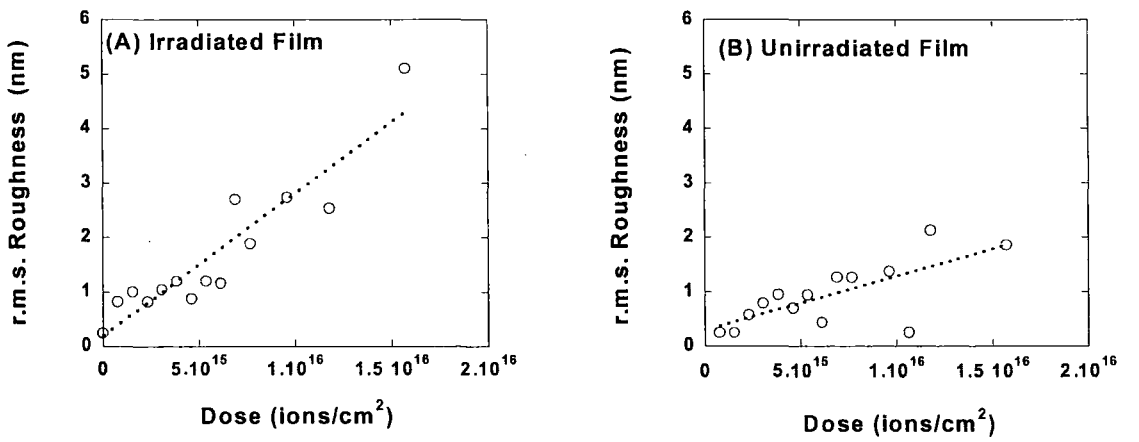

Fig 4.5: Root mean square surface roughness for irradiated 10 nm think NiFe film as a function of ion dose (A). Plot (B) shows the increase in surface roughness on unirradiated 20 μm × 20 μm areas immediately adjacent to regions exposed to different ion beam doses. Trend lines are least squares fits.

Surface roughness of non-irradiated areas immediately adjacent to ion irradiated regions also increased with ion fluence, consistent with redeposition of

[1] Step height and surface rougnhess measurements described here were performed using a Digital Instruments 3a Nanoscope scanning probe microscope, operated in atomic force microscope (AFM) contact mode with a silicon nitride tip.

sputter material. R.M.S. roughness was calculated over 45 × 45 μm^2 raster (irradiated region) and 20 × 20 μm^2 raster (non-irradiated region) scans, performed at a scan rate of 2Hz, and a tip velocity of 180 μm/s. Once Φ has been determined – the ion dose at which no room temperature ferromagnetic ordering is observed, it is possible to locally magnetically pattern films to high precision.

4.4 Planar Nano-wire Fabrication

Because FIB is a scanning probe technique, it is possible to locally modify the magnetic properties of a ferromagnetic thin film, in a reproducible manner on a nano-metre length scale. Lateral FIB patterning resolution depends on the aperture size, which determines the ion beam current, and hence the ion beam diameter.

Before exposing the NiFe film with the FIB, beam definition files were created containing the ion beam scan parameters for the desired patterns. Beam definition files contain the beam dwell time per pixel, the nominal dimensions of features to be defined (measured in units of the specified beam diameter), and the pattern exposure time. The depth of the resultant milled features is determined by the total beam exposure time. During the patterning process, great care is taken to ensure that the ion beam never scans over the part of the structure that is to remain magnetically active. Three patterning steps were performed in the lateral patterning of NiFe nanostructures, all steps performed *in situ* in the FIB chamber without breaking vacuum, with a fixed stage position.

First a high resolution, isolating cut was made with a 10-pA beam of Ga^+ ions to isolate the desired structure from the continuous magnetic film (Figure 4.6.A). Each individual XY coordinate in the beam definition file corresponds to a pixel size of dimensions 11.4 × 11.4 nm^2 – the approximate beam diameter of the 10-pA beam.

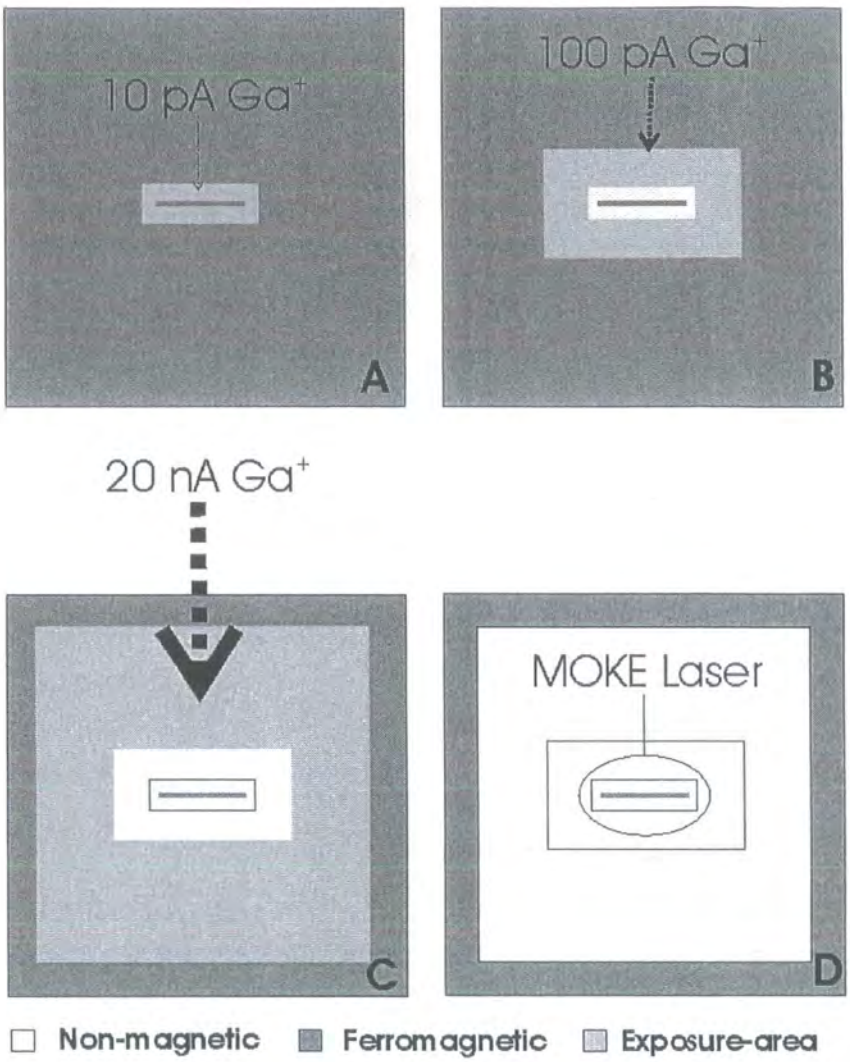

Fig 4.6: Schematic of 3-step milling process. (A) High resolution 10 pA isolating cut to define structure sides. (B) Low resolution 100 pA exposure to clear magnetic film from area surrounding pattern. (C) 20 nA exposure to define 120 × 120 μm^2 non-magnetic square, around patterned structure. (D) MOKE measurement. (Not to scale).

■ represents ferromagnetic film, ■ indicates area of film surface under irradiation, □ represents irradiated, non-magnetic film.

Generally the ion beam was rastered parallel to the structure sides, spot by spot. Once one complete ion beam scan over the field of view has been completed (with the pre-defined structural features still unexposed to Ga^+ ions), the ion beam returns to the origin of the pattern field of view, for subsequent raster scans. This high-resolution milling step, performed at 10 pA, is the sole milling step in which the ion beam touches the patterned structure sides, defining the structure edges. A 10-pA

beam size is used as a small spot size enables patterning with reduced ion implantation into fabricated structure sidewalls, and good feature acuity.

For the low resolution, second fabrication step, a 100-pA beam current ferromagnetically quenches the magnetic film further away from the defined structure edges. The stronger the ion current, the larger the spot size, and the higher the sputter rate (Figure 4.6.B). The 100 pA beam has a ~20 nm beam diameter.

Finally a 20 nA beam current is used to mill all magnetic material within a 120 × 120 μm^2 area surrounding the magnetic structure, so the MOKE magnetometer does not pick up any spurious magnetic signal from the surrounding film (Figure 4.6.C-D). The 20 nA beam has a ~60 nm beam diameter.

Figure 4.6.D shows a MOKE laser spot placed over a ferromagnetic wire isolated from the magnetic film by 3 successively lower resolution, but quicker milling stages.

Sets of wire arrays of nominal track width, W = 60-500 nm, and a constant length, L = 9 μm, were patterned from a T(thickness) = 5 nm film. Φ was determined at ~3×10^{15} ions/cm^2 for a 5 nm thick NiFe film. A constant 1 μm inter-wire edge-to-edge separation was maintained for elements in each array to lessen magnetic stray field interactions between wires. Scanning electron microscopy (SEM) and FIB microscopy was used to image patterned structures, and check for defects. For presentational purposes additional structures were fabricated for imaging, therefore measured magnetic properties of samples were not compromised by an additional Ga^+ radiation dose incurred during imaging.

4.5 Planar Nanowire Magnetic Properties

4.5.1 Wire Easy Axis Coercivity: H_c

The magnetic properties of $Ni_{81}Fe_{19}$ planar wire arrays, and individual magnetically isolated wires were investigated. High aspect ratio wires of varied width, 60 nm ≤ W ≤ 500 nm, fixed length, L = 9 μm, and fixed thickness, T = 5 nm were studied by MOKE. Uniformly spaced wire arrays, with a constant 1 μm inter-wire edge-to-edge separation were fabricated.

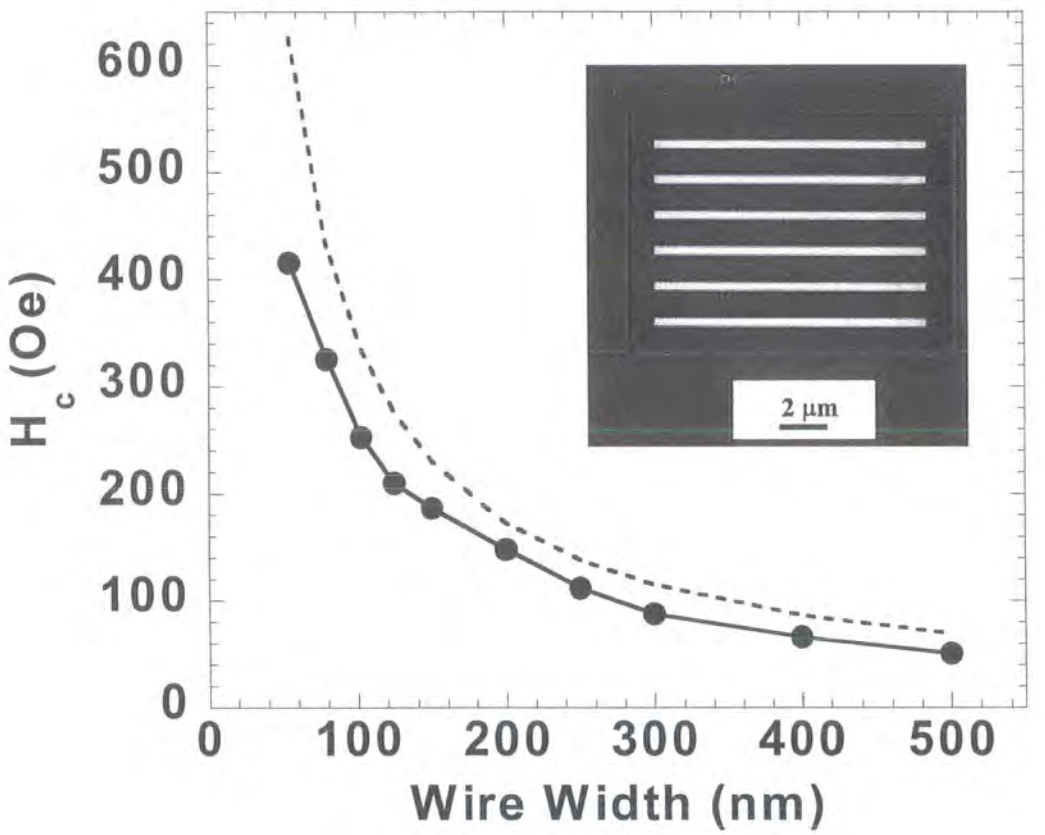

Fig 4.7: Experimentally measured switching field, H_c, for W = (60-500 nm), L = (9 μm), T = (5 nm) $Ni_{81}Fe_{19}$ planar nanowires, patterned by FIB (—•—). The dashed line (-----) represents an analytic solution of H_c. Inset is a FIB secondary electron image from a W = 300 nm 6-element planar wire array.

Figure 4.7 exhibits the relationship between H_c and W, for patterned planar 6-element wire arrays. A strong increase in H_c with the recipricol of W is observed – sample geometry has a dramatic effect on the magnetization reversal field. A similar trend has been observed for isolated wires. This relation holds at least to wires as

narrow as 60 nm, with H_c = 415 Oe. W = 60 nm was the lowest wire width investigated. For increasing W, H_c tends very gradually towards the coercivity of a 5 nm thick thin film ~ 1-2 Oe, due to a reduction in shape anisotropy. The effects of Ga^+ wire sidewall implantation may lead to a greater dicergence between measured and calculated H_c as the wire width is reduced, as a greater net width of the wire is rendered non-magnetic. For the wire dimensions studied, internal dipolar fields control H_c, i.e. wire coercivity depends on the demagnetizing field of the sample. From Stoner-Wohlfarth analysis, an absolute upper bound of H_c for an elongated particle with uniaxial anisotropy is given by an analytic expression of the form [Yuan 1992]:

$$H_c = \frac{8M_s T}{W}.S \qquad [4.2]$$

where M_s is the saturation magnetization, and S is a finite length shape anisotropy factor. This is the magnetostatic energy barrier associated with reversing magnetization of the entire wire in-plane, parallel to the short axis – reversal by coherent rotation. The expression is appropriate in the thin film limit, where sample magnetization is constrained in-plane, and micromagnetic configurations such as vortices with out of plane spins are not energetically favoured.

$$S = \left[\frac{(\rho - \frac{1}{\rho})}{\sqrt{1+\rho^2}} \right] \qquad [4.3]$$

Here, ρ = L/W is the in-plane aspect ratio.

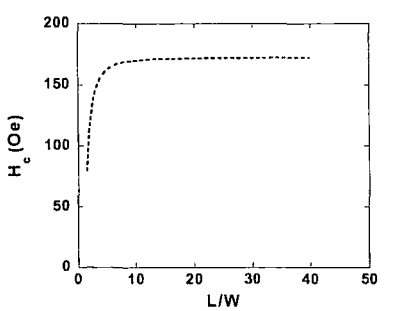

Fig 4.8: Calculated H_c for a fixed width, W = 200 nm wide, T = 5 nm, wire, as a function of aspect ratio.

Since $\rho \geq 18$ for the wire dimensions studied, S tends to 1, and H_c is independent of wire length. The experimental and analytic values of H_c are in excellent qualitative and reasonable quantitative agreement. Calculated values of H_c generally represent an upper limit on experimentally measured values. The analytic calculation represents a 0 K estimation of H_c in a perfect wire geometry with no edge roughness - which may lower wire switching field [Gadbois 1995], in the absence of width or thickness variation, or compositional inhomogeneity.

H_c is calculated by analogy to a coherent rotation reversal mechanism. For magnetic field applied parallel (//) to the wire long axis, (the energetically most favoured axis), reversal is assumed to be by domain wall expansion and propagation [Kirk 2001]. Results presented here are in quantitative agreement with low temperature magnetization reversal investigations on NiFe wires of similar dimensions, in which magnetization reversal is mediated by a small nucleus that spreads down the wire [Uhlig 2004]. Low temperature switching investigations enable calculation of a critical activation volume needed for magnetization reversal by domain wall motion, see also [Wernsdorfer 1996]. Nucleation is a localized event, followed by rapid domain expansion.

In general the task of interpreting magnetic hysteresis curves in terms of the magnetic spin structure of nanomagnets can be complicated. However, for the wire geometries studied, magnetization is aligned parallel to the wire long axis in the absence of applied field. Figure 4.9 shows representative M-H loops for wire arrays investigated. The magnetic ground state of elongated 5 nm thick NiFe planar wires is the single domain state - the dimensions of the system are such that a domain wall is not energetically favoured. For the high aspect ratio [L/W] wires investigated, $18 \leq$

L/W ≤ 150, wire magnetization is aligned in plane at remanence (zero applied magnetic field), due to a large planar demagnetizing field.

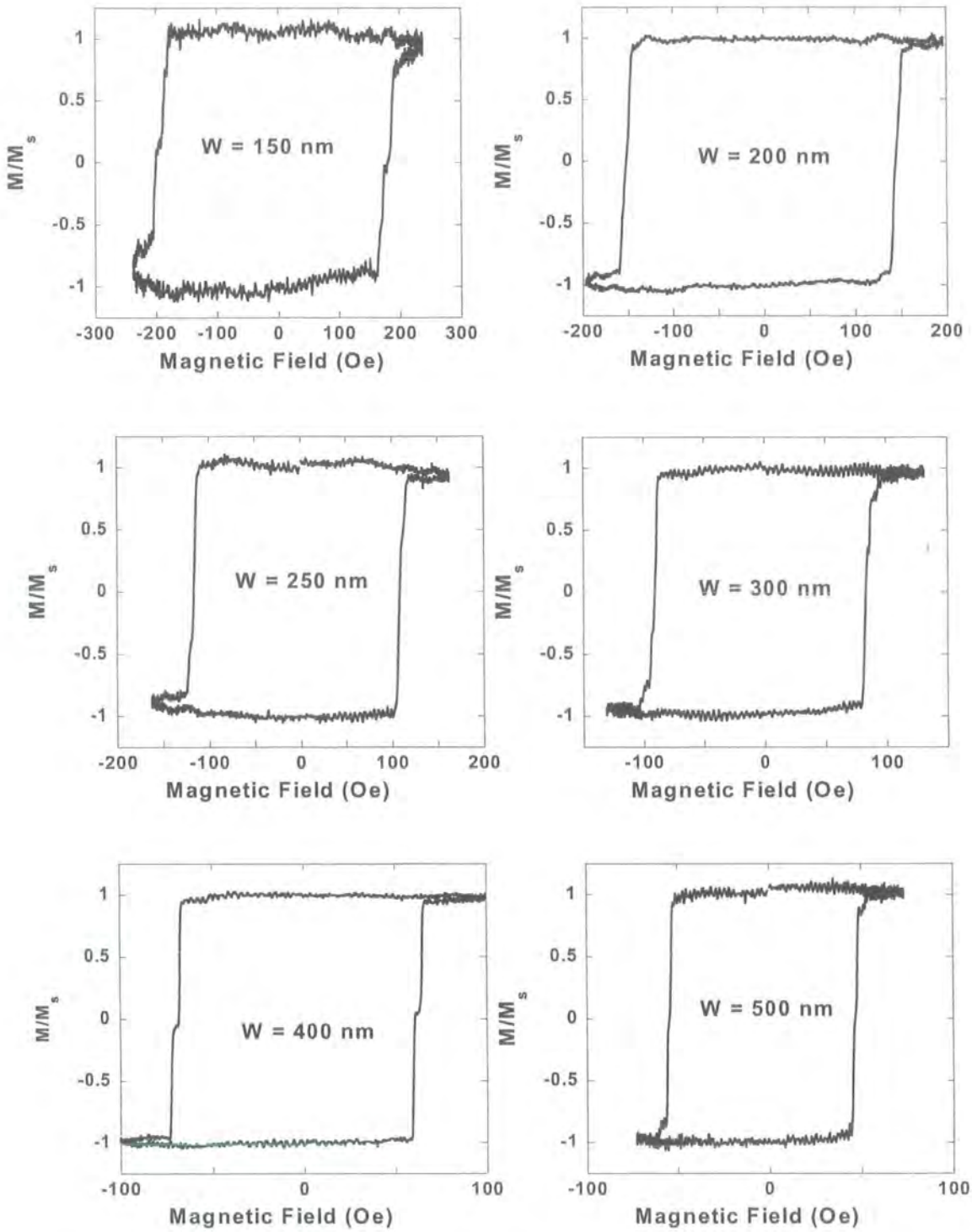

Fig 4.9: Representative easy axis M-H loops for 6 element wire arrays, with 1μm inter wire edge-to-edge separation in each wire array. Each magnetic hysteresis loop was time averaged for at least 1600 field cycles.

Magnetic hysteresis loops were magnetically saturated to field values well in excess of H_s to verify the magnetic field at which arrays became saturated. This confirmed that small openings in some M-H loops above H_s are optical and not magnetic effects. Measured M-H loops exhibit high coercivity, and high remanence - direct evidence of the bi-stable single domain state – wires are nearly fully magnetized in the absence of an external applied field. Switching of individual wires, in each 6-element arrays, are evident in the M-H loops of the W = 150, 300, 400 nm wide arrays.

4.5.2 Switching Field Angular Dependence: $H_c(\theta)$

The angular dependence of the switching field was studied for wire arrays of W = 150, 300, and 500 nm, with field orientation varied from parallel (//) to perpendicular (⊥) to the wire easy axes of magnetization.

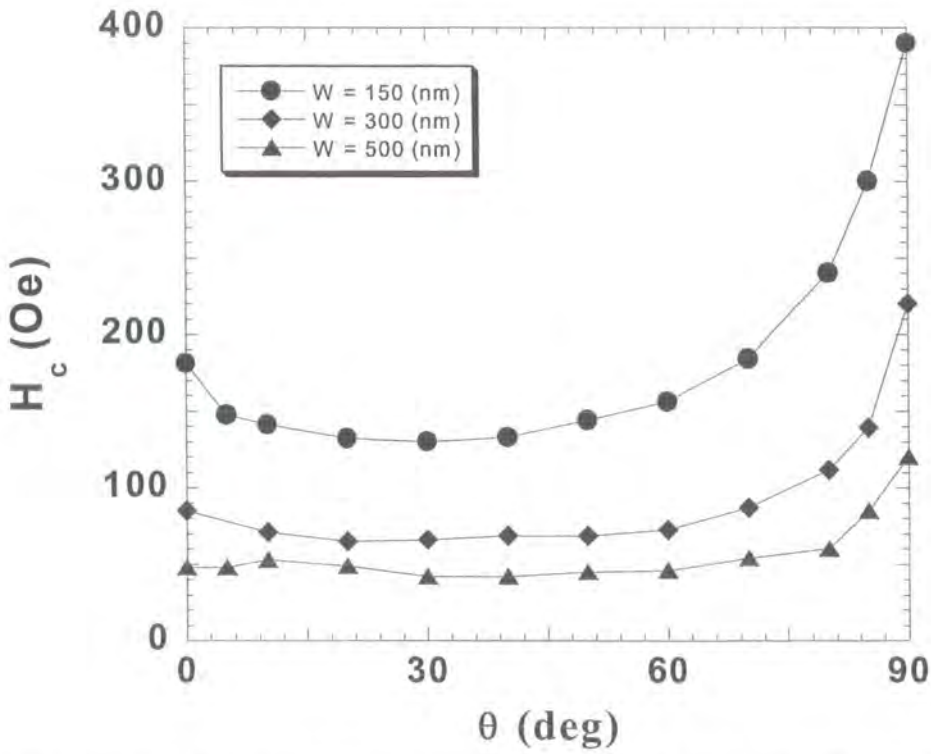

Fig 4.9: Angular dependence of coercivity, $H_c(\theta)$ vs. angle θ for wire arrays of W = 150-500 nm for 6 element wire arrays

The angle between the wire easy axis, and the applied field is defined as θ. $H_c(\theta)$ is defined as the applied field at which magnetization of time averaged M-H loops is 0. Measurements performed on wires of W = 150-500 nm show a strong angular variation of the switching field. For W = 150 nm wire arrays, a local maximum of switching field is evident at θ = 0, $H_c(0°)$ = 181 ± 1 Oe, but as θ is increased and therefore the angle between external field and wire easy axis increases, the switching field decreases, such that $H_c(30°)$ = 130 ± 1 Oe. This is analogous to Stoner Wohlfarth switching behaviour for a strongly exchange-coupled single domain particle [Stoner/Wohlfarth 1948]. The characteristic exchange length, $l_{ex} = \sqrt{A/(M_s^2)}$ over which the exchange interaction dominates, is calculated at only l_{ex} = 4.0 nm for an exchange constant, A = 1.3 × 10^{-11} J/m, and M_s = 8.00 × 10^5 A/m. However high spatial confinement in narrower 5 nm thick $Ni_{81}Fe_{19}$ wires may lead to an elevated effective exchange constant. For example, the switching behaviour for W = 150 nm wires, particularly an initial drop in $H_c(\theta)$ at low θ is qualitatively in agreement with angular switching field measurements performed on cylindrical Ni wires of W < 75 nm at 0.13-6 K [Wernsdorfer 1996]. Wernsdorfer noted that narrower wires may have different reversal mechanisms. For W = 300 nm wires, Figure 4.10, the decline in $H_c(\theta)$ for low θ is less pronounced, than in W = 150 nm wires, and at varied θ the reversal mechanism may change.

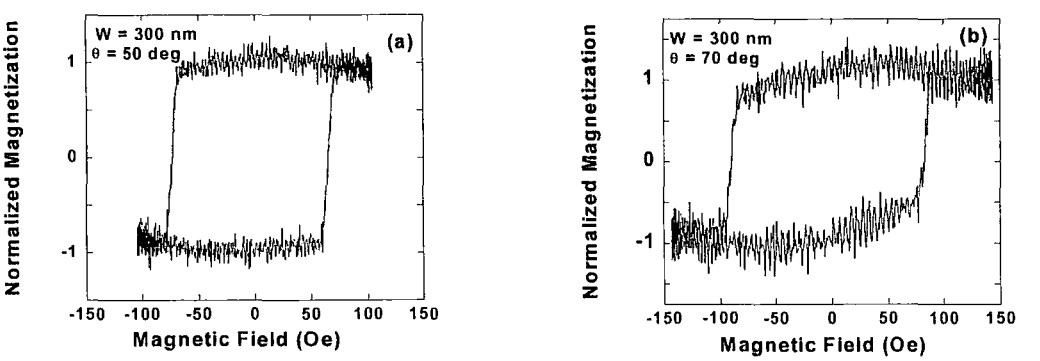

Fig 4.10: Magnetic hysteresis loops for a W = 300 nm wire array, at θ = 50° (a) and 70° (b).

For example $H_c(0°) = 85 \pm 1$ Oe, and a small drop in angular switching field is apparent, such that $H_c(30°) = 66 \pm 1$ Oe. For W = 500 nm wires, an analogy between angular switching fields and the Stoner-Wohlfarth single domain approximation does not hold, since $l_{ex} << W$. Here $H_c(\theta)$ is similar to results derived for a curling-type analytic model, and mirrors results obtained in 50 nm thick 150 nm arrays of permalloy platelets with low aspect ratio [Lederman 1993], or in Ni, NiFe, or CoNiFe electroplated nanowire arrays [Han 2003]. A Kondorsky model, $H_c(\theta) = H_c(0°)/\cos(\theta)$, see for example [Lim 2003], may be used to describe wire reversal by domain wall propagation. A Kondorsky model explains W = 300-500 nm angular switching data reasonably well for low θ, but is better suited to systems where a free wall exists, as opposed to pseudo-end domains.

4.6 Raster control of the ion beam

4.6.1 Raster: Wire Easy Axis Coercivity - H_c

In the fabrication of nanoscale magnetic elements by FIB, the ion beam raster direction should be carefully considered.

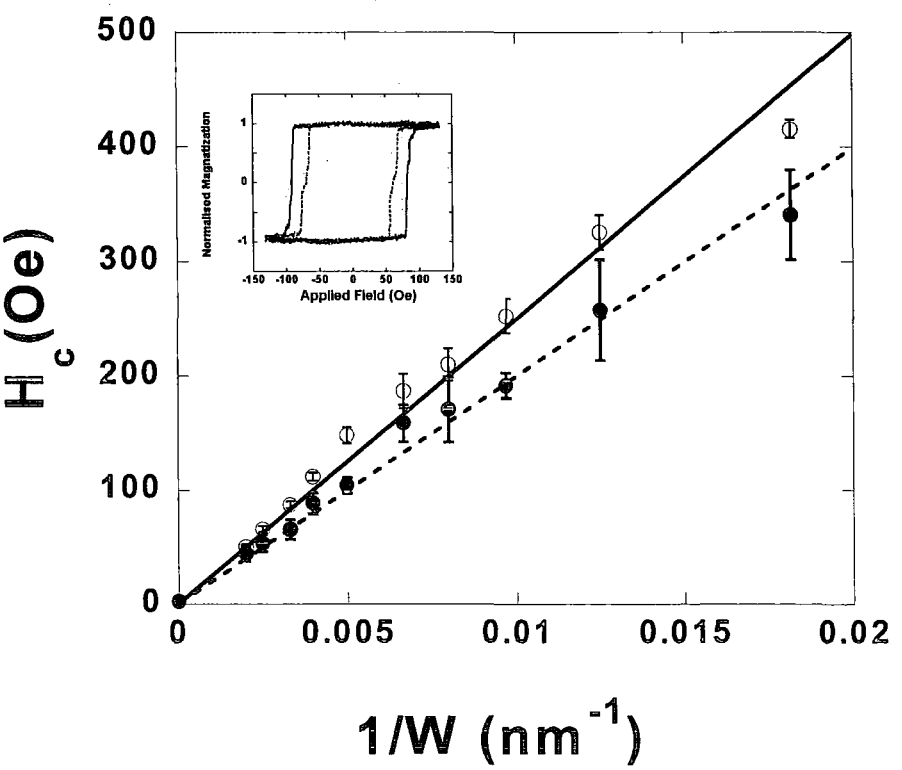

Fig 4.11: Coercivity vs. the inverse of wire width. Ion beam scan direction parallel (—○—), or perpendicular (--•--) to the wire long axis during fabrication. Upper and lower error bars represent H_s and H_n of measured M-H loops for 6-element wire arrays. The inset plots representative M-H loops for 300 nm wide wire arrays milled // (—) or ⊥ (--) to the wire long axes, of 6-wire arrays.

It was found that rastering the ion beam either parallel (//) or perpendicular (⊥) to the wire long axis has a large effect on magnetic properties of resultant wires of nominally identical dimensions. Figure 4.11 shows that in the width range studied, W = 60-500 nm, wire arrays milled (//) or (⊥) to the long axis exhibit an inverse width dependence on H_c. Identical magnetic fields, and uniform field sweep rates were used to characterise each pair of wire arrays with nominally identical dimensions, with a field sweep rate of 360 Oe/s for W = 60 nm wires, and 67 Oe/s for W = 500 nm wires. Similar to Section 4.5, characteristic fixed wire dimensions were L = 9 μm, T= 5 nm, with a 1 μm edge-to-edge inter-element separation between wires in each array. Critically, samples of nominally identical dimensions milled in different ion beam scan directions were in close proximity (typically 150 μm from each other on the same parent film), and were fabricated and magnetically characterised under uniform experimental conditions.

Rastering the ion beam (⊥) to the wire major axis results in a lowering of wire array magnetic hysteresis loop H_n, H_c, and H_s relative to wires ion beam milled (//) to the wire major axis. Figure 4.11 exhibits this reduction, due to ion beam raster direction, in switching field values for arrays of W = 300 nm wires. M-H loops for wires milled with either beam scan direction display high coercivity, and remanence. Note that because wire arrays as opposed to isolated wires are under consideration, H_n corresponds to the field value at which the first wire in the array starts to switch, and H_s is the field value at which the array is fully magnetically saturated in the opposite direction.

A useful quantity when discussing magnetic hysteresis loops is the switching field dispersion, defined as $\sigma_{disp} = [(H_s-H_n)/H_c]$. This relationship describes the width of magnetic switching transitions in assemblies of magnetic elements normalized to

H_c. A very low σ_{disp}, means the range of magnetic switching fields averaged across many bodies is low. σ_{disp} therefore gives some insight into sample switching reproducibility.

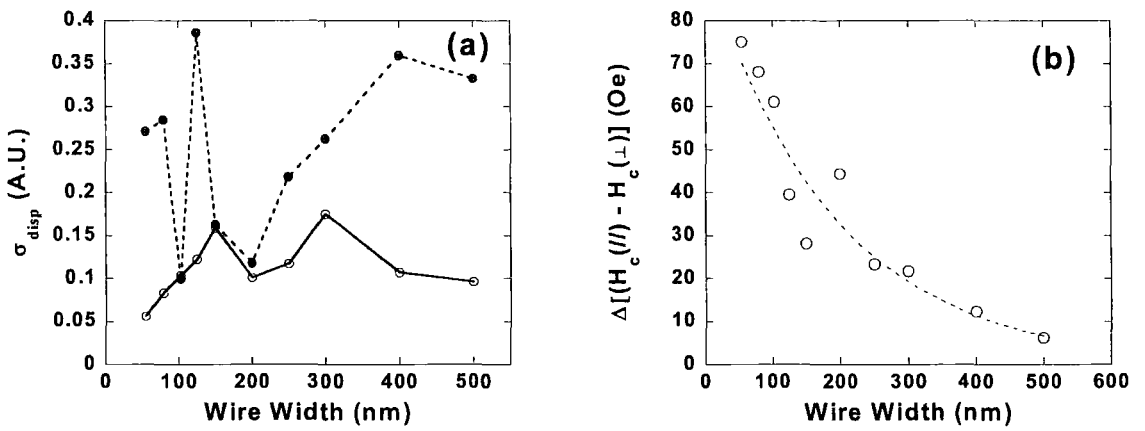

Fig 4.12: M-H loop dispersion, σ_{disp} for ion beam scan direction parallel (—o—), or perpendicular (--•--) to the wire long axis (4.12.a). Plot 4.12.b shows the net reduction in H_c for milling ⊥ to the wire major axis, as opposed to // to the wire long axis, for W = 60-600nm, nominally identical wire arrays.

In the wire width range investigated, W = 60-500 nm, milling (//) to the array magnetic easy axis clearly results in an enhanced ability to control the switching field dispersion of wire arrays, relative to wires milled (⊥) to the magnetic easy axis (Fig 4.12.a). Further, Fig 4.12.b plots the net change in H_c for nominally identical patterns utilising (//) and (⊥) ion beam rastering directions. The net change in wire coercivity, $[H_c(//) - H_c(\perp)]$ expressed in Oe, becomes more pronounced for narrower wires. For nanomagnets of reduced lateral dimensions, as W tends to zero, the effect of ion beam scanning direction plays a crucial role in the switching tolerance and also the switching field of the resultant fabricated magnetic nanowire arrays.

It is instructive to study magnetic behaviour of isolated patterned structures or particles. Dispersion of magnetic parameters in assemblies of structures and resultant

smearing M-H loop switching transitions can be a barrier to understanding basic mechanisms associated with a reduction in particle size.

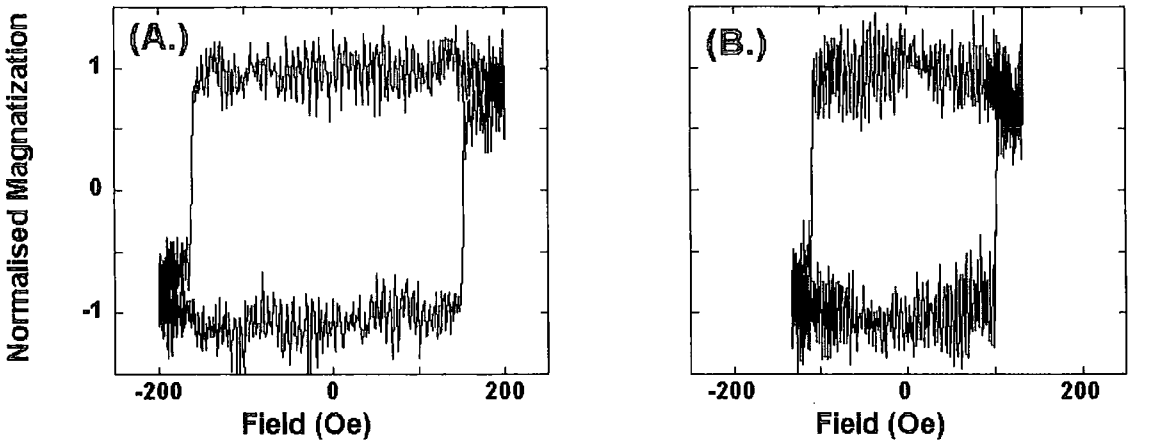

Fig 4.13 M-H loops for individual W=200 nm, planar nanowires milled // (A.), and ⊥ (B.) to the wire long axis.

Figure 4.13 shows representative magnetic hysteresis loops for isolated W = 200 nm wires, milled (//) or (⊥) to the wire easy axis of magnetization, such that $H_c(//) > H_c(\perp)$, similar to the trend shown for wire arrays. Switching transitions for wires milled either // or ⊥ to the wire major axis are very sharp. Magnetization reversal is assumed to be by domain wall growth at wire ends, and rapid propagation for both samples. The sharp M-H loop switching transitions indicates that domain wall pinning during the magnetization reversal process is negligible for W = 200nm wires fabricated by ion beam milling either (//) or (⊥) to the major axis.

This suggests that a larger M-H loop switching dispersion for wire arrays milled (⊥) to the wire easy axes of magnetization relative to nominally identical wire arrays milled (//) to the major axis may be due to a broader distribution of nucleation fields of individual wires in arrays milled (⊥) to the easy axis. A larger distribution of domain wall pinning sites is possible in wires milled (⊥) to the long axis, but the

threshold field for domain wall propagation for the samples studied here is far below H_n.

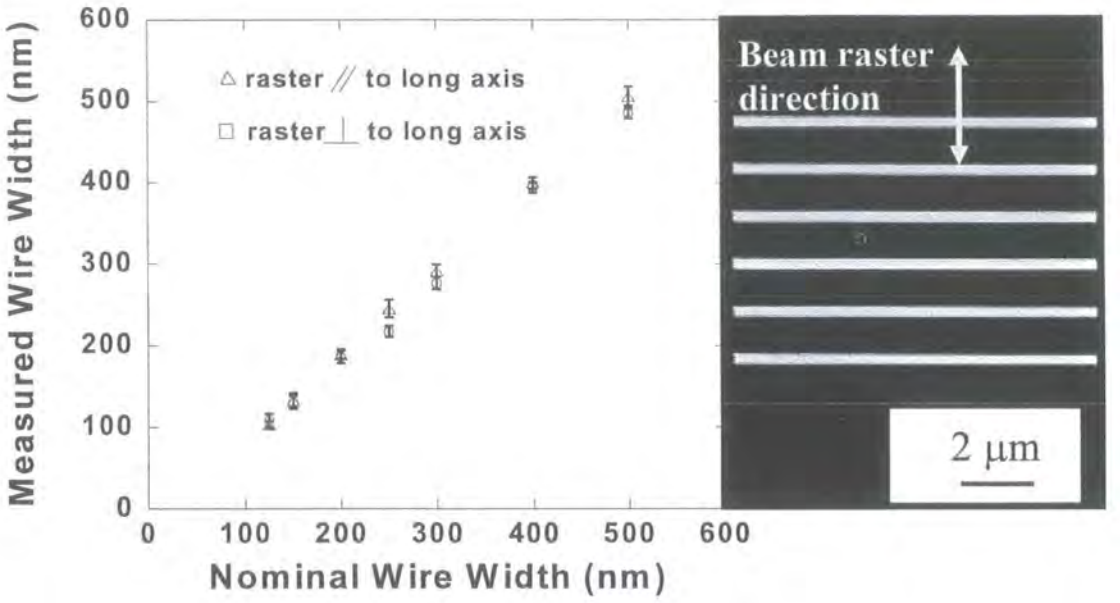

Fig 4.14 Measured wire width vs. nominal wire widths for varied width wires, W = 125-500 nm, milled // (Δ), and ⊥ (□) to the wire array major axis, measured by analysis of SEM images. A FIB secondary electron image of wires is also shown.

Wire width has a major influence on H_c – see for example Figure 4.7, Figure 4.11.A. A comparison of FIB images of wire arrays milled either (//) (Figure 4.7) or (⊥) (Figure 4.14) to the wire major axis reveals no large qualitative difference in the wire size, shape or edge structure of fabricated wires. By measuring the wire width for different beam scan directions, using high-resolution electron beam microscopy, a large difference in actual wire width vs. nominal wire width defined in beam definition files, for either ion beam milling direction is not apparent - Figure 4.14. Error bars correspond to the standard deviation of 10 separate width measurements of 1 wire, chosen at random from each wire array. Measuring wire widths by analysis of electron beam grey scale intensity images, suggested that wires milled (//) to the long axis may even be slightly wider than wires milled (⊥). It is known that small deviations in edge roughness, with an amplitude as low as 5-10 nm, and a wavelength

of from 10-30 nm can have a large effect on the switching field [Gadbois 1995], and hard axis anisotropy field [Cowburn 2000] of NiFe in-plane magnetized submicron elements. Subtle differences in wire size, shape and morphology, on a nanometre length-scale (~5-10 nm) localised at wire edges, due to ion beam interaction with wire sidewalls, are a suggested cause for the striking dependence of H_c on beam raster direction. Ga^+ ion induced changes to M_s would also change H_c.

4.6.2 Raster: Wire Hard Axis Field - H_k

The wire demagnetising field is to first order independent of the absolute size of a magnetic element, but depends on the ratio of the thickness to the width, and M_s. It is a function of the shape of wire ends [Kirk 1997], and scales linearly with H_c for thin film in-plane magnetized patterned elements. The wire hard axis field, H_k, is estimated by measuring a M-H loop with magnetic field applied parallel to the wire minor axis. H_k was approximated for wires milled using both (//) and (⊥) raster methods by a linear fit to the MH loop where magnetization is not saturated, and interpolating with fits to the positively and negatively magnetically saturated or near saturated sections of hysteresis loops.

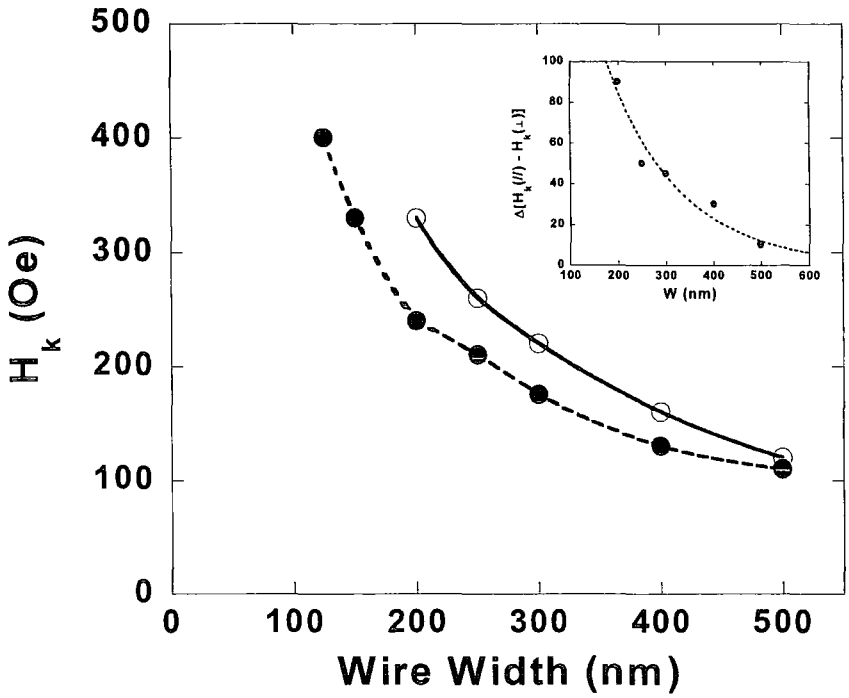

Fig 4.15 Measured hard axis anisotropy field, H_k, vs. wire width for wire arrays milled // (—○—), and ⊥ (--●--) to the wire array major axis. Inset is the net change in H_k for // and ⊥ raster directions, $\Delta[H_k(//)-H_k(\perp)]$. Lines are guides for the eye.

There is a large increase in the minor axis saturation field of the submicron wires -Figure 4.15, in comparison to M-H loops measured along the major axis. This is an indication of the wire magnetic shape anisotropy, which is lower for wider wires. Milling parallel to the wire long axis results in a larger measured H_k than wires milled using the ($\perp$) raster method, mirroring the response of H_c to ion beam raster direction - Figure 4.11. Further, the inset to Figure 4.15 demonstrates that as wire lateral dimensions are reduced, the net difference in wire shape anisotropy for (//) and ($\perp$) ion beam raster directions relative to the wire major axis, $\Delta[H_k(//) - H_k(\perp)]$ becomes more pronounced. To avoid excess heating of the field magnet coils, fields in excess of $\pm$ 400 Oe were not applied. Figure 4.16 displays hard axis M-H loops using different beam scanning directions on nominally identical, W = 250 nm wires. Milling (//) to the wire major axis, Fig 4.16.A, results in a fully saturated M-H loop, the form of which is linear, displaying good uniaxial anisotropy.

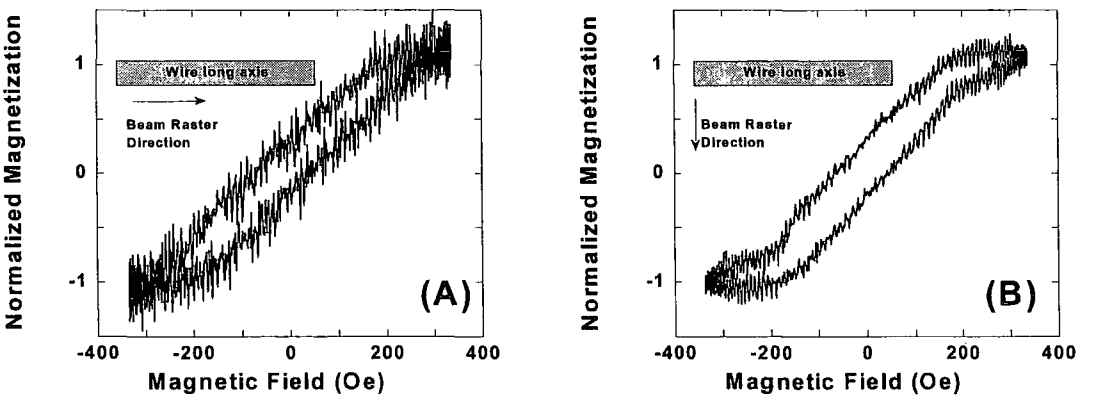

Fig 4.16 Representative hard axis M-H loops for W = 250 nm wire arrays

Figure 4.16.B shows that milling perpendicular to the wire long axis, results in a lower estimated value of H_k ~180 Oe.

4.6.3 Wire Long Axis Orientation

We have demonstrated that the ion beam raster direction has a strong effect on H_c, H_k, and hysteresis loop switching field dispersion of planar magnetic nanowires. Further, as wire lateral dimensions are reduced, changes in H_k and H_c due to the ion beam rastering direction become more pronounced. Results presented in Section 4.5, Section 4.6.1, and Section 4.6.2 are for wires oriented with major axes parallel to the FIB chamber X-axis. To further investigate the relationship between wire geometry, beam raster direction, and H_c, wires were patterned using both X and Y-rastering directions, with different wire easy axis angles (α) relative to the ion beam chamber X-axis. Figure 4.17 shows typical wire orientations investigated.

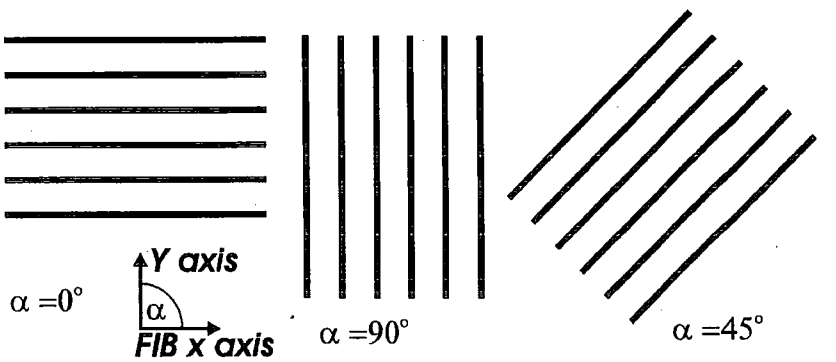

Fig 4.17 Schematic of wire orientations investigated, relative to the FIB vacuum chamber X-axis, for (//) and (⊥) raster directions.

α (°)	*X-raster H_c (Oe)*	*Y-raster H_c (Oe)*	*ΔH_c (Oe)*
0	132	108	24
45	96	106	10
90	126	140	14
135	109	109	0

Table 4.1: Measured H_c for individual ion beam milled planar nanowires, with W = 200 nm wires. α was varied from 0-135° with X and Y raster directions employed

Wire arrays and individual wires were fabricated with α = 0°, 45°, 90°, 135°. X and Y raster directions correspond to the X and Y-axis of the ion beam chamber. Table 4.1 indicates that when ion beam raster direction and wire long axis coincide, wire H_c is relatively "high." When the ion beam raster direction is normal to the wire long axis, measured wire H_c is relatively "low." If α = 45° or 135°, the ion beam can no longer raster parallel to the wire axis, and H_c for X or Y raster directions are close, given experimental errors such as film defects, and the random walk of the ion beam chamber stage during patterning [Petit 2004]. The magnetic hysteresis of sets of 6-wire arrays, fabricated under uniform conditions, was investigated to add statistical significance to results.

Six sets of 6-element wire arrays were fabricated and investigated, at α = 0°, 45°, and 90°, using ion beam raster direction parallel and perpendicular to the FIB chamber X-axis. Therefore in total the switching of 216 wires was investigated. Switching results are shown in Tables 4.2, 4.3 and 4.4, with findings addressed in Section 4.7.

$\alpha = 0°$

	Mean Nucleation Field (Oe) $\overline{H}_n \pm \sigma_{Hn}$	*Mean Coercive Field (Oe)* $\overline{H}_c \pm \sigma_{Hc}$	*Mean Saturation Field (Oe)* $\overline{H}_s \pm \sigma_{Hs}$
X Raster Direction	105 ± 6	115 ± 7	124 ± 7
Y Raster Direction	87 ± 5	101 ± 6	108 ± 8

Table 4.2: Experimental data for switching of 200 nm wide 6-element wire arrays, oriented with $\alpha = 0°$, wire long axes (//) to the FIB stage X-axis. Six sets of arrays were milled for each of the X and Y ion beam raster directions. Data for 72 wires is displayed.

$\alpha = 90°$

	Mean Nucleation Field (Oe) $\overline{H}_n \pm \sigma_{Hn}$	*Mean Coercive Field (Oe)* $\overline{H}_c \pm \sigma_{Hc}$	*Mean Saturation Field (Oe)* $\overline{H}_s \pm \sigma_{Hs}$
X Raster Direction	95 ± 7	107 ± 7	121 ± 5
Y Raster Direction	115 ± 7	125 ± 8	139 ± 9

Table 4.3: Experimental data for switching of 200 nm wide wire arrays, oriented $\alpha = 90°$, with wire long axes ($\perp$) to the FIB stage X-axis. Six sets of arrays were milled for each of the X and Y ion beam raster directions. Data for 72 wires is displayed.

$\alpha = 45°$

	Mean Nucleation Field (Oe) $\overline{H}_n \pm \sigma_{Hn}$	*Mean Coercive Field (Oe)* $\overline{H}_c \pm \sigma_{Hc}$	*Mean Saturation Field (Oe)* $\overline{H}_s \pm \sigma_{Hs}$
X Raster Direction	106 ± 5	114 ± 6	127 ± 4
Y Raster Direction	105 ± 3	113 ± 4	127 ± 4

Table 4.4: Experimental data for switching of 200 nm wide wire arrays, milled at $\alpha = 45°$ to the ion chamber X-axis. Six sets of arrays were milled for each of the X and Y ion beam raster directions. Data for 72 wires is displayed.

4.7 Discussion and Conclusion

Thin magnetic films such as $Ni_{81}Fe_{19}$/Si can be ferromagnetically quenched by a uniformly applied dose of 30 keV Ga^+ ions. The reduction in ferromagnetic ordering as a function of controlled Ga^+ fluence is primarily by the sputtered erosion of near surface Ni and Fe atoms, at the vacuum/$Ni_{81}Fe_{19}$ interface. This concept is discussed in more detail for $Ni_{81}Fe_{19}$ films of varied thickness in Chapter 5. By concurrently performing AFM and MOKE measurements on irradiated areas of a thin film, the threshold Ga^+ dose, Φ, needed to quench room temperature ferromagnetic ordering can be accurately determined.

The direct write capabilities of FIB to produce high precision deep submicron 2-d arrays and patterns, with arbitrary control over the spatial dimensions has been demonstrated. By controlling the ion dose, and beam location, 3-D topographic magnetic features can be realised. Both the geometry and the placement of wires/features have been controlled. The exact position of magnetic features, relative to each other, and a reference position on the substrate can be controlled, using beam definition files.

Measured H_c of fabricated wires was inversely proportional to wire width, at least down to 60 nm. M-H loops at remanence exhibit high squareness and coercivity. The angular switching field, $H_c(\theta)$ shows strong similarity to Stoner-Wohlfarth type switching for W = 150 nm wire arrays, where the exchange force still dominates and the Stoner-Wohlfarth single domain approximation holds as θ is varied. However, the Stoner-Wohlfarth reversal mode is by coherent rotation, in the low θ limit at least, elongated wires are assumed to reverse by domain wall motion. For increasing wire widths, W = 300–500 nm, as the shape anisotropy of the wires decreases, and small deviations from a uniformly magnetized state may occur, the Stoner-Wohlfarth single

domain approximation is less valid. $H_c(\theta)$ shows a trend analogous to curling in an infinite cylinder, calculated analytically by Frei [Frei 1957]. Experimental observations of a relatively constant H_c at low θ, rising slowly for $\theta > 45°$ towards H_k is qualitatively similar to results reported by other workers [Wernsdorfer 1996][Han 2003].

The transition from Stoner-Wohlfarth type angular switching behaviour, to the curling-like description occurs between $300 \leq W \leq 500$ nm. This is higher than reported values by other workers – Wernsdorfer found the S-W model to hold valid below 75 nm in electrodeposited Ni wires, and Han found S-W analytic expressions applicable below W = 30 nm electrodeposited NiFe wires. Due to the high level of spatial confinement of spins in 5 nm thick patterned wire elements, Stoner Wohlfarth-type switching behaviour occurs at larger W, than in pseudo-round elongated electrodeposited wires. Similar to switching experiments in Permalloy spin-valves, exploring the Stoner-Wohlfarth asteroid, quite complex angular switching mechanisms become evident as element width increases, and aspect ratio falls [Sun 2001]. A Kondorsky model qualitatively explains angular switching data for 300 and 500 nm wide wires, but a reasonable fit to experimental data is not realised, because no free wall resides in these single domain wires.

Ion beam scanning direction relative to a wire easy axis is found to have a large effect on wire H_c, H_k, and switching field dispersion width. This is attributed to a beam induced wire sidewall roughening, at an amplitude of the order of the beam diameter, (~10 nm). Scanning the pencil of ions // to the wire long axis results in higher H_k, with a concomitant increase in H_c, and a lower switching dispersion in the M-H loops of wire arrays. Taking a fitted expression for H_k from experimental data, $H_k = [(15.2)M_s.T]/W$, it is calculated that a change of wire width of 30 % is needed to

account for the difference in $H_k(//)$ and $H_k(\perp)$ for wires milled using identical beam definition source files. High-resolution electron microscopy measurements indicate that such a discrepancy in wire widths is absent.

Significantly, as W is reduced, the impact of beam scan direction on both H_k (Figure 4.14) and H_c (Figure 4.11) becomes more pronounced. Both H_k and H_c are enhanced by milling parallel to the wire long axis. This has major implications in the utilization of focused ion beam patterning of thin films for data recording investigations [Albrecht 2003][Lohau 2001], where a high thermally stable bit density is imperative. An understanding of the effects of ion beam raster direction on properties of nano-magnets of reduced dimensions, will result in less smearing of M-H loops for many body arrays, and enhanced thermal stability of fabricated nano-bits, due to better control over H_c and H_k, with higher switching fields and well defined anisotropies.

Hard axis M-H loops for wires ion milled ($\perp$) to the easy axis become magnetically saturated at a higher external applied field than nominally identical wires milled (//) to the wire major axis. This is considered consistent with an edge roughness model, whereby both switching field [Gadbois 1995] and effective shape anisotropy [Cowburn 2000] can be reduced in thin Permalloy patterned elements in the presence of small edge roughening. Some small irregularity of wire sidewalls is inevitable (for example the beam has a circular spot profile), when the ion beam scans normal to the wire easy axis. Spins at wire edges may point into small edge irregularities (presumed to be of an amplitude close to the beam diameter ~ 10 nm), lowering the effective H_k.

Tables 4.2-4.3 indicate that by matching ion beam scanning direction to wire geometry, a higher H_c may be realised for 200 nm wide nanowires. When beam raster

direction, and wire easy axis coincide, a high H_c, indicative of high H_k and a strong uniaxial anisotropy results.

Further Table 4.4 demonstrates that by milling wires at 45° relative to the FIB chamber x-axis, the effect of beam-induced anisotropies resulting from beam rastering direction can be reduced. Switching fields of wires in this $\alpha = 45°$ wire orientation are approximately independent of raster direction. Specifically, for 36 measured wires of nominal 200 nm track width, at $\alpha = 45°$, milling (//) to the chamber X-axis resulted in $\overline{H}_c \pm \sigma_{Hc} = 114 \pm 6$ Oe. At $\alpha = 45°$, milling ($\perp$) to the chamber X-axis resulted in $\overline{H}_c \pm \sigma_{Hc} = 113 \pm 4$ Oe for 36 wires. This represents excellent experimental agreement. Data in Tables 4.2-4.4 rule out either ion beam astigmatism or stage drift as the primary cause of the relationship between H_c and ion beam raster direction.

We note that at a microscopic level, different ion beam raster directions may result in slightly different ion implantation distributions in wire sidewalls lowering wire M_s. Depending on beam direction, different Ni and Fe sputter rates may apply at sidewalls. Furthermore rastering an ion beam in different directions is known to produce different trench depths and profiles for nominally identical doses [Litvinov 2002]. It may be energetically more preferential to knock out certain target atoms in the vicinity of the wire edge depending on ion beams scan direction. Both H_c vs. wire width for (//) and ($\perp$) scan directions, and hysteresis loop switching dispersion measurements as a function of scan direction were replicated on another separately grown patterned 5 nm $Ni_{81}Fe_{19}$ film, to confirm the observed trends described in this chapter.

We conclude that matching beam raster direction and wire easy axis results in a high H_c and good control of topographic features and wire magnetic switching behaviour. An original vectorial ion beam-scanning method was employed for

structures described in Chapters 6-7, ensuring that the ion beam scan direction is always parallel to the fabricated structure edge, even for complex wire geometries [Cowburn 2001], ensuring good wire sidewall smoothness. This enables fabrication of 2-D wire networks where magnetic switching by domain wall can be precisely engineered. For complex planar structures FIB beam definition files are utilised at 10 pA, where the ion beam is controlled vectorially, scanning in either X or Y directions, in a serpentine manner, parallel to wire sides, further away from wire sides in successive traces.

Good wire edge smoothness and low minimum resolvable feature acuity is essential to enable controlled domain wall propagation at low external field values [Chapters 6-7] and consistently high nucleation fields in the absence of a domain wall.

4.8 References

[Albrecht 2002] M. Albrecht, C. T. Rettner, M. E. Best, B. D. Terris, Appl. Phys. Lett. **83**, 4363 (2002)

[Bell 2002] C. Bell, G. Burnell, D. J. Kang, R. H. Hadfield, M. J. Kappers, M. G. Blamire, Nanotech. **14**, 630 (2003)

[Carter 2001] G. Carter, J. Phys. D. **34**, R1 (2001)

[Cannon 2004] D. M. Cannon, B. R. Flachbart, M. A. Shannon, J. V. Sweedler, P. W. Bohn, Appl. Phys. Lett. **85**, 1241 (2004)

[Cowburn 2000] R. P. Cowburn, D. K. Koltsov, A. O. Adeyeye, M. E. Welland, J. Appl. Phys. **87**, 7067 (2000)

[Cowburn 2001] An original software program and algorithm devised by R. P. Cowburn, currently unpublished.

[Folks 2000] L. Folks, M. E. Best, P. M. Rice, B. D. Terris, D. Weller, J. N. Chapman, Appl. Phys. Lett. **76**, 909 (2000)

[Frei 1957] E. H. Frei, S. Shtrikman, D. Treves, Phys. Rev. **106**, 446 (1957)

[Gadbois 1995] J Gadbois, J-G Zhu, IEEE Trans. Mag. **31**, 3102 (1995)

[Gierak 2004] J. Gierak, D. Mailly, P. Hawkes, R. Jede, L. Bruchhaus, L. Bardotti, B. Prével, P. Mélinon, A. Perez, R. Hyndman, J.–P. Jamet, J. Ferré, A. Mougin, C. Chappert, V. Mathet, P. Warin, J. Chapman, Appl. Phys. A **00**, 1 (2004)

[Han 2003] G. C. Han, B. Y, Zong, P. Luo, Y. H, Wu, J. Appl. Phys. **93**, 9202 (2003)

[Johnson 2000] M. Johnson, B. R. Bennett, P. R. Hammar, M. M. Miller, Solid State. Elect. **44**, 1099 (2000)

[Jung 2004] Y. J. Jung, Y. Homma, R. Vajtai, Y. Kobayashi, T. Ogino, P. M. Ajayan, Nano Lett. **4**, 1109 (2004)

[Kirk 1997] K. J. Kirk, J. N. Chapman, C. D. W. Wilkinson, Appl. Phys. Lett. **71**, 539 (1997)

[Kirk 2001] K. J. Kirk, M. R. Scheinfein, J. N. Chapman, S. McVitie, M. F. Gilles, B. R. Ward, J. G. Tennant, J. Phys. D: Appl. Phys. **34**, 160 (2001)

[Langford 2001] R. M. Langford, A. K. Petford-Long, J. Vac. Sci. Technol. A. **19**, 982-985 (2001)

[Lederman 1993] M. Lederman, G. A. Gibson, S. Schultz, J. Appl. Phys. **73**, 6961 (1993)

[Li 20001] J. Li, D. Stein, C. McMullan, D. Branton, M. J. Aziz, J. A. Golovchenko, Nature, **412**, 166 (2001)

[Lim 2003] C. K. Lim, G. Yi, J. N. Chapman, W. A. P. Nicholson, S. McVitie, C. D. W. Wilkinson, J. Phys. D. **36**, 3099 (2003)

[Litvonov 2002] D. Litvinov, S. Khizroev, Nanotech. **13**, 179 (2002)

[Lohau 2001] J. Lohau, A. Moser, C. T. Rettner, M. E. Best, B. D. Terris, Appl. Phys. Lett. 78, 990 (2001)

[Matsui 1996] S. Matsui, Y. Ochiai, Nanotech. 7, 247 (1996)

[Ozkaya 2002] D. Ozkaya, R. M. Langford, W. L. Chen, A. K. Petford-Long, J. Appl. Phys. **91**, 9937 (2002)

[Petit 2004] D. Petit, C. C. Faulkner, S. Johnstone, D. Wood, R. P. Cowburn, Rev. Sci. Instrum. **76**, 026105 (2005)

[Reyntjens 2001] S. Reyntjens, R. Puers, J. Micromech. Microeng. **11**, 287 (2001)

[Sigmund 1969] P. Sigmund, Phys. Rev. **184**, 383 (1969)

[Stamm 1998] C. Stamm, F. Marty, A. Vaterlaus, V. Weich, S. Egger, U. Maier, U. Ramsperger, H. Fuhrmann, D. Pescia, Science, **282**, 449 (1998)

[Ston./Wohlf. 1948] E. C. Stoner, E. P. Wohlfarth, Phil. Trans. Roy. Soc. A **240**, 599 (1948)

[Sun 2001] J. Z. Sun, J. C. Slonczewski, P. L. Trouillard, D. Abraham, I. Bacchus, W. J. Gallagher, J. Hummel, Yu Lu, G. Wright, S. S. P. Parkin, R. H. Koch, Appl. Phys. Lett. **78**, 4004 (2001)

[Tseng 2004] A. A. Tseng, J. Micromech. Microeng. 14, R15 (2004)

[Uhlig 2004] W. C. Uhlig, J. Shi, Appl. Phys. Lett. 95, 701(2004)

[Wernsdorfer 1996] W. Wernsdorfer, B. Doudin, D. Mailly, K. Hasselbach, A. Benoit, J. Meier, J. –Ph. Ansermet, B. Barbara, Phys. Rev. Lett. **77**, 1873 (1996)

[Yuan 1992] S. W. Yuan, H. N. Bertram, J. F. Smyth, S. Schultz, IEEE Trans. Magn. **28**, 3171 (1992)

[Xiong 2001] G. Xiong, D. A. Allwood, M. D. Cooke, R. P. Cowburn, Appl. Phys. Lett. **79**, 3461 (2001)

Chapter 5. Focused ion beam irradiation of magnetic bilayers

5.1 Introduction

Results of a systematic investigation of the effect of heavy Ga^+ ion irradiation on in-plane magnetized ferromagnetic bilayers are presented. Thin and ultra-thin $Ni_{81}Fe_{19}$ layers (2-12 nm) were sandwiched between a Si substrate and a non-magnetic capping layer – either Al or Au. All samples were irradiated until a critical ion dose, Φ, to quench room temperature ferromagnetic ordering was exceeded. We describe the loss of ferromagnetic ordering in terms of surface, bulk, and interface interactions between incident ions and the target atoms. We show how the loss of measured ferromagnetic ordering is due to surface sputtering, ion implantation, and ion beam induced collisional intermixing at interfaces. The rate of magnetic patterning and the principal mechanism for quenching of ferromagnetic ordering is very strongly dependent on NiFe thickness, t_{NiFe}. Significantly, we demonstrate that the addition of a non-magnetic capping layer to a thin in-plane magnetized film (t_{NiFe} < 10 nm) results in quenching of room temperature ferromagnetism at a significantly lower Ga^+ ion dose compared to uncapped NiFe control samples of the same t_{NiFe}. This is due to radiation-induced transport of interfacial atoms, also known as collisional intermixing.

Some studies by other workers are detailed in Section 5.2 to put the contents of this chapter in context. Section 5.3 investigates the effect of Ga^+ ion irradiation on $Si/Ni_{81}Fe_{19}$ films of t_{NiFe} = 3.5-25 nm. The response of sample magnetization, easy axis coercivity, and hard axis anisotropy field to controlled radiation exposures is addressed. Next the irradiation of the $Si/Ni_{81}Fe_{19}/Al$ system is treated, in Section 5.4. Both NiFe and Al thicknesses were varied to gain detailed understanding of the effect

of irradiation on bilayers of different composition. Experimental results are supported by Monte Carlo simulations. The blurring of interfaces as a function of ion dose has been described by a mathematical model. The intermixing lengthscales are demonstrated to be proportional to the square of the Ga^+ ion dose for different cap species.

$Ni_{81}Fe_{19}$ films of varied thickness (t_{NiFe} = 2-6 nm) buried under 7nm Au capping layers were investigated as a function of ion fluence in Section 5.5. The localised irradiation of buried NiFe films for the fabrication of functional magnetic patterns embedded in a superparamagnetic layer between a non-magnetic cap and substrate is treated in Section 5.6. A discussion and conclusion in Section 5.7 ends the chapter.

5.2 Literature

Ion irradiation is a versatile technique for the modification of the structural, magnetic or electrical properties of materials. It can be used for direct substrate patterning and cleaning by sputtered removal of target atoms, for disordering an atomic lattice or surface [Eklund 1991], for increasing magnetoresistance in multilayers [Kelly 1994], for enhancing the exchange biasing of ferromagnet/antiferromagnet FeMn samples [Juraszek 2002], or for reducing the biasing in exchange-bias samples [McGrouther 2004]. Semiconducting materials can be doped by irradiation, leading to a change in electrical properties. Many early fundamental studies are reviewed by Sigmund [Sigmund 1969].

Here we demonstrate enhanced magnetic patterning rates in buried NiFe films, compared to uncapped control samples, by Ga^+ ion beam intermixing at interfaces. We point to existing techniques such as reactive ion etching to enhance the sputtering yield, and hence patterning rate of materials. In this technique chemical treatment of the target results in a lower surface binding energy of surface atoms, and hence an

enhanced sputter yield per incident ion. For example Sugimoto and co-workers used Cl_2 gas as the etching agent in a photoluminescence study of FIB ion damage in semiconductor GaAs substrates [Sugimoto 1990].

Many fundamental studies have documented ion beam intermixing of layered samples, for example Xe intermixing of Pt layers embedded in Si [Sigmund 1981], silicide formation in Pt, Ni or Hf layers on silicon irradiated by Ar^+, Kr^+, or Xe^+ ions [Tsaur 1979], or as shown in Fig. 5.1, light ion irradiation studies of Au and Ag films [Mayer 1981].

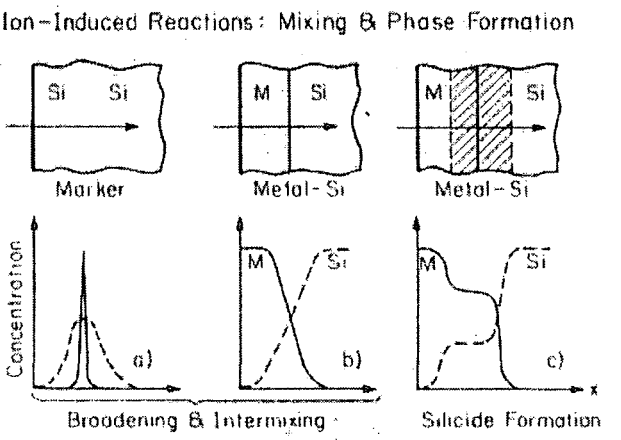

Fig. 1. The change in the concentration profile due to the penetration of energetic ions through a) a thin marker layer and a metal–semiconductor interface when b) intermixing, or c) compound formation occurs.

Figure 5.1: Ion beam interaction with a marker layer, or metal-Si interface [Mayer 1981].

Ion irradiation is of interest for magnetic patterning of thin films [Bernas 2003], because it is typically a dry, resist-free process. For example ion irradiation of perpendicular magnetic anisotropy (PMA) thin film systems has recently been shown to causes a change in coercivity, uniaxial anisotropy, Curie temperature, and magnetic moment, as a function of incident ion flux [Chappert 1998][Carcia 1990][Devolder 2001][Vieu 2002][Weller 2000]. Patterning has been demonstrated in Co/Pt to sub-50 nm resolutions with a silica mask [Devolder 1999][Devolder 2000/1], and in other

PMA media such as FePt [Terris 2000]. Noble gas irradiation of PMA systems is known to cause intermixing or alloying at interfaces [Vieu 2002][Carcia 1990][Devolder 2000/2][Weller 2000].

Direct ion beam irradiation also has interesting applications, such as control of interlayer exchange coupling in Fe/Cr/Fe trilayers [Demokritov 2003]. The focused ion beam (FIB) system has been widely used in irradiation studies of films, or PMA layered systems [Aign 1999][Hyndman 2001][Warin 2001]. It is of fundamental interest to consider the effect of irradiation on in plane magnetized samples - for example workers have recently engineered the hard axis anisotropy field direction of NiFe samples irradiated in the presence of an ordering magnetic field [Woods 2002]. In addition the fabrication of layered thin films and multilayer samples magnetized in plane has numerous documented technological uses, such as exchanged biased magnetic tunnel junctions [Parkin 1999]. Kaminsky et al. demonstrated the potential for Ga^+ irradiation of thick 15.5 nm NiFe films capped with NiCr, removing room temperature ferromagnetic ordering at a critical dose, $\Phi = 1 \times 10^{16}$ ions/cm^2. This is a relatively high radiation dose. Loss of ferromagnetism was attributed to ion implantation in the NiFe layer, while the protective NiCr layer had been radiation thinned but not completely eroded [Kaminsky 2001]. Little systematic work has been performed on the effect of a capping layer when irradiating in-plane magnetized films. This is the motivation of the work presented here.

5.3 Ga^+ irradiation of $Ni_{81}Fe_{19}$/Si films (t_{NiFe} = x nm)

5.3.1 MOKE Signal Vs. Dose

The uniform irradiation of uncapped Si/NiFe films of varied thickness was investigated, in all cases to ion doses above the critical fluence to quench measured

room temperature ferromagnetic ordering, defined as Φ, in units of areal dose ions/cm^2. The method of sample irradiation and magneto-optical investigation is delineated in Section 4.3.3. Previous studies in Permalloy have tended to investigate thicker films at Ga^+ doses where ferromagnetism is not quenched, or single films [Baglin 1997][Ozkaya 2002][Park 2004][Park 2002]. Figure 5.2 shows the measured MOKE signal from easy axis time averaged hysteresis loops, for NiFe films of t_{NiFe} = 10-25 nm, grown simultaneously, as a function of Ga^+ irradiation.

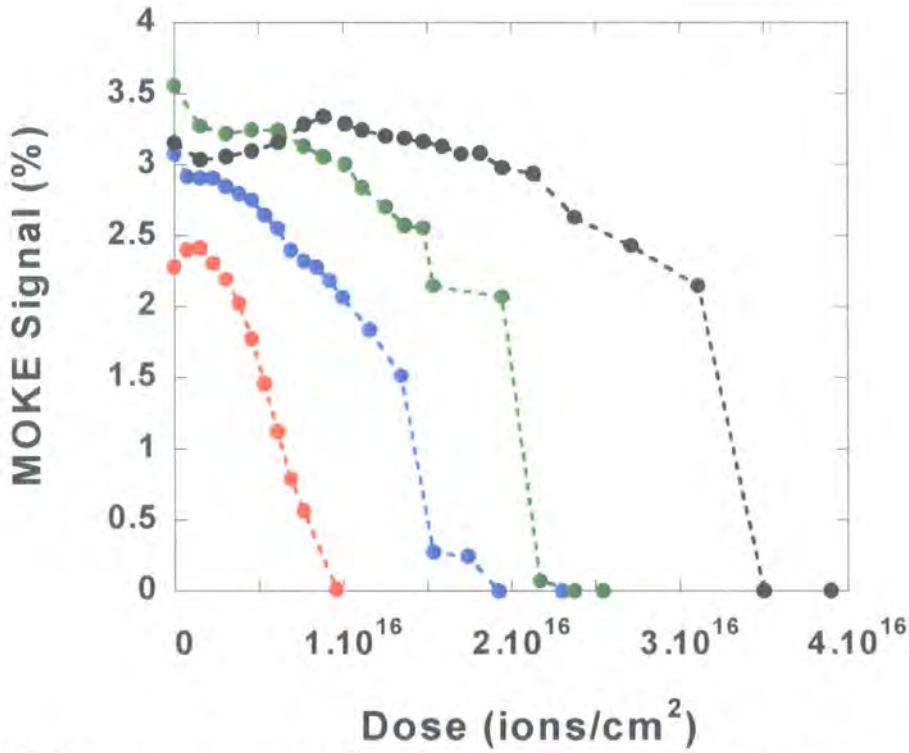

Figure 5.2: Measured magneto-optical Kerr effect signal for NiFe/Si films as a function of Ga^+ ion beam radiation. Nife thicknesses are 10 nm (--●--), 15 nm (--●--), 20 nm (--●--), and 25 nm (--●--), respectively.

Even the lowest ion dose, *D*, (for these samples 6×10^{14} ions/cm^2) resulted in an experimentally significant change in the measured MOKE signal from irradiated films as compared to pristine control samples. In the 15 and 20 nm thick films, the Kerr effect signal decreases for the lowest applied dose evidence of a radiation-induced modification in the film magnetic properties.

With increasing Ga^+ ion fluence, MOKE signal for films with t_{NiFe} = 10-25 nm drops to 0. The Kerr effect signal from the 25 nm thick film shows a complex response to radiation at low D ($< 9 \times 10^{15}$ ions/cm^2), because the NiFe thickness is greater than the thickness at which the MOKE signal becomes saturated. In Chapter 3 we showed that a 25 nm thick unirradiated NiFe film has a lower MOKE signal than a 20 nm thick film, due to interference effects. In bulk magnetic films above a certain critical thickness, the total MOKE signal consists of a superposition of contributions from different depths, which differ slightly in phase, and this lowers the overall measured MOKE signal [Hubert 1998]. For an optimised thin film system, with maximum MOKE signal, the entire light signal should be generated with the same phase. We attribute this phenomenon as the cause of a lower observed Kerr signal in the 25 nm film vis-à-vis a 20 nm thick film. At $D > 9 \times 10^{15}$ ions/cm^2 the $t_{NiFe} = 25$ nm sample follows the same trend as other NiFe films irradiated at the free vacuum-NiFe interface, i.e. a reduction in Kerr effect signal from samples of different thicknesses is observed as a function of dose. The rate of MOKE signal reduction as a function of ion fluence becomes more pronounced at doses close to Φ, when the film has been significantly radiation etched. The reduction in MOKE signal is interpreted as a radiation induced decrease in target magnetic moment.

There is however, a measured increase in Kerr effect signal observed in the 10 nm thick sample, at relatively low ion doses, $D < 2.5 \times 10^{15}$ ions/cm^2. This effect was observed in many irradiated NiFe films with $t_{NiFe} \leq 10$ nm. For example a relative increase in Kerr effect signal of up to 9% as compared to the as prepared film, was measured in a 3.5 nm thick NiFe film irradiated with $D = 1.2 \times 10^{14}$ ions/cm^2.

Similar effects, such as a dose-induced increase in Faraday ellipticity have been reported by workers in other thin film media [Fassbender 2004], such as

Pt/Co/Pt irradiated by Ga^+ [Vieu 2002], nitrogen irradiation of Co/Pt [Weller 2000], or He^+ irradiation of CoPt [Devolder 2000/2]. This anomaly is interpreted not as an irradiation induced enhancement of the absolute magnetization, M_s, but rather as a relative change in the MO response of the irradiated target alloy constituent species resulting from preferential surface sputtering of either Ni or Fe atoms from the surface [Train 1999]. In sputtering of composite layers such as an iron nickel alloy, preferential sputtering from the surface layers can cause a depletion of one of the elements, relative to the other atomic species in the target. The Kerr effect changes relative to the ratio of Ni and Fe atoms in the target, and may change due to a different Ni:Fe ratio at different depths within a thin film or the presence of a native oxide layer. Radiation induced modification of substrate properties may also affect the measured MOKE signal. Significantly, Figure 5.2 demonstrates that Φ does not scale linearly with t_{NiFe} – this finding is addressed in Section 5.3.4.

5.3.2 Coercivity Vs. Dose

In the following we consider the effect of irradiation on the easy axis coercive field of NiFe/Si samples of t_{NiFe} = 10-25 nm.

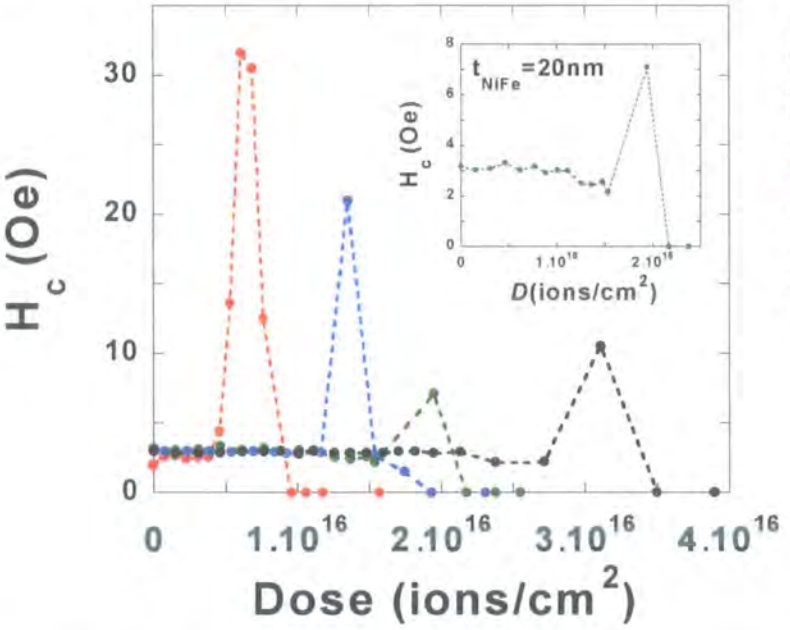

Figure 5.3: Easy axis coercivity for NiFe films as a function of Ga^+ ion beam radiation. NiFe thicknesses are 10 nm (--●--), 15 nm (--●--), 20 nm (--●--) [inset is the t_{NiFe} = 20 nm isolated data], and 25 nm (--●--), respectively.

Figure 5.3 shows the relationship between the easy axis coercive field, H_c, for t_{NiFe} = 10-25 nm films, and incident Ga^+ ion flux. Similar to MOKE signal measurements, data was taken from time averaged M-H loops, and unirradiated areas of each thin film sample were also investigated.

In uncapped irradiated NiFe films up to t_{NiFe} = 25 nm, H_c is observed to decline gradually as a function of ion fluence. The very gradual decrease of coercivity is evident in the inset of Fig. 5.3, for a t_{NiFe} = 20 nm film. There is a radiation-induced reduction in nucleation and domain wall propagation fields, as the film thickness decreases due to radiation etching from the free vacuum/NiFe surface. In general H_c increases in continuous NiFe films with increasing thickness, due to increasing stray field energy. Thinner films (i.e. t_{NiFe} = 5-10 nm) show a more pronounced rate of reduction in H_c with fluence, per unit volume of magnetic material.

Comparing to the literature, in 560 nm thick NiFe films on Al_2O_3-TiC substrates, little change in coercivity was measured at intermediate ion doses [Park 2002], because the film was not sufficiently thinned. For elements of reduced geometry – for example anti-dot arrays of lateral dimensions up to 10 μm an increase in H_c with dose has been directly observed by Lorentz microscopy [Owen 2002].

A sharp peak in H_c is observed at fluences immediately prior to Φ, as previously reported in $Ni_{81}Fe_{19}$(5 nm)/Si [Xiong 2001], or FeCoN(130 nm) on glass [Park 2002]. The coercivity peak is characteristic of a magnetization reversal process in a highly amorphous, disordered sample, where the domain wall propagation field may be higher than the nucleation field, before the onset of room temperature superparamagnetism. M-H loops measured in this ion dose range are highly rounded, evidence of a high density of pinning sites hindering magnetization reversal processes. At these radiation doses the film may be discontinuous, with little or no

preferred magnetization direction. For any of the irradiated NiFe layers, H_c was not measured at values lower than 1 Oe, prior to the onset of superparamagnetism.

5.3.3 Uniaxial Anisotropy Field Vs. Dose

To a good approximation, a uniaxial anisotropy field can be assumed for polycrystalline as-deposited NiFe films. We investigated the effect of irradiation on the uniaxial anisotropy field of a t_{NiFe} = 5 nm sample. The anisotropy field of NiFe/Si samples increases as a function of thickness, in the thickness range 3-25 nm, for films grown in uniform conditions. The value of the uniaxial anisotropy field, H_k was determined from a linear fit to non-saturated portions of hard axis M-H loops.

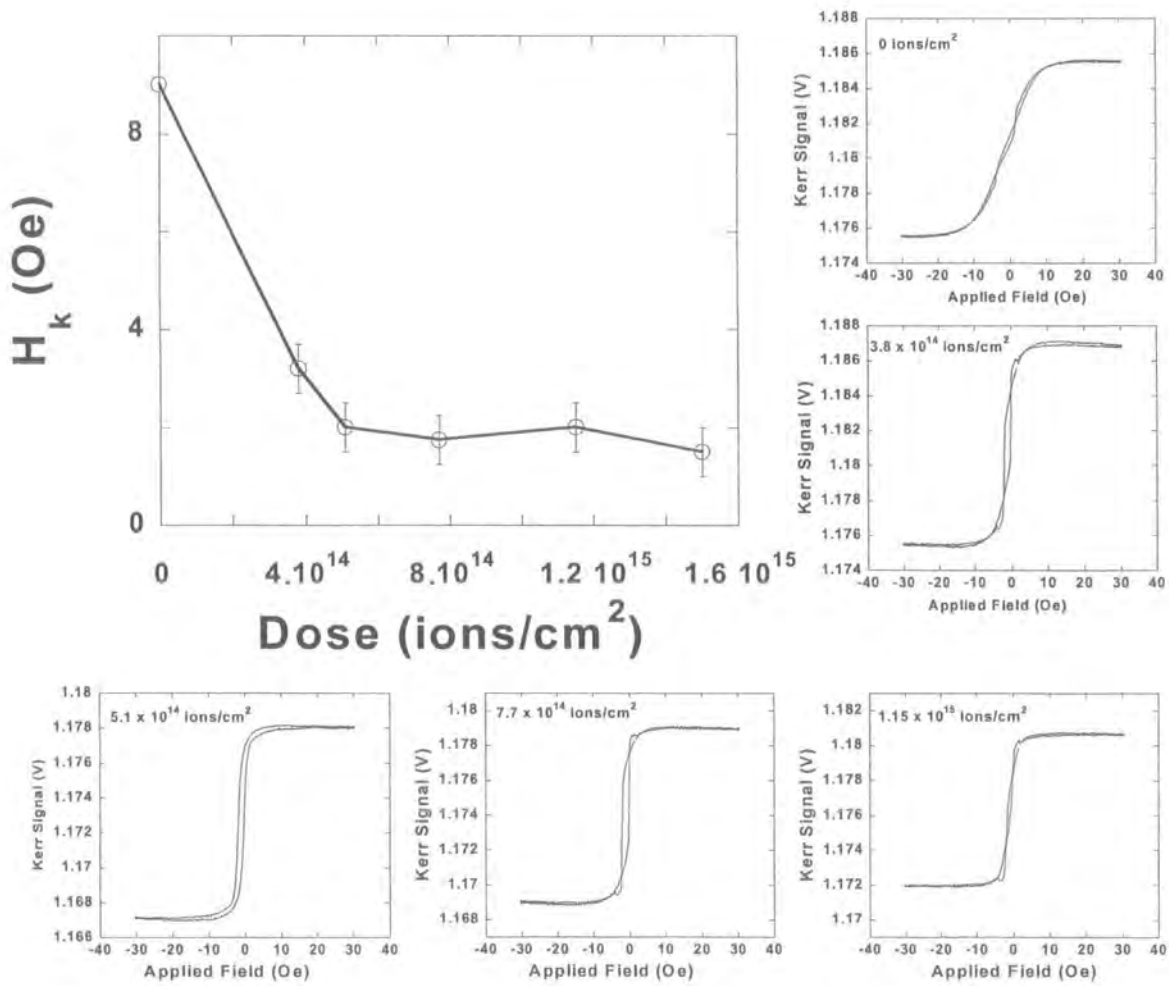

Figure 5.4: Plot of H_k with increasing ion fluence, under uniform irradiation conditions for a t_{NiFe} = 5 nm polycrystalline film. Representative hard axis saturation loops for $D = 0 - 1.15 \times 10^{15}$ ions/cm^2 are also shown

Figure 5.4. (previous page) displays the decrease in the H_k as a function of ion fluence, with accompanying hard axis M-H loops for varied D, under uniform applied field conditions. K_u was calculated for the as-deposited film, [$K_u = 390 \pm 40$ J/m^3], taking $H_k = 2K_u/M_s$ in a polycrystalline NiFe film, of $t_{NiFe} = 5$nm. M_s for Permalloy is taken as 0.8 T.

The magnetic anisotropy is a local quantity, and is thus very sensitive to symmetry considerations – either in a bulk matrix, or at a thin film-vacuum or substrate interface. It is therefore interesting to note that there is a very sharp fall in H_k from the as grown sample at a low dose of D = of 3.8×10^{14} ions/cm^2, from H_k = 9.0 ± 1.0 Oe to 3.2 ± 0.5 Oe. This decrease tails off at higher doses tending to a field value similar to that of the easy axis coercivity, at which stage the local atomic environment in the thin film is already assumed to be significantly disordered.

A complete description of the irradiation induced change in magnetic anisotropy, as a function of Ga^+ irradiation is hard to build. Strain in films can arise from various sources, such as intrinsic strain brought about by the deposition process, and non matching lattice parameters of adjacent layers, and is known to contribute to the magnetic anisotropy [Johnson 1996]. Ion irradiation is known to release strain in layered thin and ultrathin film samples [Devolder 2000/2], and we attribute a strain release mechanism as a primary cause for the sharp initial drop in H_k for the low ion dose, $D = 3.8 \times 10^{14}$ ions/cm^2. Even a low dose of Ga^+ radiation will cause release in strain at the target substrate interface, and causes re-arrangement of Ni and Fe constituent target atoms in the lattice, releasing further strain. At intermediate fluences, 3.8×10^{14} ions/cm^2 $< D <$ 1.5×10^{15} ions/cm^2 the radiation induced reduction in H_k is apparent but less pronounced. Symmetry of the system is reduced due to irradiation induced blurring at the NiFe/Si interface, causing a further

anisotropy reduction. Furthermore, the sputtered removal of Ni and Fe atoms near the surface-vacuum interface accounts for some of the measured reduction due to the irradiation erosion effect. (Since $H_k \propto 1/t_{NiFe}$, a thinner magnetically active target layer has a lower H_K and is therefore assumed to have a lower K_u).

We have shown that we can reduce the hard axis magnetic anisotropy field in a controlled manner, as a function of increasing ion dose. At high dose, just prior to the superparamagnetic peak and Φ, H_k tends to H_c and the sample is virtually isotropic. We note that similar results were also observed on other films of t_{NiFe} = 15 nm, and t_{NiFe} = 20 nm. For NiFe/Si samples investigated (t_{NiFe} = 5-25 nm), at low and intermediate doses relative to Φ, the same ion dose causes a larger relative change in H_k than H_c. The salient point is that at low radiation doses, the hard axis anisotropy field is radiation reduced at a quicker rate than can be accounted for by a change in magnetic moment of the sample.

5.3.4 Surface, Bulk, & Interface Effects

Theory

We now consider gallium bombardment of the Si/$Ni_{81}Fe_{19}$/vacuum system in more detail. When an energetic ion impacts upon a surface, if the ion energy (E_{ion}) exceeds the potential energy barrier posed by the surface atoms, it penetrates the target-vacuum interface and burrows into the target/substrate bulk [Section 4.3.2]. The ion is deflected by an initial collision with a surface or near surface atom, and loses energy. A 30 keV Ga^+ ion has a high impact momentum. The Ga^+ ion penetrates into the solid, losing kinetic energy in subsequent collisions, and becoming further deflected from the original trajectory normal to the sample surface [Sigmund 1969]. The ion comes to rest when it's ion kinetic energy is no longer sufficient to overcome the internal energy barriers posed by each successive layer of target or substrate

atoms. During the quenching process, energy transferred from the ion to the target and substrate atoms may be sufficient to cause displacement of the atoms from their equilibrium lattice positions – this is recoil mixing. Much of the incident ion energy is deposited in a region surrounding the ion trajectory in the target bulk. A vacancy and a dynamic recoil atom may be created at each atomic lattice position. Secondary displacement recoils generated by recoiling target atoms can result if the recoil is sufficiently energetic. This in turn can trigger a cascading effect, with large numbers of low energy recoils contributing to the quenching of E_{ion}. The time-scale involved in this collisional phase of damage events can be of the order of 10^{-15} seconds [Carter 2001], and is often considered as a ballistic process.

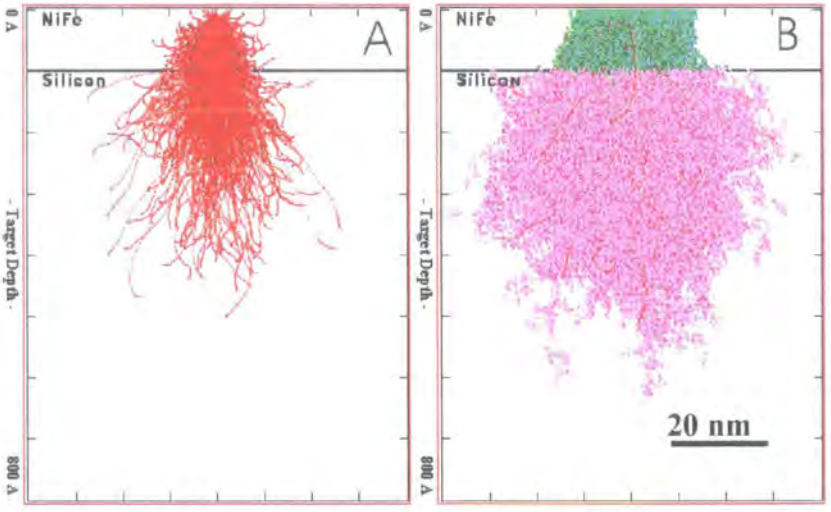

Figure 5.5: A damage cascade cross-section calculated by TRIM for 1000 Ga^+ incident normal to a Si (100nm)/$Ni_{81}Fe_{19}$ (10nm) sample surface.
(A) Shows the Ga^+ ion trajectories and stopping positions in the target in red.
(B) Shows recoiling Ni and Fe atoms (green) and Si atoms (Purple).

The capacity of a target to slow a projectile is called the stopping power. We define $\bar{i}_{SD}$ as the mean stopping distance of an ion in the host material – for 30 keV Ga^+ ions in $Ni_{81}Fe_{19}$, it is calculated by TRIM at 98 Å – see Table 5.1.

Target Species	*Ion Longitudinal Range (Å)*	*Ion Lateral Range (Å)*	*Ion Radial Range (Å)*	*Vacancies/ion*	*Sputter Yield Atoms/Ion*
Silicon	278 [104]	65 [83]	101 [58]	745	2.72
$Ni_{81}Fe_{19}$	98 [50]	34 [43]	52 [30]	799	7.63
Al	239 [89]	56 [70]	85 [47]	380	3.88
Au	92 [55]	48 [62]	75 [46]	727	16.99

Table 5.1: Stopping ranges, vacancies per ion, and sputter yields per ion, for varied target materials, irradiated with 30 keV Ga^+ ions incident normal to the sample surface. All data shown is for full damage and cascade calculations. Straggle is indicated in brackets. Lateral range corresponds to ion deflection relative to the y-axis, and radial range to ion deflection relative to the z-axis.

Ion-atom collisions were studied using TRIM Monte Carlo simulations in which successive ion collisions are treated as independent [Ziegler 1985]. The simulation code gives a quantum mechanical treatment of ion-atom collisions by describing the interaction in terms of a screened Coulomb interaction. It is a continuum model but does not treat dynamic effects, rather treating successive collisions as independent. Sample crystal structure and grain boundaries are not considered. The depth of ion damage in a solid target is largely determined by $\bar{i}_{SD}$. Because TRIM is based on the Monte Carlo method, a large number of incident ions were used in each simulation to add statistical significance to calculated results. Tseng found calculated sputter yields converged when the incident ion number exceeded 500 [Tseng 2004]. For all results described here, at least 1000 incident ions were employed per calculation. Table 5.1 shows summary data pertinent to the target species considered in this chapter irradiated by 30 keV Ga^+ ions. In general energetic Ga^+ ions have a lower sputter yield and a larger $\bar{i}_{SD}$ in light target species such as Al

relative to heavier elements such as Gold. Note that the mean ion penetration depth, or ion stopping distance, $\bar{i}_{SD}$ increases as a function of ion energy, as does the sputter yield per ion, and the number of vacancies per incident ion [in the incident ion energy range 5-50 keV]. [See Appendix. B for the results of further calculations on ion implantation depths in various target materials.]

In an experimental system, ion entrance positions in a solid are statistically distributed. Individual ion trajectories, and stopping positions are also statistically distributed, and are additionally dependent on the target stopping power, which changes as a function of dose. Sputtered surface, or near-surface target atom distributions of energy, emission direction and yield per incident ion also reflect the statistical nature of the collision process. Additionally we note that channelling effects can permit ion implantation of a small number of incident ions at a depth far in excess of the mean penetration depth, $\bar{i}_{SD}$, if ions find preferred trajectories to propagate through the lattice. This is especially likely in crystalline materials such as Al [Reyntjens 2001].

To gain a qualitative dynamic understanding of the transport of incident ions in the target, and the displacement of target and substrate atoms over time and higher doses (D), we regard the target-vacuum interface as a sputter front [Carter 2001]. The vacuum/target interface propagates deeper into the bulk target normal to the beam radiation direction, as a function of incident radiation fluence. The erosion wavefront is preceded in the target bulk by a region of damaged target material beneath the vacuum-target interface. The spatial extent of the ion damage band under the propagating vacuum-target interface is determined by the ion implantation depth, which may change with radiation dose. For a given target, with increasing ion fluence, more Ga implant ions reside in the target bulk, and the crystal lattice has suffered

more damage effects. Furthermore as a function of ion dose, the sputter yield may change [Reynolds 1981], reflecting a radiation-induced change to target structural properties.

Surface Sputtering

As shown in Section 4.3.3, the rate of surface erosion, as a function of ion dose can be investigated by atomic force microscopy (AFM) step-height measurements. It is clear from the experimentally measured step-height measurements in Table 5.2 that propagation of the sputter wavefront, and therefore sputtered removal of surface atoms accounts for much of the reduction in measured ferromagnetism in the $Ni_{81}Fe_{19}$ samples of varied thickness studied.

t_{NiFe} *(nm)*	*Unirradiated* H_c *(Oe)*	Φ *(ions/cm^2)*	Φ/t_{NiFe} *(ions/nm^3)*	*AFM step height at* Φ *(nm)*
3.5	2.6	1.9×10^{15} [$\pm 2 \times 10^{14}$]	5.4 [±0.6]	-
5	1.1	2.7×10^{15} [$\pm 2.5 \times 10^{14}$]	5.4 [±0.5]	-
10	2.0	9.6×10^{15} [$\pm 1 \times 10^{15}$]	9.6 [±1.0]	8.5 [±1.0]
15	2.8	1.9×10^{16} [$\pm 1 \times 10^{15}$]	12.6 [±0.7]	11.5 [±1.6]
15*	2.5	-	-	10.5 [±1.5]
20	3.2	2.5×10^{16} [$\pm 1 \times 10^{15}$]	12.5 [±0.5]	-
25	3.0	3.5×10^{16} [$\pm 2 \times 10^{15}$]	14.0 [±0.8]	-

Table 5.2: Summary data for $Si/Ni_{81}Fe_{19}$ samples irradiated, under uniform experimental conditions, with t_{NiFe} = 3.5 – 25 nm. Easy axis H_c, the critical ion dose at which no room temperature is measured by MOKE, and AFM step height measurements at the critical ion dose are shown. * denotes a sputtered NiFe film.

For the data shown t_{NiFe} does not correspond to the measured AFM steps height at Φ. Ion damage and implantation are other mechanisms for loss of measured ferromagnetic ordering besides sputter erosion of the target free surface.

Ion implantation

Ion implantation is the process of introducing impurities or dopants into a solid by directing energetic ions at the target. It is a bulk effect. Considering a film with t_{NiFe} = 10 nm, we calculate that an ion dose of $D = 9.6 \times 10^{15}$ ions/cm^2, yields a Ga^+ implant atomic concentration of ~ 5% relative to the target bulk. Many of these gallium atoms are implanted in the non-magnetic substrate, $\bar{i}_{SD}$ = 98 Å. An increasing concentration of Ga^+ ions are stopped in the Si substrate and not the $Ni_{81}Fe_{19}$ layer with increasing dose, because the $Ni_{81}Fe_{19}$ layer has been radiation thinned. Even an implant concentration of a few percent causes a change to target spontaneous magnetization [Park 2002]. We note that ion implantation generally requires high doses of the order of 10^{16}–10^{17} ions/cm^2 to produce a concentration of implanted ions in excess of a few atomic percent. A foreign atom concentration of ~ 20 % is estimated to dilute ferromagnetism to zero in an iron based alloy [Corb 1985]. The ion implantation technique for magnetic patterning is complicated by large sputtering effects at the vacuum-target interface. Large ion doses mean a concomitant increase in sample irradiation times due to longer ion exposures. Other phenomena such as the creation of point defects (vacancies and interstitials) also need to be considered in the target bulk.

Silicide & Alloy Formation

Here we consider the effect of Ga^+ implant ions passing through the NiFe/Si interface. It is well known that Ga^+ irradiation of thin films causes a change in magnetic properties of the sample, due to ion implantation and sputtering at the vacuum/target interface.

We point out that the interaction between energetic incident radiation, magnetic target, and non-magnetic substrate must also be considered, if $\bar{i}_{SD} > t_{NiFe}$. It is known that silicides can form at a metal/Si interface such as at the NiFe/Si transition region [Mayer 1981][Talmadge 2004]. These stable phases may be magnetic or non-magnetic in nature, and are likely to become more spatially extended as a result of diffusion and enhanced atom mobility at interfaces triggered by ion bombardment. For example non-magnetic silicide phases such as FeSi have been identified by Talmadge and co-workers in rf sputtered NiFe films on Si substrates, without any energetic ion bombardment. Ion-atom and secondary atom-atom collisions can drive Ni or Fe atoms further into the underlying Si substrate from their original lattice positions, and the ion radiation can also trigger movement of Si atoms into the $Ni_{81}Fe_{19}$. A blurred Si-rich layer at the $Si/Ni_{81}Fe_{19}$ interface may cause a change in sample magnetic properties. For high D intermixing may occur at the $Si/Ni_{81}Fe_{19}$ interface even if at $D = 0$, $t_{NiFe} > \bar{i}_{SD}$, due to sputtering from the sample surface over time.

5.4 Ga^+ irradiation of $Ni_{81}Fe_{19}$ (t_{NiFe} = x nm) /Al (t_{Al} = y nm) Bilayers

5.4.1 MOKE Signal Vs. Dose (t_{NiFe} = x nm)

The effect of Ga^+ ion irradiation on $Ni_{81}Fe_{19}$ layers embedded between a non-magnetic capping layer and substrate was next investigated. $Si/Ni_{81}Fe_{19}/Al$ films were systematically irradiated and investigated magnetically by MOKE. Magnetic layer thickness, and non-magnetic cap thickness were varied systematically, t_{NiFe} = 2-12 nm, t_{Al} = 4-16 nm. Room temperature magnetic properties were investigated as a function of Ga^+ fluence, similar to unburied films discussed in Section 5.3. TEM

imaging and GIXR was used to verify the quality of interfaces of these samples, which were grown without breaking vacuum, Chapter 3.

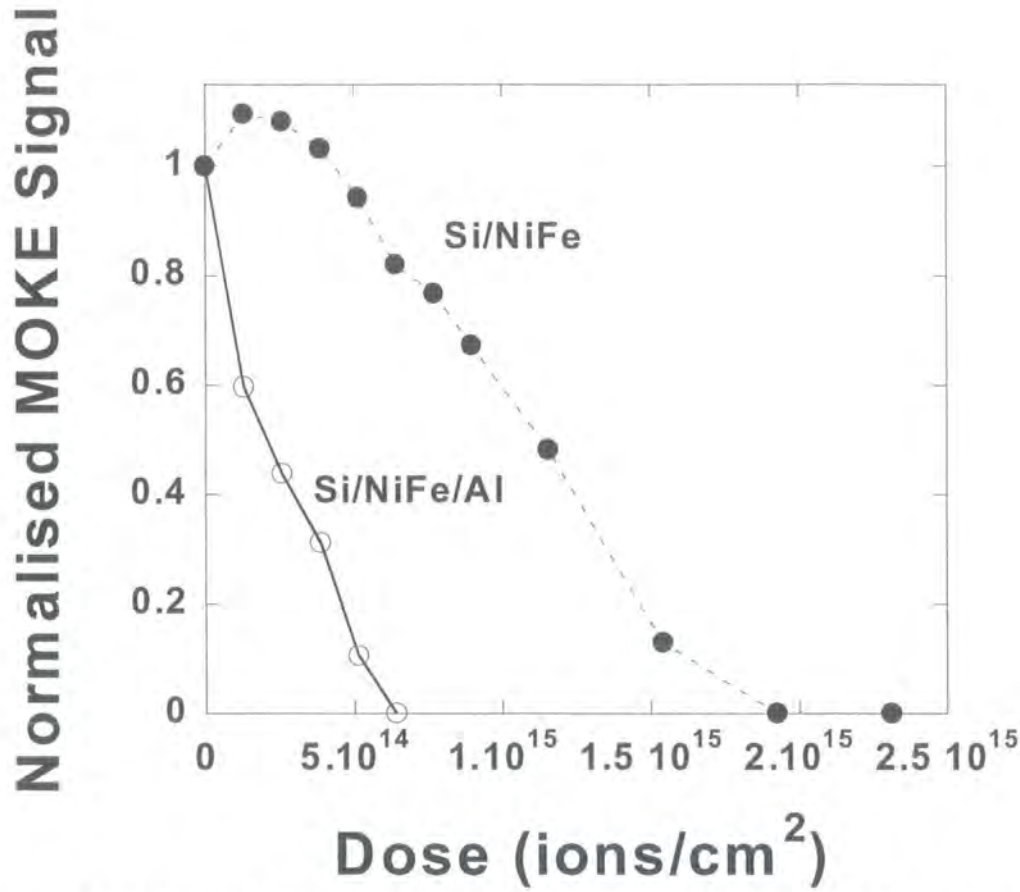

Figure 5.6: Measured room temperature MOKE signal, as a function of Ga^+ ion irradiation, for separate 3.5 nm thick NiFe films grown in identical deposition conditions. (—•—) indicates an uncapped continuous film, and (—o—) indicates an identical ferromagnetic layer buried beneath a 10 nm thick Al non-magnetic protective cap. Data is normalized w.r.t. the as deposited uncapped film.

Figure 5.6 shows the normalized MOKE signal as a function of dose, for simultaneously grown $Ni_{81}Fe_{19}$ films on Si. One sample was buried under a t_{Al} = 10 nm cap, and the other film was an uncapped reference sample.

For the uncapped $Ni_{81}Fe_{19}$ film, there is a radiation induced increase in MOKE signal at $D < 5.2 \times 10^{14}$ ions/cm^2, the origins of which are discussed in Section 5.3.3. For $D > 5.2 \times 10^{14}$ ions/cm^2 the MOKE signal decreases monotonically to a background signal at $\Phi = 1.9 \times 10^{15}$ ions/cm^2. The MOKE signal response of the Si/NiFe(3.5nm)/ Al(10nm) sample, suggests a significantly faster quenching of room

temperature ferromagnetic ordering, compared to the NiFe(3.5 nm)/Si reference sample. For films grown and irradiated in uniform conditions, there is a striking decrease in Φ for a thin ferromagnetically ordered film, upon addition of a protective non-magnetic overlayer. For the capped film, $\Phi = 6.4 \times 10^{14}$ ions/cm^2.

Taking an atomic density of Al of 6.03×10^{22} atoms/cm^3, and a sputter yield of 3.88 atoms/ion for 30 keV Ga^+ irradiation [TRIM], it is calculated that an Al thickness of 0.4 nm is radiation etched from the sample surface of the Si/NiFe/Al sample at Φ. Clearly the capping layer is still largely intact, yet room temperature ferromagnetic ordering has been radiation quenched.

AFM step height measurements of irradiated 100 μm^2 areas of Al/Si samples demonstrate that Al is radiation etched at a lower rate than corresponding $Ni_{81}Fe_{19}$ films of the same thickness, adding experimental validation of numerical simulations. A t_{al} = 10 nm film on a silicon substrate was radiation eroded to a measured step height of 10 nm at $D = 1.5 \times 10^{16}$ ions/cm^2. A 10 nm NiFe film irradiated using the same procedure showed a 10 nm measured step height at $D = 1.1 \times 10^{16}$ ions/cm^2. Assuming a constant sputter rate, at $\Phi = 6.4 \times 10^{14}$ ions/cm^2 for the capped NiFe sample, step height measurements suggest ~0.6 nm of the Al capping layer is sputtered from the vacuum-target interface.

The uncapped sample experiences a radiation induced quenching of ferromagnetism principally due to radiation erosion of Ni and Fe atoms at the free surface. Both TRIM simulations and experimental atomic force microscopy step height measurements show sputtered removal of atoms cannot be responsible for radiation induced loss of magnetic ordering in the Si/NiFe/Al sample. Further samples were investigated to understand the origins of this remarkable finding – thin in-plane magnetized films with an interface between incident radiation and the magnetic layer

can be magnetically patterned quicker than samples with radiation incident on a free surface.

Figure 5.7 plots the effect of increasing Ga^+ dose on bilayer sample MOKE signal, when systematically varying t_{NiFe}, for fixed thickness 10 nm Al capping layers.

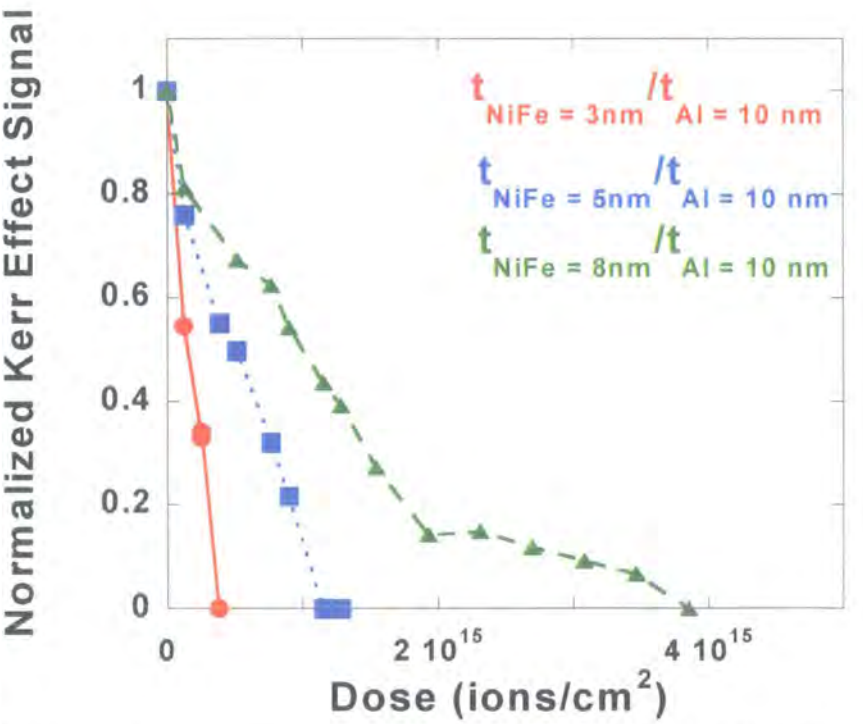

Figure 5.7: Measured room temperature MOKE signal, as a function of Ga^+ dose, for t_{NiFe} = 3, 5, and 8 nm films grown in identical deposition conditions. All films are capped with a t_{Al} = 10 nm layer. Data is normalized w.r.t. the Kerr signal from the t_{NiFe} = 8 nm as-grown film. t_{NiFe} = 3 nm (—●—), 5 nm (—■—), 8 nm (—▲—).

The t_{NiFe} = 3 nm sample, exhibits a dramatic linear decrease in MOKE signal as a function of ion dose, culminating in quenched room temperature ferromagnetic ordering at $\Phi = 4.0 \times 10^{14}$ ions/cm^2. The trend for a t_{NiFe} = 5nm sample is similar, a steady linear decrease in MOKE signal with increasing fluence, with $\Phi = 1.1 \times 10^{15}$ ions/cm^2. Clearly the rate of magnetic patterning per unit volume of NiFe, is markedly different in buried films of varied t_{NiFe}. These doses are markedly lower than for uncapped control samples of comparable NiFe thickness.

For a thicker t_{NiFe} = 8 nm bilayer, there are two distinct trends evident in the MOKE signal vs. D curve. Below $D = 1.9 \times 10^{15}$ ions/cm^2, the MOKE signal falls linearly with ion dose, similar to thinner samples. The gradient of this curve is markedly less pronounced than the 3 or 5 nm curves, suggesting more dramatic magnetic patterning rates of buried films are confined to ultra-thin layers. However for the fluence range $1.9 \times 10^{15} < D < 3.8 \times 10^{15}$ ions/cm^2, before ferromagnetic quenching is measured, a marked change in the slope of the curve is observed, and a dramatically slower monotonic decrease in measured MOKE signal with respect to Ga^+ fluence is noted. This unexpected result is interpreted as follows:

At low ion fluences, ion induced interfacial intermixing [Mayer 1981] localized at interfaces causes a loss of measured ferromagnetic ordering in thin film bilayer samples. The mixing length-scales do not vary linearly with increasing ion fluence, therefore Φ does not vary linearly with t_{NiFe}. In the t_{NiFe} = 8 nm sample, a much slower magnetic patterning rate is observed.

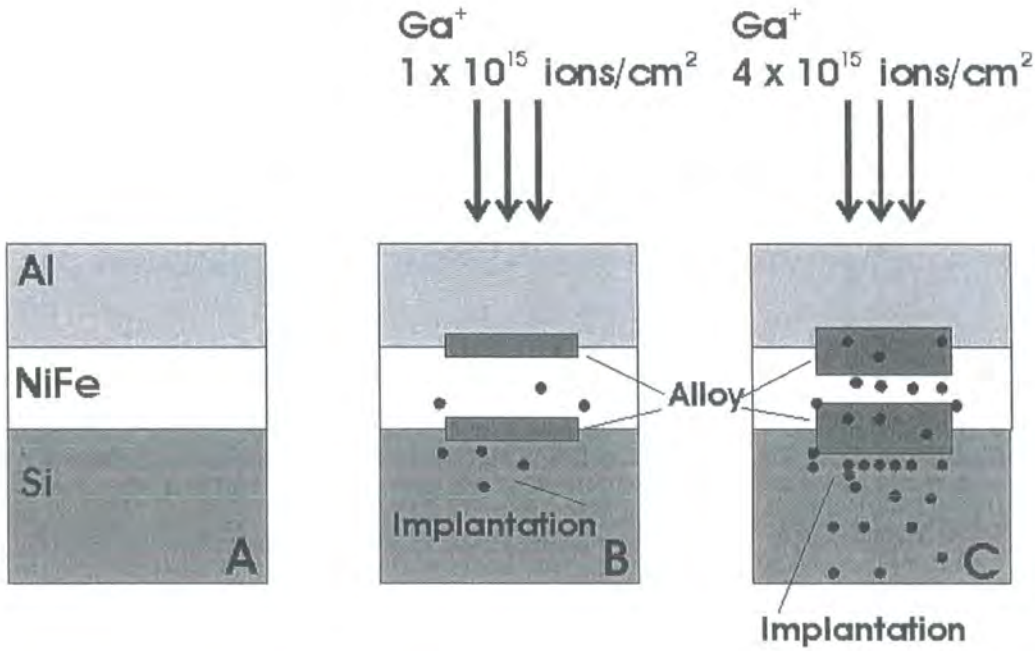

Figure 5.8: Quenching ferromagnetism in the Si/$Ni_{81}Fe_{19}$(8nm)/Al(10nm) sample. *A* shows the pristine sample, and *B* the alloyed interfaces at intermediate fluence. *C* shows the sample at Φ, with longer range alloying at upper and lower interfaces, and increased implantation in the NiFe and Si.

Even at intermediate ion doses, when interfaces are broadened by the passage of Ga^+ ions through the sample interfaces, there is still a relatively pristine magnetically active layer between upper and lower interfaces. The central $Ni_{81}Fe_{19}$ layer is ferromagnetically quenched at a slow rate partly by long range intermixing at interfaces, and partly by ion implantation – Fig. 5.8 (previous page). Hence the t_{NiFe} = 8nm MOKE signal vs fluence plot (previous, Fig 5.7) has two slopes, a sharp slope corresponding to mixing over 1-2 nm at upper and lower interfaces, and a shallow slope corresponding to long rage intermixing over at least 2-4 nm, implantation and damage effects. For the t_{NiFe} = 8nm sample, a sizeable proportion of Ga^+ ions may be stopped in the NiFe layer, therefore the lower Si/NiFe interface may be less aggressively mixed than the upper NiFe/Al interfaces, through which all Ga^+ ions are assumed to pass.

It is also worth noting here that no peak is observed in capped sample MOKE signal curves at low doses, as was observed in many uncapped samples. This was the case for all Si/NiFe/Al samples studied, and is further evidence for dramatically different mechanisms for the loss of measured ferromagnetic ordering in buried and unburied films as a function of *D*.

5.4.2 Coercivity Vs. Dose (t_{NiFe} = x nm)

The response of H_c to radiation of buried layers was next investigated. In Figure 5.9 the relationship between coercivity, measured along the magnetic easy axis, and *D* for varied t_{NiFe} is plotted.

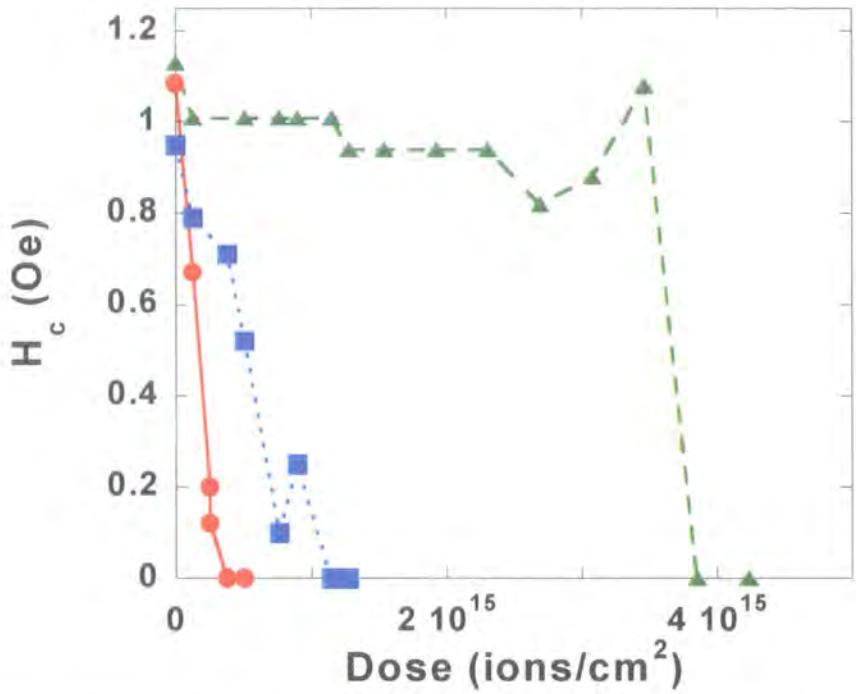

Figure 5.9: Measured easy axis coercive fields, as a function of Ga^+ irradiation, for separate t_{NiFe} = 3, 5, and 8 nm films, capped with a non-magnetic t_{Al} = 10 nm overlayer. t_{NiFe} = 3 nm (—●—), 5 nm (—■—), 8 nm (—▲—).

Data was measured from M-H loops taken in uniform field conditions at a frequency of 27 Hz. For t_{NiFe} = 3 or 5 nm the trend is for a steady linear decrease in H_c with increasing D, associated with a reduction in absolute spontaneous magnetization. It is interesting to note that switching fields for these irradiated thin films can be as low as 0.1 Oe prior to ferromagnetic quenching. This is markedly different from experimental observations for uncapped NiFe films, where radiation thinned samples exhibit a peak in H_c prior to the onset of room temperature superparamagnetism, at Φ. In the t_{NiFe} = 8 nm bilayer, for $D \leq 3.1 \times 10^{15}$ ions/cm^2 only a slight decrease in H_c is measured, from 1.1 Oe measured on an undosed reference area of the film, to ~0.85 Oe at $D = 3.1 \times 10^{15}$ ions/cm^2. The rate of decrease in H_c is considerably lower compared to the t_{NiFe} = 3 or 5 nm bilayers. For a higher ion dose, from 3.5×10^{15} ions/cm^2 $< D < 3.8 \times 10^{15}$ ions/cm^2 H_c falls sharply to zero. A small change in t_{NiFe} is thus observed to result in a large increase in the Ga^+ dose needed to remove the

experimentally measured hysteretic effects, and a striking qualitative change in the response of H_c to ion dose. For a capped t_{NiFe} = 5 nm film, $\Phi = 1.2 \times 10^{15}$ ions/cm^2. Increasing the NiFe layer thickness by just 3 nm increases Φ by over 300 %. Fig 5.9 supports a model of radiation induced interfacial mixing, at lengthscales not linearly proportional to dose. A relative plateau in the t_{NiFe} = 8 nm sample H_c, for $D \leq 3.1 \times 10^{15}$ ions/cm^2 is consistent with magnetization reversal by domain wall, in a less aggressively mixed, relatively pristine area of film, between modified upper and lower interfaces. Thicker irradiated t_{NiFe} = 12 nm samples were investigated for the same thickness Al cap. A much higher Φ was measured with a peak in H_c prior to quenching, indicating the cap may have been sputtered from the NiFe surface.

5.4.3 Variation of cap thickness (t_{Al} = y nm)

The addition of a protective non-magnetic cap to an in plane magnetized $Ni_{81}Fe_{19}$ film ($t_{NiFe} < \sim$ 10nm) results in a striking drop in the ion dose needed for room temperature ferromagnetic quenching. The effect of varying the protective aluminium overlayer thickness, t_{Al}, for fixed thickness NiFe films was investigated. Capping layer thicknesses were chosen so that the cap would not be radiation eroded at Φ. Additionally, t_{Al} must be lower than the ion penetration depth in the capping medium – for aluminium this is calculated at 24 nm [Table 5.1, previous]. Note that the experimentally determined Ga^+ penetration depths can be higher than TRIM calculated values, and that the Ga atomic concentration as a function of target depth has an exponential tail [Park 2004]. For example Park experimentally measured Ga atomic concentrations of 2 % at a depth of 150 nm in 50 keV 560 nm thick NiFe samples.

For t_{NiFe} = 5 nm, simultaneously grown bilayer samples with varied capping layer thickness, and an uncapped control sample, the response of MOKE signal and easy axis switching field to irradiation is plotted in Fig. 5.10. Samples were uniformly irradiated, in all cases to a critical ion dose needed for quenching of room temperature ferromagnetism.

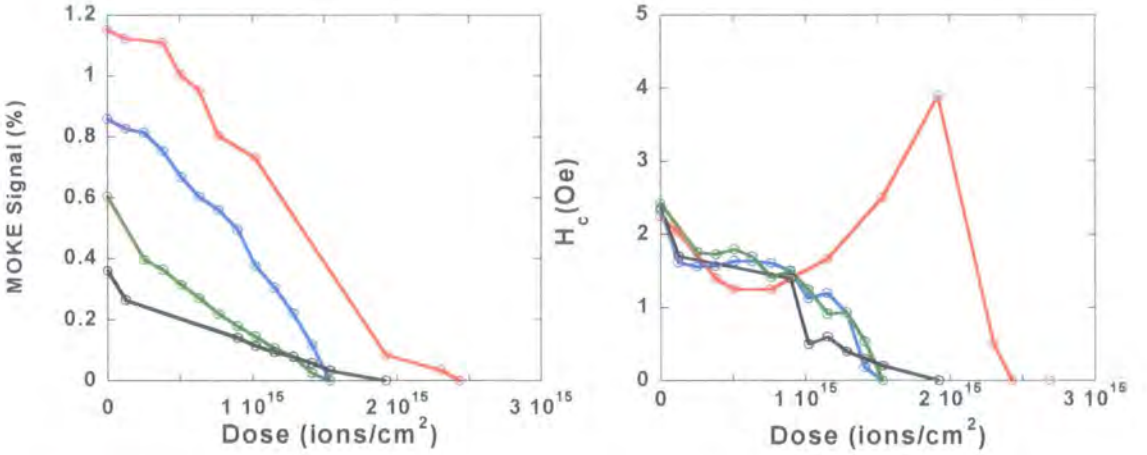

Figure 5.10: MOKE signal, and H_c, for a set of t_{NiFe} = 5 nm films. Data corresponds to t_{Al} capping layer thicknesses of (—○—) 0 nm, (—○—) 3 nm, (—○—) 7 nm, and (—○—) 10 nm respectively.

The critical patterning dose is highest for the uncapped control sample, 2.5 × 10^{15} ions/cm^2, as opposed to $\Phi = 1.5 \times 10^{15}$ ions/cm^2 for t_{Al} = 3 or 7 nm, and $\Phi = 1.9 \times 10^{15}$ ions/cm^2 for the magnetic bilayer with a t_{Al} = 10 nm cap.

All capped samples show a qualitatively very similar response to Ga^+ irradiation. The response of H_c to increasing ion fluence differs greatly for capped and uncapped films. In a 5 nm uncapped film H_c decreases from that of an unirradiated control sample until D = 8 ×14 ions/cm^2. Then there is a peak in H_c, up to 3.9 Oe, prior to ferromagnetic quenching at a higher radiation dose than buried films.

However, the response of H_c to increasing *D* is remarkably similar for t_{Al} = 3, 7, or 10 nm capped samples, indicating the prospect of reproducibly changing sample magnetic properties.

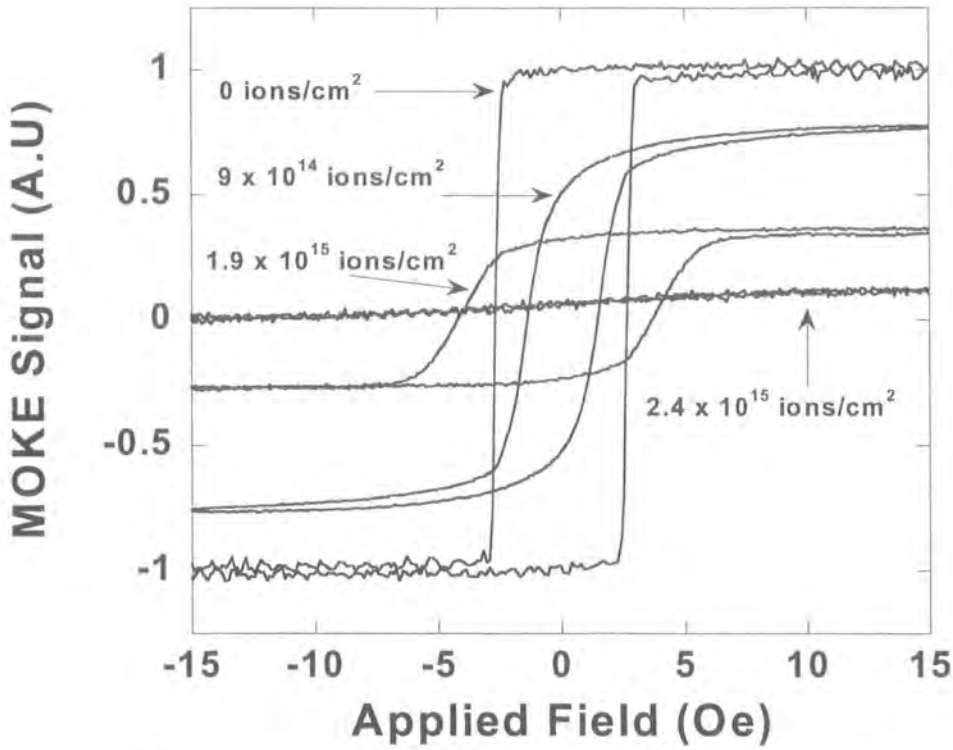

Figure 5.11: M-H loops for a 5 nm thick $Si/Ni_{81}Fe_{19}$ film as a function of incident Ga^+ radiation. MOKE signal levels are normalized with respect to the as-deposited film.

The increase in H_c and radiation induced rounding of M-H loops prior to the onset of room-temperature superparamagnetism is clearly evident in figure 5.11. Clearly, for the as deposited sample, the square nature of the M-H loop suggests the domain wall propagation field is lower than the field at which a domain wall is nucleated. With increasing fluence, e.g. $D = 9 \times 10^{14}$ ions/cm^2 or 1.9×10^{15} ions/cm^2 M-H loops become significantly rounded. The remanent squareness, M_r/M_s, is also reduced from unity. In this dose range magnetization reversal is likely to be dominated by domain wall nucleation and propagation, but the wall propagation field may exceed the nucleation field. A typical MOKE background signal trace, indicating no measured ferromagnetic ordering, for $D = 2.4 \times 10^{15}$ ions/cm^2 is also shown.

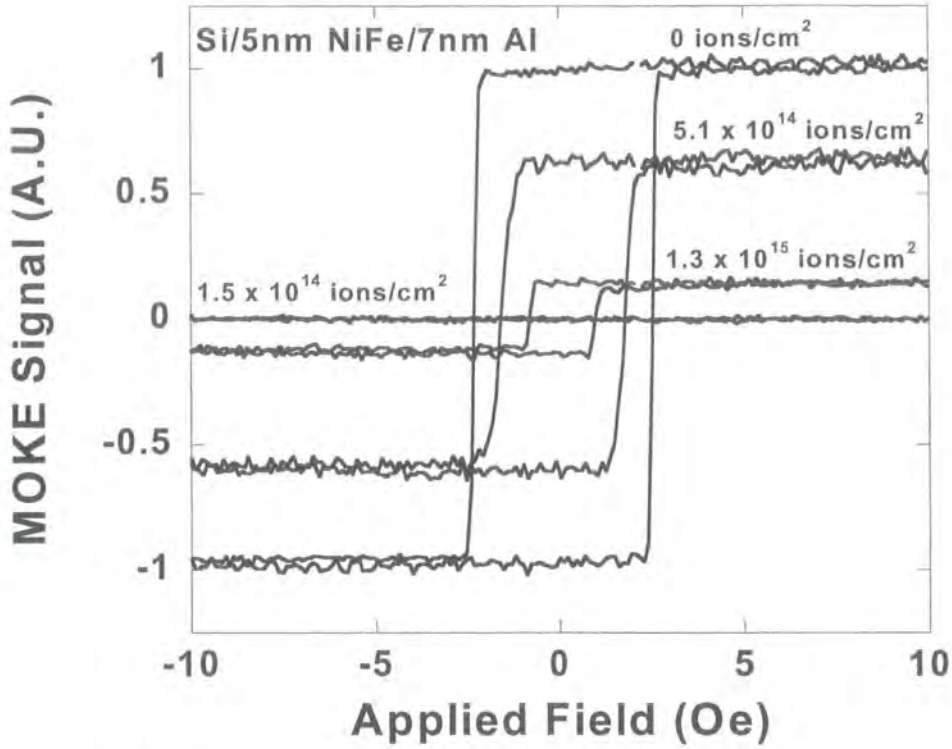

Figure 5.12: M-H loops for a buried 5 nm thick NiFe film as a function of incident Ga^+ radiation. MOKE signal levels are normalized with respect to the as-deposited film.

In Fig. 5.12 easy axis M-H loops for a buried t_{NiFe} = 5 nm film, as a function of ion fluence are plotted. Loops are seen to maintain a high M_r/M_s ratio and sharp switching transitions, with increasing *D*. The square character of the M-H loops indicates that magnetization reversal still proceeds by easy domain wall propagation. Direct comparison between Fig. 5.12 and magnetic hysteresis loops for an unburied film plotted in Fig. 5.11, grown and irradiated under uniform conditions, reveals strikingly different M-H loop responses to radiation in unburied and buried NiFe films.

The most dramatic drop in Φ per nm^3 of $Ni_{81}Fe_{19}$ is seen in thin-capped ferromagnetic layers, where a large proportion of Ni and Fe atoms are near an Al or Si interface. Therefore a set of t_{NiFe} = 2 nm samples were irradiated and investigated,

with varied t_{Al}. The H_c and MOKE signal vs. ion fluence plots are presented in Figure 5.13.

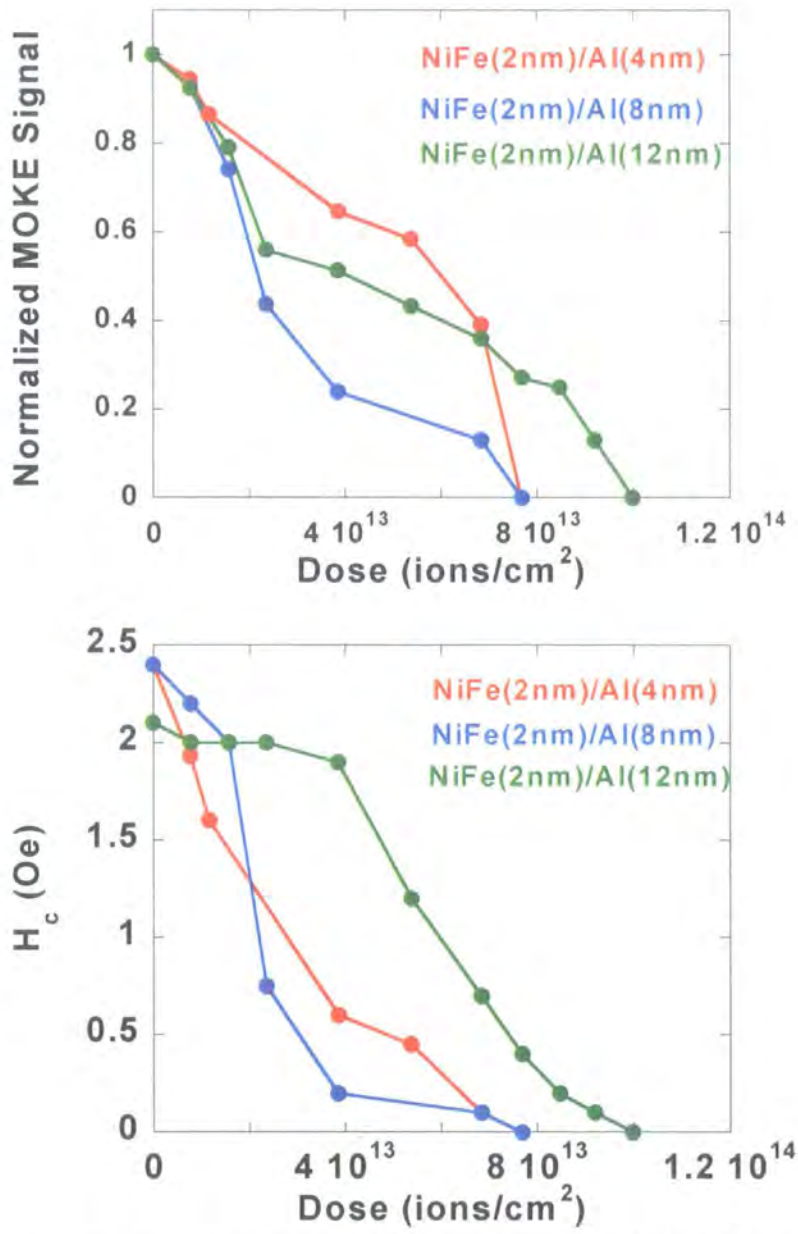

Figure 5.13: Normalized MOKE signal, and easy axis coercive field, H_c, as a function of ion fluence, for a set of 2 nm thick NiFe films. Data corresponds to t_{Al} of (—●—) 4 nm, (—●—) 8 nm, (—●—) 12 nm respectively.

Figure 5.13 shows the MOKE signal and H_c response of 2 nm thick ferromagnetic layers embedded between Si substrates and Al overlayers, with varied t_{Al}, to uniform Ga^+ radiation. We note a very strong sensitivity of H_c to ion doses, as

low as 8×10^{12} ions/cm^2 for all of these samples. H_c decreases monotonically with ion flux, as does the MOKE signal. $Ni_{81}Fe_{19}$ films with t_{Al} = 16 nm had insufficient MOKE signal for a full dose test and mapping of M-H properties as a function of dose, or an accurate measurement of Φ.

An initially thin $Ni_{81}Fe_{19}$ layer embedded between an Al overlayer and Si substrate becomes broadened with increasing ion flux, leading to a rapid change in magnetic properties. There is a striking reduction in Φ for low t_{NIFe} bilayers. For example $\Phi = 8 \times 10^{13}$ ions/cm^2 for 2 nm thick capped NiFe layers and 1.5×10^{15} ions/cm^2 for 5 nm capped NiFe layers – this is a factor of 19 difference.

In the case of t_{NiFe} = 2 nm or 5 nm bilayers, the thin films with largest t_{Al}, exhibit the highest Φ. The mean stopping distance for Ga^+ ions is 24 nm in Al and 10 nm in $Ni_{81}Fe_{19}$ at a 30 keV energy. As t_{Al} tends towards $\bar{i}_{SD}$ some Ga^+ ions may not penetrate the sample to the lower NiFe/Si interface. This would lead to a slower degradation of H_c and absolute sample magnetization with flux, since much of the intermixing may be localized at the upper NiFe/Al interface.

Pulling out the back on an envelope:

The atomic density of NiFe is ~9×10^{22} atoms/cm^2. There are approximately 2×10^{16} atoms/cm^2 in a 2 nm thick monolithic layer of Permalloy. Therefore loss of room temperature ferromagnetic ordering is observed at a ratio of 1:250 incident Ga^+ ions to Ni and Fe atoms responsible for target ferromagnetism. Sputter yields from the vacuum-target interface are of the order of 5 target atoms per every incident ion, and cannot be responsible for quenching of spontaneous ferromagnetism.

A Ga^+ concentration of ~ 20 % is needed to quench ferromagnetism by implantation, but a Ga^+ atomic concentration of only ~ 0.1 %, in the region of the

NiFe layer is likely. Ion implantation is not the principal mechanism for quenching of ferromagnetism.

There is a high degree of target atom mobility with irradiation in the target bulk. At the irradiated Al/NiFe or NiFe/Si interfaces, dilution of the NiFe layer ferromagnetism occurs by Al and Si substitutions, into vacated Ni and Fe sites in the lattice. We describe the blurring of bilayer interfaces in the forthcoming section.

5.4.4 Collisional intermixing at interfaces

Thin films can be measured in multiples of atomic planes present. For very thin layered systems many atoms occupy interface positions or are in the vicinity of an interface. During irradiation, atomic recoils and defects are generated from the bilayer sample surface inwards, resulting in the spatial redistribution of target atomic components, to a depth of the order of $\bar{i}_{SD}$. This spatial redistribution of target atom layers is effected by primary ion-atom collisions, and secondary atom-atom collisions (cascade mixing). The creation and slowing down of low energy cascades constitute the majority of target atoms set in motion. The structure and composition of the as-deposited ferromagnetic layer of the bi-layer, becomes increasingly disrupted at higher fluences, leading to a complete loss of observed room temperature ferromagnetic ordering, above Φ.

The width of an intermixed layer increases with ion mass [Fassbender 2004][Rettner 2002]. Heavy energetic ions are more effective in both surface sputtering and generating collision cascades than light ion species, thus more pronounced mixing occurs. Transmission electron microscopy cross-sections rule out the possibility of deep intermixing of the magnetic NiFe and the Al overlayer, prior to irradiation. As a result of atomic displacement in the quenching of an incident ions

kinetic energy, the original discrete layered structure is smeared out, and mixed layers are formed. Longer range "pseudo-roughening" takes place on longer length scales, of the order of several nm.

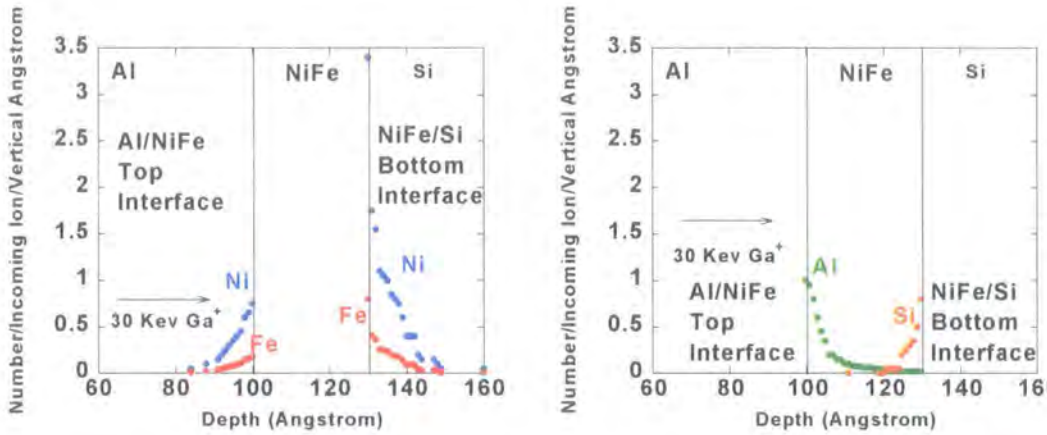

Figure 5.14: TRIM calculated profile of interfaces in an Si/NiFe(3 nm)/Al (10 nm) sample, under 30 keV Ga^+ bombardment. Incoming ions move from the left to the right of each diagram. Calculation is for redistribution of layer atomic species after 10,000 incoming ions.

The radiation induced migration of Ni and Fe atoms into the cap and substrate, with an associated spatial redistribution of Si, and Al atoms in the NiFe layer is shown in figure 5.13. Transport of interfacial atoms is on length-scales of the order of 1-2 nm. Results shown do not account for dynamic effects. Note the exponential decay of mixing lengthscales. This simple ballistic ion beam-mixing model generally underestimates the mixing lengthscales. An instantaneous heat transfer mechanism between beam and target during irradiation, that aids diffusion of interfacial atoms may need to be considered [Rettner 2002].

5.4.5 Intermixing Model

In the following, radiation induced intermixing at the film/substrate interface and the cap/film interface is addressed in terms of a quantitative model. Characteristic mixing lengthscales, λ, and foreign atom concentrations are modelled as a function of

D, using source data from TRIM simulations. Therefore the model uses source data which assumes mixing processes are ballistic and so heating and classical diffusion effects are ignored. Experimental results show it is appropriate to employ a model where the mixing width, λ increases with ion fluence according to the relationship:

$$\lambda \propto \sqrt{D} \qquad [5.1]$$

where D is Ga^+ ion dose [Tsaur 1979][Cai 2004]. I.e. radiation induced atomic displacement at interfaces results in a structural change of samples characterised by a diffusion-like process.

The method used here is similar to that employed by Vieu [Vieu 2002], in a quantitative estimation of mixing lengthscales and foreign atom concentrations in a CoPt system, subjected to Ga^+ ion beam exposure. However we have extended the approach to account for the non-symmetric nature of ion induced transport of atoms at target interfaces.

A $Si/NiFe_{2.5nm}/Al_{10nm}$ system is considered, with perfect step-like interfaces oriented parallel to the sample surface. At the NiFe/Al interface there are an average of $X_{Al/NiFe} = 8.5$ displaced atoms per NiFe layer, where $X_{Al/NiFe}$ is the mean number of displaced atoms per incident Ga^+ ion. For the Si/NiFe interface $X_{NiFe/Si} = 10.2$ displaced atoms per NiFe layer per Ga^+ ion. For a given dose, the number of displacements per atomic site is given by XD/N_s, where N_s, the atomic areal density of a NiFe layer is approximated as 1.6×10^{15} atoms/cm^2. The characteristic ion-induced mixing length λ, is given by [Vieu 2002]:

$$\lambda = \sqrt{\frac{XD}{N_S}} a^2 \qquad [5.2]$$

where a is the mean atomic spacing near interfaces, approximated to 1.7 Å for NiFe. The sandwich structure is regarded as a sequence of slices of thickness 1 ML. At $D =$

0 ions/cm^2, substrate, NiFe, and capping material each has pure atomic composition. In order to investigate the concentration of foreign atoms at interfaces in a layered film as a function of D, an expression of the following form is used:

$$C_{foreign} = \left[1 - 1/2 erf\left[\frac{(z \pm t/2)}{2\lambda}\right]\right] \qquad [5.3]$$

where $C_{foreign}$ denotes foreign atom concentrations at the interfaces, t is the NiFe layer thickness and z indicates the growth axis direction taken from the origin. The term "*erf*" represents an error function. (z + t/2) maps the concentration at the upper, and (z - t/2) at the lower interface.

For low D and hence low λ, the expression tends to a square well of thickness, t, with well-defined interfaces, and a pristine NiFe layer. As λ increases, at higher radiation doses, the interfacial edge profile becomes more rounded. More foreign atoms reside within the NiFe layer, leading to an associated increase of NiFe atomic concentration in the upper cap and lower substrate respectively – Fig. 5.15.

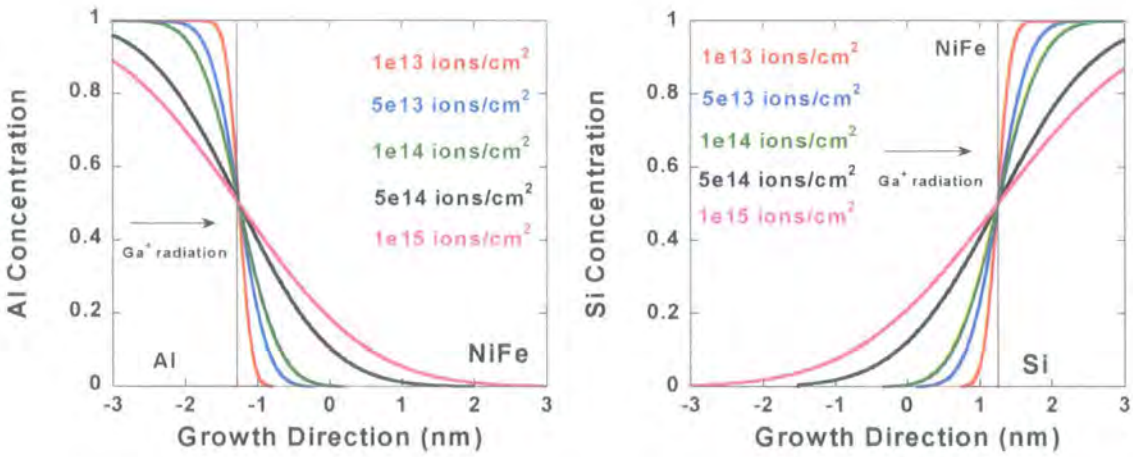

Figure 5.15: Evolution of foreign atom concentrations across the interfaces of a model Si /NiFe(2.5 nm)/Al(10 nm) layered film. 30 keV Ga^+ ion irradiation is applied from left to right.

The model shows that the sandwich interfaces become progressively more intermixed as a function of ion dose. Increasing proportions of Ni and Fe reside in the Al and Si layers, with an associated migration of Al and Si atoms into the NiFe layer. This model explains well our experimental observations.

Vacancies, implanted ions and other defects all serve to enhance transport of atoms at the interfaces. The radiation assisted intermixing at upper and lower interfaces in the Si/NiFe/Al system is asymmetric. Different alloys form at the upper and lower interfaces with aluminium rich phases expected at the upper interface and silicides such as FeSi and other alloys at the lower interface. Quenching of E_{ion} means that the magnitude of ion energy dissipated as short-range atomic displacements, may be different at the upper and lower NiFe interfaces. The characteristic mixing length λ depends on the depth of respective upper and lower interfaces in the bilayer. Further on an atomic scale, local kinematics and radiation-assisted displacement of target atoms are different for atomic species of different mass and radius.

At $D \geq 1 \times 10^{15}$, significant displacement of atoms at distances of greater than 2.5 nm are evident. Combined with measurements of corresponding magnetic properties, this supports our interpretation of local atomic displacements at the interfaces, at low Φ, where the protective capping layer remains intact.

5.5 Ga^+ irradiation of $Ni_{81}Fe_{19}$/Au Bilayers

5.5.1 $Ni_{81}Fe_{19}$/Au: Introduction

FIB Ga^+ collisional intermixing has been investigated for the rapid quenching of room temperature ferromagnetic ordering of in-plane magnetized Permalloy bilayers capped with Al. In order to investigate if ion beam mixing at interfaces could

be used as a general technique for the quenching of ferromagnetic ordering in bilayers, it was necessary to investigate another capping species. In particular, the identification of general trends extensible over any irradiated bilayer was desirable.

Gold was selected as the non-magnetic overlayer species, and was investigated with Si substrates and NiFe magnetic layers, similar to Al, as a function of Ga^+ irradiation. Au is technologically useful, and is favoured as a non-magnetic capping material due to its chemical inertness. Furthermore, Au_{79} is a heavy large atom compared to Al_{13} – it was hoped this might give additional insight into the mixing mechanism involved in quenching ferromagnetism in buried $Ni_{81}Fe_{19}$ layers.

t_{NiFe} *(nm)*	Φ *(ions/cm^2)*	*MOKE Signal (% dk/k)*	*Easy Axis Coercivity (Oe)*	*Hard Axis Saturation Field (Oe)*
2	1.2×10^{14} [$\pm 7.0 \times 10^{13}$]	0.31	1.2 [± 0.1]	2.2 [± 0.5]
3	5.1×10^{14} [$\pm 1.3 \times 10^{14}$]	0.69	1.4 [± 0.1]	3.0 [± 0.5]
4	9.5×10^{14} [$\pm 5.0 \times 10^{13}$]	0.81	1.1 [± 0.1]	4.5 [± 1.0]
6	2.6×10^{15} [$\pm 7.0 \times 10^{13}$]	1.20	1.2 [± 0.1]	6 [± 0.5]

Table 5.3: The experimentally measured critical ion fluence to quench room temperature ferromagnetic ordering is indicated for a set of 4 bilayers, with a fixed thickness 7 nm Au cap, and varied t_{Nife}. Also shown are measured magneto-optical signal from unirradiated samples, and easy and hard axis fields for as deposited samples.

Samples were grown simultaneously by thermal evaporation, as described in Chapter. 3, and dose tests were performed in a similar manner to Al capped bilayers. Table 5.3 summarizes the basic properties of the as-deposited and irradiated bilayers. The MOKE signal of buried $Ni_{81}Fe_{19}$ layers scales linearly with increasing t_{NiFe} from

2-6 nm. Note that the MOKE signal of a fixed ferromagnetic layer thickness capped with Au as compared to Al may be quite different due to plasmon resonance and other magneto-optical effects.

5.5.2 $Ni_{81}Fe_{19}$/Au: MOKE Signal

Figure 5.15 plots a smooth reduction in MOKE signal for samples of varied $Ni_{81}Fe_{19}$ thickness. All buried NiFe layers exhibit a very sharp decrease in MOKE signal, irrespective of NiFe thickness for low ion doses.

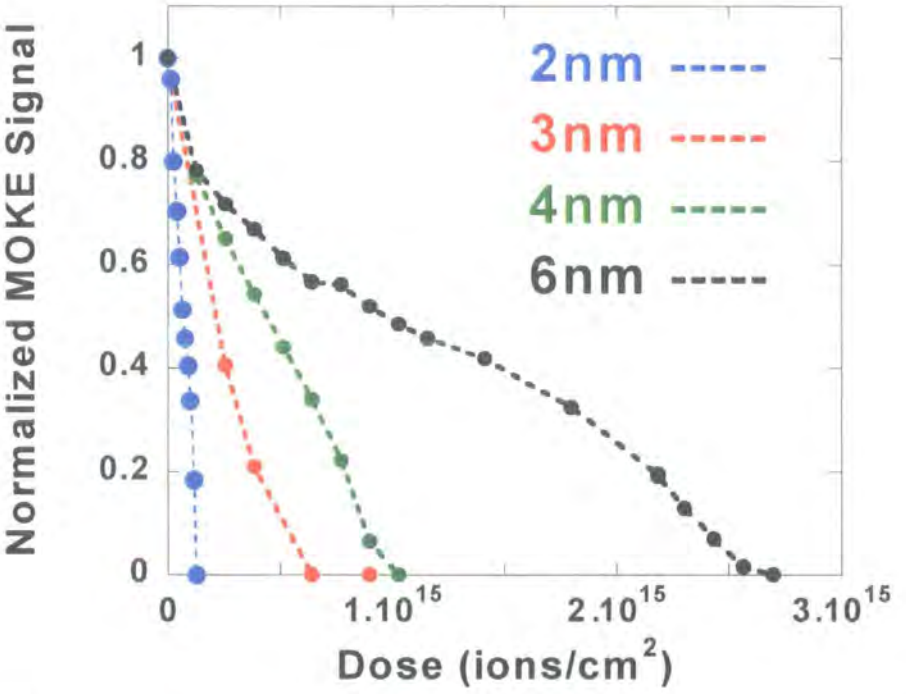

Fig 5.15: Experimentally measured MOKE signal, of NiFe/Au bilayers as a function of incident 30 keV Ga^+ ion irradiation. Signal levels are normalized to the t_{NiFe} = 6 nm sample.

For t_{NiFe} = 2-4 nm, the decrease in MOKE signal, or spontaneous ferromagnetic ordering of the sample, decreases approximately linearly with fluence. For the t_{NiFe} = 6 nm buried layer, the rate of ferromagnetic quenching is not constant with ion dose, suggesting complex mechanisms for the removal of measured ferromagnetic ordering. The critical ion fluence needed to quench ferromagnetic ordering at room temperature is again much lower than NiFe films at a free surface

for low t_{NiFe} – similar to Al overcapped films. Φ is non-linear w.r.t. increasing $Ni_{81}Fe_{19}$ thickness. This mirrors the behaviour of NiFe layers capped with non-magnetic Al layers. For example, a threefold increase in t_{NiFe} from 2–6 nm incurs a twenty-fold increase in Φ, from $1.2 \times 10^{14} \pm 7.0 \times 10^{13}$ ions/cm^2 for a $t_{NiFe} = 2$ nm layer, to $2.6 \times 10^{15} \pm 7.0 \times 10^{13}$ ions/cm^2 for the $t_{NiFe} = 6$ nm sample.

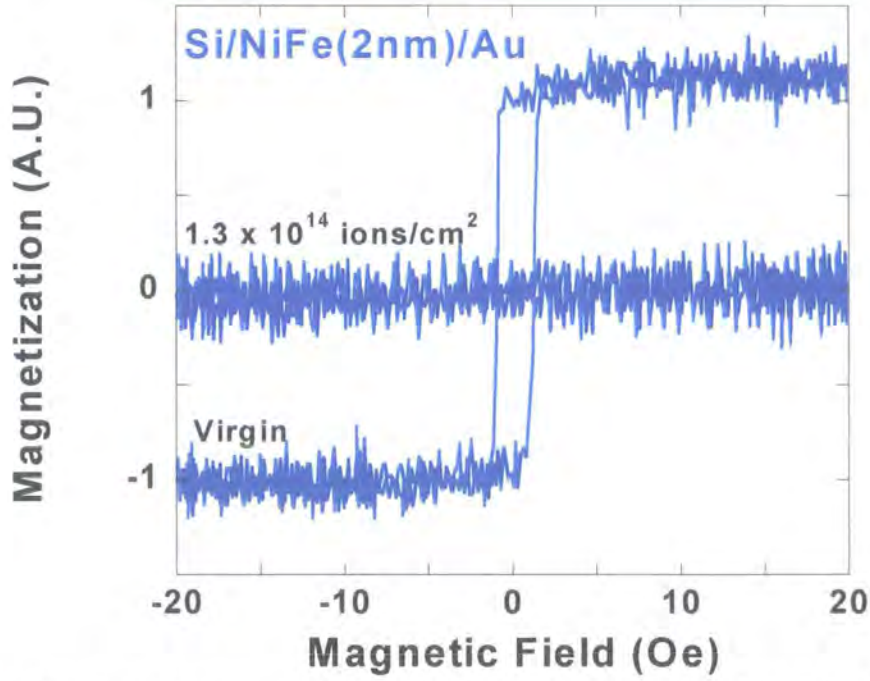

Fig 5.16: Experimentally measured MOKE traces for an as deposited and irradiated Si/NiFe/Au ultra-thin film.

Figure 5.16 exhibits a M-H loop of an as-deposited $t_{NiFe} = 2$ nm film capped with gold. The MOKE background signal trace, was measured from an area of the same film irradiated at $\Phi = 1.3 \times 10^{14}$ ions/cm^2. Remarkably room temperature ferromagnetism in this sample was quenched at a Ga^+ dose applied in a standard single ion beam raster scan over a 100×100 μm^2 surface area, at 3nA beam current, at a beam dwell time of only 1 μs per pixel.

This result illustrates well how layered media can be ferromagnetically quenched at remarkably low ion doses relative to uncapped samples. This is especially true if all atoms in the ferromagnetically active layer are near an interface.

5.5.3 $Ni_{81}Fe_{19}$/Au: H_c vs. Dose

A rapid intermixing induced reduction in H_c is very pronounced at low ion fluences in t_{NiFe} = 2 or 3 nm layers, similar to Al capped samples – Fig. 5.17. For t_{NiFe} = 2 nm the decrease in H_c with fluence is linear, and a similar but less pronounced trend is evident in the t_{NiFe} = 3 nm thick sample.

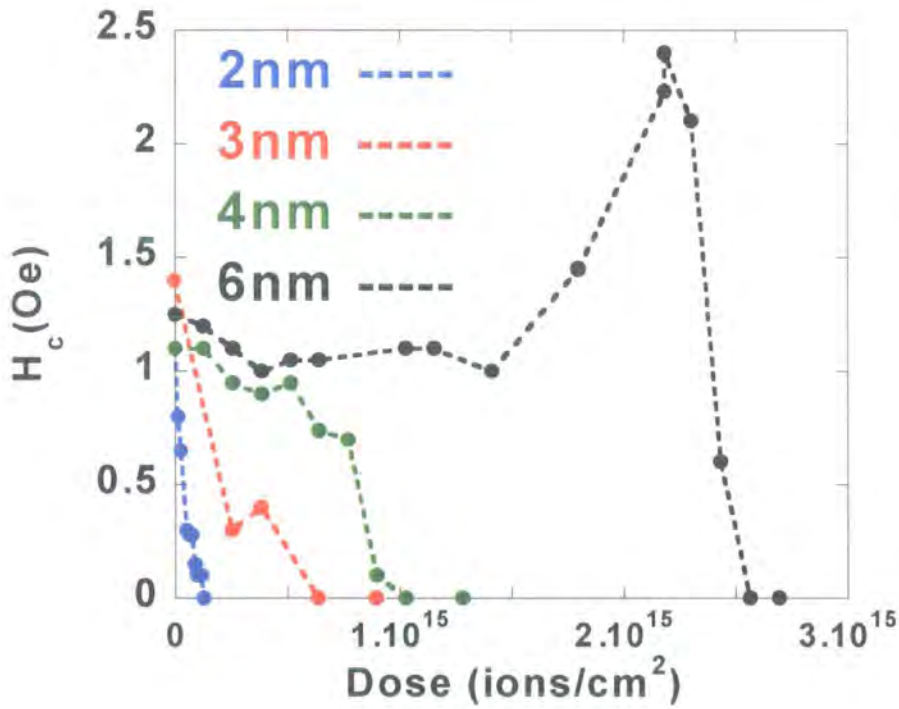

Fig 5.17: Experimentally measured easy axis H_c of irradiated films of varied t_{NiFe}, with uniform Si substrates, and non-magnetic Au capping layers.

However, for the t_{NiFe} = 4 nm sample, there are two distinct trends evident in the H_c vs. dose plot. At low to intermediate ion fluences H_c falls slowly, from 1.1 Oe for an as deposited sample, to 0.7 Oe at $D = 7.7 \times 10^{14}$ ions/cm^2 followed by a

dramatic drop in coercivity, and the onset of room temperature superparamagnetism at $\Phi = 9.5 \times 10^{14}$ ions/cm^2 $\pm$ 5×10^{13} ions/cm^2.

The increase in H_c as compared to the as-deposited samples for doses near ferromagnetic quenching in the t_{NiFe} = 6 nm layer, from $D = 1.4 \times 10^{15}$ ions/cm^2 – 2.6×10^{15} ions/cm^2 is analogous to the trend seen in unburied Permalloy films. Taking an atomic density of gold of 5. 904×10^{22} at/cm^3 we calculate a density of Au atoms of 5.904×10^{15} at/cm^3 per nm of gold in the cap. Using a calculated sputter yield of Au of 17 atoms/ion, we calculate that 5.8 nm of Au has been sputtered at a dose of 2×10^{15} ions/cm^2. Au is known to require a small sublimation energy [Sigmund 1969], and so produces a very high sputter yield per energetic incident ion.

Therefore we suggest that a peak in H_c may be seen in Ga^+ irradiated bilayers if the cap is significantly thinned, or completely radiation etched. Using a similar calculation, only ~0.35 nm of Au is calculated to be sputtered from the bilayer Au-vacuum free surface when room temperature ferromagnetism is quenched in the t_{NiFe} = 2 nm sample.

For bilayer sample where the capping layer is of sufficient thickness to remain intact at Φ, H_c falls steadily to zero with increasing ion flux. The H_c vs. dose plot may have two slopes for wider NiFe layers. If however the cap is nearly or completely radiation etched before extinction of ferromagnetism in the bilayer sample is measured, H_c increases, similar to the plots in Fig. 5.3 for uncapped NiFe layers on Si, prior to the absence of ferromagnetic ordering. For example in the t_{NiFe} = 6 nm Au capped bilayer, H_c peaks at 2.4 $\pm$ 0.1 Oe at 2.2×10^{15} ions/cm^2, compared to 1.2 Oe for the as- prepared film.

5.5.4 $Ni_{81}Fe_{19}$/Au: M_R/M_S vs. Dose

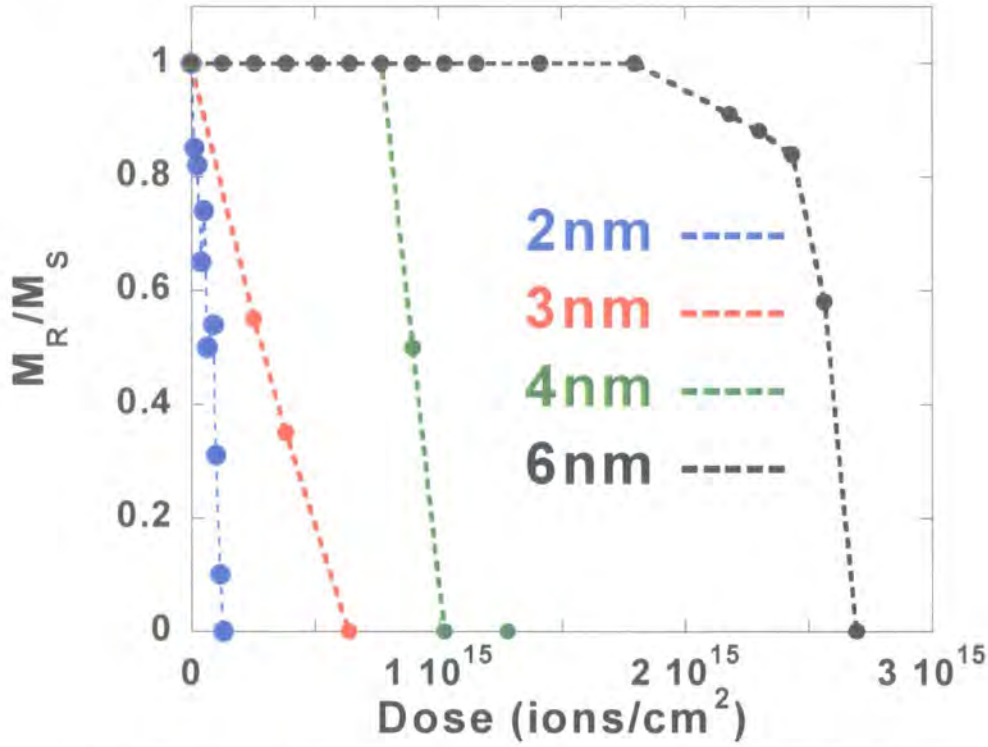

Fig 5.18: Experimentally measured M_R/M_S of irradiated $Ni_{81}Fe_{19}$/Au bilayers as a function of incident 30 keV Ga^+ ion irradiation.

The M-H loop remanence ratio is an important parameter for describing M-H loops. It describes how the sample magnetization behaves in an external field, and gives insight into the magnetization reversal process, and loop squareness. The remanence ratio is defined as M_R/M_S.

We define M_R as normalized magnetization at H = 0, and absolute magnetization, M_S as the sample saturation magnetization, i.e. the MOKE signal intensity when magnetization of each irradiated sample is saturated. Thin, t_{NiFe} = 2-3 nm layers exhibit a sharp decline in M_R/M_S at low fluences – Fig 5.18. This is similar to the dependence of H_c on dose for the same thickness samples. In the ultra-thin film limit, M-H loops become strongly inclined, even at very low ion doses ($D \leq 10^{13}$ ions/cm^2). At low ion doses, MOKE signals indicate that these samples retain

reasonable room temperature magnetic moment, but in the absence of applied field, the sample magnetization may not be uniformly aligned.

For thicker t_{NiFe} = 4 or 6 nm layers, loops exhibit perfect squareness up to intermediate fluences of $D = 7.7 \times 10^{14}$ ions/cm^2 and 1.79×10^{15} ions/cm^2 respectively. We surmise that M-H loops retain $M_R/M_S \sim 1$ until the combined intermixed regions at upper and lower interfaces extends over a similar width to t_{NiFe}. For example, formation of solid solutions of both Au-Fe and Au-Ni alloys has already been described by Tsaur [Tsaur 1981], by 100-300 keV Xe mixing of layered samples on SiO_2.

For thicker films, interfaces can become smeared, but a less ion-damaged region in the middle of the active NiFe layer, enables sample switching by easy domain wall motion. At remanence, these samples can still retain high magnetization. In more highly alloyed NiFe layers, with a presumed lower M_s than virgin NiFe, M-H loops become canted, and the M_R/M_S ratio can be tailored by controlled radiation doses. Representative M-H loops demonstrating this radiation-induced canting of M-H loops are shown in Fig. 5.19.

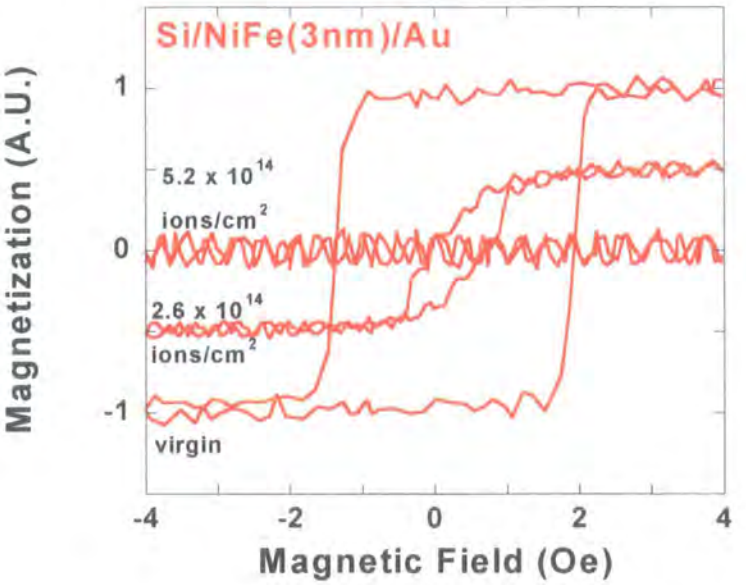

Fig 5.19: Experimentally measured M-H loops of a Si/$Ni_{81}Fe_{19}$(3nm)/Au bilayer as a function of incident 30 keV Ga^+ ion irradiation, indicating a dose induced modification of loop M_R/M_S ratio. M-H loop signal levels are normalized to the as deposited film.

5.5.5 $Ni_{81}Fe_{19}$/Au: H_k vs. Dose

Next, the response of hard axis saturation field to uniform irradiation is considered. Table. 5.3 demonstrates that the hard axis saturation field of uniformly sandwiched Si/NiFe/Au layers, of varied t_{NiFe}, scales linearly with increasing NiFe thickness – this relationship is plotted in Fig. 5.20.

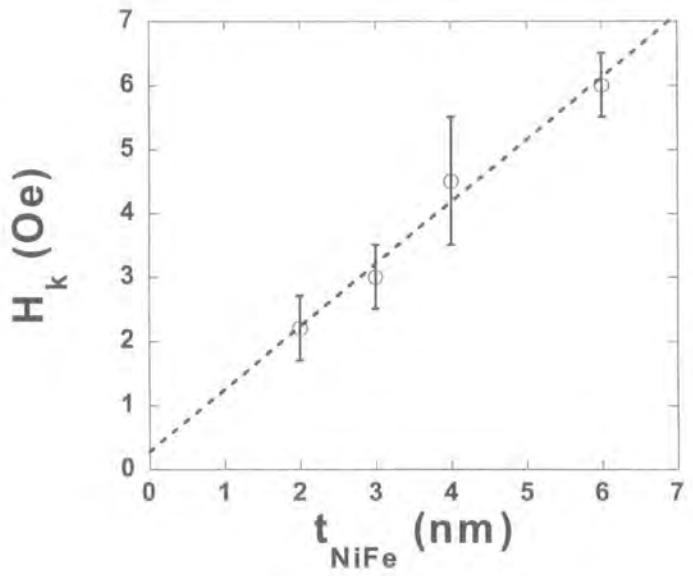

Fig 5.20: Uniaxial anisotropy field, H_k, plotted vs. NiFe thickness, for simultaneously grown Si/NiFe/Au bilayers. Trend line is a least squares fit.

Hard axis M-H loops are shown, with magnetization values normalized to the saturated MOKE signal values from the t_{NiFe} = 6 nm sample.

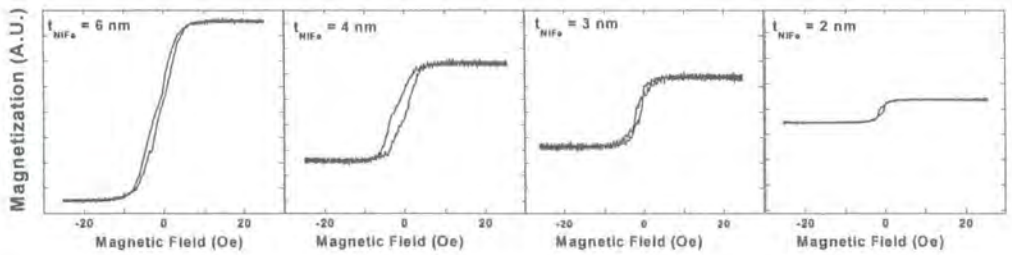

Additionally hard axis M-H loops for as-deposited films in the thickness range t_{NiFe} = 2-6 nm, are plotted in Fig. 5.20. A good uniaxial hard axis anisotropy field behaviour is shown. H_k scales linearly with t_{NiFe}, which is equivalent to scaling linearly with volume of magnetic material, up to t_{NiFe} = 6 nm.

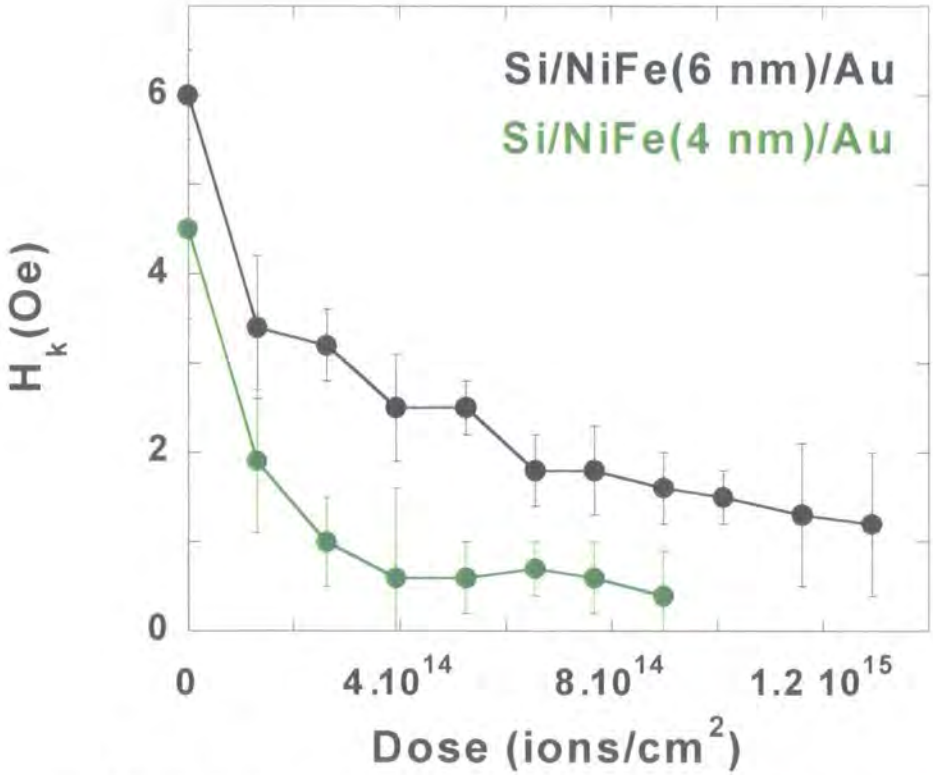

Fig 5.21: Hard axis anisotropy field, H_k, for t_{NiFe} = 6 nm (—●—) and 4 nm (—●—) layers, embedded between a 7 nm thick Au cap, and Si substrate, as a function of 30 keV Ga^+ ion irradiation.

Next, the hard axis anisotropy field response to controlled Ga^+ irradiation is considered. For the Si/NiFe(6nm)/Au sample, at a relatively low dose, $D = 1.3 \times 10^{14}$ ions/cm^2, there is a very sharp fall in the hard axis anisotropy field from 6.0 ± 0.5 Oe to 3.4 ± 0.8 Oe. At higher doses, a steady reduction in H_k with dose is measured, as the sample becomes increasingly isotropic. MOKE signal measurements suggest that the initial sharp reduction in H_k cannot be explained solely by a reduction in sample spontaneous magnetization.

Data for the Si/NiFe(4 nm)/Au sample follows the same trend under irradiation, as the t_{NiFe} = 6 nm film. We may consider the hard axis anisotropy field to be composed of a bulk or volume component, and a surface or interface component. A sharp initial reduction in H_k(Oe) at low dose may be associated with a relaxation of

stresses and magnetostrictive effects at interfaces, followed by a slower reduction in H_k at higher D due to reduction of anisotropy that may originate due to the sample volume. Both samples display a similar trend. Note that to within experimental error, the $t_{NiFe} = 6$ nm and $t_{NiFe} = 4$ nm data sets coincide, if normalized to film thickness.

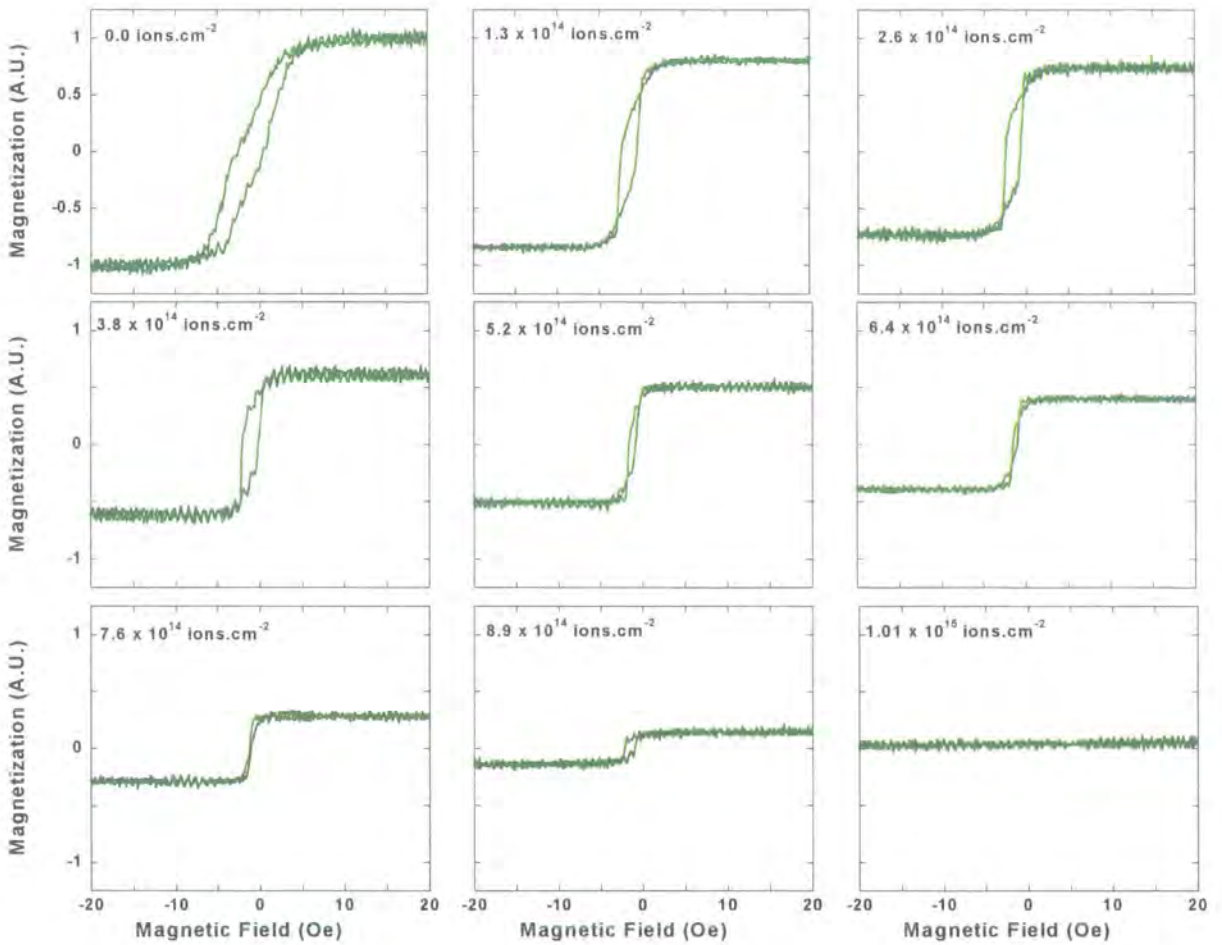

Fig 5.22: Representative hard axis anisotropy field M-H loops, for a Si/NiFe(4nm)/Au sample, as a function of Ga^+ irradiation. M-H loop signal levels are calculated w.r.t. the as-deposited reference film.

For the film thicknesses considered here, H_k is more sensitive to low ion doses than H_c or measured MOKE signal. This may help shed light on the issue of radiation induced sample amorphization.

5.6 Lateral Patterning

For either laboratory prototyping, or industrial applications, it is of interest to investigate the potential of FIB for patterning of laterally patterned magnetic buried nano-structures, as opposed to thin films.

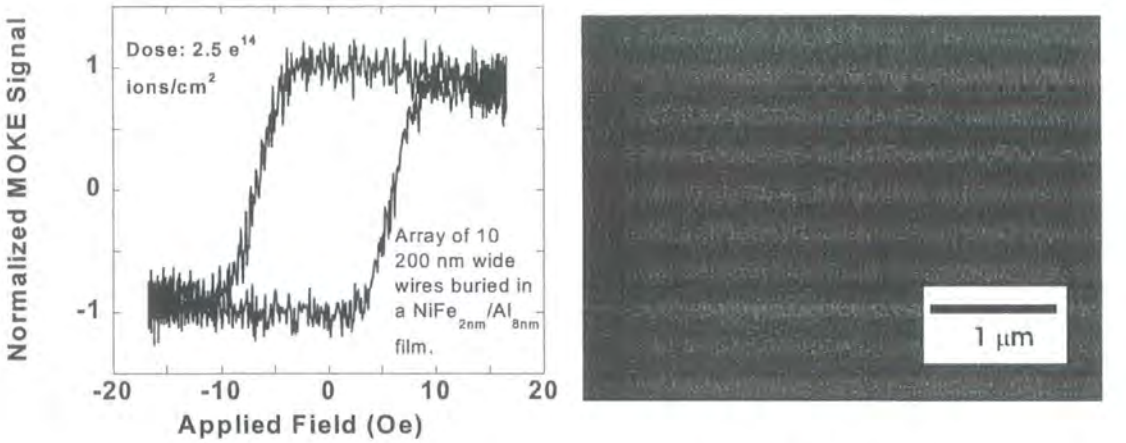

Fig 5.23: M-H loop for an array of 200 nm wide wires, buried under a protective Al capping layer, patterned by ion beam mixing. A FIB image of the magnetically patterned region is also shown – dark areas of the image correspond to regions of the Si/NiFe(2nm)/Al(8nm) sample exposed to a dose of 2.5×10^{14} ions/cm^2.

Fig. 5.23 shows a magnetic hysteresis loop for an array of 10 nominally 200 nm wide NiFe wires, of 2 nm thickness, embedded between a protective Al layer and Si substrate. Dark regions of the FIB image correspond to areas of the capped NiFe film exposed to a low dose of Ga^+ ions and therefore rendered superparamagnetic at room temperature. The wire centre-to-centre spacing was set at 450 nm.

The room-temperature M-H loop evidences very soft magnetic switching behaviour. $H_n \sim 4$ Oe, and $H_c \sim 6$ Oe, and the wire array becomes fully magnetically saturated at $\pm$ 10 Oe. The intercept of a linear fit to MOKE signal vs. t_{Al}, for a set of bilayers with t_{Al} = 4-16 nm, confirms that the NiFe layer is magnetically active to a thickness of 2.0 $\pm$ 0.5 nm. Assuming a $H_c \propto T/W$ relationship similar to planar

uncapped NiFe wires, (Section 4.5), a wire coercivity of ~40 Oe might reasonably be expected.

It has been experimentally demonstrated that at room temperature, when patterned NiFe element critical dimensions are reduced, and the threshold to superparamagnetic behaviour is neared, thermal fluctuations compete with the element shape anisotropy [Cowburn 2000], lowering the patterned element-switching field, such that a $H_c \propto 1/W$ trend is no longer observed [Uhlig 2004].

Further, upper and lower interfaces may cause a slight magnetic softening of the buried nanowires. Wire lateral profiles will have a different morphology in embedded nanowires as opposed to topographically defined wires, due to the ion beam mixing process. Lateral or radial straggling of 30 keV Ga^+ ions is estimated from TRIM to be < 10 nm in either Al or NiFe. However, taking into account dynamic processes and radiation induced displacement of recoiling Ni, Fe, Al, and Si atoms, it possible that some lateral ion beam mixing may occur on longer lengthscales to the calculated values.

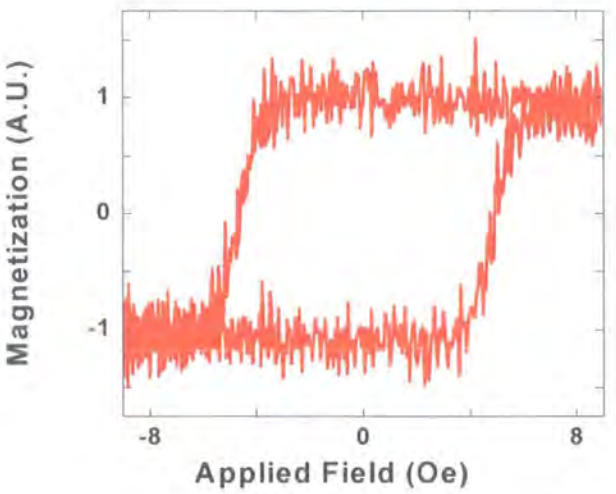

Fig 5.24: M-H loop for an array of 200 nm wide wires, buried under a protective Au capping layer, patterned by ion beam mixing. The parent film was Si/NiFe(2nm)/Au(7nm).

The Stoner-Wohlfarth model can therefore not explain wire-switching behaviour. Uhlig explained magnetic switching in 2.0 nm thick NiFe nano-lines by Arrhenius-Néel thermally activated behaviour. He found a wire activation volume of $1.25*W^2T$, very sensitive to random thermal fluctuations for $T \leq 3.5$ nm. His experimental and fitted values of H_c ~7.5 Oe for 200 nm wide wires mirror our results for Al or Au [Fig 5.24] overcapped wire arrays of the same nominal thickness and width. A M-H loop for 2 nm thick, 200 nm wide NiFe wires embedded between a Si substrate and an Au overlayer is shown in Fig. 5.24 (previous page), with H_n = 3.5 Oe, H_c = 5.0 Oe, and H_s = 5.5 Oe. A patterning dose of ~ 2×10^{14} ions/cm^2 was employed. Reproducible very soft bistable switching behaviour is evident.

Typically nanomagnet switching fields are controlled by lateral dimension modification, using for example electron beam lithography. Subtractive ion milling is also suitable for this task. Localised, quick, dry, low dose ion beam milling of a layered magnetic sample, can also facilitate tailoring of M-H loop shape for applications.

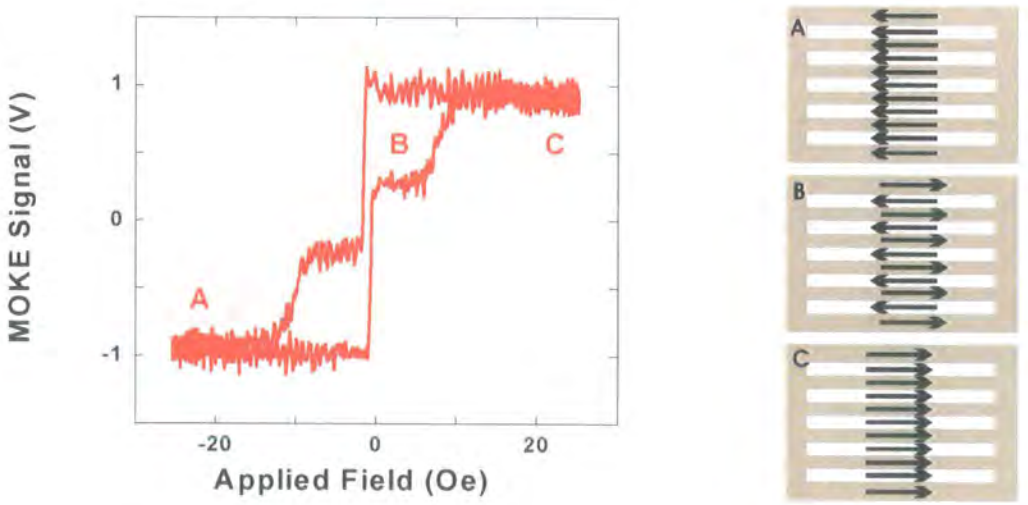

Fig 5.25: M-H loop for an array of 200 nm wide wires, embedded in a softened film, buried under a protective Al capping layer, patterned by ion beam mixing. The parent film was Si/NiFe(2nm)/Al(8nm). A schematic of magnetization orientation as the field is swept from –ve to +ve saturation of the system is shown.

Fig.5.25 describes the magnetization reversal processes of an array of buried 2 nm thick Permalloy nanowires, embedded in an artificially softened surrounding film, with two distinct switching transitions. $H_{c1} \pm 0.4$ Oe, and $H_{c2} \pm 8.5$ Oe, patterned into a parent film of $H_c = 2.2$ Oe. A patterning dose just below Φ was employed.

In principle, M-H loops with more switching transitions could be tailored, especially if a high moment film is employed. Lateral patterning of embedded magnetic nanostructures was performed with a 10-pA beam current, giving a slightly higher Φ (about a factor of 2), than the 3 nA ion beam, which was used for standard dose tests. The cause of this disparity is not well understood, but may be related to different energy transfer mechanisms between ions and target atoms at different beam currents. Further M-H loops of nanostructures patterned by FIB in sputtered Al(4nm)/NiFe(5nm)/Si bilayers are shown in Appendix. C. Controlled switching of wires, hexagons, and structures reversed by domain wall devices is demonstrated.

5.7 Discussion & Conclusions

Quenching of measured room-temperature ferromagnetism in buried $Ni_{81}Fe_{19}$ layers has been achieved at very low ion doses, ($\Phi = 8\times 10^{13}$ ions/cm^2). This very surprising result for in plane magnetized films is attributed to the atomic intermixing of interfacial atoms, caused by the dissipation of energy of incident ions in the target, much of which is localized at interfaces. We have modified the easy axis coercivity, hard axis anisotropy field, hysteresis loop remnant ratio, and M_s in a very controlled manner for in-plane magnetized ultra-thin capped films. In particular by ion beam induced intermixing at interfaces, samples with H_c as low as 0.1 Oe can be fabricated.

Ultrathin-capped films (of thickness ~ 2-5 nm) show a monotonic reduction in H_c with increasing ion dose, if the cap is still intact at Φ. H_c for unburied in-plane

magnetized films, drops for low to intermediate ion doses, but rises just prior to Φ. This coercivity peak is interpreted as domain wall pinning in a radiation thinned sample.

The hard axis saturation field H_k decreases with D in irradiated buried or unburied samples, but for the ultrathin samples studied a large reduction in H_k at low ion doses, means that H_k is reduced quicker than sample magnetization, as suggested by MOKE signal measurements. To my knowledge, no data of this type has been published for in-plane magnetized films. M-H loop remanence ratio falls as a function of ion fluence for bilayers when the active t_{NiFe} layer is of the order of 1-2 nm. Until the blurred interfaces of irradiated $Ni_{81}Fe_{19}$ bilayers are very close to meeting in the centre of the magnetically active layer, M_R/M_S retains a value close to unity. Further investigation into M-H loop M_R/M_S vs. dose, may be useful from an applications perspective.

We have shown that controlled Ga^+ ion beam irradiation at $Ni_{81}Fe_{19}$ interfaces or free surfaces results in different mechanisms for the quenching of measured room temperature ferromagnetism. The addition of a protective non-magnetic over capping layer between the vacuum and the thin film surface can lead to significantly faster magnetic FIB lithography of both thin films and magnetic structures of nanometre critical dimensions, if the ultrathin film thickness is of the order of the characteristic mixing length of the system. Kinetic energy of the projectile ions is transformed into internal excitation of the solid. Previously, studies of this nature were principally confined to high anisotropy, out of plane-magnetized systems, such as Co/Pt, Co/Pd or Fe/Pt. In unburied films, for $t_{NiFe} > \bar{i}_{SD}$, Ni and Fe atoms are radiation etched from the sample surface, and an increasing concentration of Ga atoms becomes implanted in the NiFe bulk, diluting the sample ferromagnetism. For $t_{NiFe} < \bar{i}_{SD}$, surface

sputtering is a dominant mechanism for quenching ferromagnetism, Ga atoms are stopped in the substrate, not implanted in the NiFe. However intermixing at the NiFe/substrate interface, as Ga^+ ions stream through the magnet/substrate interface enhancing the mobility of interfacial atoms, also needs to be considered.

If t_{NiFe} is of the order of the characteristic mixing length, λ, ferromagnetic quenching can be effected at very low ion doses, $\Phi < 10^{14}$ ions/cm^2. Clearly if the cap is too thick, it needs to be radiation thinned before Ga^+ ions, and displacement cascades penetrate to the depth of the active magnetic layer, making rapid magnetic patterning unfeasible. Further, if the cap is too thin it will be radiation etched prior to ferromagnetic quenching of the magnetic layer. In this manner thin capping layers can be used an agent for faster FIB patterning of ferromagnetic films. Our error function model and TRIM simulations show that in bilayers interfaces become progressively smeared as a function of ion dose. We note that mixing length scales, foreign atom concentrations, and resultant alloys are asymmetric at upper and lower interfaces.

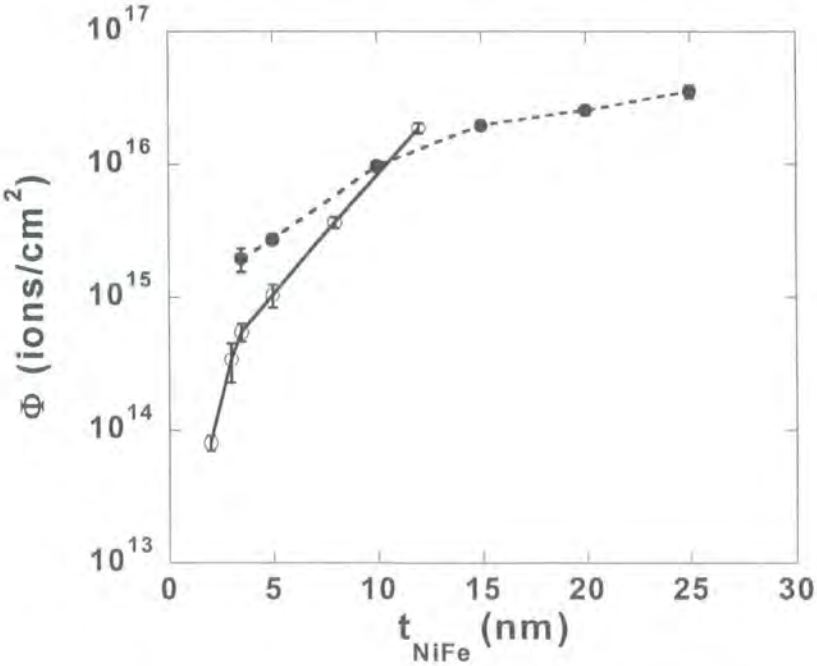

Fig 5.26: Experimentally determined critical ion dose, Φ, to quench measured room temperature ferromagnetic ordering at a free $Ni_{81}Fe_{19}$ surface [--•--], and in Si/$Ni_{81}Fe_{19}$(t_{NiFe})/Al(10nm) bilayers [—#—], as a function of t_{NiFe}.

Figure 5.26 summarizes experimentally determined Φ for $Si/Ni_{81}Fe_{19}$ and $Si/Ni_{81}Fe_{19}/Al$ samples. For unburied Permalloy films, it is clear that Φ does not vary linearly with t_{NiFe}. This is because surface sputtering, bulk implantation, and substrate/magnet intermixing are a function of t_{NiFe}, and may vary with increasing dose. A higher ion dose per unit volume is required to quench ferromagnetic ordering in the thicker films. For $t_{NiFe} < 10$ nm ferromagnetism is quenched at lower doses in the presence of an Al capping overlayer. Because buried NiFe films with low thickness, have a large proportion of Ni or Fe atoms near an interface, as t_{NiFe} tends to 0, there is a huge reduction in Φ with decreasing NiFe thickness. 30 keV Ga^+ ion beam irradiation of bilayers gives longer range intermixing compared to light ion species, and the degree of intermixing can be well controlled even at very low Ga^+ ion doses – this been shown by magnetometry measurements.

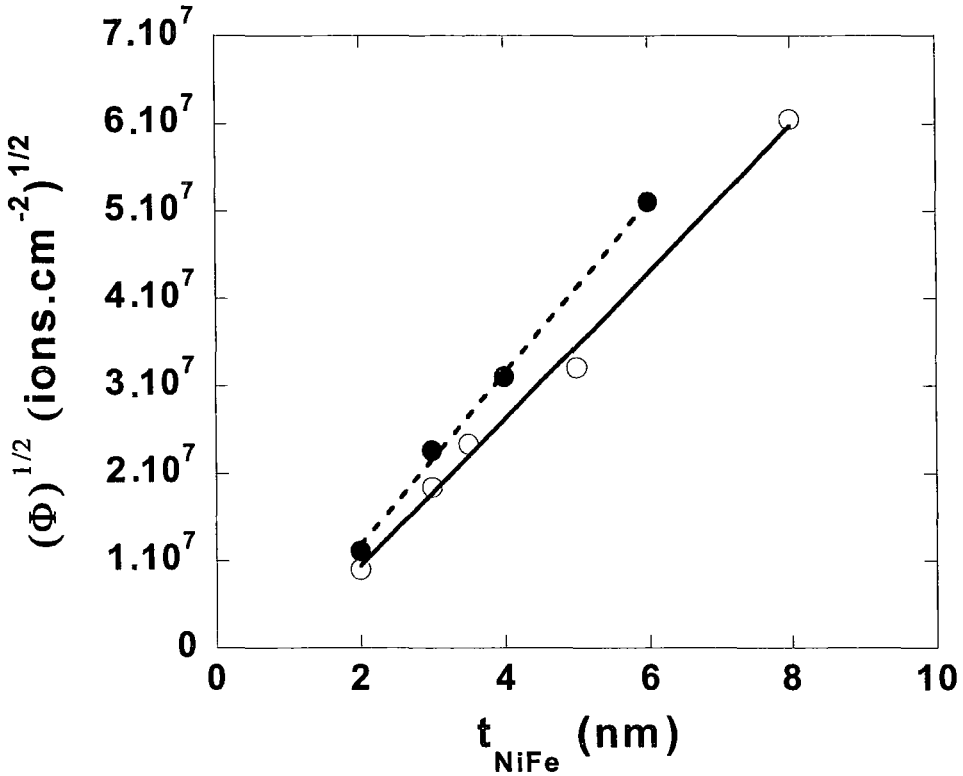

Fig 5.27: Experimentally determined critical ion dose, Φ, to quench measured room temperature ferromagnetic ordering in $Si/Ni_{81}Fe_{19}(t_{NiFe})/Al(10nm)$ [—o—], and in $Si/Ni_{81}Fe_{19}(t_{NiFe})/Au(7nm)$ bilayers [--•--], as a function of t_{NiFe}.

A linear relationship between $(\Phi)^{1/2}$ and t_{NiFe} is found [Fig 5.27], for both Al and Au overlayers. Because Al is lighter than Au, it is more given to long range intermixing than Au, and is radiation sputtered at a rate 4 times lower than Au. The ability to explain the ion induced magnetic patterning of thin-layered media by a square-root law is a significant finding. The error function method of modelling interface broadening employs similar square root behaviour. This law has been used to describe light ion mixing lengthscales of bilayers, [Tsaur 1979]. However to our knowledge it has never been applied to a radiation induced modification to magnetic properties of a layered sample.

It is predicted that in the context of ion patterning of layered magnetic media the following relation will hold:

$$\Phi \propto \sqrt{t_{bilayer}} \qquad [5.4]$$

where $t_{bilayer}$ is the magnetically active layer thickness.

This simple law should hold for PMA or in-plane magnetized systems, for light ion or FIB irradiation, for non-magnetic caps, or exchange biased systems, and for multiple layers, if some of the upper stack layers remain intact at Φ. It is a general expression, and should apply to most elements.

Low device throughput is a drawback of the FIB fabrication process, compared to electron beam lithography. The technique of FIB collisional intermixing affords the prospect of increased throughput of fabricated devices due to faster patterning rates, for thin in-plane magnetically oriented films. A reduction in stage drift, due to quicker critical cuts is an additional benefit. By selecting an appropriate combination of incident ion energy, capping thickness and species, and ferromagnet thickness, the effects of ion damage and defect injection on feature acuity may be reduced but not curtailed.

In the context of data storage, structure planarity is of paramount importance for read and write processes. Here we have demonstrated magnetic patterning at low ion doses (~1 incoming ion per every 250 magnetically active target atoms) where surface sputtering is expected to be slight. We observe that light capping elements are less given to surface sputtering making them potentially more suitable candidate for this type of application.

Buried magnetic nanowires were fabricated at low ion doses with Al and Au protective caps. Wires fabricated in this manner had low coercivity, due to superparamagnetic effects. Films patterned in this manner may be of use for some applications where a minimal demagnetising field, and hence switching field is needed for device operation. Wire edge-to-edge separation in these arrays was 250 nm. By reducing the wires edge-to-edge spacing, some insight into the lateral extent of ion beam mixing and cascading could be garnered.

Ion beam mixing is a solid-state process that permits controlled change in the composition and properties of the near surface properties of solids. The ability to tailor the coercivity, anisotropy, M_R/M_S and moment of capped samples due to atom displacement and alloying, in a controlled manner is potentially interesting, and may be a fruitful area for further investigations. Using FIB, the ion dose can be highly localized. Mixtures can be formed which would not usually be found in nature – i.e. systems that are not in thermal equilibrium. Some interesting implications and prospects for further work arise out of the results presented and discussed in this chapter including:

[I] The possibility to magnetically pattern stacks of in plane magnetized films, instead of a single NiFe layer.

[II] The prospect of patterning in plane magnetized layered films such as NiFe by light ion irradiation.

[III] The prospect of selectively writing ferromagnetism in layers of appropriate thickness and elemental composition by selective FIB writing. This would be quicker than trying to erase ferromagnetic ordering, as smaller surface areas of film would be written to. Patterning thicker magnetically active regions may circumvent issues associated with superparamagnetism.

[IV] By locally controlling ion dose exposures on either PMA or in-plane magnetized media, patterns can be fabricated with a wide range of switching fields. This could be accomplished at very low ion doses, and at high throughputs, and has obvious potential for commercial sensor applications. Figure 5.25 illustrates this proof of concept. Patterned in plane magnetized thin films with higher moment, would produce higher switching fields.

Reiterating, the prospect of magnetic patterning at lower Φ, than unburied ferromagnetic films, and the prospect of a planar topology may have attractive industrial applications. We have experimentally demonstrated a linear relationship, $\Phi \propto \sqrt{t_{bilayer}}$, that should be extensible to FIB and light ion magnetic patterning of most layered systems. For in-plane magnetized layered films, coercivity, hard-axis anisotropy field, remanence ratio, and saturation magnetization can be locally tailored by FIB irradiation.

5.8 References

[Aign 1999] T. Aign, P. Meyer, S. Lemerle, J. P. Jamet, J. Ferré, V. Mathet, C. Chappert, J. Gierak, C. Vieu, F. Rousseaux, H. Launois, H. Bernas, Phys. Rev. Lett. **81,** 5656 (1999)

[Baglin 1997] J. E. E. Baglin, M. H. Tabacniks, R. Fontana, A. J. Kellock, T. T. Bardin, Mat. Sci. For. **248**, (1997)

[Bernas 2003] H. Bernas, J.-Ph. Attané, K.-H.Heinig, D. Halley, D. Ravelosona, A. Marty, P. Auric, C. Chappert, Y. Samson, Phys. Rev. Lett. **91,** 077203 (2003)

[Cai 2004] M. Cai, T. Veres, S. Roorda, F. Schiettekatte, R. W. Cochrane, J. Appl. Phys. **95**, 1996 (2004)

[Carcia 1990] P. F. Carcia, S. I. Shah, W. B. Zeper, Appl. Phys. Lett. **56,** 2345 (1990)

[Carter 2001] G. Carter, J. Phys. D. **34**, R1 (2001)

[Chappert 1998] C. Chappert, H. Bernas, J. Ferré, V. Kottler, J. P. Jamet, Y. Chen, E. Cambril, T. Devolder, F. Rousseaux, V. Mathet, H. Launois, Science **280**, 1919 (1998)

[Chikazumi 1986] S. Chikazumi, S. H. Charap, "*Physics of Magnetism*," Krieger, John Wiley & Sons, Florida (1986)

[Corb 1985] B. W. Corb, Rev. B **31,** 2521 (1985)

[Cowburn 2000] R. P. Cowburn, D. K. Koltsov, A. O. Adeyeye, M. E. Welland, J. Appl. Phys. **87**, 7082 (2000)

[Demokritov 2003] S. O. Demokritov, C. Bayar, S. Poppe, M. Rickart, J. Fassbender, B. Hillebrands, D. I. Kholin, N. M. Kreines, O. M. Liedke, Phys. Rev. Lett. **90,** 097201 (2003)

[Devolder 2001] T. Devolder, J. Ferré, C. Chappert, H. Bernas, J.-P. Jamet, V. Mathet, Phys. Rev. B **64,** 064415 (2001)

[Devolder 2000/1] T. Devolder, C. Chappert, V. Mathet, H. Bernas, Y. Chen, J.-P. Jamet, J. Ferré, J. Appl. Phys. **87**, 8671 (2000)

[Devolder 2000/2] T. Devolder, Phys. Rev. B **62,** 5794 (2000)

[Devolder 1999] T. Devolder, Y. Chen, H. Bernas, C. Chappert, J.-P. Jamet, J. Ferré, E. Cambril, Appl. Phys. Lett. **74**, 3383 (1999)

[Eklund 1991] E. A. Eklund, R. Bruinsma, J. Rudnick, R. Stanley Williams, Phys. Rev. Lett. **67,** 1759 (1991)

[Fassbender 2004] J. Fassbender, D. Ravelosona, Y. Samson, J. Phys. D: Appl. Phys. **37**, R179 (2004)

[Hubert 1998] A. Hubert, R. Schäfer, "*Magnetic Domains – The analysis of magnetic microstructures*," Springer-Verlag, Berlin Heidleberg, 1998, p 46

[Hyndman 2001] R. Hyndman, P. Warin, J. Gierak, J. Ferré, J. N. Chapman, J. P. Jamet, V. Mathet, C. Chappert, J. Appl. Phys. **90**, 3843 (2001)

[Johnson 1996] M. T. Johnson, P. J. H. Bloemen, F. J. A den Broeder, J. J. de Vries, Rep. Prog. Phys. **59**, 1409 (1996)

[Juraszek 2002] J. Juraszek, J. Fassbender, S. Poope, T. Mewes, B. Hillebrands, D. Engel, A. Kronenberger, A. Ehresmann, H. Schmoranzer, J. Appl. Phys. **91**, 6896 (2002)

[Kaminsky 2001] W. M. Kaminsky, G.A.C. Jones, N. K. Patel, W. E. Booij, M. G. Blamire, S. M. Gardiner, Y. B. Xu, J. A. C. Bland, Appl. Phys. Lett. **78**, 1589 (2001)

[Kelly 1994] D. M. Kelly, I. K. Schuller, V. Korenivski, K. V. Rao, K. M. Larsen, J. Bottiger, E. M. Gyorgy, R. B. van Dover, Phys. Rev. B **50,** R3841 (1994)

[Mayer 1981] J. W. Mayer, B. Y. Tsaur, S. S. Lau, L-S. Hung, Nucl. Instr. Meth. **182/183**, 1 (1981)

[McGrouther 2004] D. McGrouther, J. N. Chapman, F. W. M. Vanhelmont, J. Appl. Phys. **95**, 7772 (2004)

[Owen 2002] N. Owen, H.Y. Yuen, A. Petford-Long, IEEE Trans. Magn. **38**, 2553 (2002)

[Ozkaya 2002] D. Ozkaya L, R. M. Langford, W. L. Chen, A. K. Petford-Long, J. Appl. Phys. **91**, 9937 (2002)

[Park 2004] C. M. Park, J. A. Bain, T. W. Clinton, P. A. A. van der Heijden, T. J. Klemmer, Appl. Phys. Lett. **84**, 3331 (2004)

[Park 2002] C. M. Park, J. A. Bain, IEEE Trans. Magn. **38**, 2237 (2002)

[Parkin 1999] S. S. P. Parkin, K. P. Roche, M. G. Samant, P. M. Rice, R. B. Beyers, R. E. Scheuerlein, E. J. O'Sullivan, S. L. Brown, J. Bucchigano, D. W. Abraham, Yu Lu, M. Rooks, P. L. Trouilloud, R. A. Wanner, W. J. Gallagher, J. Appl. Phys. **85**, 5828 (1999)

[Rettner 2002] C. T. Rettner, S. Anders, J. E. E. Baglin, T. Thomson, B. D. Terris, Appl. Phys. Lett. **80**, 279 (2002)

[Reynolds 1981] G. W. Reynolds, A. R. Knudson, C. R. Gossett, Nucl. Instr. Meth. **182/183**, 179 (1981)

[Reyntjens 2001] S. Reyntjens, R. Puers, J. Micromech. Microeng. **11**, 287 (2001)

[Sigmund 1969] P. Sigmund, Phys. Rev. **184**, 383 (1969)

[Sigmund 1981] P. Sigmund, A. Gras-Marti, Nucl. Instr. Meth. **182/183**, 25 (1981)

[Sugimoto 1990] Y. Sugimoto, M. Taneya, H. Hidaka, K. Akita, J. Appl. Phys. **68**, 2392 (1990)

[Talmadge 2004] J. M. Talmadge, J. Gao, M. P. Riley, R. J. Roth, S.-O. Kim, J. G. Eden, F. A. Pudonin, I. V. Mel'nikov, Appl. Phys. Lett. **84**, 4197 (2004)

[Terris 2000] B. D. Terris, D. Weller, L. Folks, J. E. E. Baglin, A. J. Kellock, H. Rothuizen, P. Vettiger, J. Appl. Phys. **87**, 7004 (2000)

[Train 1999] C. Train, P. Beauvillain, V. Mathet, G. Pénissard, P. Veillet, J. Appl. Phys. **86**, 3165 (1999)

[Tsaur 1979] B. Y. Tsaur, Z. L. Liau, J. W. Meyer, Appl. Phys. Lett. **34**, 168 (1979)

[Tseng 2004] A. A. Tseng, J. Micromech. Microeng. **14**, R15, (2004)

[Tsaur 1981] B. Y. Tsaur, S. S. Lau, L. S. Hung, J. W. Mayer, Nucl. Instr. Meth. **182/183**, 67 (1981)

[Uhlig 2004] W. C. Uhlig, J. Shi, J. Appl. Phys. **95**, 7033 (2004)

[Vaz 2001] C. A. F. Vaz, G. Lauhoff, J. A. C. Bland, B. D. Fulthorpe, T. P. A. Hase, B. K. Tanner, S. Langridge, J. Penfold, J. Magn. Magn. Mater. **226**, 1618 (2001)

[Vieu 2002] C. Vieu, J. Gierak, H. Launois, T. Aign, P. Meyer, J. P. Jamet, J. Ferré, C. Chappert, T. Devolder, V. Mathet, H. Bernas, J. Appl. Phys. **91**, 3103 (2002)

[Warin 2001] P. Warin, R. Hyndman, J. Gierak, J. N. Chapman, J. Ferré, J. P. Jamet, V. Mathet, C. Chappert, J. Appl. Phys. **90**, 3850 (2001)

[Weller 2000] D. Weller, J. E. E. Baglin, A. J. Kellock, K. A. Hannibal, M. F. Toney, G. Kusinski, S. Lang, L. Folks, M. E. Best, B. D. Terris, J. Appl. Phys. **87**, 5768 (2000)

[Wernsdorfer 1997] W. Wernsdorfer, K. Hasselbach, A. Benoit, B. Barbara, B. Doudin, J. Meier, J.-Ph. Ansermet, D. Mailly, Phys. Rev. B **55**, 552 (1997)

[Woods 2002] S. I. Woods, S. Ingvarsson, J. R. Kirtley, H. F. Hamann, R. H. Koch, Appl. Phys. Lett. **81**, 1267 (2002)

[Xiong 2001] G. Xiong, D. A. Allwood, M. D. Cooke, R. P. Cowburn, Appl. Phys. Lett. **79**, 3461 (2001)

[Ziegler 1985] J. Ziegler, J. Biersack, U. Littmark, "*The stopping of ions in matter*," Pergamon, New York, 1985; SRIM code (http://www.srim.org)

Chapter 6. Domain Wall Propagation and Pinning

6.1 Introduction

Controlled nucleation and propagation of head-to-head domain walls in laterally confined FIB patterned NiFe wire structures of complex planar geometries is treated. Section 6.2 treats some recent experimental findings concerning domain walls in the literature. A brief study of domain wall nucleation in ferromagnetic pads of low coercivity, H_c, is presented in Section 6.3 followed by experimental detail on injection mechanisms into elongated narrow wires. Subsequent domain wall (DW) propagation and annihilation mechanisms are treated.

Once it is technologically feasible to control the geometry of ferromagnetic structures on the nanoscale, it is possible to control the position of domain walls to sub-micron precision. For complex planar nanowire systems, it is possible for a specific field history or sequence to position and propagate domain walls to a high degree of accuracy, for both fundamental investigations and possible applications. In Section 6.4 the switching of rounded L-shaped continuous wire structures by controlled domain wall motion around a 90° corner is described.

The study of DW propagation is closely related to the study of varying energy landscapes and pinning sites, such as grain boundaries, defects, edge roughness, sample thickness inhomogeneity, and dislocations. Domain wall trapping has also been demonstrated at interfaces. Thus a study of domain wall propagation into and from artificial wedge shaped DW trapping sites with nominal depths from 35-125 nm is presented - Section 6.5, including quantitative experimental results for DW depinning field as a function of trap depth. Some conclusions are drawn in Section 6.6.

6.2 Literature

6.2.1 Overview

The propagation fields, velocity, and structure of magnetic domain walls were initially predominately studied in thin films, either experimentally [Konishi 1971], [Patton 1975], or computationally [Hubert 1988] following from the study of magnetic domain walls travelling in elongated iron whiskers [Sixtus/Tonks 1931]. Some recent advances in the experimental study of domain walls and domain configurations include the observation of domain wall motion with sub nanometre resolution (essentially at an atomic length scale) in garnets by Hall Probe [Novoselov 2003], magnetic force microscopy (MFM) tip stray field induced domain wall displacement [Zhu 2002], and the direct experimental observation of vortex core type domain formations in 50 nm thick NiFe elements [Shinjo 2000]. Spin polarized scanning tunnelling microscopy, has also been employed to map the in-plane and out of plane magnetization of Fe nano-islands in the vortex configuration to sub 10 nm resolution [Wachowiak 2002].

The properties of domain walls change with the geometry of the local environment. Williams revealed the change in domain configuration in iron as a result of surface scratches and non-magnetic inclusions as early as the nineteen-fourties [Williams 1949]. The interaction of domain walls with complex magnetic wire morphology is particularly interesting in systems such as the nano point-contact. For instance, magneto-resistance of up to 280 % was recently measured at room temperature in Ni atom scale point contacts [García 1999], being quantitatively explained in the context of reduced domain wall dimensions below the Bloch or Néel length by Bruno, leading to ballistic effects [Bruno 1999].

6.2.2 Spatially resolved domain Wall Experiments

Pinning, propagation, and nucleation processes of domain walls were extensively investigated in ultra-thin Fe samples [Cowburn 1998], only 10 ML thick. With the advent of enhanced lithographic techniques it is possible to engineer nanoscale magnetic structures in 3 dimensions, and therefore to engineer the switching mechanism. Ono et al. described the trapping of a single head-to-head domain wall about a notch in a submicrometer NiFe(200 Å)/Cu(100 Å)/NiFe(50 Å) wire, measured by the giant magnetoresistance (GMR) effect [Ono 1998].

Much fundamental work has also been carried out on the field-induced displacement of walls in high anisotropy Co/Pt systems, by polar Kerr effect microscopy. Magnetic force microscopy (MFM) experiments, conducted in vacuum, are now capable of detecting sub-micron head-to-head domain wall displacements in NiFe samples as thin as 5 nm. Gomez and co-workers [Gomez 1999] recently used MFM to investigate switching in many different Permalloy element aspect ratios as a function of applied field. Lorentz microscopy, in which electrons are deflected as they pass through thin film samples deposited on electron transparent membranes, is another technique for studying domain wall configurations in different structure geometries [Kirk 1999]. Wernsdorfer [Wernsdorfer 1997] detected the pinning of walls in nickel nanowires of sub 100 nm diameter, using a niobium micro-SQUID device. Advances in lithographic techniques make possible the positioning of electrical contacts to sub-micron accuracy for domain wall displacement and switching experiments characterised by I-V measurement techniques [Himeno 2003]. Kläui has been able to locally investigate spin polarized current domain wall displacement in a 1 μm wide ring structure with 8 contact wires [Kläui 2003/1]. He attributed current assisted sub-micron displacements of a single domain wall to spin-torque effects.

6.2.3 Time Dependent Domain Wall Experiments

Many time resolved domain wall studies have been performed in Co/Pt films and nanostructures, as lower domain wall velocities make observation more practible. In this manner, domain wall velocities as a function of wire width and periodic edge patterns have been measured [Cayssol 2004] for ultra-thin Co/Pt wires. In tri-layer structures [Ono 1999], the GMR effect was utilised to elucidate the switching mechanism mediated by an individual domain wall in a NiFe wire at low temperature (100 K), yielding an experimentally determined damping parameter, $\alpha = 0.63$.

Using a high-resolution Kerr effect system, Atkinson et al. successfully isolated an individual domain wall in different positions of a 2-corner planar NiFe wire. Domain wall velocities in different parts of the structure were probed. Current pulses were applied by micro-strip line, and wall velocities up to 1500 ms^{-1} were observed [Atkinson 2003], giving a damping constant comparable to virgin thin film studies. This prompted Nakatani et al. to suggest that edge roughness in such nanoscale structures could actually enhance domain wall velocity, above the theoretical Walker limit, by acting as an additional channel for energy dissipation from a system, and off-putting the onset of domain wall oscillation, and the formation of vortex type wall configurations until higher Walker fields [Nakatani 2003].

6.2.4 Domain Wall Injection

Nucleation pads of relatively large lateral dimensions (~μm) relative to a wire afford a technique to artificially introduce domain walls into nano-wires for experiment, at applied fields below the wire critical nucleation field. Several groups have utilized domain wall injection pads, as a domain wall source to perform transport, propagation, and pinning studies on magnetic domain walls. One of the first examples of this kind of experimental geometry is the work of Fournel et al. in

samples of (CoNi/Pt) defined by electron beam lithography [Fournel 1998]. The technique of controlling magnetization reversal of a continuous wire structure, by field mediated domain wall reversal was extended to 150 nm wide NiFe wires investigated by GMR [Shigeto 1999], with MFM [Yokoyama 2000] and MOKE subsequently performed [Lee 2000]. A variety of pad geometries (circular, square, diamond were investigated [Shigeto 2000] in the GMR measurement of trilayer structure switching. Wunderlich also used an area of low coercivity as a domain wall reservoir in hall cross experiments [Wunderlich 2001].

Additionally the ability to engineer the position of magnetic domain walls and the internal spin structure of nanomagnets has become increasingly important in a host of recent domain wall displacement experiments in which domain wall motion is either induced or assisted by spin polarised current [Tsoi 2003][Vernier 2004]. For example this method has been used to introduce domain walls into spin valves 0.3 μm wide, placed within coplanar wave-guides, for pulsed current domain wall displacement investigations [Lim 2004].

6.3 Domain wall injection & Propagation

Elongated NiFe wires of submicron thickness and width are typically single domain at remanence, with spins aligned parallel to wire sides due to shape anisotropy. Magnetization reversal in these structures of high aspect ratio is typified by the expansion of pseudo-end domains as a function of applied field (where spins tend to align parallel to the wire ends, orthogonal to the long easy axis), followed by a rapid domain wall propagation event, and complete magnetic reversal of the structure [Chapter 4]. Good fabrication tolerance is required to ensure that any barriers to DW propagation inherent in the fabrication process, such as edge roughness, pose a

smaller energy barrier than the threshold field energy needed for wire switching. Micromagnetic calculations predict that for a perfect symmetrical rectangular element modelled at 0K, magnetization reversal will be triggered from both ends of the wire simultaneously, leading to eventual meeting of domain walls at the wire centre and the possibility of complex 360° domain wall structures forming [Zheng 2002].

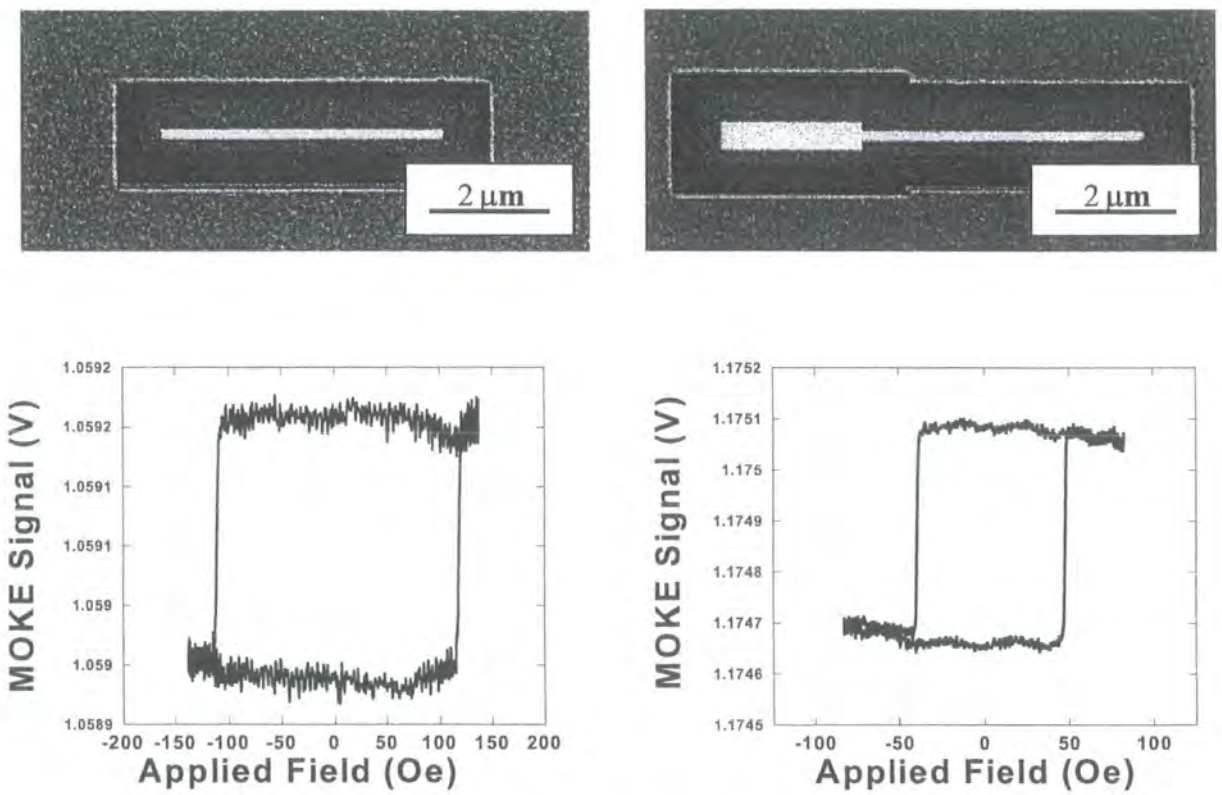

Figure 6.1: Hysteresis loops for a 200 nm wide wire, and an identical continuous wire attached to a low coercivity domain wall injection pad

In Fig. 6.1 standard wire reversal occurs at H_c = 113 Oe, for a 6 μm long, 200 nm wide flat-ended wire, patterned in 5 nm thick NiFe, with a 27 Hz sinusoidally varying applied field applied parallel to the wire easy axis. Sharp switching transitions are evidence of a single domain magnetization reversal process, unhindered by pinning centres, occurring from one or few nucleation centres. This switching field can be engineered by modifying wire aspect ratio or shape, as discussed in Chapter 4.

Consider a similar 200 nm wide wire, patterned in the same NiFe film, with a rectangular pad of material (dubbed a "domain wall injection pad"), of length 3μm, and width 600 nm attached to one end. This lower aspect ratio structure [5:1], relative to a wire of aspect ratio [30:1], has a measured switching field of H_c = 44 Oe. The sharp transitions on the hysteresis loop, which was taken with the MOKE spot over both pad and wire is evidence of a sudden switching transition. With a wire of suitable dimensions connected to the pad, a domain wall travels from the pad, down the wire, where it is annihilated at the wire end, resulting in full switching of the output wire.

Domain wall motion occurs in the direction of applied field. Magnetization seeks to align itself with the applied field, and this re-alignment is affected by the propagation of the domain wall boundary. For focused ion beam (FIB) milled samples of this geometry, domain walls propagate to the wire end at one discrete field value, at a field value above the intrinsic potential barrier posed by the edge roughness of wires. By modifying the geometry of wire ends with a domain wall injection pad, not only can the reversal field and mechanism for magnetization reversal be engineered, the initial reversal event can be localized to one wire end. Thus the direction of magnetization reversal by field controlled domain wall propagation can be controlled. Domain wall injection pad aspect ratios were investigated – in many experiments it is desirable to isolate domain walls in an experimental system at low propagation fields, H_p, compared to the nucleation field of a standard wire, H_n. Fig. 6.2 indicates that for fixed length, L, 3 μm pads, as a domain wall pad width, W, is increased, the field at which magnetization reversal starts, H_n, drops dramatically, tending towards field values consistent with thin-film switching behaviour. Data was taken from magnetic hysteresis loops of separate structures fabricated under uniform conditions.

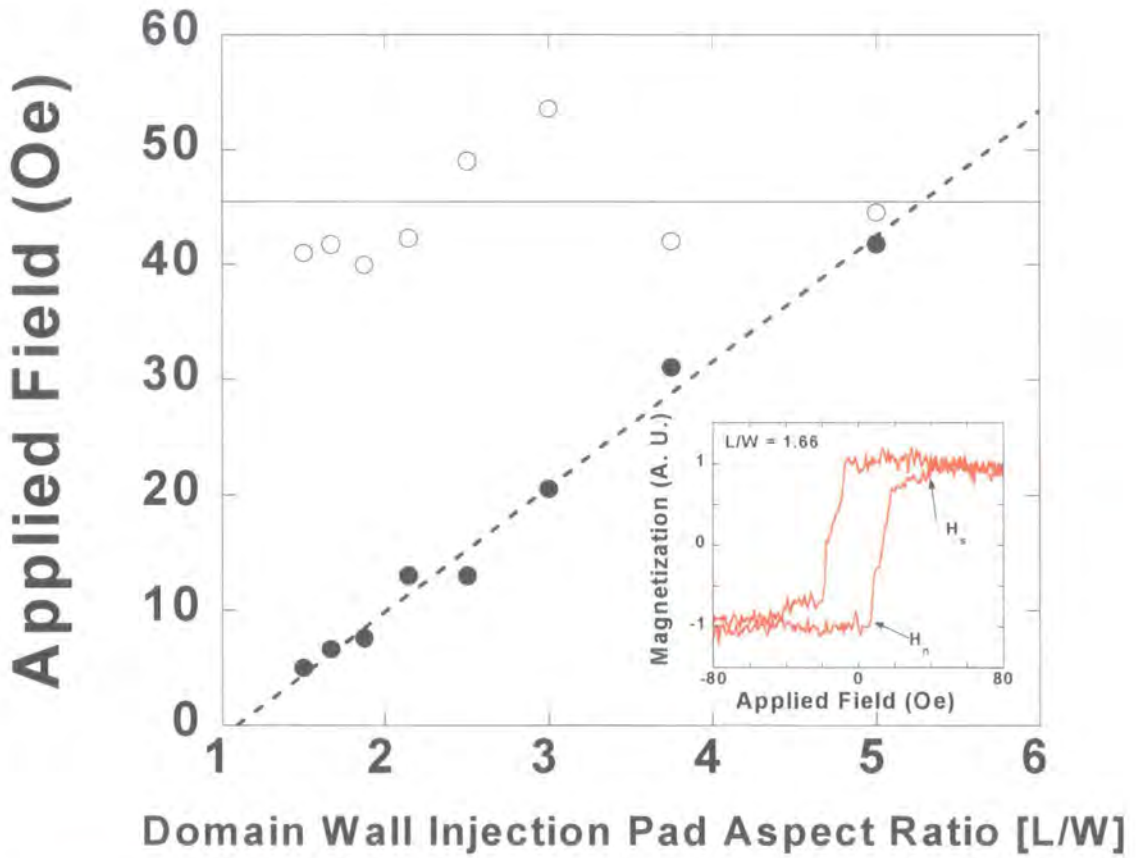

Figure 6.2: The measured nucleation field, H_n – –●– –, and saturation field, H_s ——○——, for a fixed length (3 μm) domain wall injection pad as pad width is varied from 600 nm to 2 μm. Data is explained with linear trend lines. Inset is a M-H loop for 1.8 μm wide, 3.0 μm long pad.

H_n was measured at 5.5 ± 0.5 Oe for an 1800 nm wide pad. However, H_s, the field value at which a domain wall injection pad is magnetically saturated in the opposing direction, and the minimum field at which domain wall injection into an output wire has been observed remains invariant. (Experimental scatter in H_s is attributed to defects in some samples.)

As the pad aspect ratio tends to unity, and the pad lateral dimension tends from an elongated shape towards a square-like geometry, the magnetization reversal mechanism in the pad is no longer dominated by domain wall motion, and magnetization reversal can start at very low applied fields. However, elements do not become fully saturated in the opposing direction until field values of typically above

40 Oe. As the pad width is decreased, the pad aspect ratio increases, and a magnetization reversal mode more consistent with sudden domain wall nucleation and propagation is apparent: H_n and H_s converge, and a magnetic reversal of the element at a single discrete field value is evident, with square M-H loops.

The switching pattern observed in Fig. 6.2 is similar to that described by Zhu, [Zhu 2002], in arrays of e-beam patterned sub-micron Permalloy elements. He observed that for large aspect ratio elements (>4:1) magnetization reversal occurs at discrete switching fields, between bistable states with magnetization principally oriented parallel to the wire long axis. For intermediate aspect ratio elements (≤4:1) the magnetization reversal took place by a two-step process with two characteristic switching fields.

Localized MOKE measurements on single wires with pad indicate that injection of a domain wall into the output wire occurs only after the pad is fully saturated in the appropriate direction. An injection pad geometry of 600 nm × 3000 nm was used here. This geometry yields reproducible domain wall injection fields, due to a reproducible switching mechanism.

6.4 Domain wall corner structures

For ferromagnetic wire systems with complex planar geometry, systems can be engineered to be mono-domain at remanence, see for example [Kläui 2003/2]. The preferred magnetization direction of the wire structures presented herein is parallel to the wire edge.

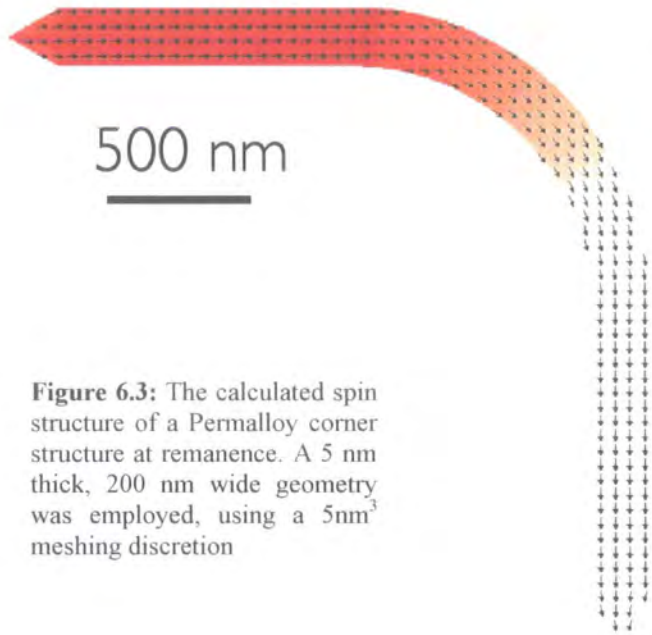

Figure 6.3: The calculated spin structure of a Permalloy corner structure at remanence. A 5 nm thick, 200 nm wide geometry was employed, using a $5nm^3$ meshing discretion

For example, Figure 6.3 shows the calculated spin orientation of a continuous planar corner, similar to the geometries studied in the chapter. Magnetization is aligned parallel to wire sides. Therefore the injection and propagation of domain walls can be performed using a rotating magnetic field in the X-Y plane. H_x and H_y are separated by a $\pi/2$ phase separation. The propagation field of walls in patterned wires, H_p, is therefore not limited to fields above the domain wall injection field, H_{inj}, as was the case in Section 6.3. By using an experimental geometry with a smoothly rounded corner, in a 27 Hz anti-clockwise rotating field, H_y can inject a DW into a wire, and H_x can propagate the wall along an output wire at low field.

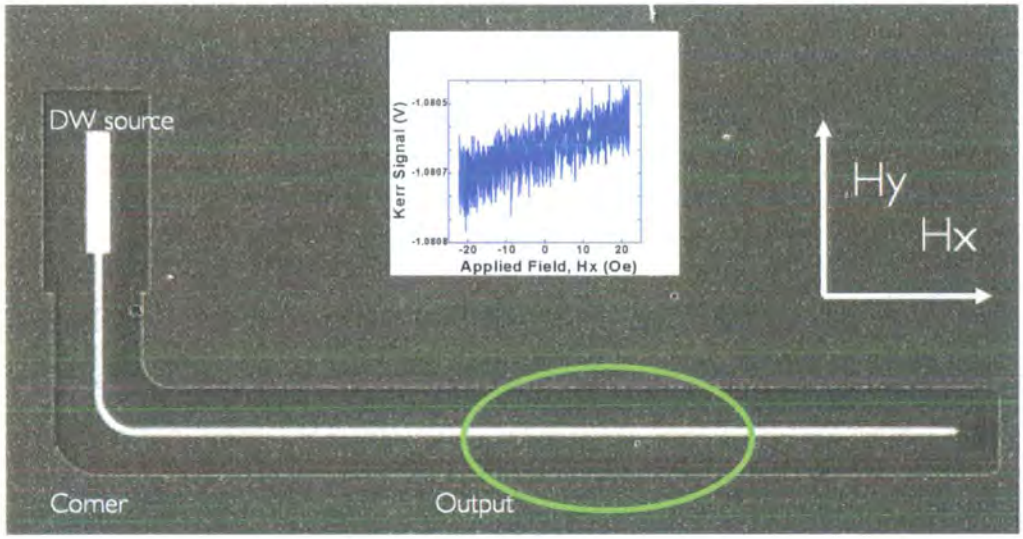

Figure 6.4: Domain wall injection pad structure (H_y = 47 Oe) with a smoothly rounded corner, and output arm (H_x = 35 Oe). A green ellipse indicates the MOKE spot position during averaging of the inset MOKE trace, which indicated no magnetization reversal of the output wire for the field profile applied.

Fig. 6.4. shows a structure consisting of a domain wall injection pad oriented parallel to the y-axis, linked to a 3 μm arm of wire width 200 nm. Samples are continuous, and the arm in which the domain wall is injected is linked to the orthogonal output arm by a smoothly rounded corner with an inside radius of curvature of 500 nm. For the 27 Hz rotating field profile applied shown in Fig. 6.4., i.e. H_y = 47 Oe, H_x = 35 Oe, no DW is injected into the system, because $H_y < H_{inj}$. The inset of Fig. 6.4 shows the background hysteresis loop measured on the output arm. No switching is observed at the output wire.

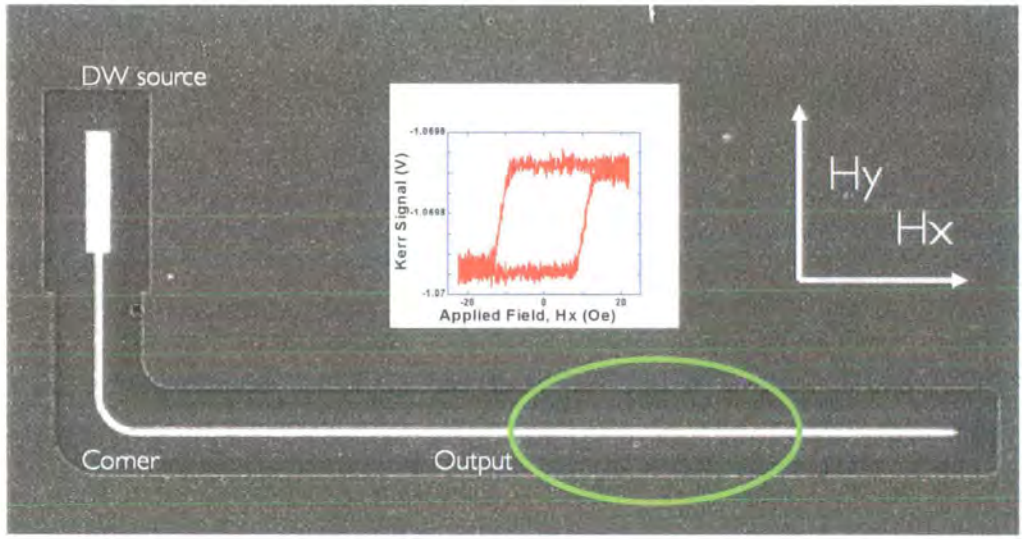

Figure 6.5: Domain wall injection pad (H_y = 53 Oe) structure with a smothly rounded corner, and output arm (H_x = 35 Oe). A green ellipse indicates the MOKE spot position during averaging of the inset M-H loop, which indicates reproducible switching of the output wire.

It is important that the chirality of the applied field profile matches the direction of DW propagation through a system – thus for the structures under consideration here, an anti-clockwise rotating field is applied. Fig.6.5 shows the switching behaviour of the structure investigated in Fig. 6.4, with $H_y > H_{inj}$. If a larger H_y rotating field component is employed, 53 Oe for the structure investigated, magnetization reversal is initiated in the pad of low coercivity material. It is then injected into the continuous wire, where it propagates to the corner. With no component of external field in the x-direction, the wall remains at the corner. By

applying a moderate H_x – low enough to preserve wire magnetization parallel to wire sides in the part of the experimental structure oriented along the y-axis, the DW moves from the corner, and propagates along the output to the wire end.

A measured MOKE signal level of 250 μV is consistent with MOKE signal levels expected from switching of a 200 nm wide wire. This indicates the output wire fully reverses on each DW injection event. Importantly, full switching of the output wire occurs by 13 Oe. Therefore experiments can be performed in the long output wire, at lower fields than those possible when using solely a DW injection pad and output wire (H_{inj} ~ 40 Oe). In the absence of a domain wall injection pad, the nucleation field of a corner structure was measured at ~ 140 Oe in a clockwise rotating field.

We now consider the rotating field vector applied to a corner structure in more detail. The absolute field vector, $\overline{H}_{total}$ may be expressed as:

$$\overline{H}_{total} = \overline{H}_x + \overline{H}_y = H_{x0}\cos\omega t + H_{y0}\sin\omega t$$

where t is time (s) and the angular frequency $\omega = 2\pi f$. The frequency of the applied field, f = 27 Hz, with a phase separation of 90° between $\overline{H}_x$ and $\overline{H}_y$. Note that using this method, elliptical field profiles where the magnetization direction and also vector length change every field cycle can be applied – see Fig. 6.6.

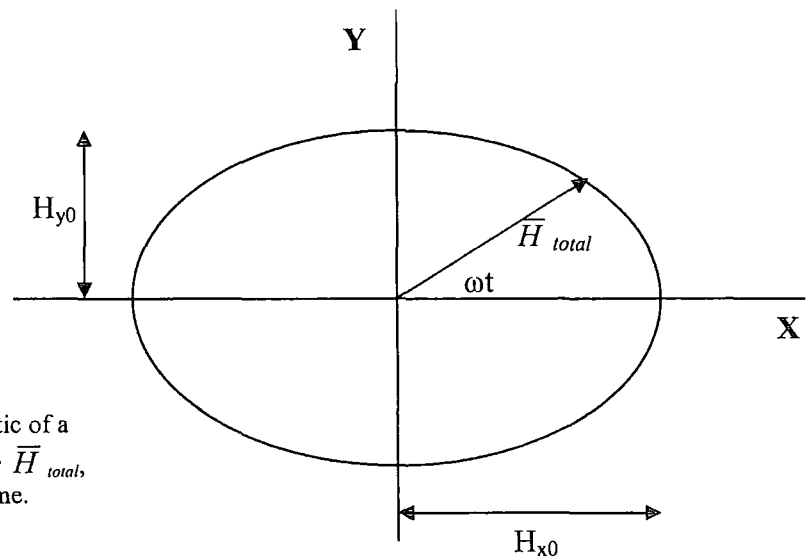

Fig. 6.6: A schematic of a magnetic field vector $\overline{H}_{total}$, rotating with time.

The propagation of a single head-to-head domain wall was investigated in the output wire of corner structures, for different applied field profiles – more specifically the domain wall propagation field in the x-direction, H_p, was measured as a function of H_{y0}. H_p is defined as ½(M-H loop width) at a measured Kerr effect signal = 0, i.e. it corresponds to the coercive field, H_c.

Fig 6.7 shows the relationship between H_{y0} and the propagation field, H_p, of a domain wall in the long wire output. Remarkably, As H_{y0} is increased, a lower H_p was measured, corresponding to the DW propagation field along the x-axis. For example for $H_{y=47\ Oe}$, H_p = 13 (+/- 1) Oe, but a monotonic decrease in this propagation field is evident with increasing H_{y0}, thus propagation fields of 4 Oe are measured for $H_{y=94\ Oe}$. The phase separation is such that H_{y0} is low when H_p is measured along the output. Similarly, H_{x0} is low when H_{y0} is sufficient to inject walls into the vertical arms of structures. X and Y field components varying over time may change the spin structure of a domain wall propagating in a wire, and may also affect the static or dynamic

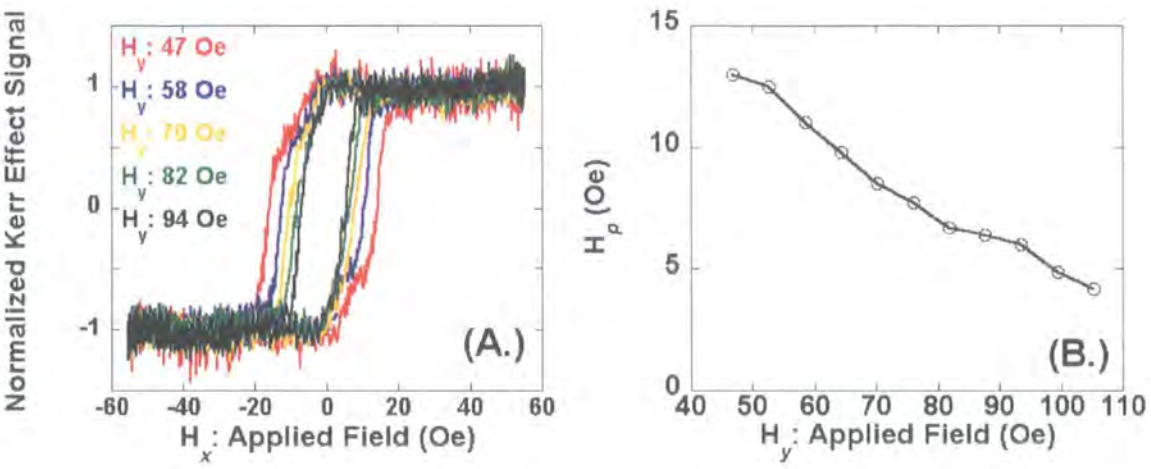

FIG. 6.7: Measured hysteresis loops on the long output of an injection pad corner structure, as a function of H_{y0}. The data describes data after the domain wall has propagated from the corner. The MOKE is configured to measure the X-component of magnetization. Graph (B.) shows a line plot of experimentally measured data.

We interpret this experimental data as follows:

For an isolated domain wall in a complex wire structure such as a corner, the DW displacement is dependent on the local wire geometry, as well as the externally applied field. For an applied H_{y0} above the threshold field value needed for domain wall injection, a wall is injected into the wire system, where it propagates to the structure corner. The wall micromagnetic spin structure may become modified by interaction with the wire sides at the corner.

The wall is propagated further into the corner, and therefore further in the X +ve direction with increasing H_{y0}, therefore a lower H_p is measured on the device output. For $H_{y=47\ Oe}$ and $H_{y=58\ Oe}$, a slight rounding or jaggedness of M-H loop corners is evident, indicative of the stochastic nature of the wall propagation from the corner structure. The canting of M-H loops in Fig 6.7 is further evidence of this stochastic process. Even at room temperature, reversal of wires of similar dimensions to those described here may be described in terms of thermally activated phenomena [Atkinson 2004].

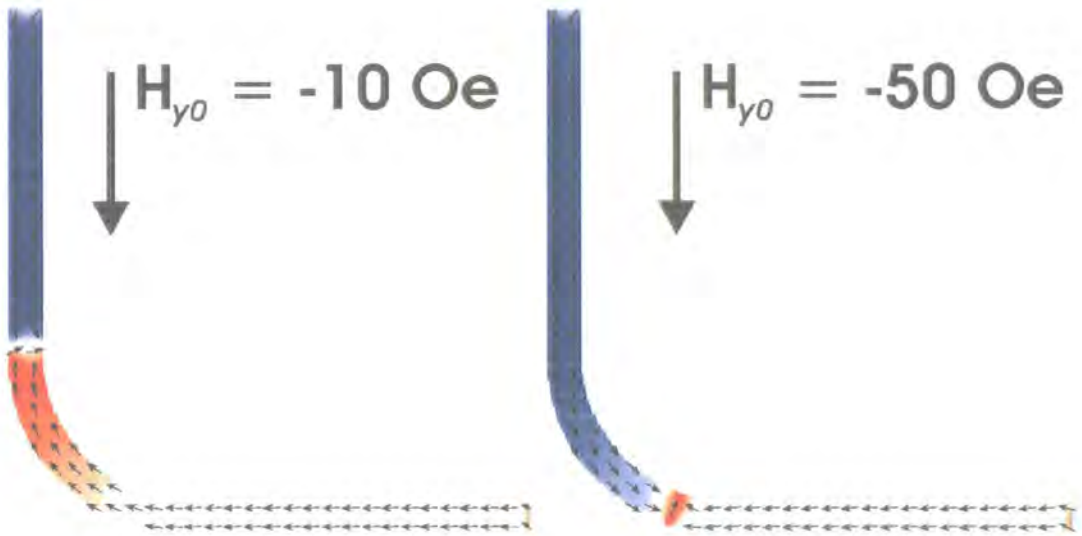

FIG. 6.8: Calculated domain wall position in a corner structure as a function of increasing H_{y0}. An edge roughness of 10 nm was used, similar to the 10-pA beam, FWHM diameter. A 5 nm cell meshing discretion was employed

Statistical spread of wall positions, subtle modifications to wall spin structure, edge roughness and fabrication tolerance, and thermal effects all combine to make the propagation of a single domain wall about a corner a complex process. Calculated domain wall positions as a function of H_{y0} are presented in Fig 6.8. Note with increasing H_{y0} the DW propagates further into the corner, supporting experimental observations. Note that care was taken using the CCD and a marker system to position the investigated samples to an estimated accuracy of better than 1° in the X-Y plane prior to characterization.

6.5 Results: Domain wall nano-traps

The study of the interaction of magnetic domain walls with trapping sites and energy barriers in nanoscale magnetic systems is of interest for a number of reasons. Firstly, fabrication limits for electron beam lithography and ion beam milling techniques are continuing to improve, making possible the study of magnetization reversal processes in very complex wire geometries [Herrmann 2000][Cayssol 2004]. As the size of nanomagnets continues to decrease, the role of defects and surface effects in these quasi 1-D systems becomes more important [Gadbois 1995], and new physical phenomena may be detected. Secondly, in the drive towards higher density magnetic random access memory systems, workers have found that magnets of reduced lateral dimensions have higher switching fields, costing more power and dissipating more energy per reversal event. One method of circumventing this problem would be to use a 'domain wall trap' system [McMichael 2000], now extended to the notched ring or 'doughnut' system [Kläui 2003/2], where a domain wall always resides in the system. Thus magnetization reversal is achieved over low field values, necessary for depinning and propagating a domain wall, as opposed to the high field values needed to activate nucleation of magnetic domains and

associated magnetization reversal. For high data storage densities, traditional single domain data bits ideally need deep submicron dimensions, meaning a high switching field – which costs energy and causes heating. In addition traps afford a means of controlling the position of domain walls at low field values for the purpose of spin current experiments [Grollier 2003], room temperature magnetoresistance measurements, dynamics experiments, or research into magnetic tunnelling processes [Gunther 1994].

Some recent studies have used domain wall injection pads as a means of initialising magnetization reversal in wires fabricated via electron beam lithography, examining domain wall propagation through wire notches [Himeno 2003], and wires of differing widths [Yokoyama 2000]. Critically, using an L-shaped experimental geometry with a smooth rounded corner, the injection field and propagation field of a domain wall can be separated, as described earlier. Such smoothly rounded L-shaped structures allow the study of domain walls at low field values, just above the intrinsic coercivity of the domain wall. Smaller domain wall trap dimensions can be investigated than those permitted by a domain wall injection pad.

In this section domain wall pinning and depinning mechanisms are reported in 200 nm wide $Ni_{81}Fe_{19}$ wires, from individual wedge shaped domain wall traps from 35-125 nm deep. Single nano-traps, (Fig. 6.9, inset (i)) were positioned at location D in Fig. 6.9 [next page]. The traps were defined by the FIB at the same time as the wire lateral dimensions were defined – i.e. the geometry of traps was defined in the FIB definition files. The MOKE spot was typically placed at positions C-E, allowing the domain wall propagation to be studied before the interaction with traps, at the traps, and after interaction with traps.

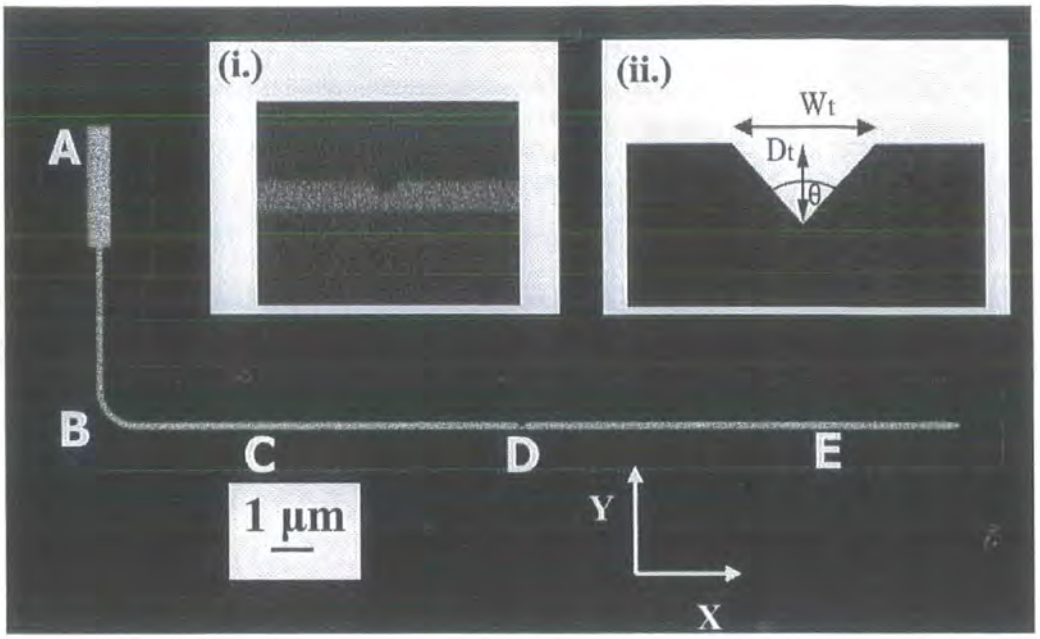

Figure 6.9: FIB image of an L-shaped rounded corner structure. 'A' denotes a domain wall injection pad (600 nm wide × 3μm long), 'B' is a smooth corner of inside radius 500 nm, 'C' and 'E' are typical MOKE measurement positions on the structure output arm, and 'D' is the location for the nano-traps. The output arm is 20 μm long in total. The traps consist of wedge shaped notches milled in the output arm. Inset (i) is an image of an 80 nm deep trap. All traps had a fixed angle, $\theta = 90°$, with trap depths, D_t ranging from 35 - 125 nm, corresponding to trap widths, W_t from 55 - 240 nm. Inset (ii) is a trap schematic.

Fig. 6.10 (i) and (ii) shows hysteresis loops measured from positions 12 μm apart on a nano-trap free structure output arm. For all measurements reported in this section a 27 Hz anti-clockwise rotating field was applied to samples. Peak field values were kept constant at an x-field component, H_{x0} = 70 Oe, and a y-field component, H_{y0} = 65 Oe. Therefore all samples were measured in identical field conditions.

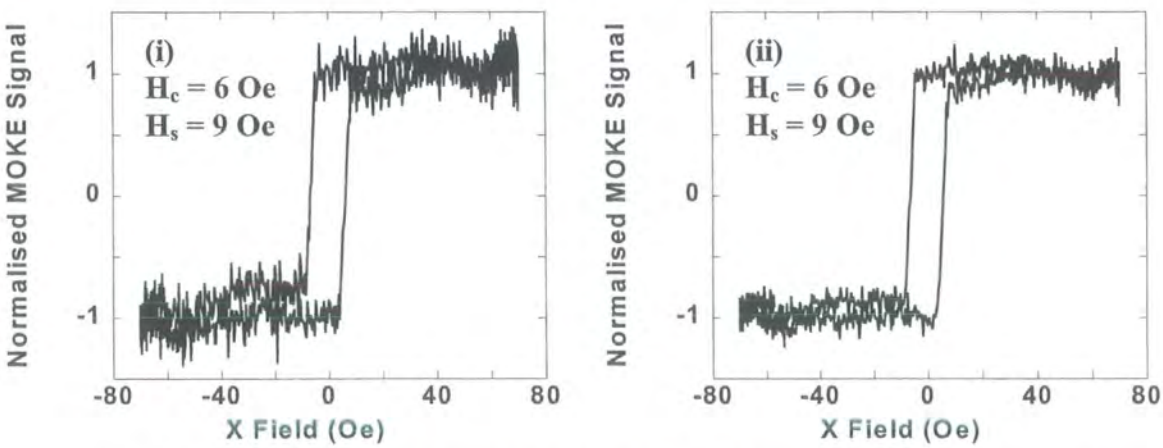

Figure 6.10: Magnetic hysteresis loops taken at positions 12 μm apart on the output arms of defect free structures (positions C [loop i] & E [loop ii] of Figure 6.9).

H_{y0} = 65 Oe ensured that all pads injected domain walls into the experimental system. H_{x0} = 70 Oe was sufficient to switch all output wires studied – either with or without traps. The fact that both loops (i) and (ii) in Fig.6.10 are very similar indicates that a domain wall propagates along the output arm from the corner without encountering any large defects or structural anomalies. The propagation field for these domain walls, H_p, is significantly lower than the domain wall injection field, $H_{inj} \approx 45$ Oe.

To investigate if an artificially fabricated trap could act as a nucleation centre for magnetization reversal, nanotraps with D_t (0-150nm) were milled into 20 μm long 200 nm wide wires with no DW injection pads and their switching was investigated in the presence of both axially applied fields, and in anti-clockwise rotating magnetic fields.

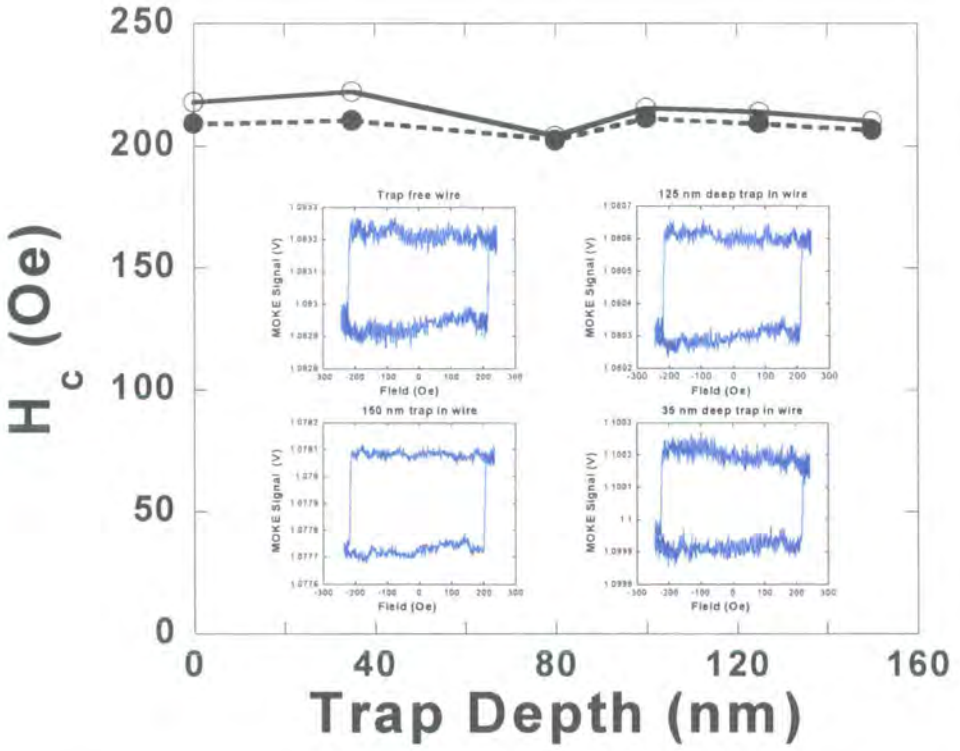

Figure 6.11: The measured H_c for 20 μm long, 200 nm wide wires as a function of trap depth from 0-150 nm deep. (H_{x0} = 250 Oe —○—). Field applied parallel to the wires long axes. (H_{x0} = 250 Oe, H_{y0} = 65 Oe – –●– –). Field applied parallel to the wires long axes, with a vertical H_{y0} component identical to that used for corner structures in section 6.9.

For all the control wires measured, the presence of a trapping site did not cause a significant change in the switching field of samples – Fig 6.11. These wires typically reversed at $H_c \sim 210$ Oe. In a rotating field the presence of a Y-field component led to a reduction of measured H_c of a few Oe. H_{y0} assists the spins to rotate off the magnetic easy axis – the wire long axis, leading to magnetization reversal at a lower H_c. Interestingly, all control samples with trapping centres milled into the wire side have similar switching fields to trap free elongated NiFe wires. Hysteresis loops have sharp transitions, and no evidence of either 2-step switching processes, or dw pinning and depinning events was seen on these control samples.

Figure 6.12: FIB image of a 20 µm wire, with a trap of D_t =150 nm in the wire side.

In the experimental geometry under consideration, D_t and W_t « wire length, a large change in the structure switching field is not observed experimentally. Were the trap critical dimensions within an order of magnitude of the wire length, a pronounced change in switching could be expected. Theory indicates that the introduction of trapping sites into a wire system acts to lower the reversal field of the system, by causing a lowering of the internal demagnetising field [Aharoni 2000]. No notable effect was noted for the system studied.

After studying the switching of elongated single domain wires in the presence of a nano-trap, domain wall propagation is now treated in corner structures (where reversal is by controlled domain wall propagation) with nano-traps. Figure 6.13 is a magnetic hysteresis loop taken with the laser spot centred over the nano-trap site (Fig.

6.9, position D), for a trap of depth, D_t = 125 nm, and width, W_t =240 nm. There are two well-defined switching transitions on this M-H loop.

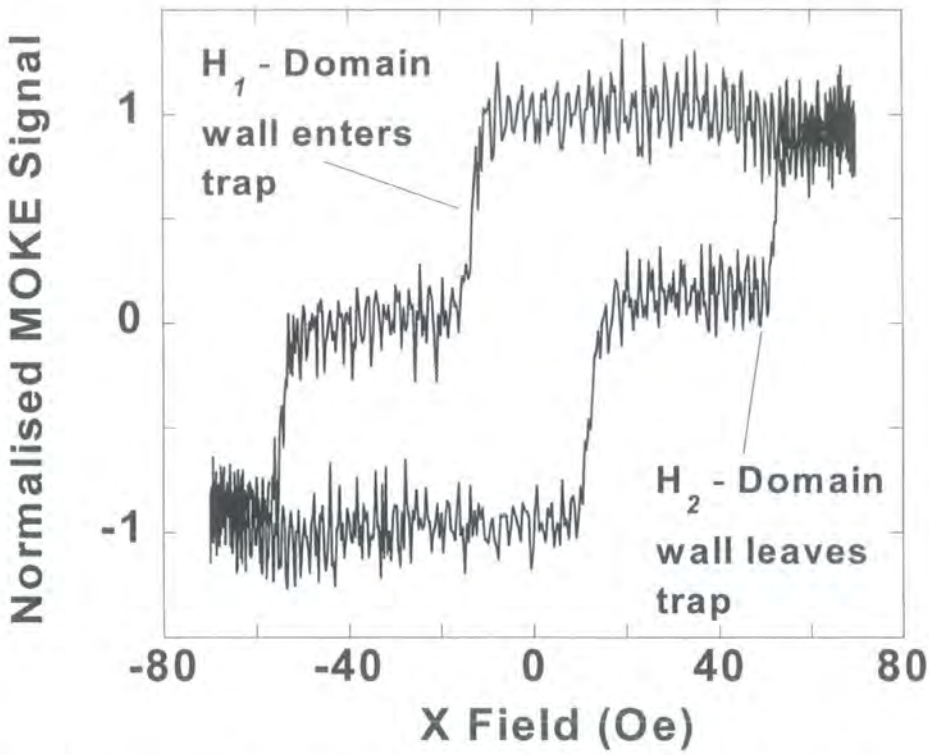

Figure 6.13: Hysteresis loop taken at position D, with the MOKE laser spot positioned over a nano-trap of depth 125 nm and width 240 nm. Loop was averaged for 60 s – for 1600 field cycles.

The initial M-H loop switching transition, at a field value H_1 approximately +/- 10 Oe, is comparable to the propagation field of an isolated DW in the output arm of defect free corner structures, and is interpreted as the domain wall propagating from the structure corner and entering the trap.

The second higher field switching event, H_2, indicates that the domain wall is now interacting with a nano-trap. The trap poses at attractive pinning potential to the domain wall. The domain wall costs exchange energy and anisotropy energy. The trapping site costs demagnetizing, exchange, and anisotropy energy.

Upon entering the domain wall trap, the wall becomes pinned, and is not depinned until a field of sufficient magnitude is reached to overcome the energy

barrier posed by the trap. For the structure in question, the depinning event occurred at approximately H_2 = +/- 53 Oe. At this point, the domain wall has sufficient energy to overcome the energy barrier posed by the trap, and it propagates to the wire end. Further representative M-H loops, showing domain wall trapping in individual 200 nm wide wires are shown in Fig 6.14.

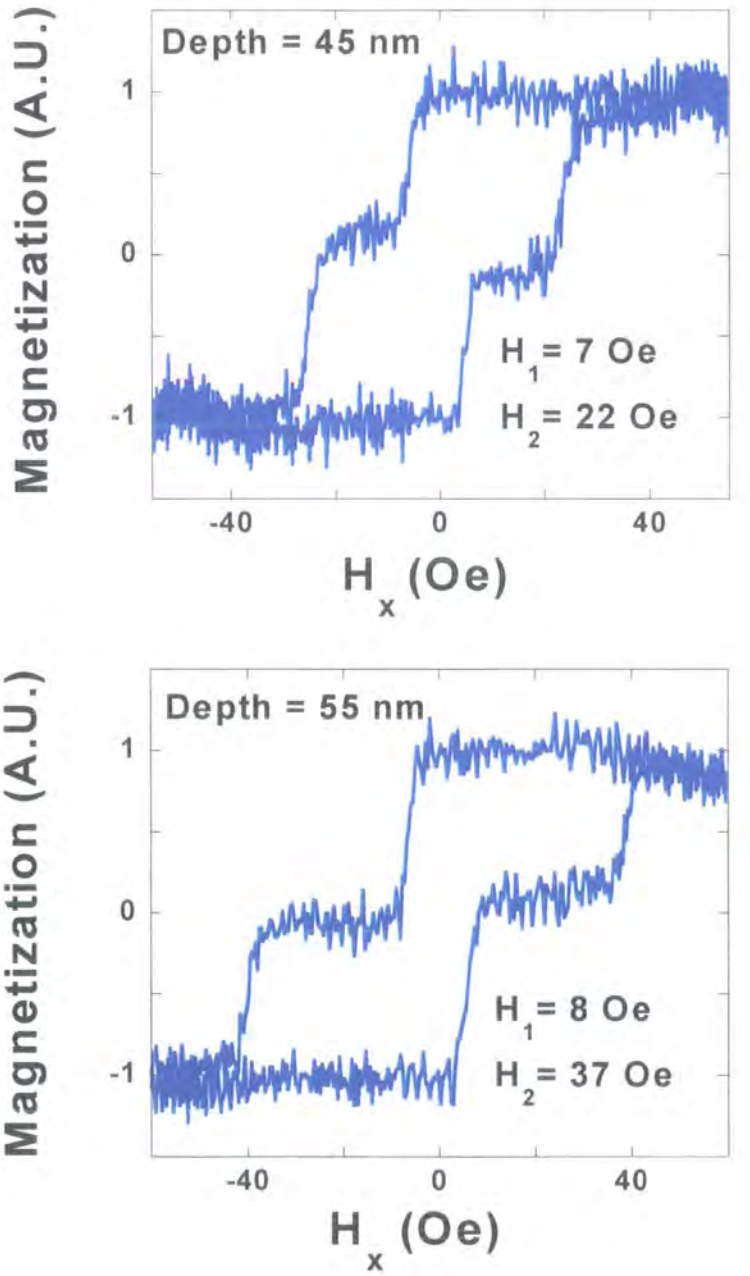

Figure 6.14: Representative hysteresis loops taken with MOKE spot centres over nano-traps of depths, 45 nm and 55 nm.

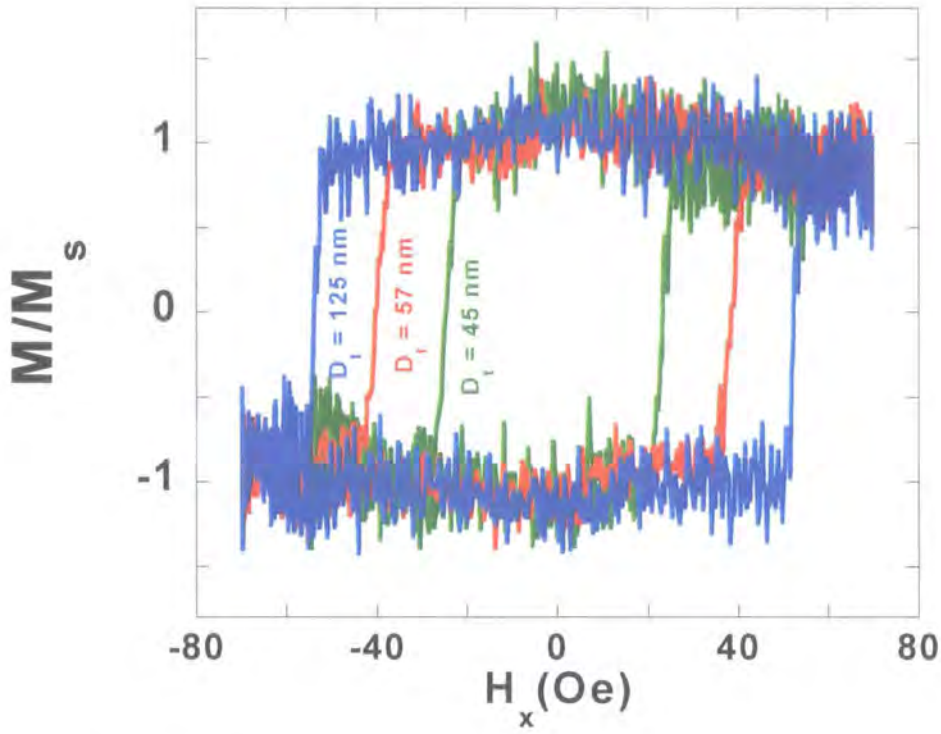

Figure 6.15: Representative hysteresis loops taken with MOKE spot centred on output wire after domain wall interaction with nano-traps of depths, 45 nm, 55 nm, and 125 nm.

The hysteresis loops shown in Fig.6.15 were measured from the end of a structure orthogonal output arm, after the domain wall had been depinned from the trap, at position E of Fig. 6.9. The magnetization switching transitions on the M-H loops are sharp, indicating unhindered domain wall motion to the wire end, once the domain wall has propagated past the nano-trap. Critically the depinning of the DW from the trap occurs at a well-defined, discrete field value. For these structures, and all other structures with traps reported here, the trap always posed a larger energy barrier to domain wall propagation than random defects in the wire structures caused by the ion beam fabrication process.

In order to quantify the depinning field as a function of trap size, three sets of samples, each consisting of five structures, with D_t ranging from 35-125 nm, and a number of nano-trap free control samples, were fabricated and magnetically characterized in identical magnetic fields.

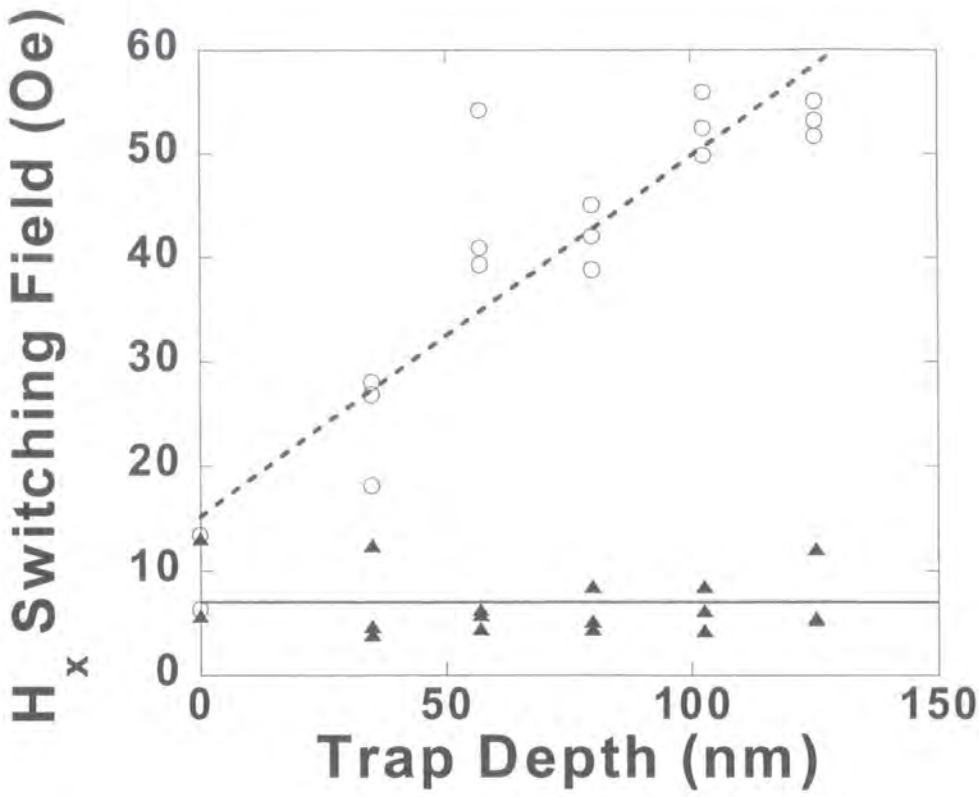

Figure 6.16: Propagation data (▲), and depinning data (○), for 3 sets of structures with 5 different trap sizes. (▲) Represents the coercivity of hysteresis loops measured prior to domain wall interaction with nano-traps (position C of Figure 6.5.), and (○) represents the coercivity of hysteresis loops measured after traps (position E of Figure 6.5.). Lines are guides for the eye.

Fig. 6.16 shows the measured horizontal switching fields before (▲), and after (○), domain walls have interacted with the nano-traps. Trap depths as shallow as 35 nm consistently pinned domain walls.

The standard deviation of the measured horizontal switching field prior to domain wall interaction with a trap, and in trap free control samples was +/- 3 Oe, indicating very good FIB fabrication accuracy for continuous wire structures of complex planar geometry. The mean domain wall propagation field in defect free samples was $\overline{H}_p = 7$ Oe. Switching fields from trap sites tended to increase with trap depth, and to display a reasonably low range of depinning fields given the small dimensions of fabricated features being investigated. Note the scatter increases for smaller feature sizes. Repeatability of measurements from structure to structure and

reasonable tolerance data require a strictly monitored and well-calibrated 10-pA ion beam aperture. Much of the random spread in the tolerance data of Figure 6.15 is attributable to stage drift, which for our system is largely isotropic, with a value of 0.6 nm/s^{-1} [Petit 2005].

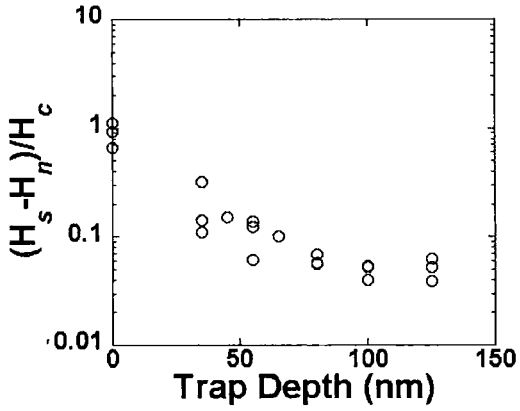

Figure 6.16 Measured dispersion of hysteresis loops defined as $(H_s - H_n)/H_c$, for structures with and without trapping sites. Each data taken for loops time averaged for at least 800 field cycle repetitions

For applications such as sensors or even data storage [McMichael 2000] sharp domain wall depinning transitions from traps are needed to enhance device tolerance. I define a switching dispersion of measured M-H loops as (H_s-H_n/H_c). [Note that because magnetization reversal is effected by domain wall propagation, H_n is not strictly a nucleation field, but the lowest field at which reversal of the wire is measured. H_s is the highest field at which time averaged M-H loops are saturated.] Fig. 6.16 depicts switching field widths, for 20 separate investigated structures, for trap free corner structures, and for samples with traps investigated after DW interaction with the trapping site. Switching transition width is larger in trap free corner samples, or wires with low trap depths, partially due to the stochastic nature of wall propagation from the corner. The switching transition width after the DW was depinned from a 125 nm deep trap was as low as 1.8 Oe, after averaging for 60 s. Without dividing (H_s-H_n) by H_c, structures with trapping centres have a significantly lower switching field width than control samples with no trap.

6.6 Discussion & Conclusion

Summary of Results

The field-controlled injection of head-to-head domain wall into ferromagnetic nanowires with rounded corners, which leads to magnetization reversal in wire structures in a controlled direction, by domain wall propagation has been demonstrated. Furthermore, by employing a rotating magnetic field vector of the appropriate chirality, the propagation of single domain walls around smoothly rounded corners has been shown.

Intentionally introducing an asymmetry into a geometry affords more control over the magnetization reversal mechanism. The effect of wedge shaped nano-traps on domain wall propagation has been investigated using planar rounded L-shaped $Ni_{81}Fe_{19}$ wire structures. By introducing artificial nano-traps into wires the intentionally impeded motion of single domain walls has been achieved. The pinning behaviour may be tuned by varying trapping site dimensions.

Traps with dimensions as small as depth, D_t = 35 nm, and width, W_t = 55 nm were found to effectively pin domain walls. Time averaged hysteresis loops demonstrated very sharp switching transitions from trapping centres. The L-shaped experimental geometry used enabled the study of very small trapping centres, below the domain wall pad injection field, and may be useful for other types of experiments, such as spin polarized current domain wall displacement studies [Tsoi 2003][Grollier 2003].

Further Work

Depinning field as a function of trap width has been plotted as a linear fit. The behaviour if investigated in more detail is predicted to be more complex. An investigation of domain wall depinning field as a function varied trap depth and

width, plotted in units of domain wall width would be a very interesting fundamental study.

Using the experimental geometry presented here, the theoretical assertion of Paul, [Paul 1982], that the trap depinning field scales linearly with trap width when trap width < wall width, and then the depinning field increases slowly with trap width as the domain wall resides fully within a trapping site, could be verified.

Another interesting study would be the preparation of specimens with multiple trap locations, investigating the density of functional traps possible in a given sample. Further improvements to the results delineated in this chapter would be use of a laser interferometer stage, and a smaller FIB milling beam. Dissociating the FIB trap milling from defining wire edges is another potentially interesting investigation. Measured depinning field from a 35 nm deep trap (~ 30 Oe) compared to a trap free control sample ($\overline{H}_p = 7 \pm 3$ Oe) suggest that significantly smaller trapping site dimensions are possible. For a suitable experimental geometry the investigation of stochastic domain wall depinning processes from a single trapping site in a wire could be interesting.

Domain Wall Logic

In the context of a possible logic schema, the reproducible transfer of information, in the form of magnetization vector orientation in a wire, over tens of microns mediated by field controlled domain wall propagation has been demonstrated. Controlled information transfer by domain wall propagation was demonstrated in elongated wires, and around corners in the presence of an appropriate external field sequence and direction. Single nanowire switching by domain wall can

be controlled not only by magnetic field, but by element geometry by intentionally introducing artificial trapping centres in wires.

Domain wall nucleation is seen to be energetically quite costly vis à vis domain wall propagation in thin NiFe wires. For possible domain wall device applications it is useful to consider the energy loss associated by magnetization reversal by field controlled domain wall propagation, verses magnetization reversal by nucleation events. The hysteresis energy, W_h, may be expressed as:

$$W_h = \oint HdB = \oint HdM \text{ J/m}^3 \text{ per cycle}$$

where B is the magnetic induction in Tesla [Bozorth 1993]. We consider the energy cost of device operation per cycle, mediated by either domain wall propagation process or nucleation events in Fig. 6.17.

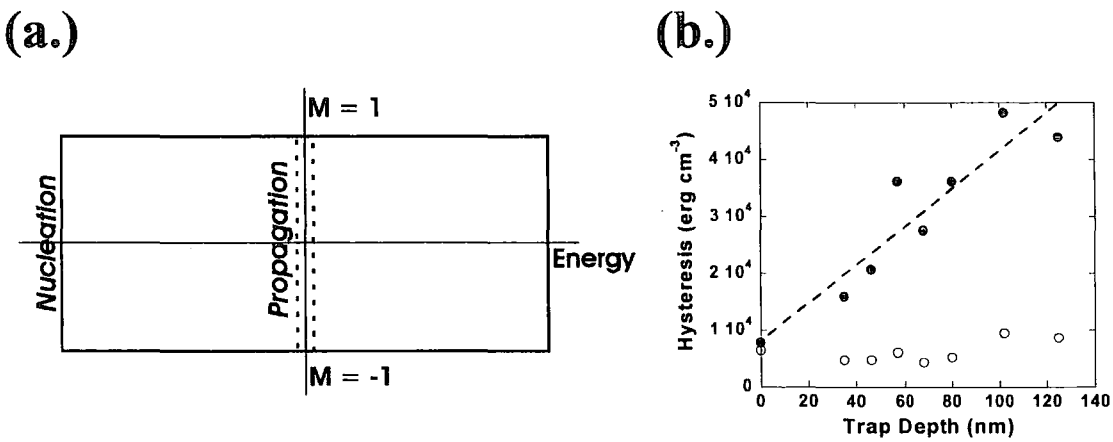

Figure 6.17 Schematic hysteresis loops (a.) for magnetization reversal in a 200 nm wide, 5 nm thick NiFe wire of high aspect ratio by domain wall propagation (- - -) as compared to nucleation-mediated reversal (——). (b.) plots the associated energy cost of domain wall depinning from artificial nano-traps (- - ⊙ - -). Line is a guide to the eye.

Taking representative values of 7 Oe for domain wall propagation and 210 Oe for reversal mediated by a nucleation event in 5 nm thick, 200 nm wide pointed end NiFe nanowires, W_h is 6000 erg cm^{-3} and 180000 erg cm^{-3} for wall propagation and nucleation events respectively. Further, by artificially modulating the nanowire

energy landscape, either by artificial domain wall traps (Fig 6.17b), or more complicated wire designs, switching of wires can be controlled at any field value between H_p and H_n. Field controlled domain wall propagation is possible in these systems at very low H_p just above the intrinsic domain wall coercivity. Information can therefore be manipulated by controlled domain wall propagation at low energy costs. This concept is further treated in the following chapter.

6.7 References

[Aharoni 2000] A. Aharoni, *"Introduction to the Theory of Ferromagnetism"*, Oxford University Press, New York, **109** (2000)

[Allwood 2002/1] D. A. Allwood, Gang Xiong, M. D. Cooke, C. C. Faulkner, D. Atkinson, N. Vernier, R. P. Cowburn, Science, **296**, 2003 (2002)

[Allwood 2002/2] D. A. Allwood, N. Vernier, Gang Xiong, M. D. Cooke, D. Atkinson, C. C. Faulkner, R. P. Cowburn, Appl. Phys. Lett. **81**, 4005 (2002)

[Atkinson 2003] D. Atkinson, D. A. Allwood, Gang Xiong, M. D. Cooke, C. C. Faulkner, R. P.Cowburn, Nat. Mat. **2**, 82 (2003)

[Atkinson 2004] D. Atkinson, R. P. Cowburn, Appl. Phys. Lett. **85**, 1386 (2004)

[Bozorth 1993] R. M. Bozorth, *"Ferromagnetism,"* IEEE Press, New York (1993)

[Bruno 1999] P. Bruno, Phys. Rev. Lett. **83**, 2425 (1999)

[Cayssol 2004] F. Cayssol, D. Ravelosona, C. Chappert, J. Ferré, J. P. Jamet, Phys. Rev. Lett. **92,** 107202 (2004)

[Cowburn 1998] R. P. Cowburn, J. Ferré, S. J. Gray, J. A. C. Bland, Phys. Rev. B **58**, 11507 (1998)

[Fournel 1998] F. Fournal, Y. Chen, F. Carcenac, N. Essaidi, H. Launois, V. Kottler, C. Chappert, IEEE Trans. Magn. **34**, 1027 (1998)

[Gadbois 1995] J. Gadbois, J-G. Zhu, IEEE Trans. Magn. **31**, 3802 (1995)

[García 1999] N. García, M. Muñoz, Y.-W. Zhao, Phys. Rev. Lett, **82**, 2923 (1999)

[Gomez 1999] R. D. Gomez, T. V. Luu, A. O. Pak, I. D. Mayergoyz, K. J. Kirk, J. N. Chapman, J. Appl. Phys **85**, 4598 (1999)

[Grollier 2003] J. Grollier, P. Boulenc, V. Cros, A. Hamzić, A. Vaurès, A. Fert, G.Faini, Appl. Phys. Lett. **83**, 509 (2003)

[Gunther 1994] L. Gunther, B. Barbara, Phys. Rev. B **49**, 3926 (1994)

[Herrmann 2000] M. Herrmann, S. McVitie, J. N. Chapman, J. Appl. Phys. **87**, 2994 (2000)

[Himeno 2003] A Himeno, T Ono, S Nasu, K Shigeto, K Mibu, T Shinjo, J. Appl. Phys. **93**, 8430 (2003)

[Kirk 1999] K J Kirk, J N Chapman, C D W Wilkinson, J. Appl. Phys. **85**, 5237 (1999)

[Kläui 2003/1] M. Kläui, C. A. F. Vaz, J. A. C. Bland, W. Wernsdorfer, G. Faini, E. Cambril, L. J. Heyderman, Appl. Phys. Lett. **83**, 105 (2003)

[Kläui 2003/2] M. Kläui, C. A. F. Vaz, J. A. C. Bland, W. Wernsdorfer, G. Faini, E. Cambril, J. Appl. Phys. **93**, 7885 (2003)

[Konishi 1971] S. Konishi, S. Yamada, T. Kusuda, IEEE Trans. MAG. **7**, 722 (1971)

[Lee 2000] W. Y. Lee, C. C. Yao, A. Hirohata, Y. B. Xu, H. T. Leung, S. M. Gardiner, S. McPhail, B. C. Choi, D. G. Hasko, J. A. C. Bland, J. Appl. Phys. **87**, 3032 (2000)

[Lim 2004] C. K. Lim, T. Devolder, C. Chappert, J. Grollier, V. Cros, A. Vaurès, A. Fert, G. Faini, Appl. Phys. Lett. **84**, 2820 (2004)

[McMichael 2000] R. D. McMichael, J. Eicke, M. J. Donahue, D. G. Porter, J. Appl. Phys. **87**, 7058 (2000)

[Nakatani 2003] Y. Nakatani, A. Thiaville, J. Miltat, Nat. Mat. **2**, 521 (2003)

[Novoselov 2003] K. S. Novoselov, A. K. Geim, S. V. Dubonos, E. W. Hill, I. V. Grigorieva, Nature, **426**, 812 (2003)

[Ono 1998] T. Ono, H. Miyajima, K. Shigeto, T. Shinjo, Appl. Phys. Lett. **72**, 1116 (1998)

[Ono 1999] T. Ono, H. Miyajima, K. Shigeto, K. Mibu, N. Hosoito, T. Shinjo, Science **284**, 468 (1999)

[Patton 1975] C. E. Patton, Z. Frait, C. H. Wilts, J. Appl. Phys. **46**, 5002 (1975)

[Paul 1981] D. I. Paul, J. Appl. Phys, **53**, 1649 (1982)

[Petit 2005] D. Petit, C. C. Faulkner, S. Johnstone, D. Wood, R. P. Cowburn, Rev. Sci. Instrum. **76**, 026105, (2005)

[Shigeto 1999] K. Shigeto, T. Shinjo, T. Ono, Appl. Phys. Lett. **72**, 1116 (1998)

[Shigeto 2000/1] K. Shigeto, T. Okuno, T. Shinjo, Y. Suzuki, T. Ono, J. Appl. Phys. **87**, 5650 (2000)

[Shigeto 2000/2] K. Shigeto, T. Okuno, T. Shinjo, Y. Suzuki, T. Ono, J. Appl. Phys **88**, 6636 (2000)

[Shinjo 2000] T. Shinjo, T. Okuno, R. Hassdorf, K. Shigeto, T. Ono, Science, **289**, 930 (2000)

[Sixtus/Tonks 1931] K. J. Sixtus, L. Tonks, Phys. Rev. **37,** 930 (1931)

[Tsoi 2003] M. Tsoi, R. E. Fontana, S. S. S. Parkin, Appl. Phys. Lett. **83,** 2617 (2003)

[Yokoyama 2000] Y. Yokoyama, Y. Suzuki, S. Yusaa, K. Ando, K. Shigeto, T. Shinjo, P. Gogol, J. Miltat, A. Thiaville, T. Ono, T. Kawagoe, J. Appl. Phys. **87,** 5618 (2000)

[Wachowiak 2002] A. Wachowiak, J. Wiebe, M. Bode, O. Pietzsch, M. Morgenstern, R. Wiesendanger, Science, **298**, 577 (2002)

[Wernsdorfer 1997] W. Wernsdorfer, K. Hasselbach, A. Benoit, B. Barbara, B. Doudin, J. Meier, J.-Ph. Ansermet, D. Mailly, Phys. Rev. B **55**, 11552 (1997)

[Williams 1949] H. J. Williams, R. M. Bozorth, W. Shockley, Phys. Rev. **75,** 155 (1949)

[Zhu 2002] Xiaobin Zhu, P. Grütter, V. Metlushko, B. Ilic, Phys. Rev. B **66**, 024423 (2002)

[Zheng 2002] J. G. Zhu, Y. Zheng, p307, "*Topics in Applied Physics 83 - Spin Dynamics in Confined Magnetic Structures,*" Springer, Berlin (2002)

Chapter 7. Domain Wall Logic

7.1 Introduction

This chapter treats domain wall logic. Planar ferromagnetic multi-terminal wire junctions, with submicron critical dimensions are described. AND/OR-like junction geometries presented are suitable for integration with existing domain wall logic and data storage devices [Allwood 2002/1].

Section 7.2 gives a brief review of magnetic logic, competing and complementary logic technologies, and some longer-term perspectives. Section 7.3 describes the micromagnetics of domain wall NOT gates. Section 7.4 introduces all-metallic 3-terminal ferromagnetic structures suitable for logical AND/OR operations on magnetic logic signals. Section 7.5 details how engineering junction lateral dimensions permits control of the wire junction field operating margins. Section 7.6 outlines how the junction has been integrated with other logic gates, such as a 3-terminal fan-out structure, that acts as a signal multiplier. Phase diagrams of field operating margins of AND/OR-type junctions in a 27 Hz rotating field are presented, in the context of integration with experimentally realised domain wall NOT gates. Section 7.7 reports the results of investigations into more complex 3 or 4 terminal universal logic gates, such as a majority gate, and the NAND gate. A brief discussion and conclusion is presented in Section 7.8.

7.2 Literature

7.2.1 Magnetic logic

Perspective

Research into magnetism has often been driven by the demands of the data storage industry, where controlling the magnetization reversal mechanisms of single domain elements between bi-stable magnetic configurations is critical. The potential for magnetics as a platform for Boolean logic as well as information storage was recognised as early as the 1960's when logic circuits fabricated from magnetic cores found applications in high voltage environments [Bennion 1969].

Magnetic bubble logic was for a long time advocated as a rival to existing semiconductor technologies [O'Dell 1974][Bobeck 1975]. In this scheme the information carrier is a low coercivity, perpendicular magnetized film. Bubble diameters as small as 0.3 μm were realised, with memories of up to 16 Mbit/chip.

However, to date semiconductor logic has proved to be faster and cheaper. Moore's law, which describes the doubling of computer power every 18-24 months, has proved to be remarkably prescient and semiconductor transistor sizes have been consistently shrinking for nearly 5 decades, leading to higher chip packing densities. Due to fundamental physical limitations, the semiconductor roadmap foresees a breakdown in Moore's law in the coming years. For example, as semiconductor structure sizes reach sub-50 nm critical dimensions, the number of conduction electrons is too low to allow critical current densities. For length scales and feature sizes shorter than the De Broglie wavelength, quantum effects need to be addressed. In microelectronic devices with increasingly reduced lithographic features, larger heat sinks are needed. What happens next?

Domain Wall Logic

Information manipulation by interaction of quantum-dot cellular automata (QCA) is long established, and was recently explored as an avenue towards a low power room temperature magnetic logic scheme using individual field coupled magnetic dots [Cowburn 2000/2], or squares [Wadhwa 2004] as data cells. This scheme has evolved into a logic system where information is transferred and operated on by controlled field induced displacement of domain walls through elongated continuous ferromagnetic wires [Allwood 2002/2]. Boolean logic operations are effected by the propagation and interaction of one or more domain walls in geometrically complex planar wire circuits in an external applied field. The domain wall (DW) acts as the boundary between Boolean logical '0' and '1' in elongated wires. Advantages of domain wall logic are low power dissipation, and a reasonably high speed (in the order of 100 MHz) [Csaba 2002]. For example, modelled domain wall velocities of ~ 600 ms^{-1} [Nakatani 2003], and experimental wall velocities of ~ 1500 ms^{-1} have recently been reported in 200 nm wide $Ni_{81}Fe_{19}$ wires [Atkinson 2003/1][Atkinson 2003/2]. Non-volatility and radiation hardness are two further major advantages. Non-volatility means that memory state is maintained when power is removed. A simple 2-D architecture would easily be integrated into existing silicon-based systems. The domain wall logic system is low cost, and in principle could function on cheap substrates such as glass, or even flexible Kapton substrates.

The system is scalable – patterned ferromagnetic elements retain high saturation magnetization to sub 100 nm lengthscales, and an increase in the coercive force with reduced dimensions may enhance operating margins. The ultimate integration density is limited by the superparamagnetic limit, and the domain wall width. Results described here are for single layer structures on a Si substrate. A 2-D

architecture facilitates simple, cheap, quick fabrication. In principle, layering planes of interconnected circuits affords a means of realising a high-density 3-D architecture.

Magnetoresistive Logic Elements

The semiconductor silicon chip is compatible with magnetic data storage technologies, such as magnetic random access memory [MRAM] cells, which offer low energy dissipation, high speed and large storage densities [Parkin 1999]. One competing logic processing method recently proposed is the reprogramable single MRAM cell [Ney 2003][Koch 2004]. In this scheme two magnetic layers of different switching fields separated by a spacer layer are addressed by three separate input current lines, and read out from a separate output line. A reset operation is required between separate logic operations. Potentially all logic operations can be effected in a single magnetoresistive element. This concept of reconfigurable gates is treated in the Prinz review [Prinz 1998]. By contrast, in conventional CMOS (complementary metal oxide semiconductor) logic, at least 2 transistors are needed for each operation.

Hybrid Devices

Hybrid MRAM-CMOS devices have been proposed. Johnson has proposed single layer ferromagnetic-semiconductor devices capable of performing different Boolean functions, according to how the device is addressed by a field generating current-line [Johnson 2000/1][Johnson 2000/2]. These prototype devices also demonstrated non-volatile data storage capability, and typically consist of micron scale rectangular 16 nm thick NiFe elements. Black and other workers have investigated field programmable hybrid semi-conductor, layered tunnelling logic gates [Black 2000][Richter 2002].

7.2.2 Longer-term perspectives

Harnessing the spin degree of freedom of the electron for the manipulation as well as the storage and sensing of information affords exciting longer-term possibilities. This field of scientific research is referred to as spintronics or magnetoelectronics. It is desirable to have ferromagnetic materials that are electrically semiconducting, having fully spin-polarized conduction electrons with high mobilities. Resultant applications benefit from good magnetic and semiconducting properties. To have functional room temperature devices, a Curie temperature in excess of 500 K is needed [Coey 2004]. Coey dubs devices based around traditional ferromagnets – iron, cobalt and nickel as "first generation" spin electronic materials. One shortfall of these d-band materials is strong scattering of conduction electrons, causing a short mean free path ($\approx$ 1 nm) and quite low electron mobilities ($\approx 10^{-3}$ m^2 V^{-1} s^{-1}).

In the coming years, more functional room temperature devices in ferromagnetic semi-metals or semiconductors can be expected, which have 100 % spin polarisation of their conduction electrons. There are already interesting logic schema being investigated within this field such as α-MnAs films on GaAs(001) (which can be reversed by either an in-plane or out of plane magnetic field) which in theory should be possible to integrate with existing semi-conductor technologies [Pampuch 2003].

Low temperature single domain wall displacement studies in ferromagnetic semiconductor materials are already underway, and may lead to future applications. For example Tang recently investigated domain wall resistivity in GaMaAs by the Hall effect [Tang 2004], albeit at low temperatures ~ 4.2K. Many findings from domain wall logic investigations may find applications in emerging or as yet unrealised materials.

7.3 NOT Gate Micromagnetics

An all-metallic ferromagnetic NOT-gate signal inverter and shift register was recently reported [Allwood 2002/1]. The NOT gate consists of a continuous planar input wire, output wire, and a central stub at the input and output wire junction. By controlled propagation of domain walls through the junction region in an externally applied 27 Hz rotating field, the magnetization orientation in the device output wire is reversed relative to the direction of domain wall motion. This is a signal inversion process – a Boolean NOT operation. Small changes to the junction devices geometry of the order of ~25 nm have resulted in significant improvements to field operating margins of such structures [Allwood 2004/1].

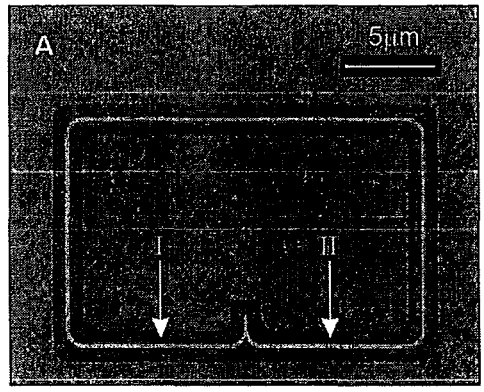

NOT	*IN*	*OUT*
	0	1
	1	0

Fig 7.1: Secondary electron FIB image of a ferromagnetic NOT gate [Allwood 2002/1], and NOT gate truth table.

Due to shape anisotropy, magnetization in the 200 nm wide, 5 nm thick NiFe wire shown in Fig 7.1 is aligned parallel to the wire long axis, even around a corner [Hirohata 2000]. If the wire formed a perfect symmetrical circle, the system would be single domain at remanence. However, the presence of a junction or stub region means that topologically at least 1 domain wall must reside in the system. The micromagnetics of the NOT gate signal inversion process was investigated numerically, in an anticlockwise rotating magnetic field of H_x = 120 Oe, H_y = 80 Oe.

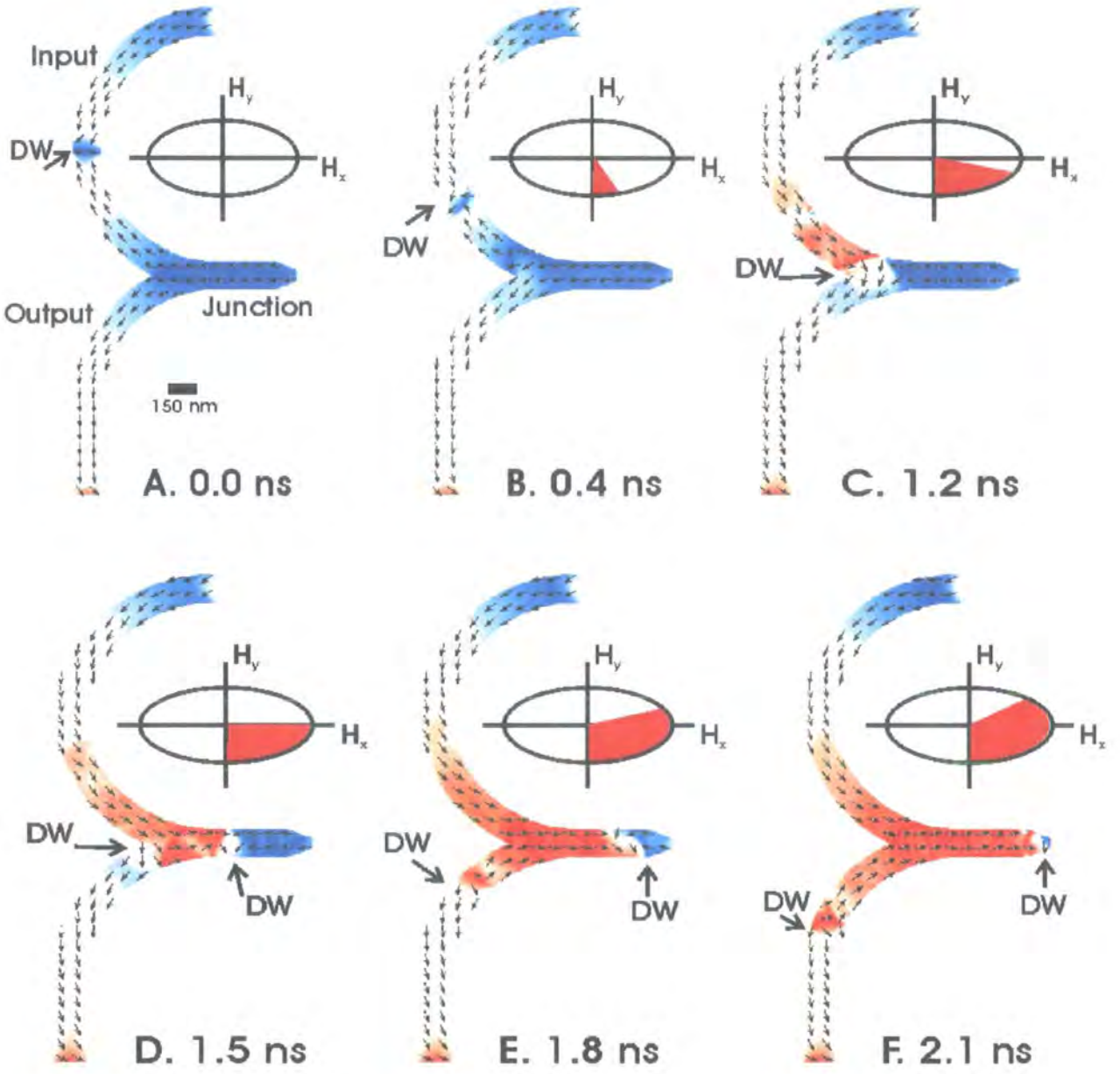

Fig 7.2: Dynamic micromagnetics of a domain wall NOT gate. 'DW' corresponds to domain wall. The red "pie" region of field diagram indicates applied rotating field history over time.

The field clocking frequency was 186 MHz. For details of the modelling process, see Appendix.A. Consider Fig. 7.2.A, in the absence of externally applied field. A domain wall is initialised in the input wire of the system. Due to shape anisotropy in general magnetization is parallel to the wire sides. Magnetization in the output wire is pointing "south."

For a negative H_y field, above the intrinsic domain pinning field, the magnetization in the input wire aligns itself with the externally applied field. Therefore the DW propagates towards the junction, Fig. 7.2.B. Because shape anisotropy is strong, with magnetization parallel to wire sides, magnetization reversal for an appropriate external field is by controlled domain wall motion.

After 1.2 ns, Fig. 7.2.C, the domain wall has propagated to the junction region – the meeting place of the input wire and the central stub. The applied field is now H_x = 113 Oe, H_y = -27 Oe. H_y has decreased over time, but the y-field component has propagated the domain wall to the junction region. A large H_x is now required to propagate the domain wall in the +ve X direction through the central junction wire.

Upon application of a sufficiently large H_x, the NOT gate junction is switched by DW motion – Fig. 7.2.D. The single domain wall that propagated to the junction region gradually expands at the meeting point of wire input and the junction wire. Due to the strong H_x component, a domain wall starts to propagate down the central stub, switching the junction region magnetization. Thus, junction wire magnetization becomes aligned with a strong external H_x.

However, due to the 3-terminal geometry, another domain wall must be created at the junction region, at the meeting point of the central wire stub, and the output wire. One domain wall has been split into 2 at the NOT gate junction, by matching an appropriate externally applied magnetic field to the wire geometry.

Fig. 7.2.E, H_x = 113 Oe; H_y = 27 Oe, shows the domain wall in the central junction region continuing to propagate to the junction end-point, due to the strong H_x. However, as H_y is increased to positive integer values over time, magnetization at the junction between the central stub, and the wire output is aligned, in the +ve Y

direction. Therefore the second domain wall begins to propagate down the junction output wire.

After 2.1 ns, the domain wall in the central junction arm been nearly annihilated, and the central junction region eventually becomes fully saturated in the +ve direction. Thereafter only 1 domain wall exists in the system, in the wire output arm. Upon application of higher H_y, the wall propagates further down the output wire, and can be read out, propagated to further logic gates, or annihilated.

One DW is split into two DW to magnetically reverse the junction region. By annihilating the wall in the central stub, a 1-domain wall state is restored. Magnetization in the output wire becomes reversed, relative to the direction of domain wall propagation, and is now oriented "north" as one DW switches magnetization in the output wire. A signal inversion has been performed.

If the junction stub is too short, the system is single domain at remanance, and reproducible DW logic functions cannot be performed. If the central stub is too long, it becomes magnetically harder, with a higher switching field, which reduces field-operating margins. Simulations were performed at 186 MHz. In principle, a simple 1-junction feedback loop can invert a signal every 3/2-clock cycles, leading to a device operating frequency of ~125 MHz. By optimising the modelled geometry, applied field amplitudes, and field sweep rate, higher frequencies may be obtained.

7.4 AND/OR-like Gates

7.4.1 Introduction

For full domain wall logic functionality, combinational logic as well as signal inversion is required, for example AND/OR, Majority, or NAND gates. Different logic gates need to be integrated to achieve logical completeness, or all logic

functions need to be united in a single universal gate. For the DW logic schema, note the following:

- The Boolean '1' logical state is defined as wire magnetization direction in the same direction as DW propagation, and '0' is therefore wire magnetization in the opposite direction to DW propagation. This definition is necessary since it has already been demonstrated in Chapter 6 that head-to-head domain walls may propagate around smoothly rounded 90° corners, and controlled propagation of a single DW about more complex geometries is possible.
- Due to the high aspect ratios of the systems studied, magnetization is generally oriented parallel to the long axis of the wires. Magnetic logic signals are transported by the controlled field induced displacement of domain walls at propagation field values (H_p) lower than the wire nucleation field, H_n.
- In full circuits rotating magnetic fields [typically anti-clockwise] are used to propagate domain walls, and to define the direction of information flow. The direction of rotating magnetic field must match the chirality of corners.
- For a fully operational domain wall logic system, very well defined switching mechanisms and switching field values are needed to enhance field operating margins, and for reproducible device operation over time.
- Field operating margins are enhanced by designing circuit geometry such that:

$$H_p << H_n \qquad [7.1]$$

Therefore very smooth wire sides, to lower the intrinsic domain wall coercivity, and high nucleation fields for samples with no domain wall present are prerequisite.

OR	*A*	*B*	*Output*
	1	1	1
	0	1	1
	1	0	1
	0	0	0

AND	*A*	*B*	*Output*
	1	1	1
	0	1	0
	1	0	0
	0	0	0

Table 7.1 Truth tables for Boolean OR and AND operations.

Table 7.1 depicts Boolean logic truth tables for OR, and AND operations. In an AND gate, the output is only "high" if both inputs are "high." For the OR gate, the output is "high" if either or both inputs are "high. For an AND/OR-like gate, 2 $Ni_{81}Fe_{19}$ input wires combine to form one output wire in a 3-terminal junction – Figure 7.3. Initially, output wire switching was studied as a function of the number of domain walls incident upon a junction, in a 27 Hz axially applied field. For nominally identical junctions 0, 1 or 2 domain walls were injected (Chapter 6.3) into the junctions, and switching of the structures was investigated by localized MOKE magnetometry measurements.

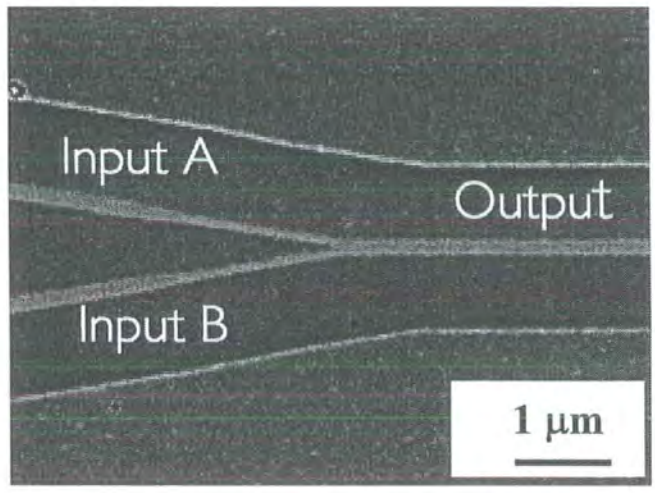

Fig. 7.3: Secondary electron FIB image of a continuous 3-terminal planar DW junction, suitable for AND/OR-like operations. Field is applied parallel to the long output wire.

Domain wall devices move domain walls (DWs) in a controlled manner at propagation fields markedly lower than the nucleation field of the device. The switching mechanism of a structure is therefore artificially engineered by domain wall displacement. In the absence of a DW, magnetization reversal is by a more energetically costly mechanism, at a higher switching field value. In Chapter.6 information transfer was demonstrated over tens of microns mediated by field controlled domain wall propagation. DW propagation was demonstrated in elongated wires, and around corners for an appropriate external field sequence and direction. Test structures were 20-25 μm long to facilitate spatially resolved magnetometry measurements. Parent films were 5 nm thick thermally evaporated Permalloy films on Si[100]. Using t_{NiFe} = 5 nm ensures that the domain walls do not have an out of plane component. The active junction region is submicrometer in dimension – Fig 7.3.

7.4.2 Results

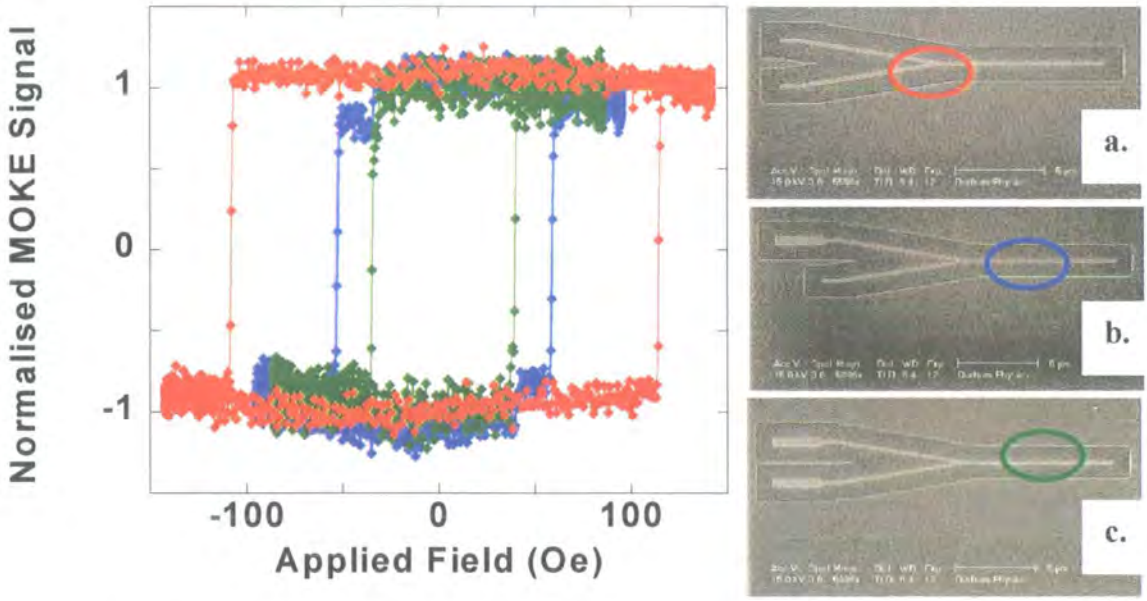

Fig 7.4: Hysteresis loops measured from the outputs of structures shown in the SEM micrographs a, b, and c. —●— corresponds to the switching of an output with 2 domain walls incident at the junction, —●— describes the switching of the output with 1 domain wall injected into the junction, and —●— denotes switching behaviour with 0 domain walls injected into the junction. An ellipse represents the position of the MOKE laser spot on each structure image.

First, the switching behaviour of padless structures was studied, Fig 7.4.a, to estimate the nucleation field of the junction, H_n. The output wire ends were terminated in 60° equilateral triangles. Fig.7.4 (——●——) denotes a hysteresis loop measured at the junction region of a structure with 0 DWs injected into the junction. H_n is 110 Oe, below the switching field for elongated 200 nm wide wires, patterned on the same film with similar end geometries.

Locally measured M-H loops at all parts of the structure were square, suggesting the magnetization reversal mechanism is mediated by DW nucleation followed by rapid DW propagation and expansion and magnetization reversal of the entire structure. Though the structure is of a complex 3-terminal geometry, magnetization reversal occurs at one discrete switching field value, with no evidence of bifurcation of switching pathways, or domain wall pinning in different parts of the structure, for a field applied axially to the output wire. H_n represents the maximum applied field at which these structures are suitable for controlled DW propagation device applications.

Secondly, structure output arms with the same junction and output arm geometry as padless structures, but with 1 DW injection pad, as shown in Fig 7.4.b, were investigated. For the 1 DW device shown in Fig.7.4 (——●——), output switching occurred at H_{1DW} = ±55 Oe. Switching transitions of the loop are sharp, and correspond to time averaging over at least 1000 field cycles.

For the film and structures under discussion, a DW was typically injected from the pad into the input wire at an injection field, H_{inj} = 35-40 Oe. The propagation field of a free DW, H_p, has been measured at typically 10 Oe in FIB milled planar nanowires [Atkinson 2003][Faulkner 2004]. Therefore the magnetization reverses for the input wire. The DW moves through the small kink in the input wires close to the

injection pads, as previously demonstrated [Cowburn 2002], and propagates to the junction, Fig 7.5. Therefore the domain wall can propagate even when the external field is not parallel to the wire long axis.

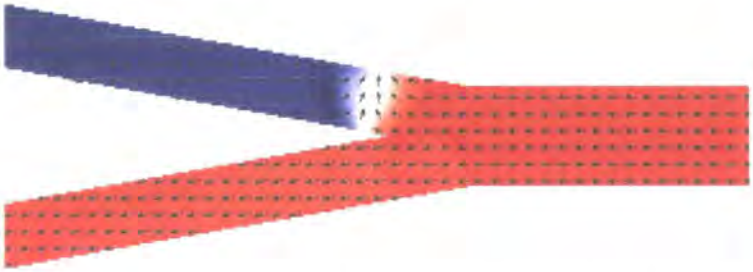

Fig 7.5: Calculated micromagnetic spin structure, in the absence of external field, for 1 DW at the junction region.

When a domain wall is propagated into the junction region, the wall surface area must increase, for magnetization reversal in the output arm to occur. The increase in domain wall surface costs applied field energy. The switching field of the output arm is lower than the H_n of the junction, if one DW is injected into an input wire. It is concluded that a DW is propagated at the domain wall injection field to the junction region, where it resides and gradually expands, analogous to a bubble, with increasing applied field, until a critical depinning field is attained. Then the DW traverses the junction, rapidly propagates along the output wire, without encountering any subsequent pinning sites. Importantly for possible device applications, 1 DW wall incident at the junction in a low externally applied field $H_{ext} < 55$ Oe will fail to switch the device output wire.

Next the case with 2 DWs incident at the device junction is considered, as shown by the micrograph of Fig 7.4.c (previous), and the accompanying MOKE trace (—•—). For the structure with 2 DW injection pads investigated here, the output wire reversed at $H_{2DW} = 37.5$ Oe, just over H_{inj}, the external field value at which 2 DWs are injected into the junction input wires. When 2 DWs are injected into the junction region, they combine to switch the output at a markedly lower field than the 1 DW case.

The DWs are injected into inputs A and B, and propagate directly to the junction region. Here they combine to switch the output at a relatively low field value. The time averaged hysteresis loop measured on the device output is very sharp, and markedly below H_n. Once the pinning potential posed by the junction region is exceeded, reversal of the output wire occurs at one well-defined field value, over many field cycles. The output wire switching behavior in the cases of 0, 1 or 2 DWs incident at the junction differs greatly.

$$H_p < H_{2DW} < H_{1DW} < H_n$$

Sharp time averaged switching transitions indicate that these are all reproducible switching events. (For all cases data was averaged for at least 30 seconds, corresponding to over 800 switching events). No practical limitation on the number of programming cycles is an important prerequisite for any logic applications. The junction geometry is symmetrical, so a DW from either input arm has the same influence on output wire coercivity.

In summary, for a 3-terminal wire geometry the output arm magnetization, and hence the Boolean logical state of the output wire is strongly dependant on the number of domain walls injected into the junction. Coupled with suitable externally applied field sequences, this provides the potential for AND/OR DW logic gate devices. Note that long thin magnetic wires function as conduits for the propagation of magnetic information, at very low fields, with no observable domain wall pinning between junctions [Allwood 2004/1]. Furthermore, the switching field of the output wire in the 2 DW case may in fact be injection pad limited, i.e., it is possible that $H_{2DW} < H_{inj}$.

7.4.3 Logic Function

Table 7.2 describes logic operations for the 3-terminal geometry described, with 0, 1, or 2 DW's incident at the junction, for different externally applied fields, and different initial logical states of the output wire.

45 Oe Junction			
A	B	OUT^0	OUT^1
1	1	1	1
0	1	0	1
1	0	0	1
0	0	0	0

85 Oe Junction			
A	B	OUT^0	OUT^1
1	1	1	1
0	1	1	0
1	0	1	0
0	0	0	0

Table 7.2: Truth tables describing AND/OR operations on the geometry described, in an external field of 45 Oe or 85 Oe. OUT^0 represents the output wire preset to logical "0", and OUT^1 corresponds to the output wire Boolean state set to logical "1".

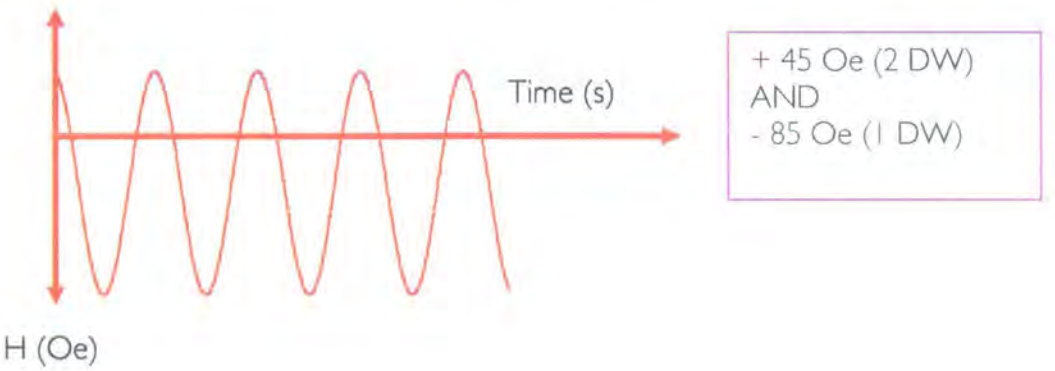

Fig. 7.6: Schematic biased axially applied field, varying over time. True AND switching behaviour of the junction output wire results.

The logical state of the output wire is a function of the initial conditions of the system, as well as the externally applied field, and the number of the DWs incident at the 3-terminal junction. Table 7.2 shows that for 1 DW incident at the junction, the output can be either Boolean "0" or "1" depending on the external field applied – 45 Oe or 85 Oe. This fact is addressed by either using a reset pulse once every field cycle, or using a biased sample, or a biased externally applied field profile. Therefore

the structures described in Section 7.4.2 are referred to as AND/OR-like. True AND or OR DW logic gates are operated with a biased rotating field.

Fig. 7.6 illustrates a schematic biased field profile, to ensure reproducible logical AND switching on the device output wire. The negative component of the applied field in effect acts as a reset operation. Operating field regions depicted in Fig 7.4 are relatively low, therefore Section 7.5 investigates the influence of wire geometry on the switching of these 3-terminal junctions in more detail.

7.5 AND/OR-Like Gate: Junction Geometry

7.5.1 Junction input width: W_{in}

In magnetic structures with restricted geometries and nanoscale critical dimensions, very small changes in structure geometry or dimensions can have a large effect on the switching field of the system. High nucleation fields coupled with low propagation fields afford the potential for complex device geometries, the integration of different junctions in a given field profile, and integration to higher functional device densities and operating frequencies.

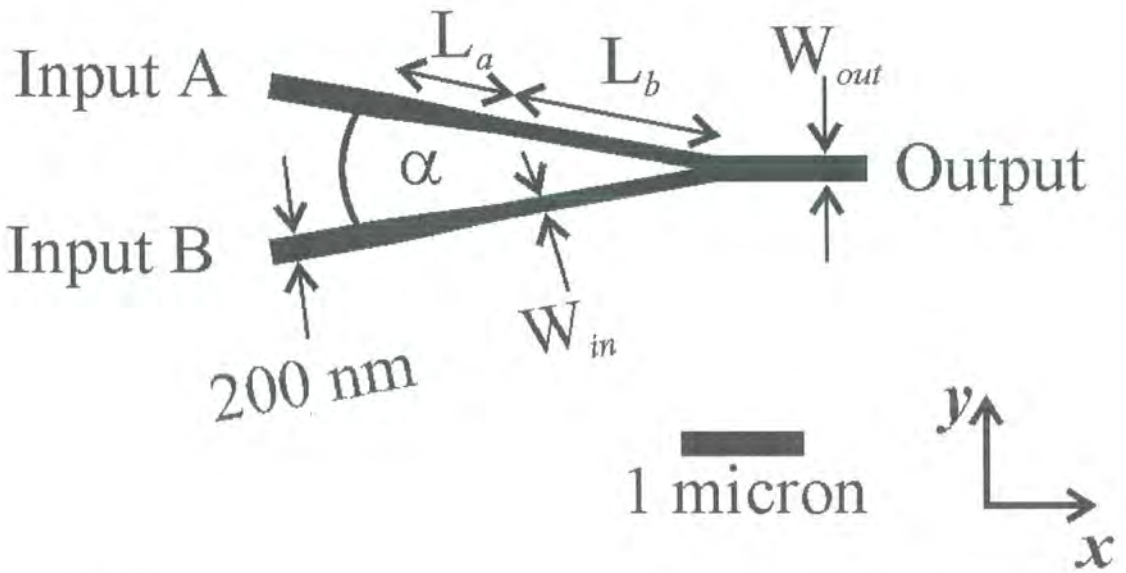

Fig. 7.7: Schematic of a 3-terminal DW junction geometry. Input and output wire widths, are denoted by W_{in} and W_{out} respectively. L_a, represents the taper length, and L_b the distance between taper end and the central junction. Applied field is typically applied parallel to the output wire easy axis.

A 3-terminal junction schematic is shown in Fig. 7.7. The angle between inputs I and II, $\alpha = 20°$. If $\alpha << 20°$, the junction region where input and output arms merge with the output wire has a large volume and width, which results in a lowered nucleation field of the junction, and hence the entire device. In contrast, for $\alpha >> 20°$, it becomes difficult to operate the device by propagation of domain walls in a magnetic field applied along the long axis of the output wire. It is important that the junction inputs are symmetrical, so input domain wall signals act equally on the junction output.

It was found that fabricating a slight taper or narrowing in input wires caused a marked change in the switching field of the junction. The M-H loops shown in Section 7.4 represent M-H loops for nominally identical junction geometries with W_{in} = 175 nm for both input wires and W_{out} = 200 nm. Wires described here are 100-200 nm wide - narrow enough to be technologically interesting, but wide enough to negate the effects of DW pinning at wire edges, due to either Ga^+ lateral implantation or side-wall damage caused by the interaction between the FIB beam and structure sidewalls during fabrication. Junction input and output arm widths were investigated as a function of the number of DWs incident at structure junctions, to determine if geometries with larger operating field margins than those evidenced in Fig. 7.4 could be fabricated. Input wires were narrowed from W_{in} = 100–200 nm by tapering wires over a distance over a fixed length, L_a = 1 μm. The narrow end of the input wire taper was a fixed distance L_b = 2 μm from the meeting point of all 3 wires at the junction. A smoothly tapered domain wall conduit is less likely to cause domain wall pinning, than an abrupt change to W_{in}. First consider the 0 DW wall switching case of injection pad free junctions with W_{in} varied from 100-200 nm, and a fixed width, W_{out} = 200 nm output wire. Magnetic field was applied parallel to the output wire long axis.

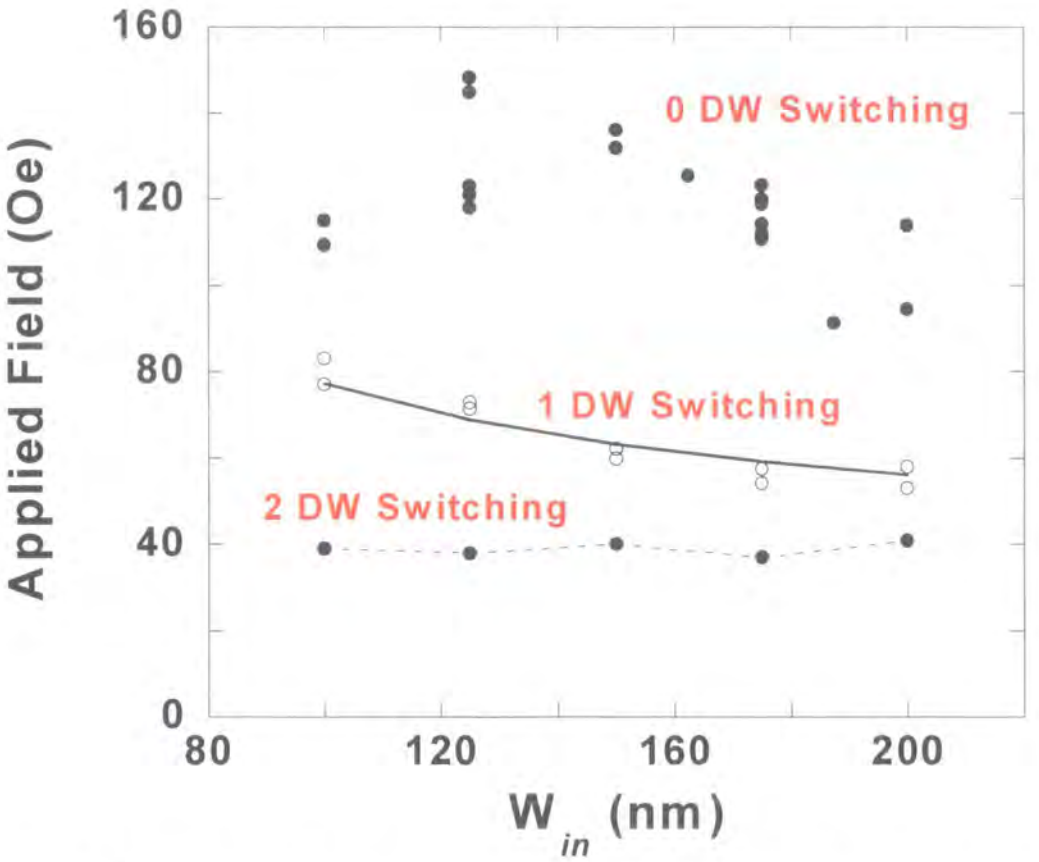

Fig: 7.8 Switching field data for output wires with 0, 1, or 2 DWs incident at the junction, as a function of input wire width, W_{in}. (•) represents H_n for structures with no DW injection pads, (—o—) is the measured switching data of wire outputs with 1 DW at the junction – upper and lower dots correspond H_s and H_c respectively. (—•—) is the measured H_s for an output wire with 2 DWs incident at the junction.

Fig. 7.8 shows that, in general, as input wires are narrowed, the nucleation field of a junction increases. This is analogous to the $H_c \propto T/W$ relation for elongated planar NiFe wires, in which the switching field is governed predominately by the strength of the internal demagnetizing field. As wire inputs are narrowed, spins (even in a geometrically complex junction geometry) are constrained parallel to wire sides, making domain nucleation more energetically costly, due to changes in the self demagnetizing field of the structure.

It is interesting to note that while long thin transition metal wires are assumed to reverse from wire ends, for these 3-terminal structures a small change to junction

geometry, in the central region of the device, has a strong effect on the structure nucleation field. For example varying W_{in} from 175 nm (mean nucleation field, $\overline{H}_n$ = 117 Oe) to 125 nm (mean nucleation field, $\overline{H}_n$ = 130 Oe) shows a small change to input wire width can cause a marked change to the switching field of the entire structure. Because spins in the junction input wires are not aligned with the applied field, nucleation may be more likely in the central part of a structure. Some of the scatter in the experimentally determined H_n for these junctions is attributed to contaminating particles on the domain wall track, [Allwood 2004/1], and to the polycrystalline nature of the film.

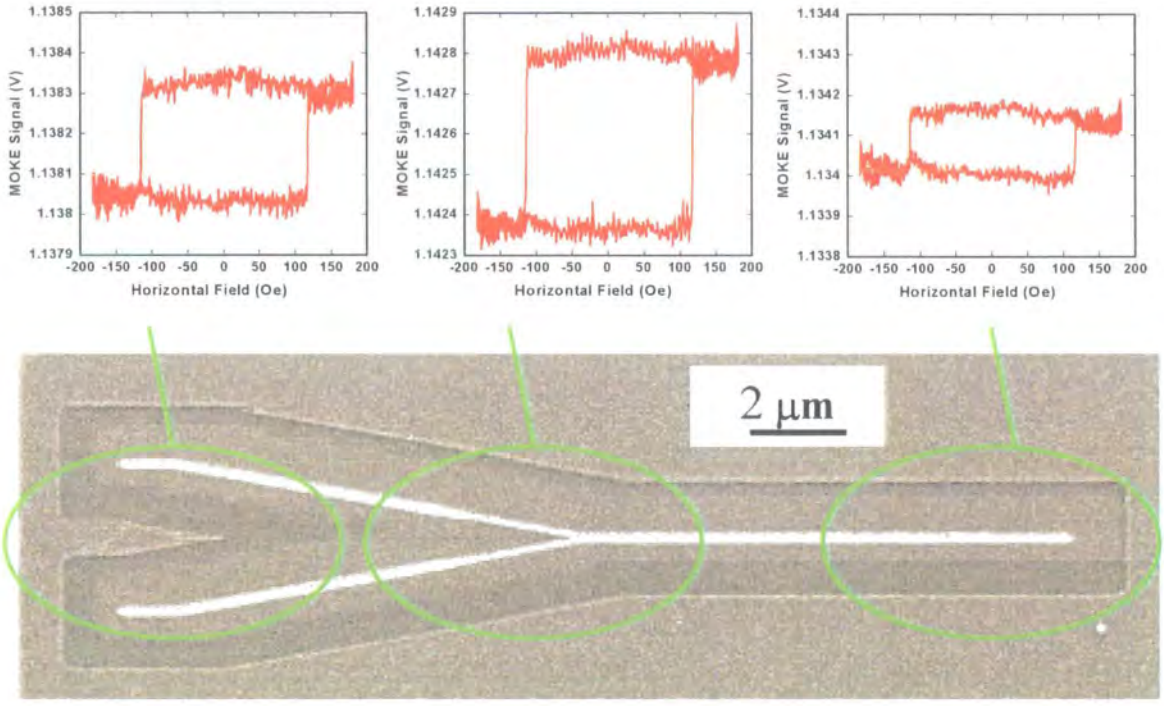

Fig. 7.9: Spatially resolved Moke hysteresis loops on a 3-terminal junction with input wires tapered to W_{in} = 125 nm. The FIB secondary electron image shows the position of the laser spot for each measurement.

Spatially resolved magnetometry measurements were also performed on 3-terminal structures of this nature - Fig. 7.9 (previous page). Magnetization reversal is seen to occur at one discrete switching field across the entire structure – spatially resolved loops have the same H_n. There is no pinning of domain walls observed, after a nucleation event, despite the complex 3-wire geometry. M-H loops differ only in measured signal level (a function of the volume of magnetically active material being probed).

Now we treat the case of 1 DW injected into the junction. W_{in} on wire inputs A and B was varied from 100-200 nm for a fixed width output wire, W_{out} = 200 nm. Fig. 7.8 (previous) shows that for one DW injected into a 3-terminal junction, the output arm-switching field increases with W_{in}.

By field-controlled expansion of the single DW, an energetically favourable reversal mechanism for the junction output wire exists at a field below H_n of a sample with no DW present. It is suggested that H_{1DW} increases with decreasing W_{in}, because of the increased exchange stiffness posed by the DW input wire with no DW present. With 2 DWs injected into the junction region, with W_{in} varied from 100-200 nm, the output switching field was consistently just above H_{inj} [Fig. 7.8 (previous)], and markedly below H_{1DW}. Remarkably, small changes to the geometry of the terminal of complex planar nanostructures (of the order of nanometres) can influence the output wire switching field at micron length scales. While it is interesting to investigate continuous chains of magnetically coupled dots for fundamental studies and interaction effects [Novosad 2003], the continuous wire or domain wall conduit is an effective means of transporting magnetic information between nodes in an information network. This places lower tolerance demands on a network of junctions.

7.5.2 Junction output width: W_{out}

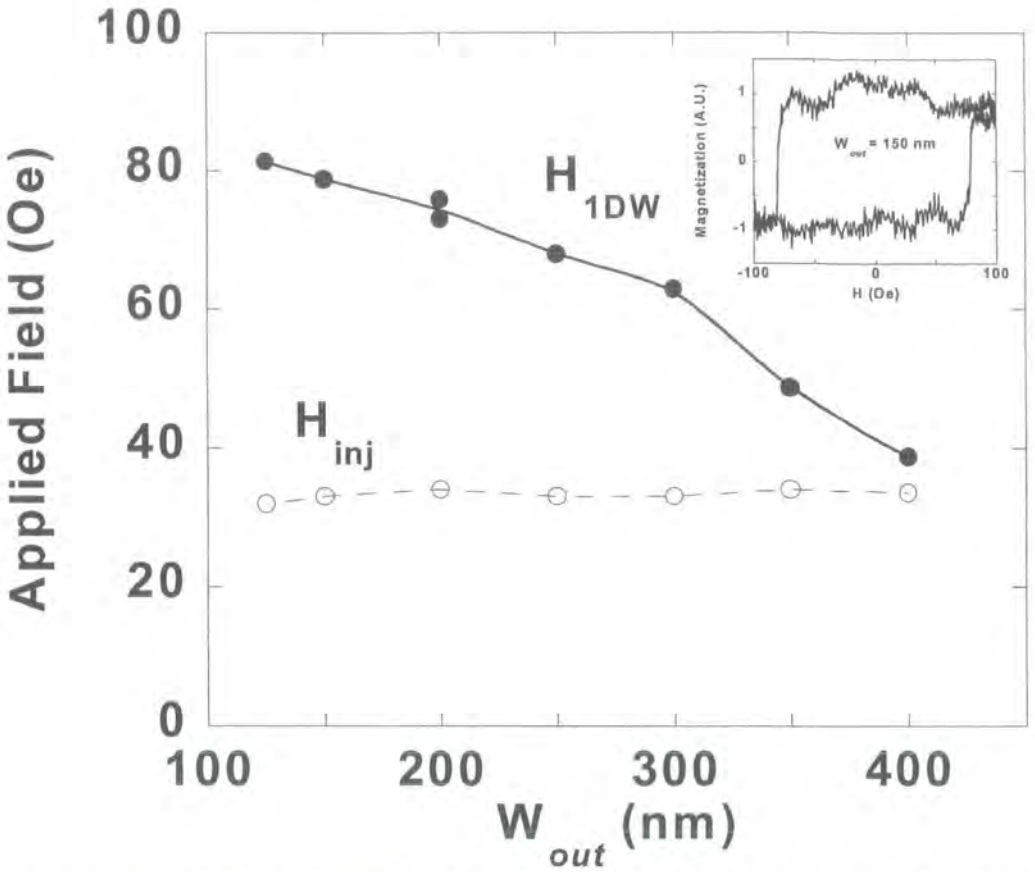

Fig. 7.10: Switching field measurements on 3-terminal junctions for a varied output wire width, W_{out}. H_{inj} represents the switching fields at which a DW was injected into the junction region of each individual test structure. H_{1DW} represents the switching field of output wires of varied width, with 1 DW injected into each junction.

For the case of one DW injected into 3-terminal junctions, the output wire switching field was investigated for W_{out} = 100-400 nm, and fixed input wire widths, W_{in} = 125 nm. For W_{out} = 125-400 nm there is a monotonic decrease in output wire switching field, with 1 DW injected into the junction region. With one DW at the junction, the output wire coercivity, H_{1DW}, decreases with increasing W_{out}. With increasing W_{out} the output wire becomes magnetically softer, due to a larger internal self-demagnetizing field in the output wire.

7.6 Rotating Field & Phase Diagram

7.6.1 Rotating Field

The sense of rotation of an applied magnetic field defines the direction of magnetic signal flow in DW logic devices. It is necessary to link logic gates together so multiple logic functions may be performed. The DW logic scheme offers the prospect of linking multiple logic gates without the need for electrical or semiconductor interconnects, or a layered architecture. NOT, AND/OR, signal fan-out junctions and signal cross-over[1] junctions give logical completeness. DWs propagate around corners of the same chirality as the driving field rotation. Junction magnetic switching in a rotating magnetic field (Chapter 6.4) was investigated to prepare an AND/OR-like junction operating field phase diagram. Note that a biased field can be integrated into a rotating field.

7.6.2 Fan-out

The domain wall fan-out junction was proposed by Cowburn, and acts as a domain wall signal multiplier by dividing one input signal into two [Allwood 2003]. Upon application of a suitable external field, 1 DW propagating into a 3-terminal, 1 input and 2 output "tuning fork" geometry divides into 2 DWs and reverses both output arms of the logic gate.

Fig. 7.12: Schematic of magnetization reversal of a domain wall "fan-out" junction.

Using this structure both input wires of a planar AND/OR-like junction can be operated on with the same DW signals in a rotating field.

[1] The cross over is a cross geometry of 2 wires oriented at right angles to each other. 1 DW may be propagated through the cross geometry, reversing 1 of the 2 wires.

7.6.3 Field Operating Phase Diagrams

The propagation of a single domain wall around a corner was described in Section 6.4.

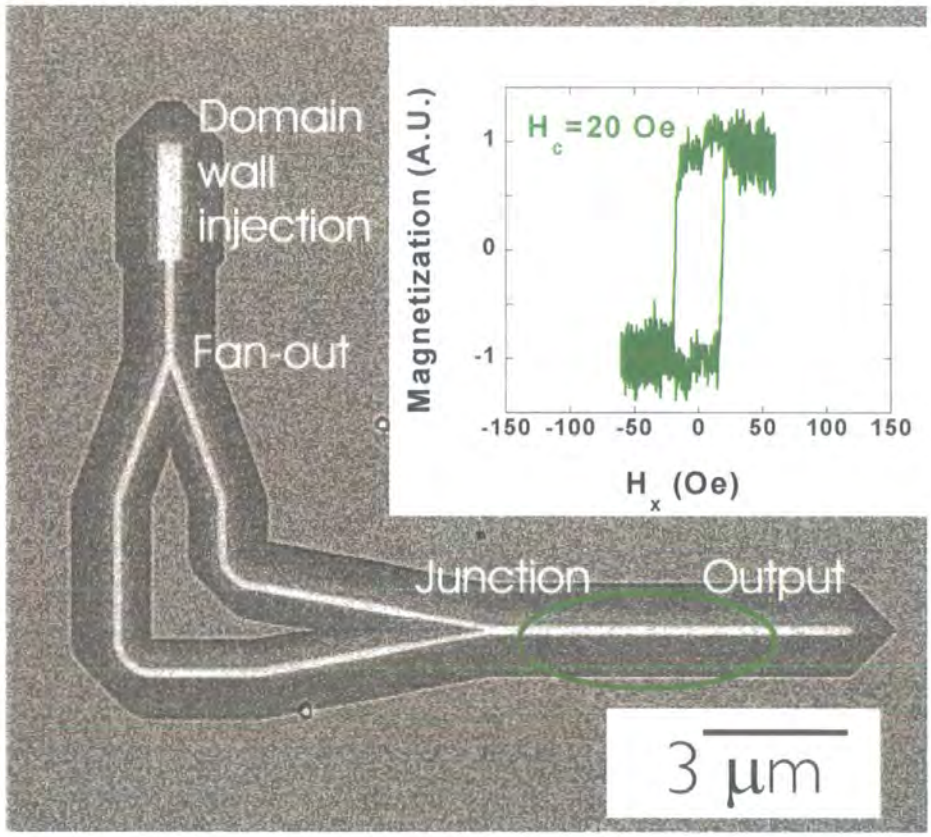

Fig. 7.13: Secondary electron FIB image, and output arm M-H loop, of a planar nanowire circuit with domain wall injection pad, domain wall fan-out junction, 2 corners, an AND/OR-like junction, and output wire. The green ellipse denotes the position of MOKE laser spot during M-H loop averaging. An anti-clockwise 27 Hz rotating field of $|H_x| = 65$ Oe, $|H_y| = 70$ Oe is applied.

Here results of investigations of AND/OR-like junctions integrated with 2 corners and a fan-out junction are shown, in a rotating field. This enables determination of field operating margins [Allwood 2004/1] for integration of AND/OR-like junctions with other logic gates. Consider the structure illustrated in Fig. 7.13. $|H_x|$ and $|H_y|$ are defined as the x and y field components of a 27 Hz, anti-clockwise rotating field. For a suitable $|H_y|$, the domain wall injection pad acts as a domain wall reservoir for the system. 1 DW is injected from the DW injection pad and split into 2 DWs at the fan-out junction, and these 2 separate DW propagate

to the two corners. For a suitable $|H_x|$, the 2 domain walls are propagated from the corners, where they combine at the AND/OR-like junction, and for a given field may switch the output arm. This geometry allows the investigation of 2 DWs injected into the AND/OR-like junction in a rotating magnetic field.

For the patterned t_{NiFe} = 5 nm film under investigation, a DW injection pad injected a DW into a wire at ~40 Oe. However, $|H_y| \geq 70$ Oe is needed to switch the fan-out junction, in the presence of a fixed $|H_x| = 60$ Oe field. At $|H_y| = 70$ Oe, 1 DW is divided into 2, at the fan-out junction, as sketched schematically in Fig. 7.12 (previous). Then 2 DW are propagated to the 2 corners of the planar wire circuit.

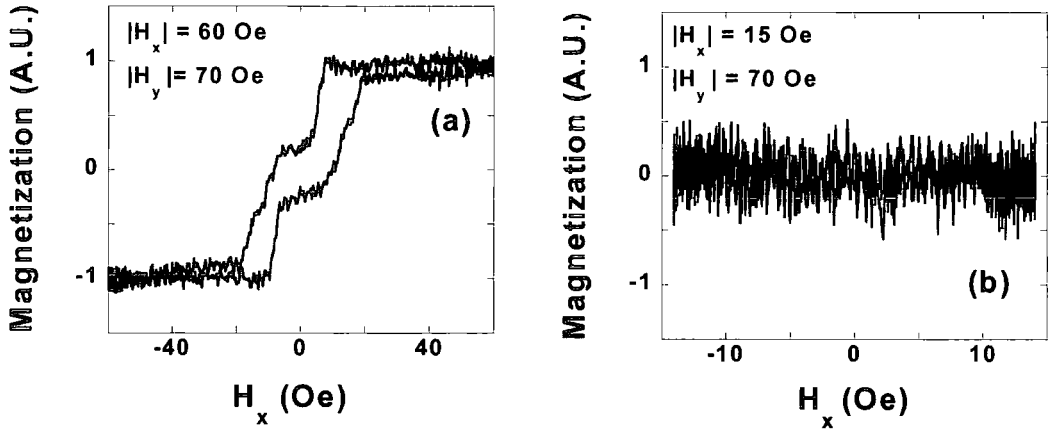

Fig. 7.14: M-H loop (a) was taken at the AND/OR-like junction, simultaneously measuring junction inputs and output. M-H loop (b) was taken on the structure output in a low $|H_x|$ field.

It is important to verify that switching of the output wire shown in Fig. 7.13 is by controlled DW propagation. Fig. 7.14 (a) shows a locally taken M-H loop averaged at the intersection of the 2 junction input wires and the AND/OR-like junction output. A stepped hysteresis loop is evident. The first switching transition is at ± 10 Oe. This is the DW propagation field from a corner as described in Chapter 6, Section 6.4, and is interpreted as DW propagation into the junction region. The second switching transition, at ± 20 Oe, corresponds to the field value at which the output wire is

magnetically switched, after 2 DWs have been divided from the fan-out structure, and propagated around two separate corners, to recombine at the AND/OR-like junction. Furthermore by positioning the MOKE laser spot further along the structure output wire, Fig.7.14 (b) shows that for 2 DWs in the system, for insufficient $|H_x|$, the output wire remains unswitched (only a MOKE background signal is recorded - no hysteresis is measured), even if the $|H_x|$ propagation field for DWs into the junction has been exceeded. Therefore for a low $|H_x|$ the output of the circuit does not switch.

Next the case of only 1 DW injected into an identical AND/OR-like junction (W_{in} = 125 nm, W_{out} = 200 nm), as that treated in Figs. 7.13-14, in an external rotating field is addressed. The geometry shown in Fig. 7.15 (next page) has no DW fan-out structure, but in all other respects is identical to the structure in Fig. 7.13. 1 DW is injected from the injection pad and propagates into the lower output wire of the AND/OR-like junction. For $|H_x|$ = 65 Oe, $|H_y|$ = 70, no DW is present in the upper AND/OR-like input wire – it remains unswitched. For $|H_y| > \sim 140$ Oe, the upper DW wire input switches. The inset M-H loop evinces very sharp magnetic switching behaviour at H_c = 60 Oe. Localized MOKE measurements show that the output arm switching is triggered by a magnetization reversal event in the DW injection pad, and subsequent propagation of a DW to the corner, and thence to the AND/OR-like gate junction. Here the DW waits until the $|H_x|$ component is sufficient to enable switching of the output arm. Information in the system thus flows in an anti-clockwise sense.

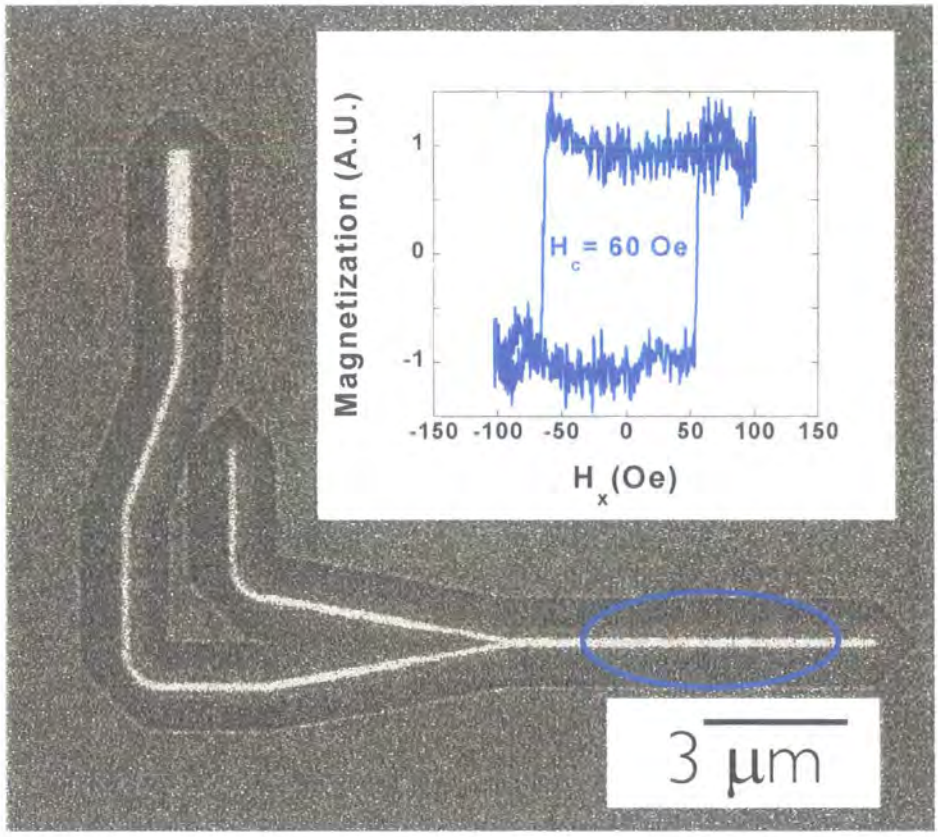

Fig. 7.15: Secondary electron FIB image and inset output arm magnetic switching, in a planar nanowire circuit with domain wall injection pad, an AND/OR-like junction, and output wire. The blue ellipse denotes the position of MOKE laser spot during M-H loop acquisition. An anti-clockwise 27 Hz rotating field of $|H_x| = 65$ Oe, $|H_y| = 70$ Oe is applied.

For 12 nominally identical AND/OR-like junctions further switching results are set forth in Table 7.3. Given restrictions on fabrication accuracy such as stage drift during patterning, or particulate contamination, reasonably reproducible magnetic switching is shown between separate structures.

Sample	*H_c(0DW) (Oe)*	*H_c(1DW) (Oe)*	*H_c(2DW) (Oe)*
1	138 ± 4	70 ± 4	16 ± 4
2	141 ± 5	65 ± 3	21 ± 2
3	139 ± 5	61 ± 3	33 ± 4
4	144 ± 4	78 ± 6	25 ± 7

Table 7.3: Typical AND/OR-like output arm switching data, for 12 separate structures, with 0, 1, or 2 domain walls injected into the junction, in a rotating field. Error bars account for field values at which M-H loops become magnetically saturated and start to switch respectively.

To summarize, with 2 DWs propagating into the AND/OR-like junction, the output arm coercivity, $H_c \sim 25$ Oe. For 1 DW propagating into the junction, $H_c \sim 65$

Oe. For structures with no DW injection pad, nucleation from the junction region was ~ 140 Oe. Sections 7.4-7.5 treat the switching of 3-terminal junctions in either a field applied along the long axis of junctions or a rotating field. Allwood et al. recently described the field operation margins of DW NOT gates with operating field phase diagrams [Allwood 2004/1]. By propagating 0, 1, or 2 DWs around corners into separate AND/OR-like junctions, varying the rotating field components, and studying device output wire magnetic switching, a similar operating field phase diagram was prepared for the AND/OR-like gate junction.

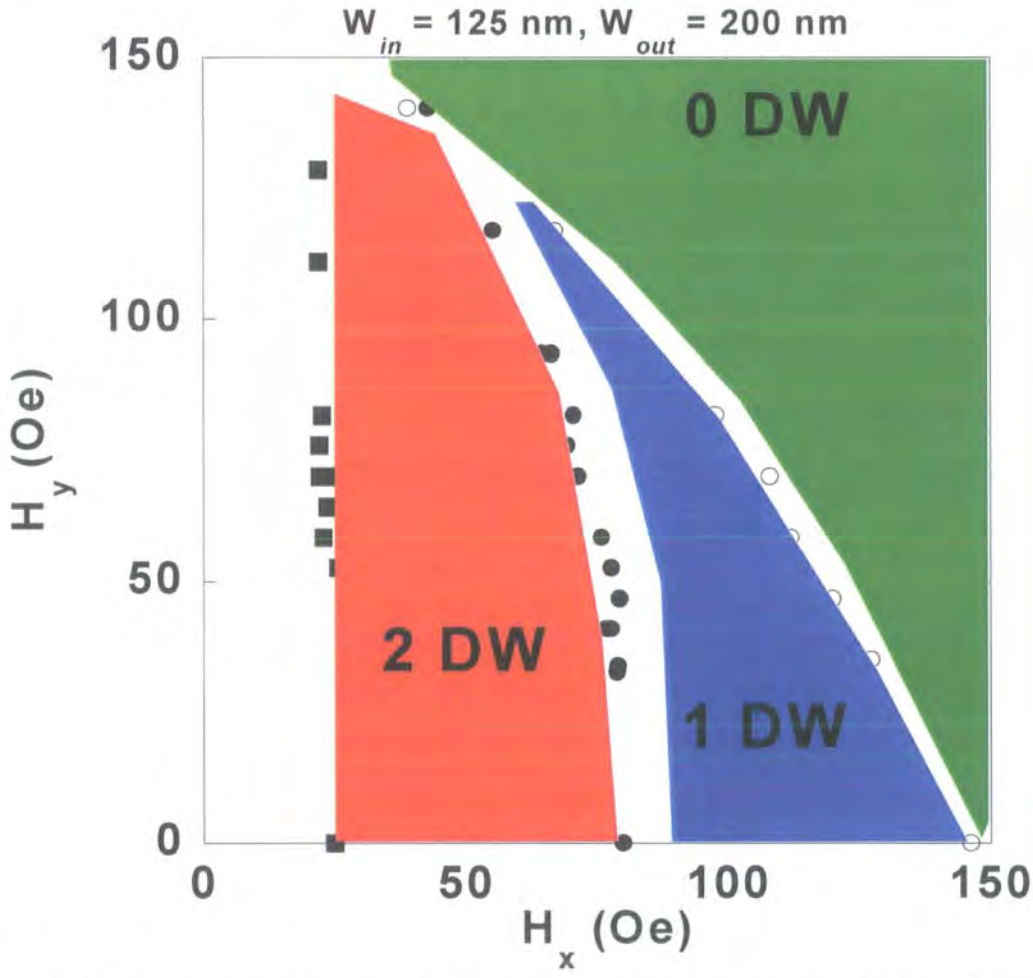

Fig. 7.15: Experimentally determined phase diagram describing the magnetic switching of AND/OR-like junction output wire, with 0 ■, 1 ■, or 2 ■, domain walls incident at the junction, in a 27 Hz anti-clockwise rotating field.

Phase diagram: 0 DW

Consider Fig. 7.15. In a rotating field the green area represents the field values at which the output wire switches, with no free DWs propagated into the junction. The output wire therefore reverses by a nucleation event. The $|H_y|$ component of the rotating vector field forces the magnetization to rotate away from the easy axis direction, therefore lowering the effective nucleation field, as $|H_y|$ increases. For field values below the green region of the field map, the output wire will not switch.

Phase diagram: 1 DW

For 1 DW incident at the junction, in a rotating field, the output wire-switching field is reduced. The blue region of the phase diagram indicates field values at which output wire switching is triggered after the injection of 1 DW into the junction. If applied field values are too high, the output wire may switch by a nucleation event – marked in green. For low $|H_x|$, 1 DW remains trapped at the junction and the output arm does not switch.

Phase diagram: 2 DW

The red region of the phase diagram indicates field values at which output wire switching is triggered after the injection of 2 DWs into the junction.

The prototype structures investigated in this chapter used 3 structures at a time to investigate output wire switching field with either 0, 1, or 2 DWs at the junction. The geometry presented here has subsequently been integrated into complex planar DW functional magnetologic circuits with NOT-gates, signal fan-out, and DW cross over junctions unified in one circuit [Allwood 2004/2].

7.7 Universal logic gates

7.7.1 NAND Gate

By localizing all logic operations in a single junction, device packing density, and operating frequency are greatly enhanced. Power consumption and unwanted heating is reduced. The NAND gate is an AND gate signal inverter [Sorge 2004].

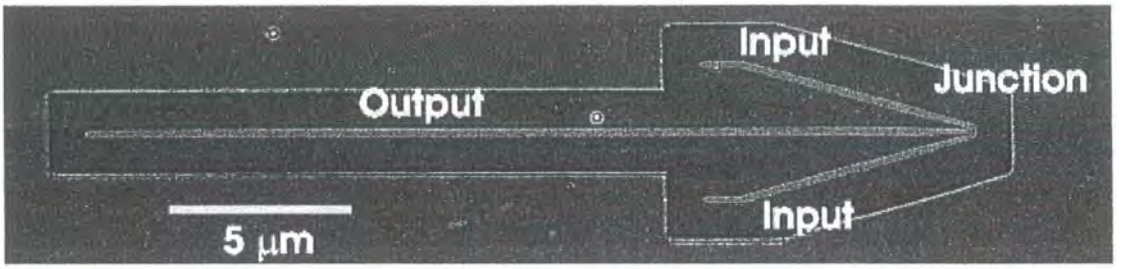

NAND	*A*	*B*	*Output*
	0	0	1
	0	1	1
	1	0	1
	1	1	0

Fig. 7.16: Secondary electron FIB image of a NAND gate test structure, and NAND gate truth table.

It was hoped that 1 DW or 2 DWs incident at the 3-terminal junction would result in markedly different reproducible switching fields of the device output wire, and provide the potential for a NAND gate. Fig 7.17 (next page), shows M-H loops for NAND gate test structures, with no domain wall injection pads. Sharp switching transitions are evident on samples 1-3, for a 27 Hz axially applied external field, with switching fields of ~ 120 Oe for the entire structure. As the junction is rounded or flattened, samples 4-5, multiple switching transitions are evident at M-H loops measured on the junction region. The different arms of test structures reverse at different field values. Due to the rounded junction geometry, a perfect single domain state at remanence is not energetically favourable, and a lower nucleation field for some parts of the structure results [Liu 2004].

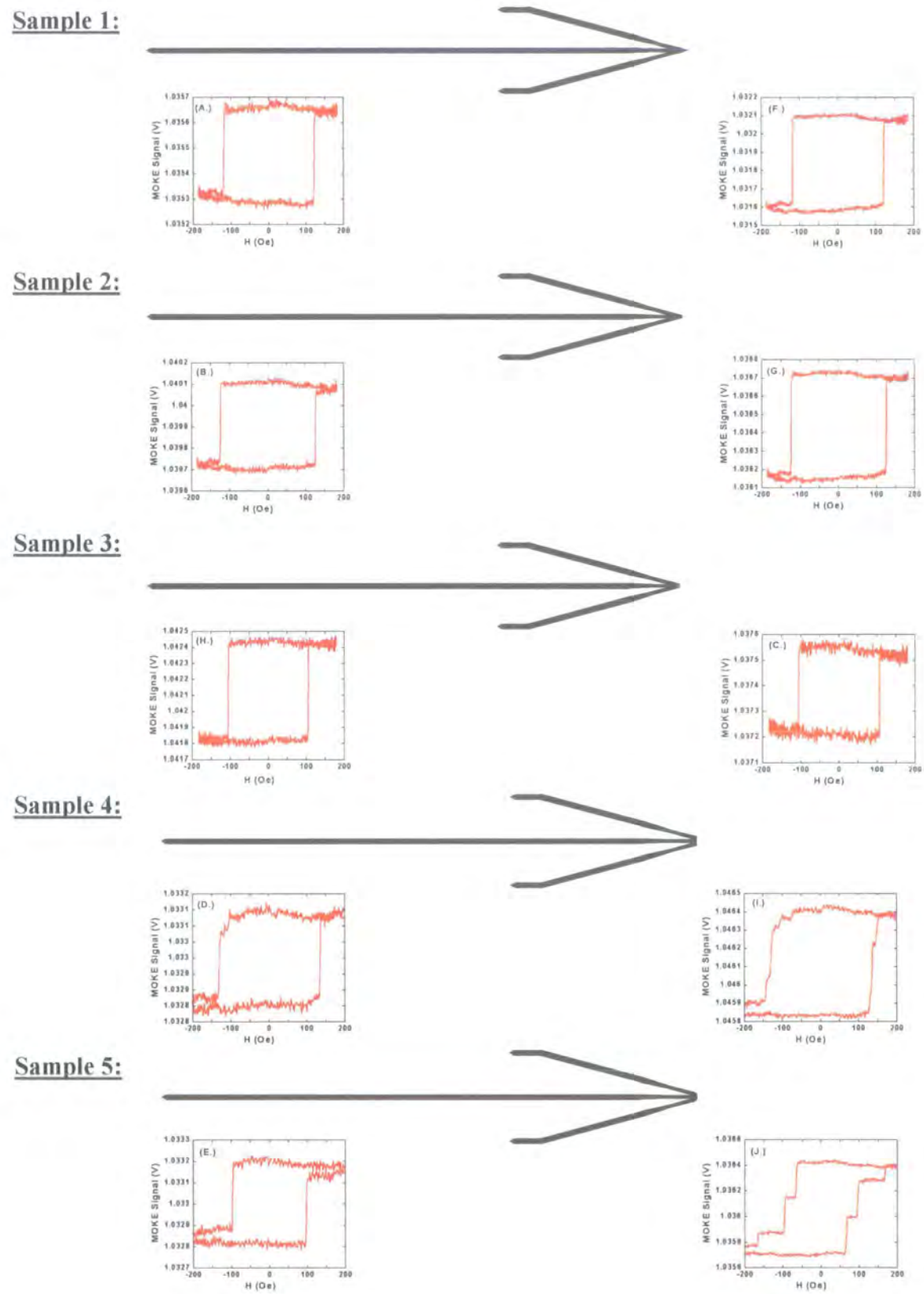

Fig. 7.16: M-H loops for 3-terminal structures of different junction geometries, for NAND gate investigations. Loops (A-E) correspond to hysteresis loops averaged on the central output wire of the test structures. Loops (F-J) are loops were averaged on the junction regions of samples 1-5 shown.

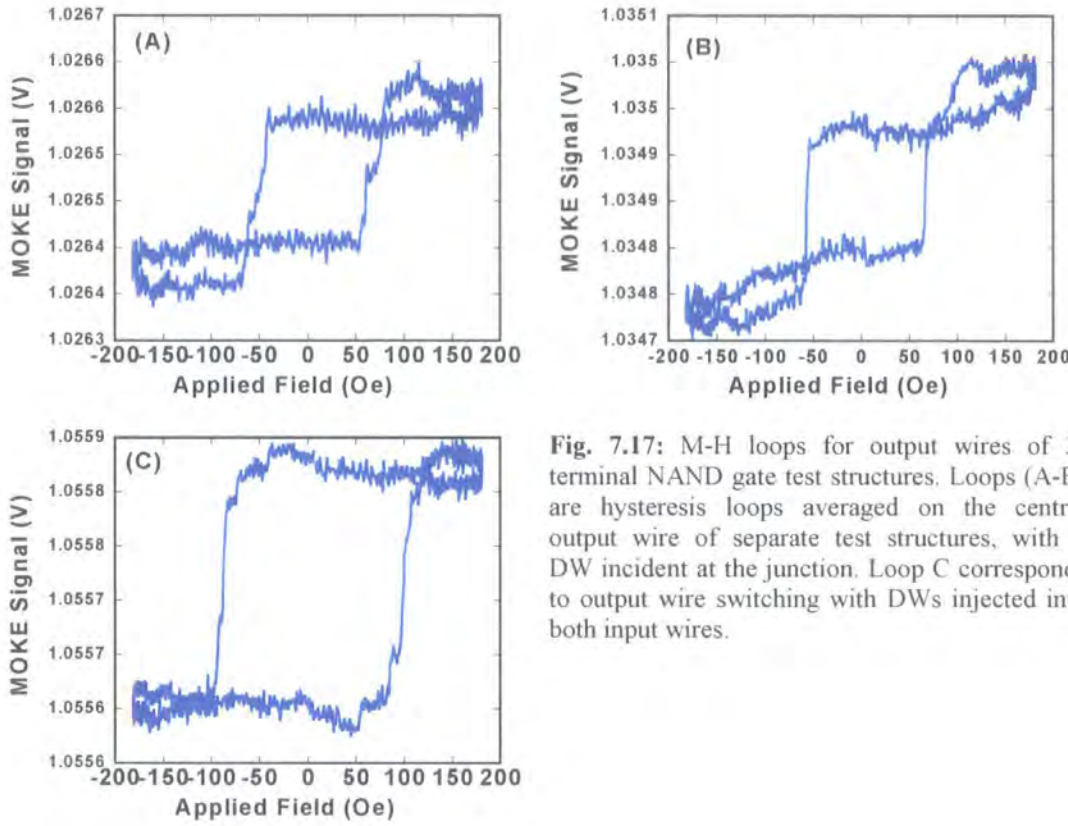

Fig. 7.17: M-H loops for output wires of 3-terminal NAND gate test structures. Loops (A-B) are hysteresis loops averaged on the central output wire of separate test structures, with 1 DW incident at the junction. Loop C corresponds to output wire switching with DWs injected into both input wires.

It was found that injecting 1 DW into NAND gate test structures (Fig. 7.17 A-B) led to a lowering of the output switching field relative to control samples (Fig 7.16) with no DW injection pad. Injecting 2 DWs into a nominally identical junction led to fully saturated output wires at a higher field value than the 1 DW case. For the many test structures investigated 2 DW incident at the NAND gate terminal did not combine to switch the output wire at a markedly lower switching field than the 1 DW case, to provide the switching contrast that for an appropriate external field could lead to a DW NAND gate.

7.7.2 Majority Gate

The majority gate is a universal logic gate that offers the prospect of logical completeness in a single gate or terminal. A majority gate has one central junction or operating region addressed by three nominally identical inputs, with one output. The majority gate output assumes the binary state of the majority of the inputs. A majority gate may be biased or locked by fixing one of the 3 gate inputs to a logical "1" or "0." If the fixed input is in the "0" state, an AND function is performed by the other two inputs. A biased or "reduced" majority gate serves as a programmable AND/OR gate.

Majority	*A*	*B*	*C*	*Output*
	0	0	0	0
	1	0	0	0
	0	1	0	0
	0	0	1	0
	1	1	0	1
	1	0	1	1
	0	1	1	1
	1	1	1	1

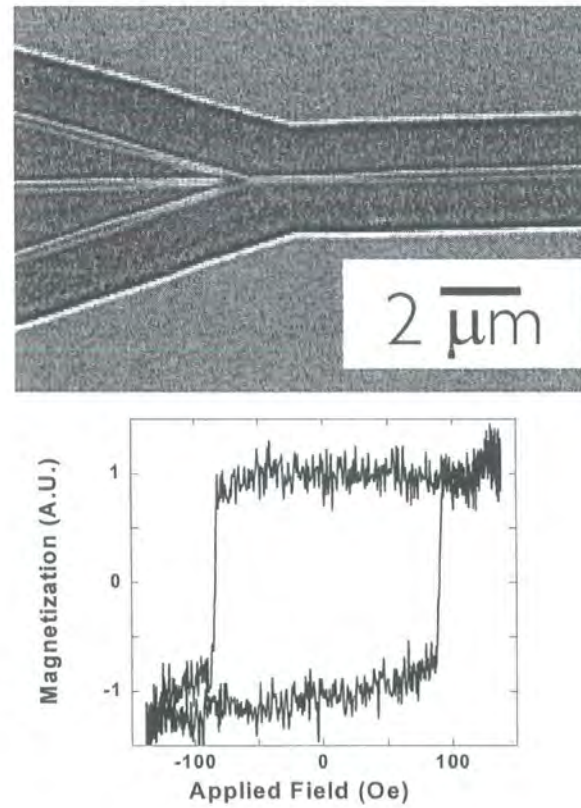

Fig. 7.18: Majority gate truth table, electron micrograph of a 4-terminal majority gate test structure, and M-H loop of a 4-terminal structure.

Fig.7.18 shows the type of 4-terminal geometry fabricated and investigated magnetically. It was found that the nucleation field of 4-terminal junctions was increased by narrowing input wires and increasing the angle between input wires. We did not succeed in reproducibly controlling the output wire magnetization state as a function of the number of DWs (1-3) at the junction.

7.8 Discussion & Conclusions

The magnetization reversal of complex planar magnetic nanostructures, mediated by controlled domain wall propagation has been studied. By engineering the geometry of continuous 3-terminal ferromagnetic wire junctions, the magnetic switching field of the output wire can be controlled.

The micromagnetics of a DW NOT gate was studied numerically to operating frequencies in excess of 100 MHz. The junction reversal process proceeds by the division of a single domain wall into 2 domain walls, to switch magnetization in both the junction and the output arm. The NOT gate acts as a domain wall fan-out, or signal divider, reversing the output wire magnetization relative to the direction of DW propagation. In each operation the output of the central stub region is discarded. If the central stub is too short (~100-300 nm) no domain wall exists in the system at remanence, and the device does not function. If the junction is too long, it becomes magnetically "harder," leading to lower field operating margins for the device.

I have demonstrated that the magnetization state of an elongated output wire from a 3-terminal wire junctions may be set by the field controlled displacement of 1 or 2 domain walls into the junction. This provides the magnetic switching contrast necessary for DW AND/OR gates in a biased field.

Small changes to the wire widths at the junction geometry (~25 nm) are found to have a significant effect on the output wire switching field. For 1 DW incident at the junction reducing input wire widths from 200-100 nm leads to an increase in the output wire switching field. Increasing the output wire width leads to a reduction in the output wire switching field.

A prerequisite for the DW NOT gate is a rotating field. AND/OR-like test structures with [0-2] DWs incident at nominally identical junctions were characterised

in a 27 Hz anti-clockwise rotating field. The AND/OR-like junction was successfully integrated with DW fan-out signal dividers. An operating field phase diagram for AND/OR junctions in a rotating field is presented, needed for integration of the structure with other DW magnetologic gates.

DW logic devices are flat, cheap to fabricate, and promise low power consumption. Test structures investigated here are tens of microns in length, but the logic junctions have submicron critical dimensions. In theory the junction dimensions are limited only by the width of domain wall. For high integration densities functional junctions could be packed approximately 5-10 domain wall widths apart.

In the future more complex 3-D geometries, a universal DW magnetologic gate, or a DW logic paradigm realised in a next generation spintronics material could be envisaged.

7.9 References

[Allwood 2004/1] D. A. Allwood, Gang Xiong, M. D. Cooke, C. C. Faulkner, D. Atkinson, R. P. Cowburn, J. Appl Phys. **95**, 8264 (2004)

[Allwood 2004/2] D. A. Allwood, Gang Xiong, R. P. Cowburn [Unpublised results]

[Allwood 2003] D. A. Allwood, Gang Xiong, R. P. Cowburn, [Unpublised results]

[Allwood 2002/1] D. A. Allwood, Gang Xiong, M. D. Cooke, C. C. Faulkner, D. Atkinson, N. Vernier, R. P. Cowburn, Science, **296**, 2003 (2002)

[Allwood 2002/2] D. A. Allwood, N. Vernier, Gang Xiong, M. D. Cooke, D. Atkinson, C. C. Faulkner, R. P. Cowburn, Appl. Phys. Lett. **81**, 4005 (2002)

[Atkinson 2003/1] D. Atkinson, D. A. Allwood, Gang Xiong, M. D. Cooke, C. C. Faulkner, R. P.Cowburn, Nat. Mat. **2**, 82, (2003)

[Atkinson 2003/2] D. Atkinson, D.A. Allwood, C.C. Faulkner, Gang Xiong, M.D. Cooke, R.P. Cowburn, IEEE Trans. Magn. **39**, 2663 (2003)

[Bennion 1969] D. R. Bennion, H. D. Crane, D. Nitzan, *"Digital Magnetic Logic"*, McGraw-Hill, New York, 1969

[Black 2000] W. C. Black, B. Das, J. Appl. Phys. **87**, 6674 (2000)

[Bobeck 1975] A. H. Bobeck, E. Della Torre, *"Magnetic Bubbles"*, North Holland, Amsterdam, **14**, (1975)

[Coey 2004] J. M. D. Coey, S. Santivo, J. Phys. D. **37**, 988, (2004)

[Chikazumi 1964] S. Chikazumi, S. H. Charap, *"Physics of Magnetism,"* Wiley, New York, (1986)

[Cowburn 2002/1] R. P. Cowburn, D. A. Allwood, G. Xiong, M. D. Cooke, J. Appl. Phys. **91**, 6949 (2002)

[Cowburn 2000/2] R. P. Cowburn, M. E. Welland, Science, **287**, 1466 (2000)

[Csaba 2002] G. Csaba, A. Imre, G. H. Bernstein, W. Perod, V. Metlushko, IEEE Trans. Nanotech. **1**, 209 (2002)

[Faulkner 2004] C. C. Faulkner, M. D. Cooke, D. A. Allwood, D. Petit, D. Atkinson, R.P. Cowburn, J. Appl. Phys. **95**, 6717 (2004)

[Hirohata 2000] A. Hirohata, C. C. Yao, H.T. Leung, Y. B. Xu, C. M. Guertler, J. A. C.Bland, IEEE Trans. Mag. **36**, 3068 (2000)

[Johnson 2000/1] M. Johnson, B. R. Bennett, P. R. Hammar, M. M. Miller, Solid State. Elect. **44**, 1099 (2000)

[Johnson 2000/2] M. Johnson, IEEE Trans. Mag. **36**, 2758 (2000)

[Johnson 1993] M. Johnson, Science, **260**, 320 (1993)

[Koch 2004] C. Pampuch, A. Ney, R. Koch, Europhys. Lett. **66**, 895 (2004)

[Liu 2004] X. Liu, J. N. Chapman, S. McVitie, C. D. W. Wilkinson, Appl. Phys. Lett. **84**, 4406, (2004)

[Miyake 2002] K. Miyake, K. Shigeto, K. Mibu, T. Shinjo, T. Ono, J. Appl. Phys. **91**, 3468 (2002)

[Nakatani 2003] Y. Nakatani, A. Thiaville, J. Miltat, Nat. Mat. **2**, 521 (2003)

[Ney 2003] A. Ney, C. Pampuch, R. Koch, K. H. Ploog, Nature, **425**, 485 (2003)

[Novosad 2003] V. Novosad, M. Grimsditch, J. Darrouzet, J. Pearson, S. D. Bader, V. Metlushko, Y. Otani, H. Shima, K. Fukamichi, Appl. Phys. Lett. **82**, 3716, (2004)

[O'Dell 1974] T. H. O'Dell, *"Magnetic Bubbles"*, Macmillan, London, (1974)

[Pampuch 2004] C. Pampuch, A. Ney, R. Koch, Europhys. Lett. **66**, 895, (2004)

[Pampuch 2003] C. Pampuch, A. K. Das, A. Dey, L. Däweritz, R. Koch, K. H. Ploog, Phys. Rev. Lett. **91**, 147203 (2003)

[Parkin 1999] S. S. P. Parkin, K. P. Roche, M. G. Samant, P. M. Rice, R. B. Beyers, R. E. Scheuerlein, E. J. O'Sullivan, S. L. Brown, J. Bucchigano, D. W. Abraham, Yu Lu, M. Rooks, P. L. Trouillourd, R. A. Wanner, W. J. Gallagher, J. Appl. Phys. **85**, 5828 (1999)

[Prinz 1998] G. A. Prinz, Science, **282**, 1660 (1998)

[Richter 2002] R. Richter, L. Bär, J. Wecker, G. Reiss, Appl. Phys. Lett. **80**, 1291 (2002)

[Sorge 2004] K. D. Sorge, A. Kashyap, R. Skomski, L. Yue, L. Gao, R. D. Kirby, S. H. Liou, D. J. Sellmyer, J. Appl. Phys. **95**, 7414 (2004)

[Tang 2004] H. X. Tang, S. Masmanidis, R. K. Kawakami, D. D. Awschalom, M. L. Roukes, Nature, **431**, 52 (2004)

[Wadhwa 2004] Pooja Wadhwa, M. B. A. Jalil, Appl. Phys. Lett. **85**, 2367 (2004)

Chapter 8. Summary And Future Work

"I sought a theme and sought for it in vain
I sought it daily for six weeks or so..."
The Circus Animals' Desertion, W. B. Yeats

8.1 Introduction

Two of the principal themes of this thesis are:

FIB modification of magnetic properties of in plane magnetized bilayers

Measured room temperature ferromagnetism can be quenched for 2 nm thick in-plane magnetized $Ni_{81}Fe_{19}$ ultra-thin films at very low doses of heavy Ga^+ ion irradiation (8×10^{13} ions/cm^2), by addition of an upper interface or capping layer. The reduction in measured magnetic properties is explained by radiation-induced transport of interfacial atoms. Sample coercivity, uniaxial anisotropy field, remanence ratio, and saturation magnetization can be tailored by controlled Ga^+ ion doses in capped ultra-thin film samples. Fabrication of buried magnetic nanowires is demonstrated.

FIB lateral patterning of complex planar wire geometries for magnetization reversal by controlled domain wall displacement

Reproducible domain wall displacement through a smoothly rounded 90° corner geometry, and domain wall pinning at trapping sites of 35 nm depth is demonstrated. The switching field of the output wire in a three-terminal ferromagnetic wire junction can be well controlled according to the number of domain walls (0-2) incident at the junction. This makes it suitable for domain wall magnetologic applications.

In the following, results presented in Chapters 4-7 are summarised, and some possible avenues for future research are briefly suggested.

8.2 Focused Ion Beam patterning of planar magnetic nanowires

The magnetic switching field of 60-500 nm wide planar $Ni_{81}Fe_{19}$ wires fabricated by FIB displayed an inverse width dependence, consistent with a Stoner-Wohlfarth model. Wires were fabricated by localized FIB subtractive surface milling. Wire easy axis coercive field, and hard axis anisotropy field are found to be highly sensitive to ion beam raster direction during wire fabrication. For reduced wire lateral dimensions the effect of beam raster direction becomes more pronounced. Milling (//) to the wire long axis results in higher sample coercivity, anisotropy field, and better switching tolerance for wire arrays. These effects are attributed to ion beam interaction with wire sidewalls during fabrication.

Fabrication of narrower wires then 60 nm is in theory possible. For narrower wires a lower aspect ratio than 10:1 may be useful to lower the wire coercivity. A study of this nature could give insight into lateral ion implantation into wire sidewalls during fabrication.

An investigation into the feasibility of using the FIB fabrication process for transport property investigations of magnetic nanostructures is currently needed.

8.3 Focused ion beam irradiation of magnetic bilayers

Ultrathin $Ni_{81}Fe_{19}$ films embedded between a non-magnetic cap and Si substrates were magnetically quenched by ion beam intermixing, while leaving the capping layer intact. Typically 30 keV Ga^+ ions can surface sputter ~ 10 target atoms per incident ion, but up to ~ 10^3 atoms may be displaced on short lengthscales in the target bulk. Therefore buried in-plane magnetized $Ni_{81}Fe_{19}$ magnetic layers were ferromagnetically quenched at significantly lower ion doses then $Si/Ni_{81}Fe_{19}$ films

irradiated at the free NiFe-vacuum interface. Capped $Ni_{81}Fe_{19}$ films were reproducibly ferromagnetically quenched at ion doses as low as $\Phi = 8 \times 10^{13}$ ions/cm^2. Low dose patterning of in plane magnetized bilayer films promises rapid prototyping of devices and near-planar topologies.

Bilayer easy axis coercivity, uniaxial anisotropy field, remnant magnetization, and absolute magnetization as indicated by MOKE, were tailored by controlled radiation doses. Functional buried 200 nm wide nanowires embedded between a non-magnetic capping layer and substrate were fabricated.

By using a localized ion dose below Φ, magnetic softness of a bilayer can be locally modified. Wires with a "high" coercivity can be embedded in an irradiation softened surrounding magnetic film of "low" coercivity. Stepped M-H loops result, with interesting potential field sensor applications.

Critically, the ion dose to quench measured ferromagnetism, Φ, was found to be proportional to $(t_{NiFe})^2$ where t_{NiFe} is the $Ni_{81}Fe_{19}$ thickness. In the context of magnetism, light and heavy ion irradiation is used to modify the properties of monolithic films, exchange biased samples, inter-layer exchange coupled samples, giant magnetoresistive media, perpendicular magnetic anisotropy media, and standard thin film capped samples. To my knowledge, the simple square law presented here is the first quantitive description of the effect of ion beam intermixing on magnetic properties of a sample.

Over the coming years, some groups will continue to spend much time investigating ion beam intermixing effects by detailed studies of different ion doses, energies and species, layer species, and layer thicknesses. It is clear FIB gives more aggressive intermixing than light ion irradiation. The magnetism community could

turn to basic techniques such as Rutherford backscattering to further investigate mixing effects [Tsaur 1978].

A more fundamental study may be to verify the square root relationship for both PMA and in plane magnetized films, for both light and heavy ion irradiation. This fundamental study could unify much current work on irradiation of layered media, and help to quantify the ion induced atomic transport at irradiated interfaces.

Further, it is necessary to verify the extent of Ga^+ ion lateral straggle in layered media - this is another pressing study. This is important for determining the minimum resolvable magnetic feature sizes possible in FIB fabricated layered structures.

8.4 Domain wall trapping

Domain wall propagation around smoothly rounded corner geometries was experimentally demonstrated. By localized domain wall nucleation in one arm of an L-shaped rounded corner geometry, and investigating domain wall propagation in the other arm of the structure an average domain wall propagation field of $\overline{H}_P = 7 \pm 3$ Oe was found in an externally applied rotating field. A linear fit approximately explained the depinning field from symmetric traps of depths from 35-125 nm.

In principle, sub-20 nm trapping depths are possible. A detailed phase diagram of depinning field vs. trap dimensions in units of the domain wall width would be an interesting fundamental study. Asymmetric domain wall traps with different pinning potentials may have interesting applications in the future.

Simply line scanning the FIB across patterned structures may facilitate an alternate method of creating domain wall traps.

Being able to isolate a single domain wall at a corner, or a trap with a low pinning potential is useful in the context of future dynamics, and especially spin polarized current domain wall excitation and displacement studies [Chappert 2004]. For example, domain wall trapping and current induced domain wall motion in ferromagnetic semiconductor structures was recently reported [Ohno 2004].

8.5 Domain wall logic

A 3-terminal continuous ferromagnetic wire junction was described. The output wire-switching field is strongly dependent on the number of domain walls (0-2), incident at the junction. This makes the junction a suitable candidate for integration with existing domain wall magnetologic devices, to perform logical AND/OR operations for a suitable external field.

Domain wall logic circuits will continue to be investigated in the coming years. Challenges are to increase gate-packing density, and field tolerance-operating margins, while investigating dynamic effects. The promise of low power consumption and simple to fabricate 2-D architectures promise many applications, such as low cost consumer goods.

Imaging complex wire circuit switching by controlled domain wall motion using a technique such as Lorentz microscopy is an interesting prospect.

The AND/OR-like junction, NOT gate, and the domain wall "fan-out" signal divider all consist of 3-terminal junctions which function by the field controlled propagation of 1-2 domain walls. A detailed fundamental investigation of the micromagnetic energy terms involved in the magnetic switching of these structures may be useful. The influence of complex geometries and spatial confinement on

domain wall size and properties is an interesting emerging research topic [Jubert 2004].

A universal domain wall magnetologic gate, the majority gate, may be experimentally realizable. Domain wall input wires need to be engineered by a geometrical modification, or otherwise, so they are not magnetically switched before the output wire with 0-2 domain walls injected into input wires of a 4-terminal junction.

Some hybrid field/spin-polarised current, or spin-polarized current domain wall device paradigms may emerge. Domain wall logic in ferromagnetic semiconductors is also a possibility – domain wall magnetoresistance and dynamics experiments are already underway [Tang 2004].

8.6 References

[Chappert 2004] C. Chappert, T. Devolder, **432**, 162 (2004)

[Jubert 2004] P. –O. Jubert, R. Allenspach, A. Bischof, Phys. Rev. B, **69**, 220410(R), (2004)

[Ohno 2004] M. Yamanouchi, D. Chiba, F. Matsukura, H. Ohno, Nature, **428**, 539 (2004)

[Tang 2004] H. X. Tang, S. Masmanidis, R. K. Kawakami, D. D. Awschalom, M. L. Roukes, Nature, **431**, 52 (2004)

[Tsaur 1978] B. Y. Tsaur, Z. L. Liau, J. W. Mayer, Appl. Phys. Lett, **34**,168 (1978)

Appendix. A Micromagnetics

Results from micromagnetics calculations presented in this thesis were performed using the OOMMF (Object Oriented Micromagnetic Framework) public domain code, from the National Institute of Standards and Technology. The 2-D code, developed by M. J. Donahue and D. G. Porter, release 1.1b0 was employed[1].

Micromagnetics problems were solved by integrating the Landau-Lifshitz Gilbert (LLG) equation of motion, over a series of time steps until a pre-defined convergence event is met.

A finite element modelling technique is employed. A two-dimensional mesh of nodes defines structure lateral boundaries, each cube representing a single magnetic spin. A 5 nm meshing discrimination was used for all simulations shown.

Standard Permalloy parameters were used for calculations. An exchange constant of $A = 1.3 \times 10^{-11}$ Jm^{-1}, and saturation magnetization value, $M_s = 8 \times 10^5$ Am^{-1} were used. A damping constant of $\alpha = 0.015$ was set for dynamic simulations. The simulations were performed at 0 K.

[1] http://math.nist.gov/oommf/

Appendix. B Trapping and Range of Ions in Matter

Calculated TRIM[1] results for the mean ion penetration depth, the surface sputter yield per incident ion, and the number of vacancies per incident ion, for $Ni_{81}Fe_{19}$, Si, Al and Au.

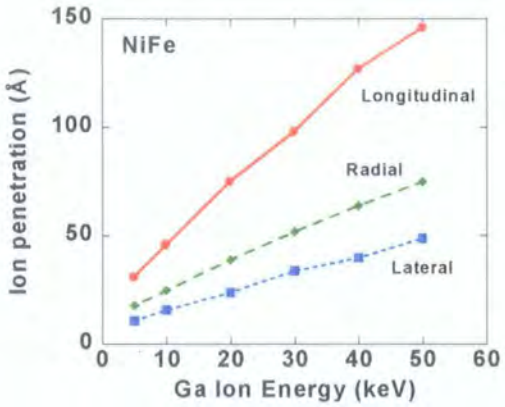

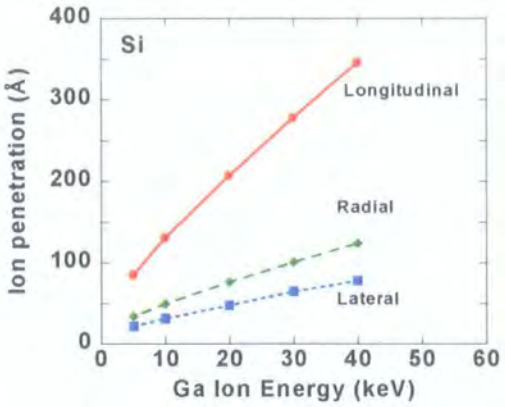

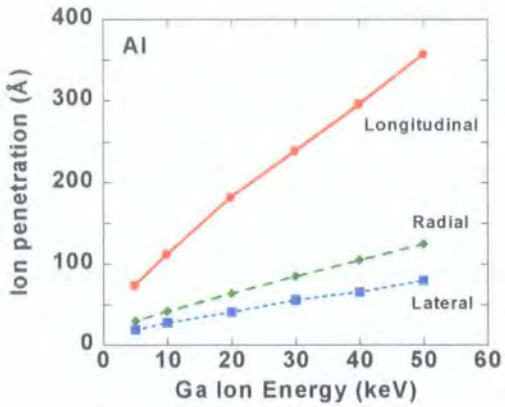

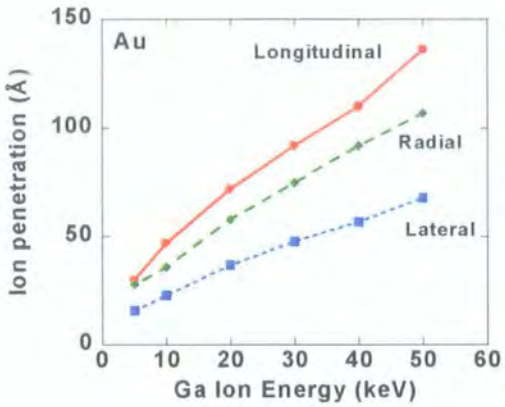

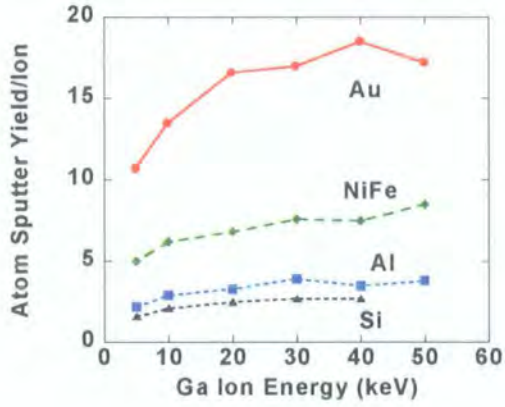

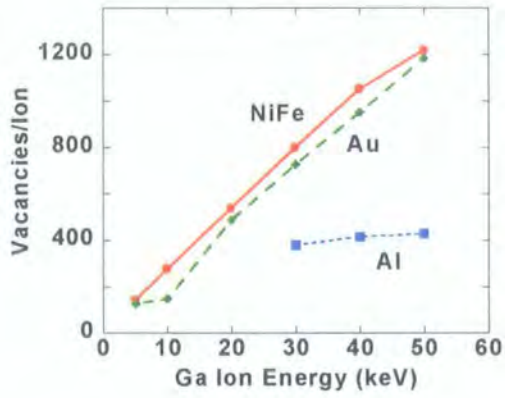

[1] Ion-atom collisions were studied using ballistic TRIM Monte Carlo simulations in which successive ion collisions are treated as independent. J. Ziegler, J. Biersack, U. Littmark, The stopping of ions in matter (Pergamon, New York, 1985); SRIM code (URL: http://www.srim.org)

Appendix C. FIB patterned ferromagnetic structures in sputtered Al(4nm)/NiFe(5nm)/Si

Sputtered NiFe(5nm)/Si

Initial investigations into the Ga^+ ion induced quenching of measured ferromagnetism in bilayers were performed on sputter grown magnetic thin films.

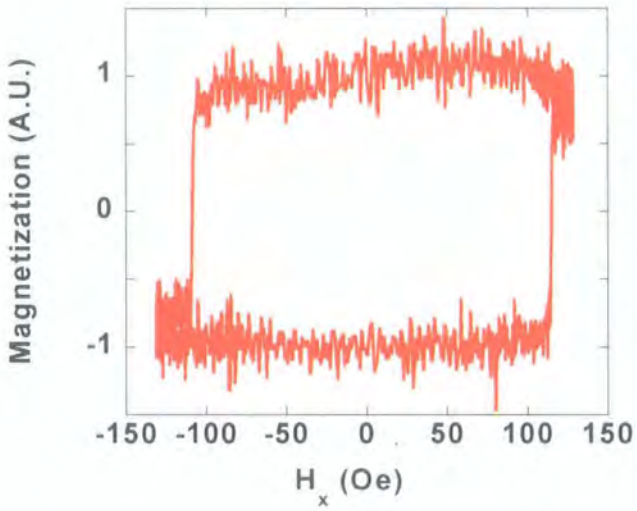

Fig.1: Time averaged M-H loop for a high aspect ratio 200 nm wide NiFe wire on a Si substrate, patterned by Ga^+ ion irradiation, incident at a free vacuum/NiFe surface.

Fig.1 evinces good single domain switching behaviour for a FIB patterned high aspect ratio 200 nm wide NiFe wire on a Si substrate, with no capping layer.

Sputtered Al(4nm)/NiFe(5nm)/Si

Here we present M-H loops for nano-wires, domain wall injection pads structures, patterned arrays and corner structures fabricated in a layered sputter deposited film. An Al(4nm)/NiFe(5nm)/Si parent film was patterned by localized ion beam milling. Capped structures were fabricated with reproducible switching and sub 200 nm resolution feature sizes.

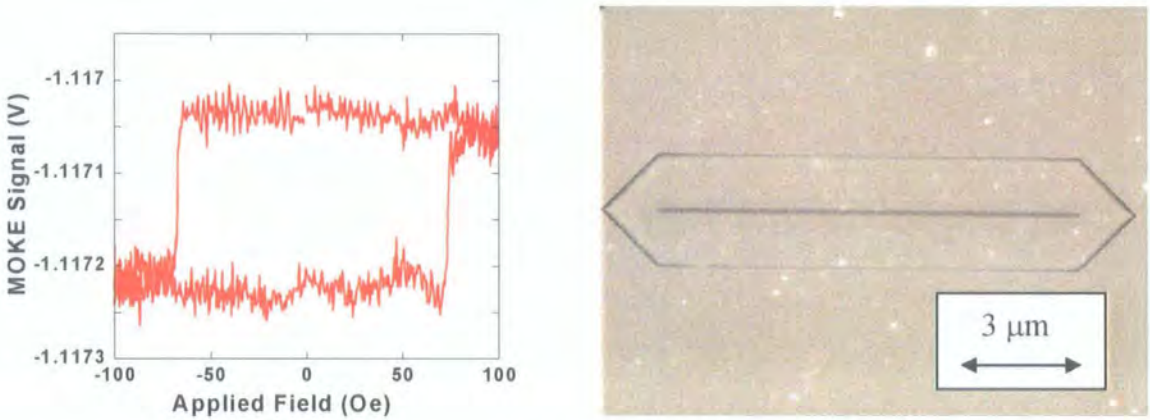

Fig.2: Time averaged M-H loop for a high aspect ratio 200 nm wide NiFe wire capped with Al on a Si substrate, patterned by Ga^+ ion irradiation, incident at the vacuum/Al surface. Wire ends are pointed. Also shown is an SEM image of the wire.

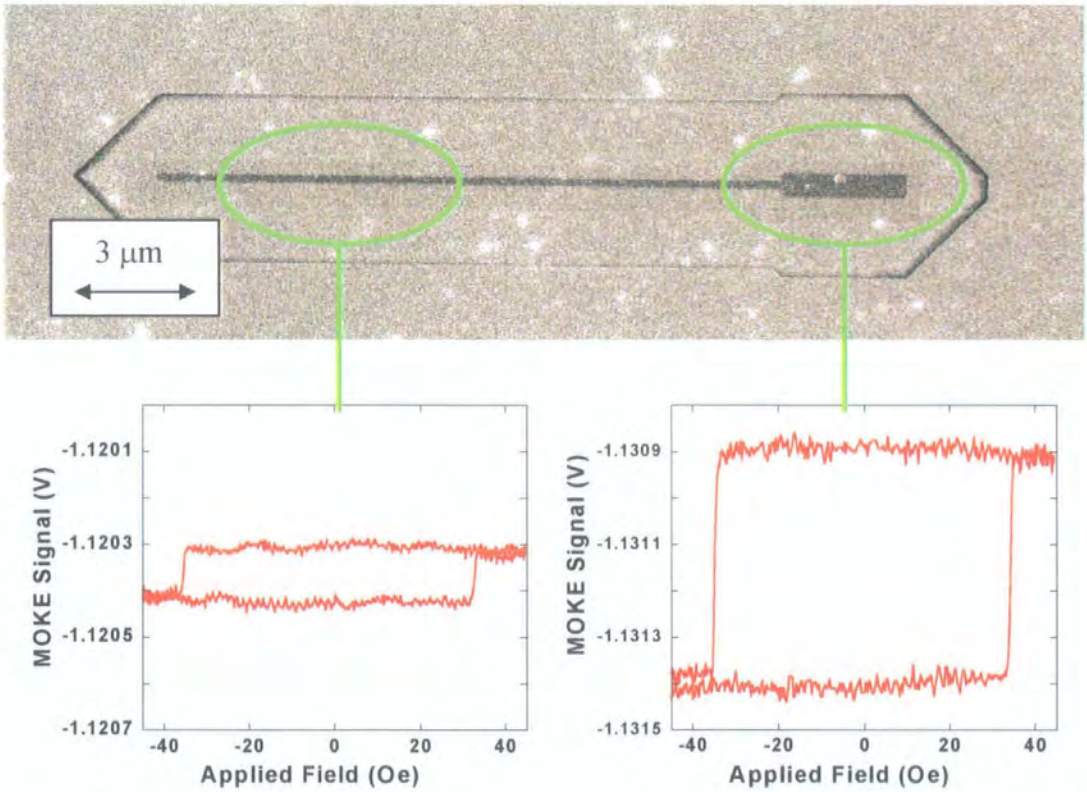

Fig.3: Time averaged localized M-H loops of a domain wall injection pad structure for a high aspect ratio, 200 nm wide NiFe wire capped with Al on a Si substrate. Patterning was by Ga^+ ion irradiation, incident at a free vacuum/NiFe surface. Also shown is an SEM image of the structure.

Figures 2-3 demonstrate bistable switching in a patterned Al/NiFe/Si wire sample at a switching field of ~ 70 Oe (Fig. 3), and magnetic switching engineered by domain wall injection at 35 Oe (Fig. 4).

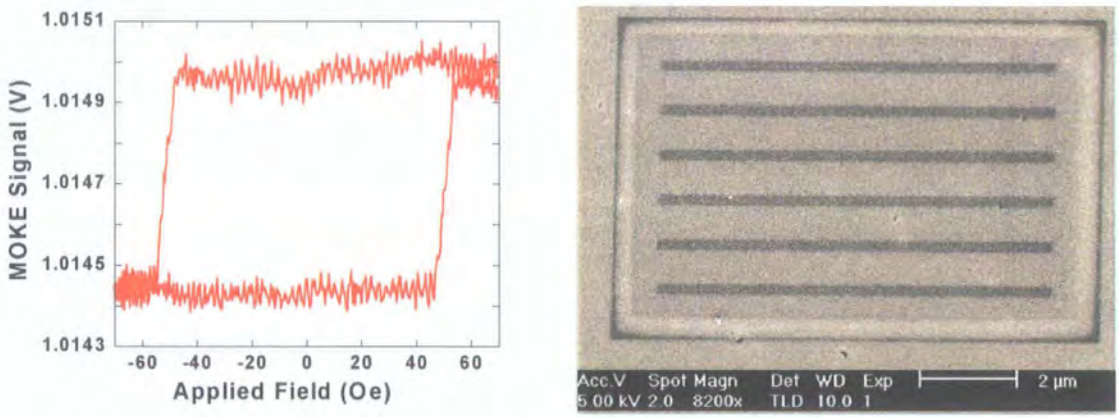

Fig.4: Hysteresis loop for an array of 6 flat-ended 200 nm wide wires, 8 microns long, and the associated scanning electron micrograph.

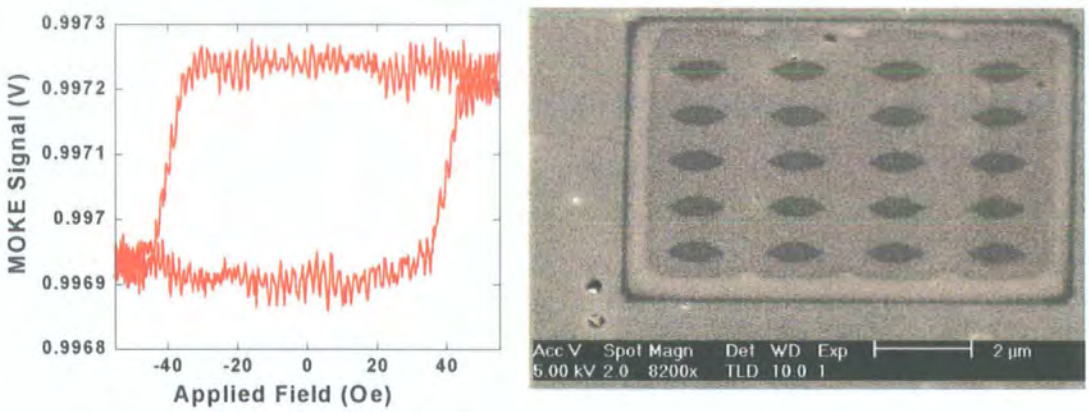

Fig.5: M-H loop for an array of 20 capped hexagons, 1200 nm long and 400 nm wide, and a SEM micrograph of the fabricated structures, showing good structural uniformity over an array of 20 components.

Figures 4-5 demonstrate good reproducible magnetic switching for arrays of patterned structures in capped NiFe films.

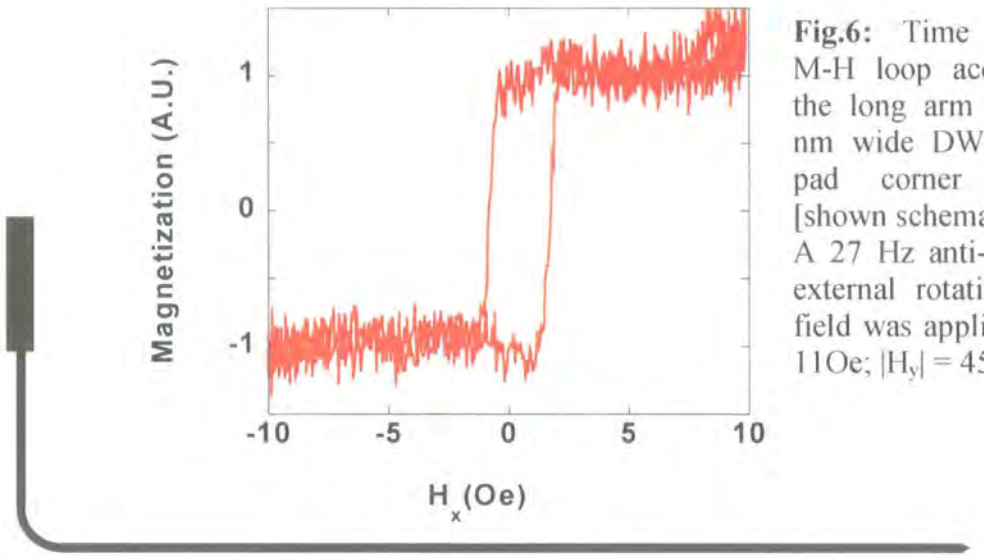

Fig.6: Time averaged M-H loop acquired on the long arm of a 200 nm wide DW injection pad corner structure [shown schematically]. A 27 Hz anti-clockwise external rotating vector field was applied [$|H_x|$ = 11Oe; $|H_y|$ = 45 Oe].

Fig. 6 shows switching along the output wire of a corner structure in a capped film, engineered by domain wall injection.